DISCLAIMER:

This document does not meet the
current format guidelines of
the Graduate School at
The University of Texas at Austin.

It has been published for
informational use only.

The Dissertation Committee for Brian William Goodfellow Certifies that this is the approved version of the following dissertation:

Colloidal Nanocrystal Assemblies: Self-Organization, Properties, and Applications in Photovoltaics

Committee:

Brian A. Korgel, Supervisor

James R. Chelikowsky

Ananth Dodabalapur

John G. Ekerdt

David A. Vanden Bout

Colloidal Nanocrystal Assemblies: Self-Organization, Properties, and Applications in Photovoltaics

by

Brian William Goodfellow, B.S.

Dissertation

Presented to the Faculty of the Graduate School of

The University of Texas at Austin

in Partial Fulfillment

of the Requirements

for the Degree of

Doctor of Philosophy

The University of Texas at Austin

December 2011

Dedication

To Jessica and my parents

Acknowledgements

The time I have spent in graduate school has been some of the most rewarding years of my life thus far—enriched with exceptional learning opportunities and personal growth. I owe a great deal of gratitude to the many people that have provided guidance, support, and friendship along the way.

First, I would like to thank my research advisor, Dr. Brian Korgel, for providing the opportunity and the resources to accomplish this work over the past five years. His enthusiasm for science and his constant stream of ideas and insight are truly inspirational. I am grateful for all the knowledge and advice he imparted to me and that he encouraged me to develop and pursue my ideas.

I would like to thank my fellow Korgelites who were so incredibly enjoyable to work with. In particular, I would like to thank Dr. Vahid Akhavan and Matt Panthani for their work on the photovoltaics project. There was never a dull moment—even when we were spending days on end "watching paint dry." I would like to thank Dr. Danielle Smith for teaching me about nanocrystal superlattice assembly and Mike Rasch for his assistance in exploring the amazing properties of assemblies of very small gold nanocrystals. I would like to thank Dr. Reken Patel, Dr. Andy Heitsch, Vince Holmberg, Dr. Colin Hessel, Hyun Park, Julian Villarreal, Yixuan Yu, and Chris Bosoy for braving research trips with me to CHESS and spending many sleep-deprived days doing experiments. I thank Dr. Hsing-Yu Tuan, Dr. Doh Lee, Dr. Dayne Fanfair, Dr. Damon Smith, Dr. Bonil Koo, Aaron Chockla, Justin Harris, Chet Steinhagen, Dr. Jose Luis Hueso, Kate Shipman, Tim Bogart, and Xiaotang Lu for many discussions and for being great colleagues. I especially thank Dr. Andy Heitsch for allowing me into the "fortress

of solitude" for many lively and insightful discussions in front of his chalkboard. Recently, I have had the pleasure to work with Yixuan Yu and Chris Bosoy on nanocrystal assembly and Taylor Harvey and Jackson Stolle on nanocrystal-based photovoltaics. I would like to thank them for their hard work and their fresh perspectives on this ongoing research. I would also like to thank super-undergraduate researchers Danny Hellebusch and Dariya Reid whose work on the photovoltaics project was invaluable.

I was lucky to collaborate with many talented scientists during my graduate studies. I would like to thank Dr. Detlef Smilgies whose D1 beamline at CHESS offered an enormous opportunity to study the structure and behavior of nanocrystal assemblies and who always entertained my sometimes "crazy" experiments and provided very helpful advice and discussion. I would like to thank Micah Glaz, Dave Ostrowski and Dr. David Vanden Bout whose LBIC microscopy of our photovoltaic devices was key in understanding their performance. I would also like to thank Dr. Paul Barbara, Dr. Ananth Dodabalapur, Dr. Allen Bard, Takuji Adachi, Dr. Johanna Schmidtke, Dr. Heechang Ye, Hyun Park, Dr. Lawrence Dunn, and Dr. Chris Lombardo who also collaborated with me on the photovoltaics work.

Finally, I would like to thank my family. It certainly would have not been possible for me to come this far without the continuing support of my parents, Peggy and Ray Goodfellow, who have always believed in me. Thanks also go out to my sister, Katie Goodfellow, for her enthusiasm of my endeavors. Last but not least, I owe an enormous amount of gratitude to Jessica Shafer who has been there for me though many celebrations and disappointments and has always encouraged me to continue striving for the best. Her optimistic and enthusiastic nature has a continuing influence on my life and her love and support has enabled this milestone achievement.

Colloidal Nanocrystal Assemblies: Self-Organization, Properties, and Applications in Photovoltaics

Brian William Goodfellow, Ph.D.

The University of Texas at Austin, 2011

Supervisor: Brian A. Korgel

Colloidal nanocrystal assemblies offer an attractive opportunity for designer metamaterials. The ability to permute chemical composition, size, shape, and arrangement of nanocrystals leads to an astounding number of unique materials properties that find use in an extensive array of applications—ranging from solar cells to medicine. However, to take full advantage of these materials in useful applications, the nature of their assembly and their behavior under external stimuli must be well-understood. Additionally, the assembly of colloidal nanocrystals into thin films provides a promising pathway to the solution-processing of inorganic materials that are prohibitively too expensive and/or difficult to deposit by conventional methods.

Nanocrystal superlattices (NCSLs) of sterically stabilized nanocrystals were assembled by slow evaporation of colloidal dispersions on various substrates. Detailed analysis of the NCSL structures was carried out using transmission and scanning electron microscopy (TEM and SEM) and small-angle x-ray scattering (SAXS). Body-centered cubic (bcc) NCSLs, in particular, were studied in detail and ligand packing frustration was proposed as a significant driving force for their assembly. The behavior of NCSLs was also studied by SAXS under mild heating and solvent vapor exposure revealing

several remarkable order-order, order-disorder, and amorphous-crystalline structural transitions.

Colloidal $Cu(In_{1-x}Ga_x)Se_2$ (CIGS) nanocrystals were synthesized by arrested precipitation and formulated into inks. These inks were spray deposited into thin films under ambient conditions to serve as the active light absorbing material in printed low-cost photovoltaic (PV) devices. These devices, which were fabricated without the need for high temperature processes, have achieved power conversion efficiencies above 3 % under AM1.5 illumination. While the efficiencies of these devices are still too low for commercial viability, this work does provide a proof of concept that reasonable efficient solar cells can be created with a low-cost printable process using nanocrystal inks. Since high temperatures are not used to form the light-absorbing layer, nanocrystal-based solar cells were built on flexible light weight plastic substrates. The main obstacle to achieving high power conversation efficiencies was found to be the ability to extract the photo induced charge carriers. Nanocrystal films suffer from poor transport that leads to high recombination rates in thicker films. To date, the best efficiencies have been achieved with thin light absorber layers that only absorb a fraction of the incident light.

Table of Contents

List of Tables

List of Figures

Figure 2.6: GISAXS measurements of BSLs assembled with 6.1 nm and 11.5 nm Au and Fe_2O_3 nanocrystals. The white circles in (a) correspond to the simulated diffraction spot pattern for a slightly distorted sh-AB_2 BSL with lattice dimensions b=c=13.8 nm, a=12.7 nm, γ=123.0^o, which corresponds also to a centered orthorhombic (SG 65, *Cmmm*) unit cell oriented with the [010] direction normal to the substrate with dimensions a=c=13.8 nm, b=21.273 nm. The grey circles in (a) correspond to (011) and (111) spots of an sh-AB_2 lattice oriented with the crystallographic direction [001] normal to the substrate with unit cell dimensions of a=b=13.8 nm, c=12.3 nm. (see Figure 2.8 for a complete simulation and indexing of the (001) orientation) (b) Simulated diffraction spots for sh-AB2 BSLs oriented on (100) planes with unit cell dimensions and a uniaxial lattice compression in the [210] direction of (grey dots) 13.8 nm, 12% and (white circles) 14.3 nm, 8% (which corresponds to a centered orthorhombic (SG65, *Cmmm*) lattice oriented in the [010] direction normal to the substrate with unit cell dimensions of (grey dots) a=c=13.8 nm, b=21.0 nm, and (white circles) a=c=14.3 nm, b=22.8 nm.) (c) Scattering pattern with rings of small spots indicated with dashed lines (A-F). (d) Radial integration of the scattering data in (c); Table 2.2 provides the q-values, d-spacings, and indices of the GISAXS data. (e) Schematic of the GISAXS configuration: incident x-ray beam, sample and sample manipulation, scattered beams, and area detector.....28

Chapter 1: Introduction[†]

The unique properties of nanometer-sized materials have been used for hundreds, perhaps thousands, of years. For example, the vivid red color of medieval stained-glass windows is a result of very small gold particles that were formed when gold ions were reduced during the production of the glass. The red color of these small gold particles differs significantly from the color of bulk gold due to their size-dependent interactions with optical electromagnetic radiation. Today, this optical phenomenon is well-understood. The concept that the properties of a material can dramatically change when it is sufficiently spatially confined has invigorated scientists in recent years, resulting in a prolific stream of new discoveries and technologies based on nanomaterials.

In the last several decades, the ability to synthesize colloidal nanomaterials by arrested precipitation with controlled size, shape, and composition has unlocked a new materials platform useful for studying fundamental properties at the nanoscale and for developing new technologies. To date, colloidal nanocrystals of a wide range of materials—including metals, semiconductors, insulators, and magnetic materials—have been synthesized and exhibit size-, shape-, and composition-dependent properties which can be synthetically tuned. Furthermore, if the nanocrystals have a sufficiently narrow size distribution, they will self-assemble into ordered structures with well-defined symmetry and spacing upon the evaporation of the solvent in which they dispersed. These ordered nanocrystal assembles, or superlattices, represent unique *metamaterials* in which the nanocrystals serve as modular building blocks for nanostructures with spatial complexity. Unlike atoms, the nanocrystal components making up the superlattices can

[†] Portions of this chapter appear in Goodfellow, Brian W.; Korgel, Brian A., "Reversible Solvent Vapor-Mediated Phase Changes in Nanocrystal Superlattices." *ACS Nano* (2011), 5(4), 2419-2424 and Akhavan, Vahid A.; Goodfellow, Brian W.; Panthani, Matthew G.; Korgel, Brian A., "Towards a Next Generation of Ultra-ow-cost Photovoltaics Using Nanocrystal Inks." *Modern Energy Review* (2010), 2(2), 27-29

be engineered to exhibit a desired property. Therefore, these so-called "artificial solids" can be designed with an astounding number of collective properties due to the ability to permute chemical composition, size, shape, and arrangement of the nanocrystals. The remarkable versatility and unique properties of nanocrystal assemblies make them attractive for a variety of applications from solar cells to medicine. However, successful application of colloidal nanocrystal assemblies will first require a detailed understanding of how the nanocrystals self-organize and the properties of the nanocrystal superlattices under various external stimuli.

This dissertation discusses the self-assembly of nanocrystals into superlattices, the properties of the assemblies at elevated temperature, and the use of semiconductor nanocrystals as light-absorbing layers in low-cost solar cells.

1.1 Self-Organized Nanocrystal Assemblies

A wide variety of materials self-organize into complex and precisely defined arrangements. Perhaps the most elaborate of these are biological materials, like polypeptides, that encompass only a limited number of individual components and assemble into a seemingly limitless range of structures, performing countless biological functions. Many natural non-living materials also exhibit sophisticated organization by self-assembly. The Brazilian opal is a good example of this, composed of highly monodisperse collections of sub-micrometer silica particles molded over time and packed tightly into a lattice. As synthetic methods for nanocrystals of a wide range of materials have developed—along with an understanding of their unique properties—nanocrystal self-assembly has been targeted as a route to obtain materials with complicated structure and unprecedented function.[1-3] The concept is simple: combine nanocrystals and allow

(or coax) them to self-assemble into ordered superstructures. In order to harness the power of self-assembly in artificial, engineered systems, a fundamental understanding of the forces and processes that control self-assembly are needed.

1.1.1 Energetic Considerations for Nanoscale Assembly

Based on simple packing rules of spheres, a monodisperse collection of spherical, organic ligand-coated nanocrystals is expected to form a face-centered cubic (fcc) lattice. When dispersed in a good solvent, the nanocrystals experience a short-ranged steric repulsion, pretty close to that of hard spheres.[4] When the nanocrystals are compressed together and the density of the collection exceeds a critical value—for example when the solvent is evaporated from the dispersion—the nanocrystals spontaneously order into a superlattice. This ordering transition is driven by entropy. With negligible energetic interactions between nanocrystals, only the excluded volume of each particle matters and the structure with the highest entropy is favored. It is easy to appreciate that the fcc lattice is the structure with the highest packing entropy by considering the entropy of an ideal gas of N particles in a volume V: $S/N = k \ln V$ (k is Boltzmann's constant). The *free volume entropy* depends on the way the particles are arranged. For a collection of hard spheres of volume v_s, the free volume is $V - Nv_s = 1 - (\phi/\phi_c)$, expressed in terms of the volume fraction of particles ϕ, and the jamming limit or maximum density of the spheres ϕ_c, determined by the specific structural arrangement, and the free volume entropy is $S/N \propto k \ln(1 - (\phi/\phi_c))$. A disordered collection of spheres can only pack to a limit of $\phi_c = 64\%$ before becoming *jammed*. Spheres in an fcc lattice—the densest possible arrangement of spheres—can achieve much higher densities, up to $\phi_c = 74\%$. It is obvious then that the free volume entropy of particles at density of 64% is much higher

when arranged in an fcc lattice than in a jammed configuration (where S=0). Indeed, fcc superlattices of a wide variety of nanocrystals have been observed.[1,2,4,5]

But when the solvent has evaporated, the nanocrystals are clearly not interacting as hard spheres. The nanocrystals in a "dry" superlattice are held together by strong cohesive interactions between neighboring ligands and nanocrystals. The melting point of dodecanethiol for example is about -8^{o}C, but a superlattice of dodecanethiol-capped gold nanocrystals is a solid at room temperature. Perhaps not surprisingly then, a variety of superlattice structures in addition to fcc have been observed, including hexagonal close-packed (hcp),[6,7] body-centered cubic (bcc),[2,8,5] body-centered tetragonal (bct)[2,5] and the simple hexagonal (sh)[7] lattice. The bcc, bct and sh lattices are particularly interesting because they are not close-packed structures and the free volume, or packing, entropy of the spheres is not maximized. For example, $\phi_c = 68\%$ for a bcc lattice. The situation has become ever more complicated with the study of ordered arrangements of nanocrystals of two different sizes, so-called binary nanocrystal superlattices. By 2006, a tremendous structural diversity of binary nanocrystal superlattices had been observed, many of which do not follow simple space-filling rules expected for hard spheres.[3]

Nonetheless, most superlattices, even binary nanocrystal superlattices,[9-11] do not deviate all that far from expectations based on maximized sphere packing density, and this concept has served as a pretty good conceptual guideline for understanding superlattic structure. The challenge has been to understand how the ligand shell contributes to superlattice order. Unlike sub-micrometer colloidal particles such as those that form opals in nature, ligand-coated nanocrystals have a significant volume of deformable soft organic shell material, making them "soft spheres" with an inner rigid non-deformable core.[4]

1.1.2 Multicomponent Nanocrystal Superlattices

When two distinct types of nanocrystals, each with their own size distribution, are deposited onto a substrate by solvent evaporation, the nanocrystals can arrange into a complex superlattice containing both types of nanocrystals instead of two separate fcc superlattices. Some of these binary superlattices, such as the simple hexagonal AB_2 superlattice shown in Figure 1.1 are expected to form based on space-filling arguments. However, many other structures have now been observed with can not be explained by hard-sphere packing. Therefore, a complex mix of factors to the interparticle potential have been proposed to account for this behavior, including van der Waals attraction, steric repulsion, electrostatic and dipolar interactions, and depletion attractions.

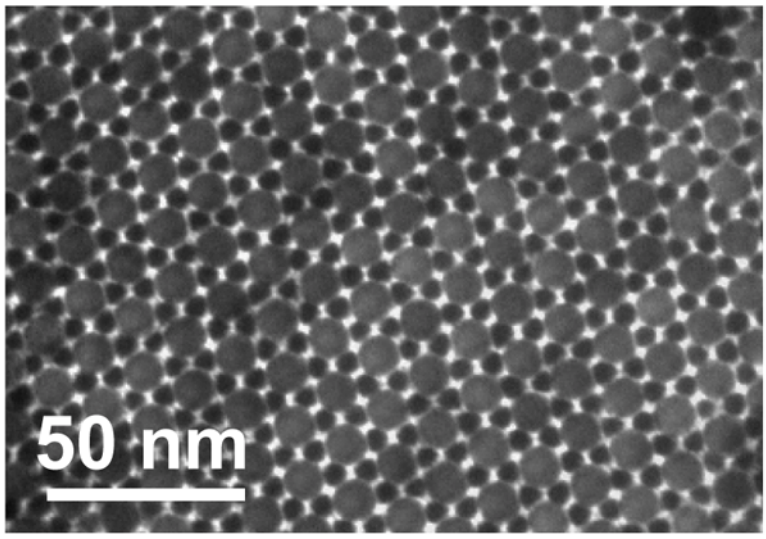

Figure 1.1: TEM image of a binary nanocrystal superlattice (BNSL) consisting of dodecanethiol-capped gold nanocrystals (small) and oleic acid-capped iron oxide nanocrystals (large). The nanocrystals have arranged into a simple hexagonal AB_2 structure which is structurally analogous to the mineral AlB_2.

Multicomponent nanocrystal superlattices like the one shown in Figure 1.1 can provide a platform to design and study materials with unprecedented structural complexity and unique functions. Unlike conventional composite materials, like fiber reinforced polymers, in which the constituent materials act in tandem to display a desired intermediate property, multicomponent nanocrystal superlattices where nanocrystals in close proximity can induce synergistic processes in each other can exhibit collective properties that significantly differ from the properties of the individual constituents.

1.1.3 Temperature-Induced Structural Transformations

From a fundamental perspective, nanocrystals are simple molecular models that can be manipulated and studied to test statistical mechanical and thermodynamic models of crystallization and disorder. The structural relationship between nanocrystal superlattices and the atomic crystal structure of minerals have given credence to the idea that nanocrystal assembles are "artificial solids". However, these metamaterials are governed by different forces than their atomic analogues. These forces are tunable in the case of nanocrystals and can be engineered to study the thermodynamic behavior of crystals in new ways. Many materials exhibit complex phase behavior based on temperature, pressure, and composition. The study of the phase behavior of nanocrystal solids under elevated temperature or pressure is still in its infancy. Further studies can lead to a greater understanding not only of the forces that contribute to nanocrystal assembly but also the thermodynamics of crystals in general—advancing the ability of scientists to engineer materials with new properties.

1.2 NANOCRYSTAL-BASED PHOTOVOLTAICS

The average price of solar power is now \$0.29/kWh,[12,13] which is about three times higher than the retail cost of electricity in the US.[14] At the moment, more than 50% of the total cost of photovoltaic (PV) electricity is associated with the price of the module, and grid parity requires significant reductions in solar cell manufacturing costs. The solar cell market is dominated by crystalline silicon-based modules[15] and since 2004, the cost of these modules has decreased by only 5%.[15] Significant price reductions for crystalline silicon-based solar cells have been slow because it is both a relatively mature technology with largely optimized device efficiency,[12,16] and the raw materials costs are significant. The cost of silicon alone contributes as much as 50% of the module cost and 28% of the total cost[12] because very thick silicon layers of more than 500 μm are needed (silicon is a very inefficient light absorber) and the competition for highly purified electronic grade silicon with the microelectronics industry keeps the price of silicon high.[17]

1.2.1 Alternatives to Silicon

A "second generation" of silicon-alternative PV technologies that utilize thin absorber layers has been developed, utlizing materials like amorphous silicon, CdTe, and copper indium gallium selenide (CIGS).[18] The device efficiencies are not quite as high as those using crystalline silicon, but the manufacturing costs are significantly lower. The cost of solar power depends roughly on the ratio of the efficiency to the manufacturing and installation costs, making these technologies competitive with silicon, and now garner about one-fourth of the PV market share.[15] First Solar's new CdTe PV technology has recently been reported with a module sale price of only \$0.98/W_p,[19] just below the \$1/Wp level that many considered the target for grid parity.

The manufacturing processes for these silicon alternatives nonetheless are still relatively slow and expensive, requiring high temperature processing steps that make an order of magnitude reduction in manufacturing cost unlikely. New approaches, with the potential for dramatic reductions in cost, are desired.

1.2.2 Third-Generation Photovoltaics and the Printed Inorganic Thin-Film Solar Cell

At the moment, a materials system and processing approach with the potential for both high efficiency and ultralow cost has not been identified. Such a technology would most likely need to be compatible with high-throughput roll-to-roll deposition and inexpensive plastic flexible and light-weight substrates. The "third generation" PV devices would yield efficiencies above 10%, as needed for commercial viability, but with dramatically reduced manufacturing costs.[18]

One target has been to create a technology for fabricating plastic disposable solar cells. As a step in this direction, photovoltaic devices made with organic light-absorbing materials have been made—so-called organic photovoltaics (OPVs)— with efficiencies as high as 7.4%.[20] For commercial viability, the device efficiency must still be improved and the materials costs for these record devices are in fact relatively expensive. And there is a concern about long-term OPV device stability under the typical operating conditions in the field.

Another approach to PV fabrication that has the processing attributes of organic materials, but combines the proven device performance and stability of inorganic materials, is to formulate nanocrystal inks that can be deposited under mild conditions using high throughput continuous processes like roll coating, spray-coating, spin coating, dip-coating, drop casting, ink-jet printing, doctor-blading, screen printing, etc.[21] If solar cells could be made without the need for high temperature or high vacuum processing,

these inks could dramatically lower solar cell module manufacturing costs. A light-weight solar cell on plastic would also significantly lower the installation costs. Since the module price accounts for only half of the total solar energy cost, this is a very important consideration.[12] The conventional solar cell fabrication processes, requiring high temperature, must be carried out on heavy glass or metal supports, which comprise the majority of the weight in commercial solar modules. Light and flexible panels would change the way solar cells are installed, enabling more efficient transportation and installation. The "panels" could be unrolled like a carpet and mounted on residential rooftops with no need for mounting brackets and structural reinforcement to the roof.

1.2.3 Nanocrystal Ink Formulation

Chemical methods have been developed to synthesize nanocrystals of many different materials suitable for PV devices. The nanocrystals are made by a process called arrested precipitation. Chemical reactants are decomposed in a solvent in the presence of "capping ligands" that bond to the nanocrystal surface as illustrated in Figure 1. The capping ligands are an integral part of the nanocrystal formulation, enabling good dispersion in solvents by preventing aggregation. This is important for uniform film deposition and device fabrication.

Many research teams have now demonstrated that it is indeed possible to print inorganic layers of light-absorbing semiconductors from nanocrystal inks and make functioning solar cells. Nanocrystals of cadmium and lead based chalcogenides (i.e. CdS, CdSe, CdTe, PbS, PbSe, and PbTe) have been incorporated into PV devices with reasonable efficiencies between 2% and 5%.[22-26] Cu_2S solar cells made from a nanocrystal ink has also been made, with efficiencies of up to 1.6%.[27] And nanocrystals of relatively complicated composition have also been synthesized, including tertiary and

quaternary compounds.[28-31] Of these materials, some of the most interesting have been copper indium gallium selenide (CIGS)[28,29] and copper zinc tin sulfide (CZTS),[30,31] as these are proven solar cell materials and do not face the same negative environmental implications as widespread Cd and Pb incorporation into solar cells.

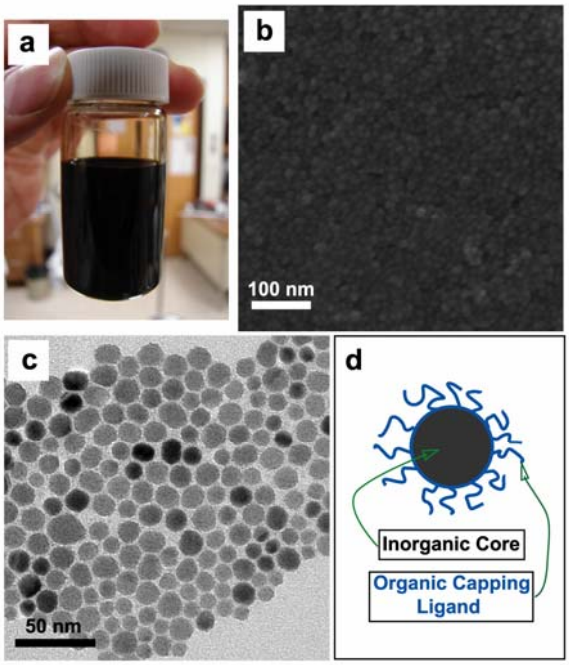

Figure 1.2: (a) Photogrpah of a CIGS nanocrystal ink; (b) a large-area scanning electron micrograph of a nanocrystal film deposited by spray-coating the ink; (c) transmission electron micrograph of CIGS nanocrystals; and (d) an illustration of a nanocrystal, that depicts the inorganic crystalline core coated by the organic capping ligand layer that stabilizes the nanocrystals.

1.2.4 Copper Indium Gallium Selenide Nanocrystal Inks

To date, the highest device efficiency achieved by a photovoltaic device fabricated by nanocrystal ink deposition is just over 10%, reported by Hillhouse and Agrawal for CIGS.[32] This work provides an important and encouraging benchmark for

PV devices made using nanocrystal inks, and has demonstrated that nanocrystal inks can indeed provide commercially viable efficiencies. There is a catch however, in that these efficiencies were achieved by annealing the films at rather extreme temperatures, exceeding 500°C, under Se atmosphere. Such extreme processing conditions make it impossible to fabricate devices by a roll-to-roll process, or on cheap plastic substrates. Nonetheless, CIGS is a particularly interesting semiconductor for a nanocrystal ink-based approach to solar cell fabrication.

Single-junction CIGS cells fabricated using state-of-the-art high temperature vacuum deposition processes have achieved device efficiencies of nearly 20%.[33] These devices are made with polycrystalline films, so these very high efficiencies are rather remarkable. Theoretical calculations and experimental analyses have shown that polycrystalline CIGS films can behave similar to a perfect single crystal in terms of minority carrier transport.[34,35] Since nanocrystal-based films inherently have very high concentrations of grain boundaries, this property of CIGS makes it a promising material for a nanocrystal ink approach to solar cell fabrication in terms of potentially achieving commercially viable efficiencies

Quaternary elemental stoichiometry and specific crystal structure of CIGS film make the vacuum deposition process very challenging across large substrate areas.[36] In this context, nanocrystal inks can be synthesized with the desired composition and stoichiometry and then deposited from the ink onto the substrate. In fact, we've demonstrated that that CIGS layers with controlled stoichiometry can be spray-painted in air at room temperature with nanocrystal inks, and that these films can be used to construct PVs with efficiencies of about 3% without any high temperature post-deposition processing (see Figure 1.3). The same concept has been demonstrated with CZTS nanocrystals as well.[38, 30] The inks make it possible to deposit semiconductor

absorber layers of materials with complicated phase behavior that are difficult or may even be impossible to deposit effectively by vapor-phase processes.

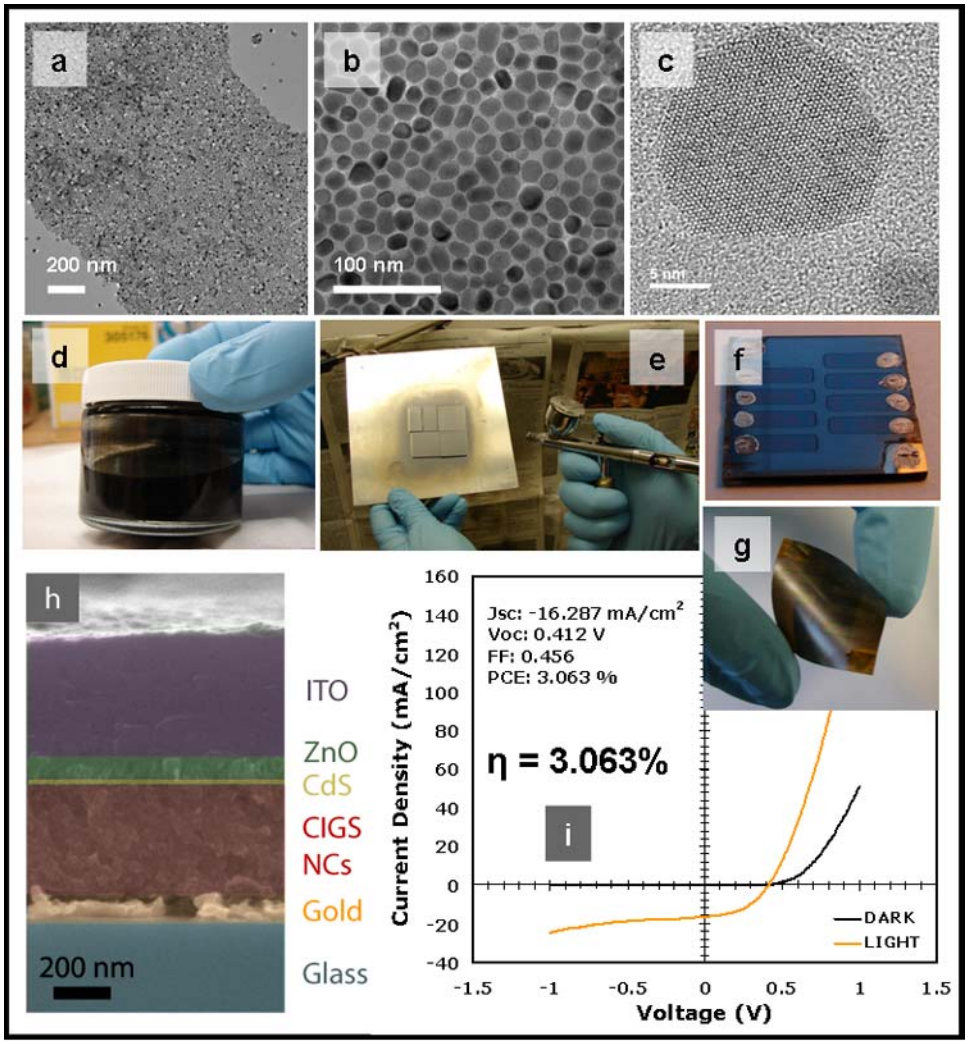

Figure 1.3: (a-c) Transmission electron microscopy (TEM) images of CIGS nanocrystals, (d) CIGS nanocrystal-based "ink" used in making solar cells, (e) spray-deposition of "ink" to form a light-absorbing layer, (f) image of a CIGS nanocrystal-based solar cell on a glass substrate and (g) on a flexible plastic substrate, (h) cross-sectional scanning electron microscopy (SEM) image of a solar cell made with CIGS nanocrystals, (i) I-V curves of a solar cell made with CIGS nanocrystals that shows a power conversion efficiency of more than 3%.

Thus far, CIGS PVs made from nanocrystal inks without post-deposition processing have achieved efficiencies of just over 3% (Figure 1.3i). The device layers exhibit the desired compositional uniformity, however, the significant presence of grain boundaries between particles in the absorber layer limits the device efficiency. These printed inorganic PVs exhibit open circuit voltage and fill factor near those made by vapor deposition processes, but the short circuit currents are much less than those of state-of-the-art CIGS devices (Figure 2). Electrons and holes are trapped at interfaces between the nanocrystals in the absorber film, leading to losses in efficiency. It is encouraging, however, that the nanocrystal inks can be deposited on any type of support (Figure 3g) to fabricate PV devices and achieve similar efficiencies. The key issue to address is the role of the grain boundaries and how to passivate them. Routes to improving the electrical properties of nanocrystal films without resorting to high temperature annealing, still remains and active area of research with much that is not known.

1.3 DISSERTATION OVERVIEW

The synthesis of simple hexagonal AB_2 binary nanocrystal superlattices composed of Au and Fe_2O_3 nanocrystals and their structural characterization by TEM, SEM, and GISAXS is discussed in Chapter 2. Non-close-packed body-centered cubic (bcc) superlattices and the roll of ligand packing frustration in their assembly are discussed in Chapter 3. The temperature-induced melting, sintering, and chemical transformations of bcc superlattices of oleic acid-capped PbSe nanocrystals are discussed

in Chapter 4. Order-order phase transitions of heated dodecanethiol-capped Au nanocrystal superlattices are discussed in Chapter 5. The use of $Cu(In_{1-x}Ga_x)Se_2$ nanocrystal inks as precursors for light-absorbing layers in low-cost printable solar cells is discussed in Chapter 6. The mapping of local performance of $Cu(In_{1-x}Ga_x)Se_2$ nanocrystal-based solar cells by scanning optical microscopy is discussed in Chapter 7. A summary of the work presented in this dissertation and suggested future research directions are presented in Chapter 8.

1.4 REFERENCES AND NOTES

1. Murray, C. B.; Kagan, C. R.; Bawendi, M. G., Self-Organization of CdSe Nanocrystallites into Three-Dimensional Quantum Dot Superlattices. *Science* **1995**, *270*, 1336-1338.
2. Whetten, R. L.; Shafigullin, M. N.; Khoury, J. T.; Schaaff, T. G.; Vezmar, I.; Alvarez, M. M.; Wilkinson, A., Crystal Structures of Molecular Gold Nanocrystal Arrays. *Acc. Chem. Res.* **1999**, *32*, 397-406.
3. Shevchenko, E. V.; Talapin, D. V.; Kotov, N. A.; O'Brien, S.; Murray, C. B., Structural Diversity in Binary Nanoparticle Superlattices. *Nature* **2006**, *439*, 55-59.
4. Korgel, B. A.; Fullam, S.; Connolly, S.; Fitzmaurice, D., Assembly and Self-Organization of Silver Nanocrystal Superlattices: Ordered "Soft Spheres." *J. Phys. Chem. B* **1998**, *102*, 8379-8388.
5. Korgel, B. A.; Fitzmaurice, D., Small-angle X-ray Scattering Study of Silver-Nanocrystal Disorder-Order Phase Transitions. *Phys. Rev. B* **1999**, *59*, 14191-14201.
6. Harfenist, S. A.; Wang, Z. L.; Whetten, R. L.; Vezmar, I.; Alvarez, M. M., Three-Dimensional Hexagonal Close-Packed Superlattice of Passivated Ag Nanocrystals. *Adv. Mater.* **1997**, *9*, 817-822.
7. Talapin, D. V.; Shevchenko, E. V.; Murray, C. B.; Titov, A. V.; Král, P., Dipole-Dipole Interactions in Nanoparticle Superlattices. *Nano Lett.* **2007**, *7*, 1213-1219.
8. Whetten, R. L.; Khoury, J. T.; Alvarez, M. M.; Murthy, S.; Vezmar, I.; Wang, Z. L.; Stephens, P. W.; Cleveland, C. L.; Luedtke, W. D.; Landman, U., Nanocrystal Gold Molecules. *Adv. Mater.* **1996**, *8*, 428-433.

9. Chen, Z.; Moore, J.; Radtke, G.; Sirringhaus, H.; O'Brien, S., Binary Nanoparticle Superlattices in the Semiconductor-Semiconductor System: CdTe and CdSe. *J. Am. Chem. Soc.* **2007**, *129*, 15702-15709.

10. Chen, Z.; O'Brien, S., Structure Direction of II-VI Semiconductor Quantum Dot Binary Nanoparticle Superlattices by Tuning Radius Ratio. *ACS Nano* **2008**, *2*, 1219-1229.

11. Smith, D. K.; Goodfellow, B.; Smilgies, D.-M.; Korgel, B. A., Self-Assembled Simple Hexagonal AB_2 Binary Nanocrystal Superlattices: SEM, GISAXS, and Defects. *J. Am. Chem. Soc.* **2009**, *131*, 3281-3290.

12. Kazmerski LL, *J Electron Spectroscopy*, **2006**; 150:103–135.

13. Singh PP, Singh S, *Renewable Energy*, **2010**; 35:563–569.

14. U.S. Department of Energy, Energy Information Administration: Electric Power Monthly. January 2009, Available at: http://www.eia.doe.gov/cneaf/electricity/epm/epm_sum.html.

15. International Energy Agency: Photovoltaic Power Systems Programme. PV Trends, **2009**

16. Swanson RM, *Proceedings of the 31st IEEE Conference*. IEEE, New York, 2005. 889–894

17. Tao M, *Electrochemical Society Interface*. **2008**; 17:30-35.

18. Green MA, Third Generation Photovoltaics: Advanced Solar energy Conversion. Springer, New York, 2003.

19. First Solar Press Release. Company Cuts Manufacturing Cost to 98 Cents per Watt in Forth Quarter, 2009: Available at http://investor.firstsolar.com/phoenix.zhtml?c=201491&p=irol-newsArticle&ID=1259614&highlight=

20. Liang Y, Xu Z, Xia J, Tsai ST, Wu Y, Li G, Ray C, Yu L, *Adv. Mater.* **2010**; in press.

21. Krebs FC, *Solar Energy Materials & Solar Cells***, 2009**; 93:394–412.

22. Gur I, Fromer NA, Geier ML, Alivisatos AP, *Science*, **2005**; 310:462-465.

23. Luther J.M, Law M, Beard MC, Song Q, Reese MO, Ellingson RJ, Nozik AJ, *Nano Lett*, **2008**; 8:3488–3492.

24. Ma W, Luther JM, Zheng H, Wu Y, Alivisatos AP,.*Nano Lett*, **2009**; 9:1699–1703.

25. Koleilat GI, Levina L, Shukla H, Myrskog SH, Hinds S, Pattantyus-Abraham AG, Sargent EH, *ACS Nano*, **2008**; 2:833-840.

26. Choi ,JJ Lim YF, Santiago-Berrios MB, Oh M, Hyun BR, Sun L, Bartnik AC, Goedhart A, Malliaras GG, Abruna HD, Wise FW, Hanrath T, *Nano Lett*, **2009**; 9:3749-3755.

27. Wu Y, Wadia C, Ma W, Sadtler B, Alivisatos AP, *Nano Lett*, **2008** ; 8 :2551-2555.

28. Panthani MG, Akhavan V, Goodfellow B, Schmidtke JP, Dunn L, Dodabalapur A, Barbara PF, Korgel BA, *J Am Chem Soc*, **2008**; 130:16770-16777.

29. Guo Q, Kim SJ, Kar M, Shafarman WN, Birkmire RW, Stach EA, Agrawal R, Hillhouse HW, *Nano Lett*, **2008**; 8:2982-2987.

30. Steinhagen C, Panthani MG, Akhavan V, Goodfellow B, Koo B, Korgel BA, *J Am Chem Soc*, **2009**; 131:12554-12555.

31. Guo Q, Hillhouse HW, Agrawal R, *J Am Chem Soc*, **2009**; 131:11672-11673.

32. Guo Q, Hillhouse HW, Agrawal R., *2009 AIChE Annual Meeting.* **2009**; 447C.

33. Repins I, Contreras MA, Egaas B, DeHart C, Schart J, Perkins CL, To B, Noufi R, *Progress in Photovoltaics*, **2008**; 16:235-239.

34. Persson C, Zunger A, *Phys Rev Lett*, **2003**; 91:26.

35. Jiang CS, Noufi R, AbuShama JA, Rmanathan K, Moutinho HR, Pankow J, Al-Jassim MM, *Appl Phys Lett*, **2004**; 84:18.

36. Noufi R, Axton R, Herrington C, Deb SK, *Appl Phys Lett*, **1984**; 45:668–670.

Chapter 2: Structure of Self-Assembled AB_2 Binary Nanocrystal Superlattices: SEM, GISAXS, and Defects†

2.1 INTRODUCTION

Binary nanocrystal superlattices (BSLs)—*e.g.*, periodically-ordered arrays of nanocrystals with two different well-defined diameters—have been reported with astonishingly diverse structures, including those that are isostructural with AlB_2,[1-8] CaB_6,[2,3] $CaCu_5$,[1-3,5,7,9,10] CuAu,[2,3,5,10] Cu_3Au,[2,3] $NaZn_{13}$,[1-4,7,11] Fe_4C,[2,3] $MgNi_2$,[2] $MgZn_2$,[2,3,7] NaCl,[2-4,12,13] and NiAs[4] compounds. Since nanocrystals can be synthesized with a wide variety of chemical and physical properties, including magnets,[14] metals,[15] semiconductors,[16] and even more complex multifunctional heterostructures,[16-25] they provide a library of assorted materials suited for new technologies in the biological sciences,[26-29] computing and information storage,[14,30] photovoltaics,[31] and thermoelectrics.[13] By merging nanocrystals into BSLs, *metamaterials* may be fabricated with new, unique characteristics that result from their nanoscale organization and interplay of their constituent properties.[32] For example, magnetic and semiconductor nanocrystals might be mixed to form new breeds of magneto-optic materials,[11] mixtures of different magnetic nanocrystals may lead to higher energy density magnetic properties,[30,33] and mixtures of semiconductors may be used for optoelectronic applications, like higher performance photovoltaics.[34] In one study that exemplifies this idea, BSLs of PbTe and Ag_2Te nanocrystals were more than 100 times more electrically conductive than superlattices of only PbTe or Ag_2Te nanocrystals.[13]

To design and engineer BSL properties, their assembly must be well understood. Some BSL structures are expected based on geometrical packing arguments for spheres,

† Portions of this chapter appear in Smith, Danielle; Goodfellow, Brian; Smilgies, Detlef-M.; Korgel, Brian, "Self-Assembled Simple Hexagonal AB_2 Binary Nanocrystal Superlattices: SEM, GISAXS and Defects." *Journal of the American Chemical Society* (2009), 131 (9), 3281–3290.

as in the case of cubic AB (NaCl) and simple hexagonal AB_2 (AlB_2) structures in which nanocrystals fill space as efficiently as possible.[34] But many observed BSL structures, such as cub-AB_{13},[11] $CaCu_5$,[1-3,5,7,9,10], Fe_4C,[2,3] Cu_3Au,[2,3] are not *closest*-packed arrangements.[35] Therefore, a variety of other factors in addition to space-filling arguments have been proposed to be important in determining BSL structure, including size- and composition-dependent interparticle forces, including van der Waals attractions,[36,37] ligand-ligand interactions,[38] capillary forces,[39] electrostatic interactions,[2] and kinetic factors.[3,9,40] But the matter is complicated by the fact that the BSL structures reported thus far have had relatively short-range order (<3 μm) and structural characterization has been carried out almost exclusively by transmission electron microscopy (TEM) of relatively thin samples. To date, no scanning electron microscopy (SEM) images or small angle X-ray scattering patterns (SAXS) of BSLs have been published, and it is therefore possible that some observed BSLs are only metastable or stabilized/induced by the substrate; thus, making it more complicated to identify the underlying forces responsible for BSL structure.

Herein, SEM and grazing incidence small-angle X-ray scattering (GISAXS) measurements of sh-AB_2 BSLs are presented, which confirm the existence of long-range order in sh-AB_2 BSLs. This data provides evidence that the sh-AB_2 BSL phase is indeed a thermodynamically stable phase for the nanocrystal size ratio studied here (0.53). BSLs, however, only formed when nanocrystals were deposited onto a tilted substrate by controlled slow evaporation from dispersions with excess oleic acid. This indicates that the forces driving BSL formation are relatively weak. Some diversity in BSL structure was nonetheless also observed, including (1) uniaxial superlattice shrinkage normal to the substrate from residual solvent evaporation; (2) nearly periodic dislocations consisting of inserted half-planes of Au nanocrystals; and in thin BSL layers, (3) an analog of an AB_{13}

phase in which Fe_2O_3 nanocrystals have substituted for Au nanocrystals in the 8a Wyckoff positions in the unit cell of space group 226, and (4) an "expanded" sh-AB_2 (100) plane.

2.2 EXPERIMENTAL SECTION

2.2.1 Materials and Supplies

All chemicals were used as received. Iron pentacarbonyl ($Fe(CO)_5$, 99.999%), oleic acid (99%), hydrogen tetrachloroaurate(III) hydrate (99.9+%), tetraoctylammonium bromide (TOAB, 98%), sodium borohydride ($NaBH_4$, 98+%), and dodecanethiol (≥98%) were purchased from Sigma-Aldrich. Dioctyl ether (>97%) was purchased from Fluka. Toluene (99.9%) was purchased from Fisher. Doubly-distilled deionized water (DI-H_2O) was used in all preparations.

2.2.2 Au Nanocrystal Synthesis

Dodecanethiol-coated 6.1 nm diameter Au nanocrystals were prepared as previously described.[41,42] In a 50 ml Erlenmeyer flask, 0.19 g of hydrogen tetrachloroaurate(III) hydrate was dissolved in 18 ml of DI water. 1.35 g of TOAB dissolved in 12.25 ml of toluene was added to the aqueous solution, and the mixture was stirred for one hour. The aqueous phase was discarded. A solution of 0.25 g of $NaBH_4$ dissolved in 15 ml of DI water was then added to the organic solution. This mixture was stirred for 20 hours. The aqueous phase was then discarded. 120 μL of dodecanethiol was added to the organic phase and the mixture was stirred for 1 hour.

The Au nanocrystals were isolated by first centrifuging the solution for 3 minutes at 8000 rpm and discarding the precipitate, which consists of poorly capped nanocrystals. The supernatant was collected and excess ethanol was added to precipitate the

nanocrystals and separate them from molecular impurities in the reaction. After centrifuging the solution for 8 minutes at 8500 rpm, the precipitate was collected and the supernatant discarded. The nanocrystals were redispersed in chloroform, followed by size-selective precipitation using ethanol as an antisolvent.[36,43] 6.1±0.73 (±12%) nm diameter Au nanocrystals were used for superlattice self-assembly.

2.2.3 Fe_2O_3 Nanocrystal Synthesis

Oleic acid-coated 11.5 nm diameter Fe_2O_3 nanocrystals with a 6% polydispersity were prepared under inert (N_2) atmosphere using standard glovebox and Schlenk line techniques and published procedures.[44] In a 25 ml three neck flask, 10 ml of dioctyl ether and 960 μL (4.56 mmol) of oleic acid were heated to 100 °C under N_2 flow at atmospheric pressure. 0.2 ml (1.52 mmol) of $Fe(CO)_5$ was injected into this solution. [Caution must be taken when preparing $Fe(CO)_5$, as it is extremely volatile and potentially hazardous (refer to MSDS before use).] The solution was refluxed at 300°C for one hour. The reaction flask was removed from the heating mantle and allowed to cool to room temperature. The flask was then opened to air for 30 minutes to oxidize the as-made Fe nanocrystals. This reaction solution containing the resulting Fe_2O_3 nanocrystals was then centrifuged for 5 minutes at 8000 rpm. The supernatant was collected and the precipitate, which consists of solid byproducts and poorly capped nanocrystals, was discarded. Excess ethanol was then added to the supernatant to precipitate the nanocrystals. This mixture was centrifuged for 10 minutes at 8000 rpm. The supernatant was discarded. The nanocrystals were further purified with two additional reprecipitation and centrifugation steps using hexane and ethanol as a solvent/antisolvent pair. 11.54±0.66 (±6%) nm diameter Fe_2O_3 nanocrystals were used for superlattice self-assembly.

2.2.4 Binary Nanocrystal Superlattice (BSL) Preparation

BSLs were assembled on various substrates, including TEM grids (carbon-coated copper 200 mesh, Electron Microscopy Sciences), Si wafers covered with native oxide (SEH America), or Si_3N_4-coated Si wafers, by controlled evaporation of a dispersing solvent as illustrated in Figure 2.1. The substrate is immersed in the dispersion (40 μL for a TEM grid, 350 μL for a Si or Si_3N_4 wafer) in a glass vial tilted at approximately 65° from vertical and the solvent is then allowed to evaporate over the course of several hours at 45°C in air. Table 2.1 shows the optimized solution conditions used to form sh-AB_2 BSLs. Extended BSL formation also required the addition of oleic acid to the nanocrystal dispersion. BSLs were not observed when dispersions were drop-cast onto flat TEM grids.

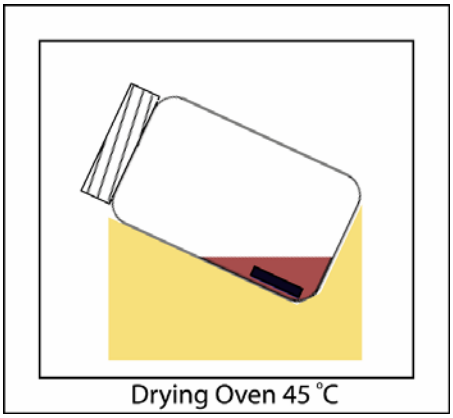

Figure 2.1: BSL self-assembly: A tilted vial with a substrate (black rectangle) immersed in the nanocrystal dispersion (shown in maroon) is placed in a drying oven at 45°C in air as shown. The substrate is left undisturbed as the solvent evaporates over the course of several hours.

Table 2.1: Binary Superlattice Preparation Parameters

Solvent	toluene[†]
Fe_2O_3 stock solution conc. (mg/mL)	4.0
Au stock solution conc. (mg/ml)	4.0
Targeted total particle conc (mg/ml)	0.5
Targeted Fe_2O_3: Au Number Ratio	1:2.5
Volume of Fe_2O_3 added (μl)	25
Volume of Au added (μl)	30
Volume of toluene added (μl)	385
Final volume (μl)	440
Number of Fe_2O_3 particles	1.9×10^{13}
Number of Au particles	4.7×10^{13}
Volume of oleic acid solution added (μl)	15.0

[†] Previous reports indicated that tetrachloroethylene (TCE),[6,7,9] or mixtures of toluene and TCE[2-4] worked best for BSL formation, but we found that toluene gave BSLs with more extensive order.

2.2.5 Materials Characterization

Transmission electron microscopy (TEM) was performed on either a Phillips EM208 TEM with 80 kV accelerating voltage or a JEOL 2010F with the field emission gun operated at 200 kV. Images were acquired digitally. Electron diffraction patterns were simulated using JEMS Electron Microscopy Software Package (Version 3.2710U2008, Copyright: P. Stadelmann, 1999-2008). Scanning electron microscopy (SEM) was performed on a Zeiss Supra 40 SEM with an in-lens arrangement at 10 keV working voltage and 5 mm lens to detector distance. Samples were grounded using copper tape to prevent charging.

Grazing incidence small angle X-ray scattering (GISAXS) measurements were performed on beam line D1 of the Cornell High Energy Synchrotron Source (CHESS) using monochromatic radiation of wavelength λ = 1.252 Å with a bandwidth $\Delta\lambda/\lambda$ of 1.5%. The x-ray beam was produced by a hardbent dipole magnet in the Cornell storage ring and monochromatized with Mo:B_4C multilayers with a period of 30 Å. The D1 area detector (MedOptics) is a fiber coupled CCD camera with a pixel size of 46.9 μm by 46.9 μm and a total of 1024 x 1024 pixels with a 14-bit dynamical range per pixel.[45] Typical read-out time per image was below 5 sec. The images were dark current corrected, distortion-corrected, and flat-field corrected by the acquisition software. The sample to detector distance was 935 mm, as determined using a silver behenate powder standard. The incident angle of the x-ray beam was varied from 0.05 º to 0.25º and typical exposure times were 100 seconds. Scattering images were calibrated and integrated using the Fit2D software.[46] The GISAXS diffraction peaks were indexed using the software package, NANOCELL[47] and our own software.[48]

2.3 RESULTS AND DISCUSSION

2.3.1 TEM and SEM

Figure 2.2 shows SEM images of BSLs of (A) 11.5 nm Fe_2O_3 and (B) 6.1 nm Au nanocrystals. The BSLs have a simple hexagonal (sh) AB_2 (AlB_2, space group 191, *P6/mmm*) structure as described in previous reports.[1-7] In the BSL, the large Fe_2O_3 nanocrystals occupy a simple hexagonal lattice with the smaller Au nanocrystals filling the trigonal prismatic interstitial spaces, as shown in Figure 2.3. Selected area electron diffraction (SAED) verified the presence of both Au and Fe_2O_3 nanocrystals in the BSLs, as shown in Figure 2.4. Figure 2.5 shows TEM images of the (100), (110) and (001)

surfaces of the BSLs. FFTs of the images index to the sh-AB_2 structure. The (100) and (001) spacings measured in TEM images were 12.6 nm and 14.1 nm, corresponding to lattice dimensions, a=14.5 nm and c=14.1 nm. From SEM images, the (100) and (001) spacings were found to be 12.2 nm and 14.4 nm, corresponding to lattice dimensions a=14.1 nm and c=14.4 nm.

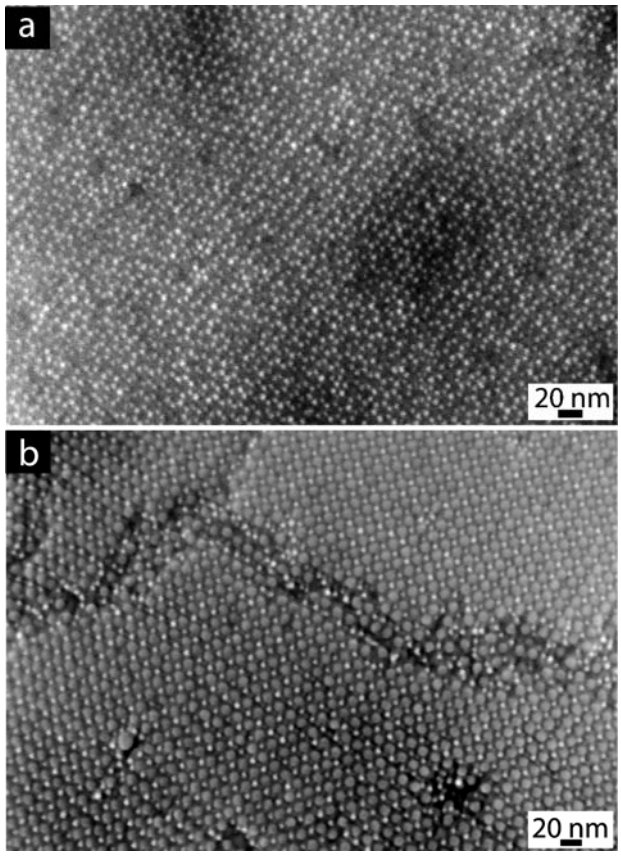

Figure 2.2: HRSEM images of sh-AB_2 BSLs on Si_3N_4-coated Si substrates with two different exposed BSL crystallographic surfaces: (a) (001) and (b) (100). Crystalline domains up to ~9 μm in diameter were observed.

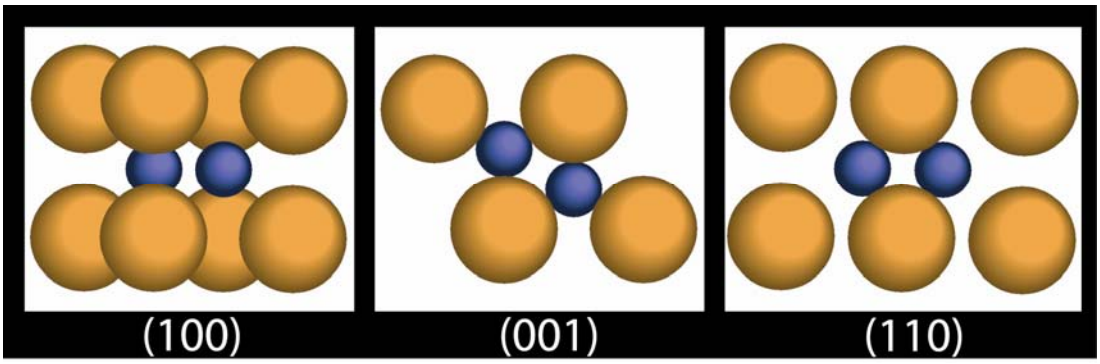

Figure 2.3: Different orientations of the sh-AB_2 (SG 191) unit cell. Orange spheres represent 11.5 nm Fe_2O_3 and blue spheres are 6.1 nm Au nanocrystals.

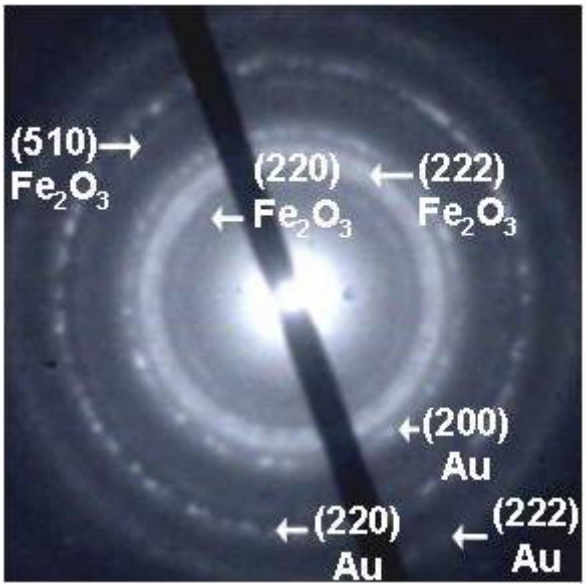

Figure 2.4: Wide-angle selective area electron diffraction acquired with the beam positioned down the $[100]_{BSL}$ sh-AB_2 BSL zone axis. The diffraction rings index to fcc Au and cubic γ-Fe_2O_3.

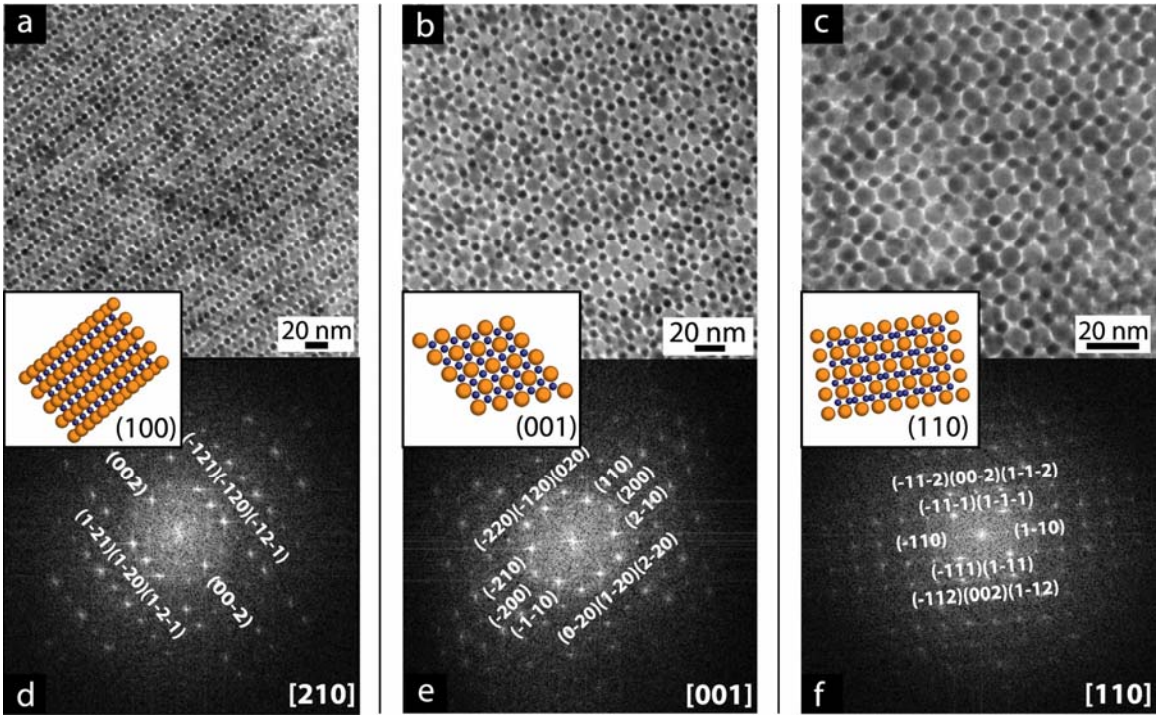

Figure 2.5: TEM images and FFTs of sh-AB_2 BSLs observed down three different zone axes to provide images of the corresponding lattice planes: (a,d) [210], (100); (b,e) [001], (001); and (c,f) [110], (110). The FFTs are indexed to sh-AB_2 lattice planes; the zone axes are given in the bottom right of the FFTs. Crystallographic models of the sh-AB_2 superlattices are provided in the insets; blue and orange spheres represent Au and Fe_2O_3 nanocrystals, respectively.

2.3.2 Grazing Incidence Small Angle X-ray Scattering (GISAXS)

GISAXS measurements were performed on the BSLs and distinct diffraction spots were observed, thus confirming relatively long range order in the superlattices. Figure 2.6 shows examples of GISAXS measurements of the BSLs, along with an illustration of the experimental system. All of the measured GISAXS patterns indexed to a sh-AB_2 BSL structure (with a slight lattice contraction of 8-12% normal to the substrate as described below). The diffraction spot sizes varied from broad to narrow features, indicating variability in the size of crystalline BSL grains and their crystallographic

superlattice orientations with respect to the substrate. Additional SEM images of BSLs are included in the supporting information, which clearly show that the BSL samples consist of multiple crystal grains with a variety of orientations on the substrate.

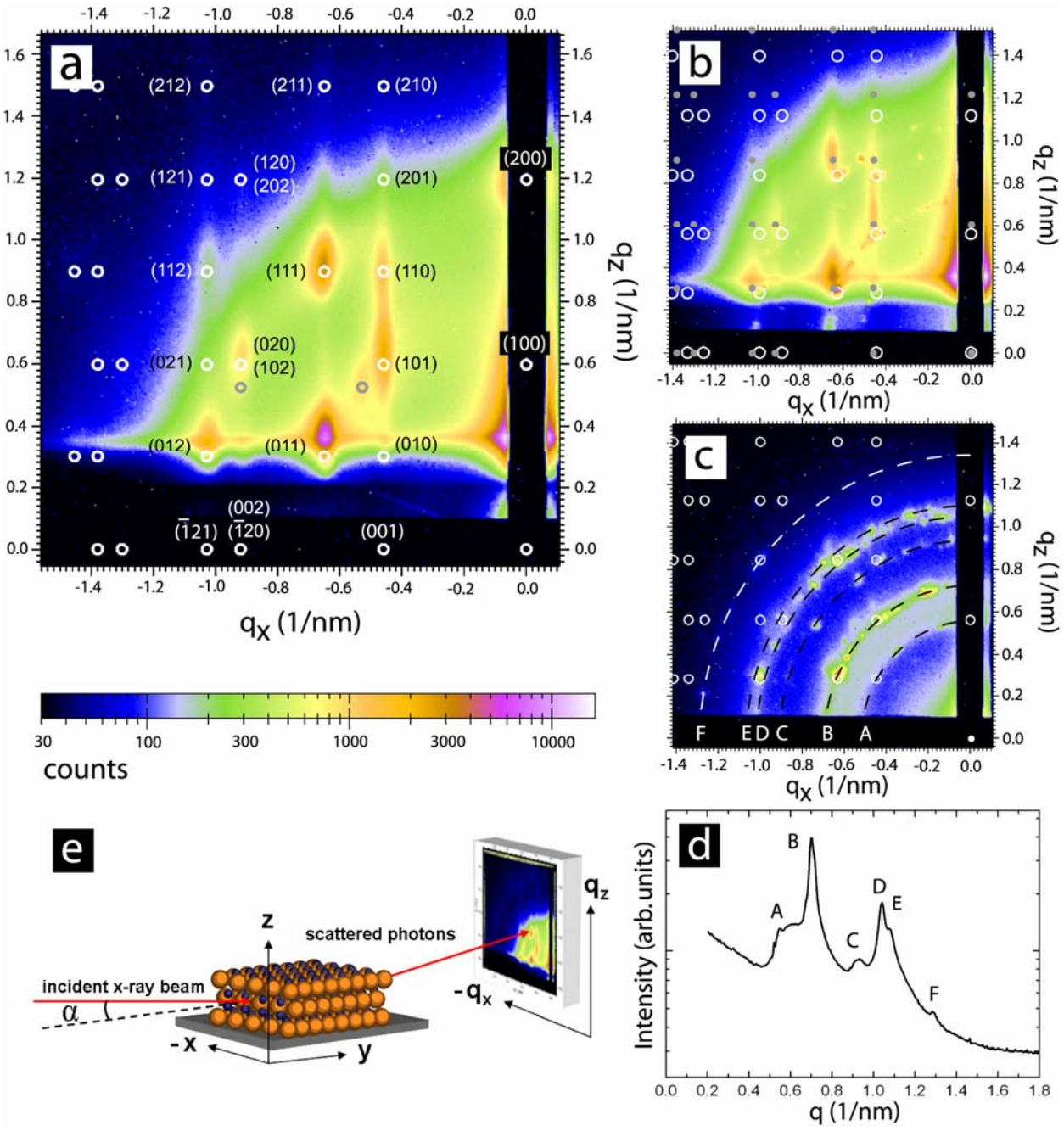

Figure 2.6: GISAXS measurements of BSLs assembled with 6.1 nm and 11.5 nm Au and Fe_2O_3 nanocrystals. The white circles in (a) correspond to the simulated diffraction spot pattern for a slightly distorted sh-AB_2 BSL with lattice dimensions b=c=13.8 nm, a=12.7 nm, γ=123.0^o, which corresponds also to a centered orthorhombic (SG 65, *Cmmm*) unit cell oriented with the [010] direction normal to the substrate with dimensions a=c=13.8 nm, b=21.273 nm. The grey circles in (a) correspond to (011) and (111) spots of an sh-AB_2 lattice oriented with the crystallographic direction [001] normal to the substrate with unit cell dimensions of a=b=13.8 nm, c=12.3 nm. (see Figure 2.8 for a complete simulation and indexing of the (001) orientation) (b) Simulated diffraction spots for sh-AB2 BSLs oriented on (100) planes with unit cell dimensions and a uniaxial lattice compression in the [210] direction of (grey dots) 13.8 nm, 12% and (white circles) 14.3 nm, 8% (which corresponds to a centered orthorhombic (SG65, *Cmmm*) lattice oriented in the [010] direction normal to the substrate with unit cell dimensions of (grey dots) a=c=13.8 nm, b=21.0 nm, and (white circles) a=c=14.3 nm, b=22.8 nm.) (c) Scattering pattern with rings of small spots indicated with dashed lines (A-F). (d) Radial integration of the scattering data in (c); Table 2.2 provides the q-values, d-spacings, and indices of the GISAXS data. (e) Schematic of the GISAXS configuration: incident x-ray beam, sample and sample manipulation, scattered beams, and area detector.

The GISAXS measurement in Figure 2.6a exhibits broad Bragg spots. These broad spots indicate that the scattering BSL grains are relatively small. The diffraction pattern indexes to a slightly distorted sh-AB_2 superlattice (AlB_2 analog, SG 191, *P6/mmm*) oriented on its (100) plane on the substrate with unit cell dimensions of $b=c=13.8$ nm, $a=12.7$ nm and $\gamma=123.0^{o}$. This structure corresponds to a simple hexagonal lattice with a uniaxial lattice contraction of 11% normal to the substrate in the [210] direction. This crystal structure is equivalent to a centered orthorhombic lattice oriented on a (010) plane with unit cell dimensions $a=c=13.8$ nm, $b=21.273$ nm (SG 65, *Cmmm*).

The GISAXS data in Figure 2.6a indicate that the sh-AB_2 BSL initially formed on the substrate with lattice dimensions of 13.8 nm and then contracted unidirectionally towards the substrate. This type of contraction normal to the substrate has been observed in other evaporated films as well, of ordered block copolymers,[49] mesoporous metal oxides,[50] and gold nanocrystal superlattices.[51] The lattice contraction results from the evaporation of residual solvent retained by the capping ligands just after BSL formation. As the residual solvent evaporates, the superlattice shrinks. But the nanocrystals cannot move laterally with respect to the substrate because their positions are fixed by adhesion to the substrate and as a result, the lattice decreases its total volume with a uniaxial compression towards the substrate.

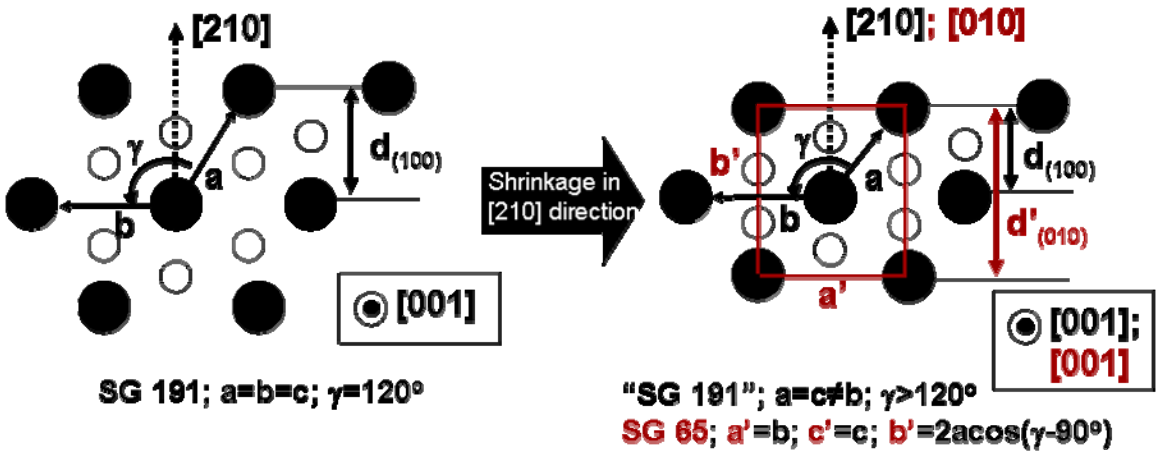

Figure 2.7: Depiction of the lattice contraction of a sh-AB_2 BSL that has contracted in the [210] direction during the late stages of drying. The BSL is oriented on its (100) plane and the contraction in the [210] direction changes the lattice symmetry from hexagonal to centered orthorhombic. The centered orthorhombic unit cell dimensions, *a*', *b*', *c*' are shown in red.

In addition to the diffraction spots in Figure 2.6a that index to sh-AB_2 BSL oriented on a (100) plane that has contracted in the [210] direction, there are two diffraction spots (labeled in gray) corresponding to sh-AB_2 BSL grains with a different crystallographic orientation on the substrate. These spots index to sh-AB_2 BSL grains oriented on their (001) planes that have contracted in the [001] direction, with unit cell dimensions of $a=b=13.8$ nm, $c=12.3$ nm. A full indexing of the diffraction spots associated with the (001) oriented BSL grains is shown in Figure 2.8.

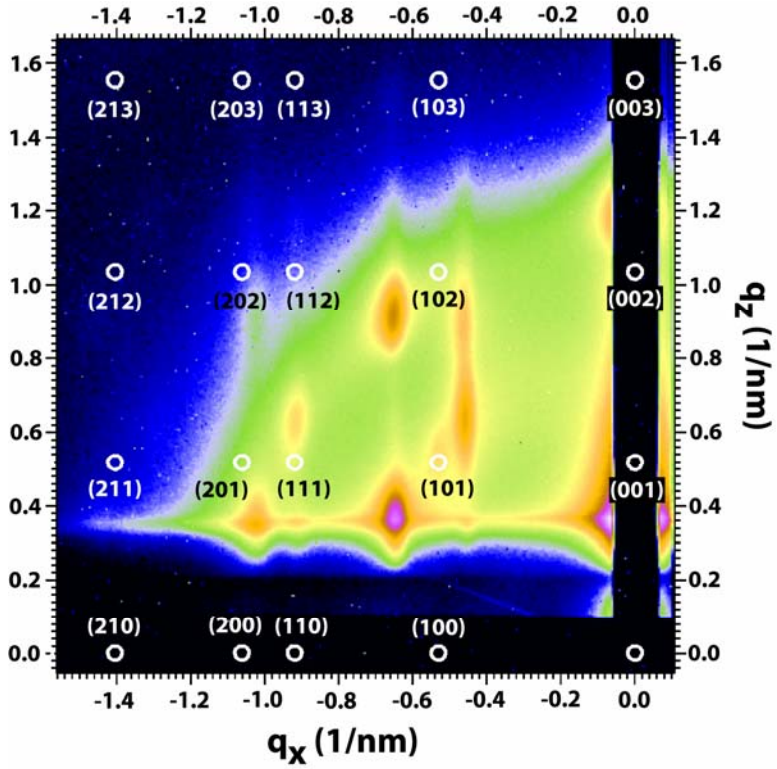

Figure 2.8: GISAXS simulation of the diffraction spot pattern produced from a sh-AB_2 (SG191; *P6/mmm*) lattice oriented with the (001) plane parallel to the substrate ([001] direction normal to the substrate) is overlaid onto GISAXS data of binary superlattices of 11.5 nm Fe_2O_3 and 6.1 nm Au nanocrystals. The lattice constants are a = 13.8 nm, b = 13.8 nm, and c = 12.28 nm, which corresponds to an 11% shrinkage along the c-axis.

The GISAXS patterns could not be indexed without considering the lattice contraction and the appropriate crystallographic orientation of the BSL grains on the substrate. Figure 2.6b provides another GISAXS example that reveals information about the superlattice orientation on the substrate and the uniaxial lattice compression that occurs perpendicular to the substrate. Both broad and narrow diffraction spots are present in Figure 2.6b, corresponding to relatively small and large superlattice grains, respectively. The broader diffraction spots indexed to a (100)-oriented sh-AB_2 BSL with lattice dimensions of 13.8 nm and a uniaxial lattice compression of 12% in the [210]

direction. One set of the narrower diffraction spots indexed to a (100)-oriented sh-AB_2 superlattice with lattice dimensions of 14.3 nm that has contracted by 8% normal to the substrate in the [210] direction. These data indicate that more lattice shrinkage has occurred in the smaller BSL grains than in the larger grains.

Figure 2.6c shows another example of a GISAXS pattern obtained from an Au/Fe_2O_3 nanocrystal BSL sample. The "rings" of small spots suggest that a coexistence of many large superlattice grains with varying orientations exists on the substrate. One set of diffraction spots indexes to an orthorhombic BSL oriented in the [010] direction normal to the substrate with unit cell dimensions a=c=14.2 nm, b=22.628 nm (corresponding to a sh-AB_2 lattice with initial unit cell dimensions of 14.2 nm that has been compressed in the [210] direction by 8%). The ring-like diffraction pattern provides averaged information about the structure of the BSL grains since the grains have various crystallographic orientations. Indexing this pattern is complicated by the fact that BSL grains will have slightly different lattice *symmetry* depending on their orientation on the substrate due to the difference in the lattice direction of the uniaxial shrinkage. Nonetheless, the pattern can be approximately indexed to a simple hexagonal lattice, with the corresponding d-spacings obtained from the q-values of the diffraction rings, $q = 2\pi/d$, provided in Table 2.2. Indexing the GISAXS data to a sh-AB_2 lattice gave lattice constants between 13.29 nm and 14.01 nm, which are consistent with what was found by TEM and SEM. But there is also a slight, but noticeable, anisotropy in the scattering rings. The diffraction features occur at slightly higher q in the x-direction than in the z-direction, which provides further indication of the lattice shrinkage normal to the substrate. Therefore, three different values of q (q_x, q_z and $<q>$) are provided in Table 2.2 for the scattering peak positions. The difference in these averaged lattice constants shows that the shrinkage is ~7%.

Table 2.2: Measured d-spacings from the GISAXS patterns in Figure 2.6c compared to the calculated d-spacings for a sh-AB2 lattice (given in parentheses)

Ring	q_x (nm^{-1})	$d = \frac{2\pi}{q_x}$ (nm)*	q_z (nm^{-1})	$d = \frac{2\pi}{q_z}$ (nm)†	<q>§ (nm^{-1})	$d = \frac{2\pi}{\langle q \rangle}$ (nm)‡	Indexed planes
A	0.51	12.320 (12.134)	0.55	11.424 (11.510)	0.55	11.424 (11.668)	{100}
B	0.68	9.240 (9.172)	0.72	8.727 (8.701)	0.70	8.976 (8.820)	{101}
C	0.90	6.981 (7.006)	0.935	6.720 (6.646)	0.935	6.756 (6.737)	{110}
D	1.01	6.221 (6.266)	1.05	5.984 (5.944)	1.05	6.041 (6.025)	{111}
E	1.06	5.928 (6.067)	1.10	5.712 (5.755)	1.10	5.818 (5.834)	{200}
F	1.28	4.909 (4.954)	1.34	4.689 (4.699)	1.34	4.689 (4.764)	{112}

d-spacings calculated for a simple hexagonal lattice (SG191) with lattice constants *a*=*b*=*c*=14.01nm,* *a*=*b*=*c*=13.29nm,† and *a*=*b*=*c*=13.47nm.‡

§ Average *q* values obtained from the radial integration of the GISAXS data in Figure 4c.

2.3.3 Dislocations in sh-AB_2 BSLs

Bright stripes of nanocrystals were visible in SEM images of some BSLs formed on Si_3N_4 wafers, as shown in Figure 2.9. The stripes were observed in superlattices with the (100) plane parallel to the substrate and were identified to be superlattice dislocations consisting of gold nanocrystal half-planes inserted into the lattice as illustrated in Figure 2.9. Tilting the sample and imaging by SEM confirmed that the stripes were not step edges.

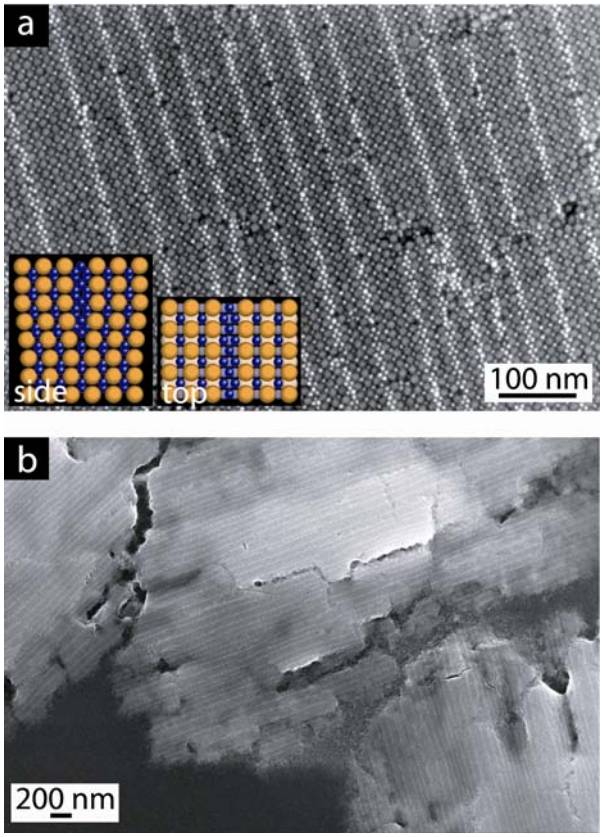

Figure 2.9: SEM images of superlattice dislocations: nearly periodic bright stripes are observed in these sh-AB_2 BSLs of 11.5 nm Fe_2O_3 and 6.1 nm Au nanocrystals oriented with (100) planes parallel to the substrate. The bright stripes are Au nanocrystal half-planes (dislocations) inserted into the lattice as illustrated in the inset in (a) as viewed from the side (looking at the (1-20) plane down the [010] axis) and from the top (looking at the (100) plane or down the [210] axis as viewed in the SEM images); the blue and orange spheres represent Au and Fe_2O_3 nanocrystals, respectively.

A correlation between the dislocation direction in neighboring superlattice islands, like those in Figure 2.9b and Figure 2.10, was observed. The inset in Figure 2.10 shows a histogram of the dislocation orientation measured from many BSL islands that were deposited on one substrate. The average dislocation orientation relative to the horizon in the figure is 37.3^o. These islands appear to break off from a common BSL layer that forms at the air/solvent interface to deposit on the substrate. Although the

drying direction is not known, the dislocation direction most likely occurs at 90^{o} with respect to the drying direction, as illustrated in the figure, arising from the strain imposed on the BSL from the curved air/solvent interface as illustrated in Figure 2.11. The dislocations relieve this strain as the superlattice forms.

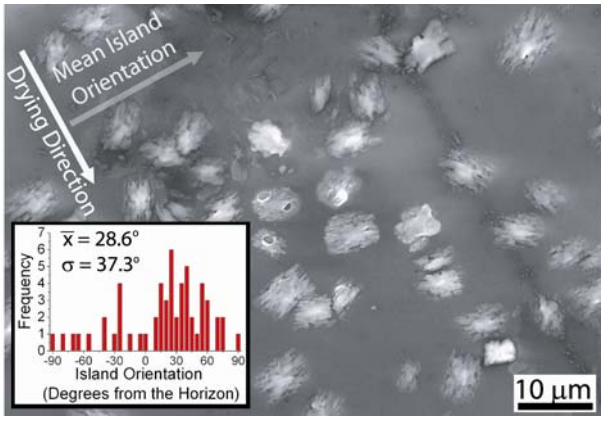

Figure 2.10: SEM image of BSL islands with visible inserted Au nanocrystal half-planes (dislocations). Inset: the orientational distribution of the dislocation direction with respect to the proposed drying direction indicated in the figure.

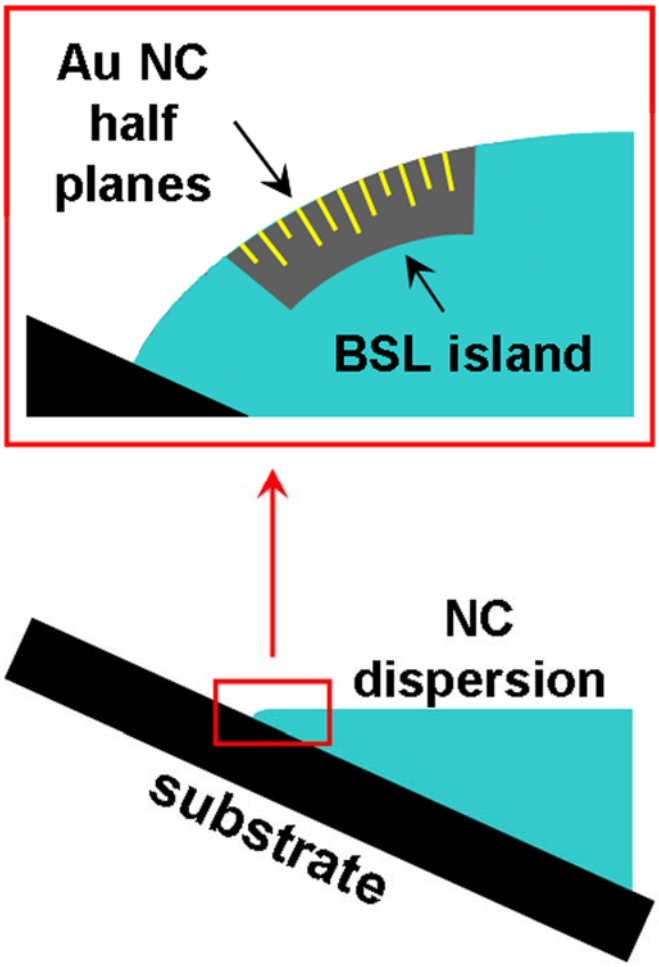

Figure 2.11: Illustration of the proposed mechanism of dislocation formation in the BSLs: gold nanocrystal half-planes insert into the crystallizing BSL to relieve strain at the curved air/solvent interface near the substrate.

2.3.4 Monolayers and Defects

An expansion of sh-AB_2 superlattice planes was observed in some thin superlattice layers. Figure 2.12a shows an example of such a sh-AB_2 superlattice, which has an unexpectedly large lattice constant of c=15.9 nm, compared to c=14.1 nm observed in thicker sh-AB_2 superlattice films such as those in Figures 2.12b and 2.12c.

The thin nanocrystal layer in the lower right corner of Figure 2.12a corresponds to a (100) sh-AB_2 plane.

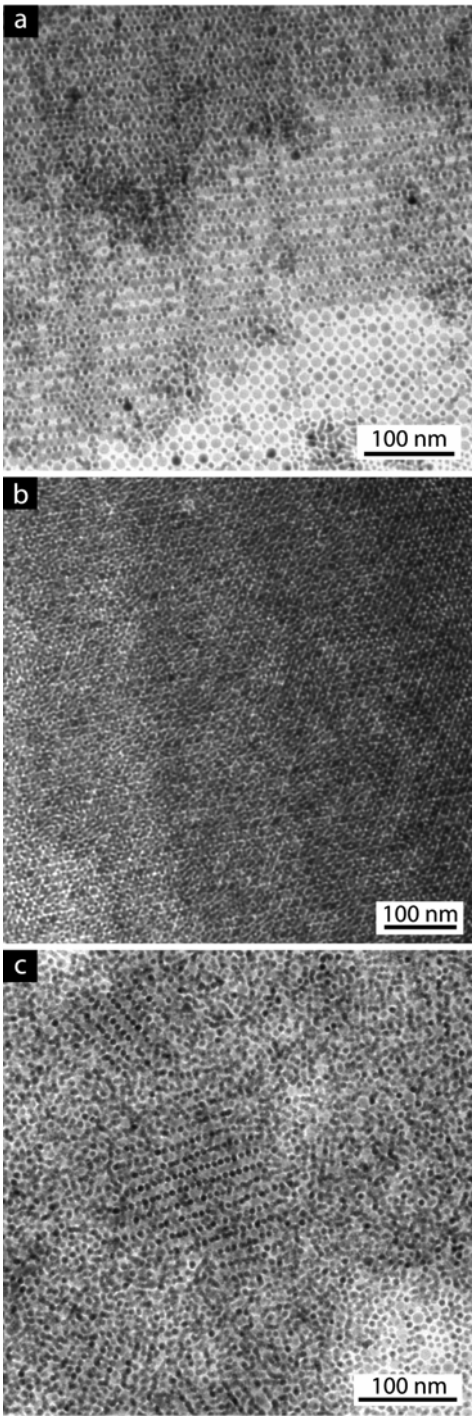

Figure 2.12: TEM images of thin sh-AB_2 BSLs. In (a) and (b) the superlattices appear to have nucleated on the substrate and crystallized from the bottom of the image to the top in (a) and from the left to the right in (b). The (100) plane is parallel to the substrate in image (a) and the (001) plane is parallel to the substrate in (b). In (c), the nanocrystals on the substrate are disordered and the BSL (with (100) orientation parallel to the substrate) does not appear to have nucleated on the substrate.

The TEM image in Figure 2.12a reveals a case in which the BSL structure (with the (100) plane parallel to the substrate) appears to assemble from a monolayer on the substrate into ordered multilayers. Another TEM image in Figure 2.12c shows an example of sh-AB_2 superlattices with lower nanocrystal layers that are disordered, suggesting that in this case the superlattices formed in solution and their assembly was not directed by the solution-substrate interface. Therefore, the influence of the substrate on BSL nucleation is presently not entirely clear, but perhaps when the superlattices nucleate on the substrate their lattice dimensions are directed by the substrate, which can give rise to an "expanded" unit cell like that in Figure 2.12a or a BSL structure different than the sh-AB_2 structure.

A new BSL structure was also observed that is similar to a (100) plane of a cuboctahedron AB_{13} superlattice (space group 226, $Fm\bar{3}c$) with Au nanocrystals substituted for Fe_2O_3 nanocrystals at the 8a Wyckoff positions in the unit cell (of space group 226). Figure 2.13 shows a TEM image of this structure. This BSL structure was observed only in thin nanocrystal layers. Although this structure is not equivalent to a cuboctahedron AB_{13} superlattice, it is structurally very similar and is not surprising that it coexists with the AB_2 superlattices since the coexistence of AB_2 and AB_{13} superlattices has been observed in a number of cases, including hard sphere colloidal particles[52-55] and binary nanocrystal superlattices.[2,3]

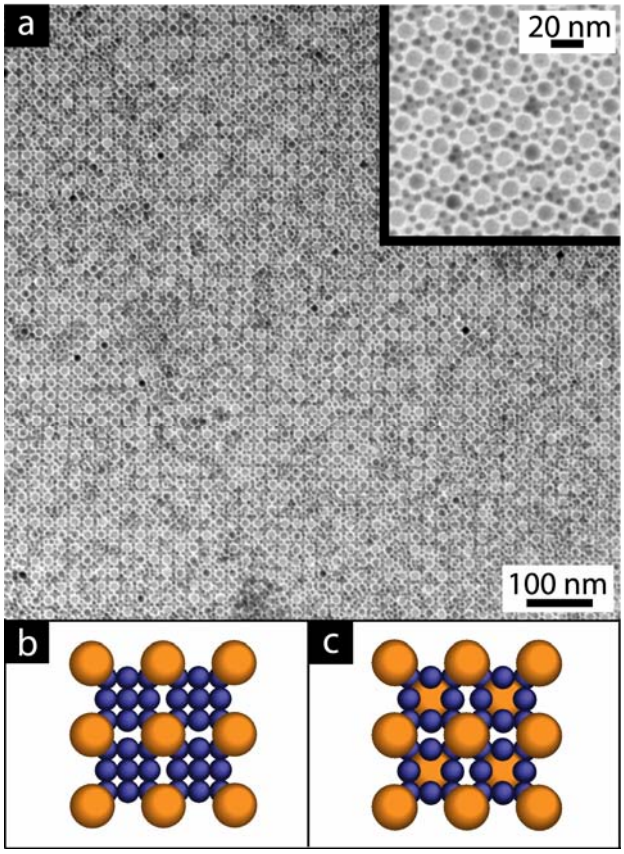

Figure 2.13: (a) TEM image of a two-dimensional BSL (a monolayer) with structure similar to the (100) plane of a cuboctahedron AB_{13} superlattice. The inset shows a higher magnification image. (b) Three-dimensional model of space group 226, a cuboctahedron AB_{13} superlattice. (c) Three-dimensional representation of a superlattice with Fe_2O_3 nanocrystals (orange) in place of Au nanocrystals (blue) at the 8a Wyckoff positions in the unit cell of space group 226.

2.3.5 BSL Formation and Space Filling in the sh AB_2 Lattice

All of the BSLs were made by slowly evaporating the solvent from concentrated dispersions with added oleic acid on tilted substrates. Phase segregation of Au and Fe_2O_3 nanocrystal superlattices was regularly observed, as shown in Figure 2.14, when oleic acid was not added in excess to the dispersion. Also, when the nanocrystals were

deposited on flat substrates, BSLs were not observed. These observations indicate that the forces directing BSL formation are surprisingly subtle.

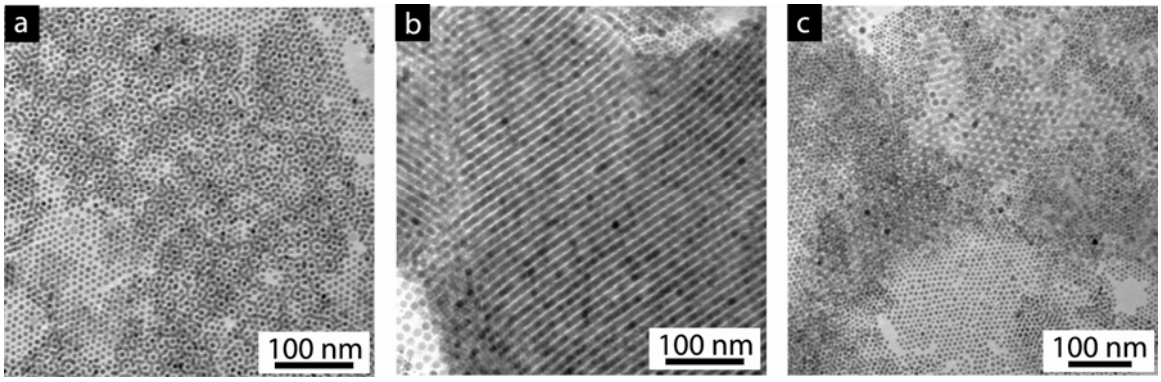

Figure 2.14: TEM images of phase separated regions of (a) Au and (b) Fe_2O_3 nanocrystals that formed when oleic acid was not added to the binary nanocrystal dispersion. Superlattices of Fe_2O_3 resulted as shown in (b), but no binary superlattices. Image (c) shows the phase separated regions are in close proximity.

Various driving forces for BSL formation have been mentioned in the literature,[2,3,7,8] but there is currently no consensus as to which forces are most influential. Some of this uncertainty probably stems from the complicating interactions of the deposition substrate, particularly in the case of thin BSL films, which have exhibited a variety of different structures. Certainly, one of the primary driving forces of BSL formation is the increase in "free volume" entropy that occurs when the bidisperse nanocrystals order into a lattice.[36,37,52,56] The sh-AB_2 lattice is a dense structure and spheres with the right size ratio (the radius ratio of large (R) and small (r) spheres that most efficiently fill space in a sh-AB_2 lattice is r/R=0.528) occupy 78% of the available volume when ordered into this lattice—this is denser than a face centered cubic (fcc) lattice (74%) of monodisperse spheres and nearly as dense as the closest-packed rock salt

lattice (79%, but only for a radius ratio of 0.414; a rock salt lattice with a radius ratio of 0.528 is much less dense than the sh-AB_2 structure).

The Au and Fe_2O_3 nanocrystals used in this study are nearly perfectly size-matched for forming sh-AB_2 BSLs. From the interparticle spacing measured by GISAXS, the *effective* radii of Au and Fe_2O_3 nanocrystals are 3.8 nm and 7.15 nm, which corresponds to r/R=0.531. The nanocrystals exhibit an effective radius in the superlattice that consists of the inorganic cores, which are 3.05 nm and 5.75 nm for the Au and Fe_2O_3 nanocrystals, along with the additional space occupied by the ligands that intervene between the inorganic surfaces in the superlattice. The volume filled by ligands is determined experimentally from the combination of the GISAXS measurements that reveal the BSL unit cell dimensions and electron microscopy, which provides the inorganic core sizes. The experimentally determined ligand volume in the BSLs compares well to the expected excluded volume for nanocrystals with monolayer capping ligand coverage, to within ±10%.[57] The Au and Fe_2O_3 nanocrystals pack together into ordered superlattices of "soft spheres," as described previously for the case of superlattices of monodisperse ligand-stabilized nanocrystals.[36,37] For these nearly ideal sh-AB_2 BSLs, there is no need to believe that exotic forces between nanocrystals, such as electrostatic charging, is playing a role in their formation; although there is no evidence here that would discount their presence either.[58]

2.3.6 Depletion Attraction and its Possible Role in BSL Formation

Additional attractive forces can further enhance BSL formation, as well as disrupt it. Van der Waals attractions,[36,37] ligand-ligand interactions,[38] capillary forces,[39] and electrostatic interactions[2] have been proposed to be important. One force that has not been discussed to any significant extent with respect to BSL formation is the *depletion*

attraction between nanocrystals that can be induced by the excess free oleic acid in the dispersion. Depletion attraction forces are those that arise between two bodies—such as two nanocrystals—are immersed in a solution of macromolecules and the interparticle separation becomes less than the size of the macromolecule.[56,59] Depletion attraction forces are typically important when the macromolecule is less than about one tenth the size of the nanocrystal and can easily move out of the intervening space between the particles, which is certainly the case of an oleic acid molecule. When the interparticle separation is less than the diameter of the macromolecule, it becomes excluded from the intervening solvent, which leads to an osmotic force that drives the intervening solvent out from between the particles and pushes them together. Asakura and Oosawa[59] first that an attractive force F, develops between two spheres of diameter D, when the interparticle separation d, is less than the size of an intervening macromolecule a, that is also present in the solution:

$$F = -\frac{\pi}{4} p_0 \left\{ (D+d)^2 - a^2 \right\}, \qquad D < a < D + d; \tag{2.1}$$

$$F = 0, \qquad a > D + d\ . \tag{2.2}$$

In Eqn (2.1), p_0 is the osmotic pressure of the macromolecular solution, $p_0 = kTN/V$, which in the case of interest is the oleic acid solution. kT is the thermal energy and N/V is the concentration. These expressions show how an increasing oleic acid concentration can enhance the depletion attraction force between nanocrystals. The depletion attraction between nanocrystals become increasingly significant as the solvent evaporates and concentrates the nanocrystals and the oleic acid. The fact that depletion attraction forces are relatively short range is also important for superlattice formation. These forces help squeeze the nanocrystals together as the solvent evaporates, but do not

lead to irreversible particle aggregation—once the macromolecule becomes excluded from between the nanocrystals, the steric repulsion between nanocrystals due to the adsorbed ligands still prevents flocculation. This is important, as the nanocrystals need the ability to orient into their lowest energy structure (i.e., the superlattice).

2.3.7 The Evaporative Front

The other question about BSL formation regards the role of the evaporative front at the liquid-air and liquid-substrate interfaces. Some data indicate that BSLs assemble by nucleating from the substrate, as in the cases shown in Figures 2.12a and 2.12b. In other images, like Figure 2.12c, ordered BSL domains are resting on a layer of disordered nanocrystals, indicating that the BSLs formed in solution first before depositing on the substrate. The SEM images provided as Supporting Information show that the BSLs crystallize from solution as grains resting on the substrate. Previous studies of gold nanocrystals have found that superlattice monolayers can assemble at the air-liquid interface of an evaporating dispersion.[60] Most of the BSLs studied here appear to crystallize at the air/solvent interface and then deposit onto the substrate as a floating interfacial layer. The curvature of the air/solvent interface leads to strain in the superlattice, which in some cases can lead to dislocations of inserted half-planes of Au nanocrystals in the BSLs with nearly periodic spacing.

2.4 CONCLUSIONS

Simple hexagonal (sh) AB_2 BSLs of 11.5 nm Fe_2O_3 and 6.1 nm Au nanocrystals were assembled and studied by TEM, SEM and GISAXS. BSL formation required the slow evaporation of a dispersing solvent with nanocrystal deposition on a tilted substrate. The addition of excess oleic acid to the dispersion solution was also found to be critically

important for BSL formation. Excess oleic acid is believed to be inducing depletion attraction forces between the nanocrystals that help overcome the kinetic barrier to BSL formation. The solvent-air-substrate interface is also important, as the BSLs form at this interface.

The GISAXS data showed Bragg spots indicating relatively long-range order in the BSLs. GISAXS also revealed two predominant crystallographic orientations with of (100) and (001) lattice planes on the substrate, but (110) oriented BSLs were also observed by TEM. GISAXS revealed a uniaxial shrinkage of 8 to 12% of the superlattice normal to the substrate that is not observable by TEM and SEM since these methods probe the structure by looking perpendicular to the substrate. The lattice shrinkage is the result of the evaporation of residual solvent that is retained in the superlattice right after deposition. For BSLs that have oriented on their hexagonal (100) planes on the substrate, this shrinkage changes the lattice symmetry to orthorhombic.

In addition to the relatively extended sh-AB_2 BSLs, some defect BSL structures were also observed. Nearly periodic dislocations of inserted superlattice half-planes of Au nanocrystals were observed, appearing as bright stripes of nanocrystals in SEM images. A new thin film BSL structure was also observed that is similar to cuboctahedron AB_{13} structure with Fe_2O_3 nanocrystals in place of Au nanocrystals at the 8a Wyckoff positions in the unit cell of space group 226. A relatively large expansion of the sh-AB_2 lattice was also observed when deposited as a thin, near-monolayer film.

BSLs provide an exciting avenue for nanomaterials design. As synthetic methods and self-assembly approaches continue to develop, it is becoming increasingly likely that new materials might be designed systematically and rationally. Presently, however, further experiments are needed to elucidate in detail how BSLs nucleate, the driving forces for BSL formation and the role of the air-solvent-substrate interface on BSL

formation. In situ GISAXS to follow BSL assembly in real time might be one next step. The SEM and GISAXS measurements presented here clearly show that BSLs are amenable to such studies.

2.5 REFERENCES AND NOTES

1. Redl, F. X.; Cho, K. S.; Murray, C. B.; O'Brien, S. *Nature* **2003,** *423*, 968-971.
2. Shevchenko, E. V.; Talapin, D. V.; Kotov, N. A.; O'Brien, S.; Murray, C. B. *Nature* **2006,** *439*, 55-59.
3. Shevchenko, E. V.; Talapin, D. V.; Murray, C. B.; O'Brien, S. *J. Am. Chem. Soc.* **2006,** *128*, 3620-3637.
4. Shevchenko, E. V.; Kortright, J. B.; Talapin, D. V.; Aloni, S.; Alivisatos, A. P. *Adv. Mater.* **2007,** *19*, 4183-4188.
5. Shevchenko, E. V.; Ringler, M.; Schwemer, A.; Talapin, D. V.; Klar, T. A.; Rogach, A. L.; Feldmann, J.; Alivisatos, A. P. *J. Am. Chem. Soc.* **2008,** *130*, 3274-3275.
6. Overgaag, K.; Evers, W.; de Nijs, B.; Koole, R.; Meeldijk, J.; Vanmaekelbergh, D. *J. Am. Chem. Soc.* **2008,** *130*, 7833-7835.
7. Chen, Z.; O'Brien, S. *ACS Nano* **2008**, *2*, 1219-1229.
8. Kiely, C. J.; Fink, J.; Brust, M.; Bethell, D.; Schiffrin, D. J. *Nature* **1998,** *396*, 444-446.
9. Chen, Z. Y.; Moore, J.; Radtke, G.; Sirringhaus, H.; O'Brien, S. *J. Am. Chem. Soc.* **2007,** *129*, 15702-15709.
10. Lu, C.; Chen, Z.; O'Brien, S. *Chem. Mater.* **2008,** *20*, 3594-3600.
11. Shevchenko, E. V.; Talapin, D. V.; O'Brien, S.; Murray, C. B. *J. Am. Chem. Soc.* **2005,** *127*, 8741-8747.
12. Saunders, A. E.; Korgel, B. A. *ChemPhysChem* **2005,** *6*, 61-65.
13. Urban, J. J.; Talapin, D. V.; Shevchenko, E. V.; Kagan, C. R.; Murray, C. B. *Nat. Mater.* **2007,** *6*, 115-121.
14. Lee, D. C.; Smith, D. K.; Heitsch, A. T.; Korgel, B. A. *Annu. Rep. Prog. Chem., Sect. C, Phys. Chem.* **2007,** *103*, 351-402.
15. Liz-Marzan, L. M. *Mat. Today* **2004,** *7*, 26-31.
16. Jun, Y. W.; Choi, J. S.; Cheon, J. *Angew. Chem., Int. Ed.* **2006,** *45*, 3414-3439.

17. Buonsanti, R.; Grillo, V.; Carlino, E.; Giannini, C.; Curri, M. L.; Innocenti, C.; Sangregorio, C.; Achterhold, K.; Parak, F. G.; Agostiano, A.; Cozzoli, P. D. *J. Am. Chem. Soc.* **2006,** *128*, 16953-16970.

18. Carbone, L.; Kudera, S.; Giannini, C.; Ciccarella, G.; Cingolani, R.; Cozzoli, P. D.; Manna, L. *J. Mater. Chem.* **2006,** *16*, 3952-3956.

19. Choi, J. S.; Jun, Y. W.; Yeon, S. I.; Kim, H. C.; Shin, J. S.; Cheon, J. *J. Am. Chem. Soc.* **2006,** *128*, 15982-15983.

20. Cozzoli, P. D.; Pellegrino, T.; Manna, L. *Chem. Soc. Rev.* **2006,** *35*, 1195-1208.

21. Kudera, S.; Carbone, L.; Casula, M. F.; Cingolani, R.; Falqui, A.; Snoeck, E.; Parak, W. J.; Manna, L. *Nano Lett.* **2005,** *5*, 445-449.

22. Kwon, K. W.; Lee, B. H.; Shim, M. *Chem. Mater.* **2006,** *18*, 6357-6363.

23. Pellegrino, T.; Fiore, A.; Carlino, E.; Giannini, C.; Cozzoli, P. D.; Ciccarella, G.; Respaud, M.; Palmirotta, L.; Cingolani, R.; Manna, L. *J. Am. Chem. Soc.* **2006,** *128*, 6690-6698.

24. Shi, W. L.; Zeng, H.; Sahoo, Y.; Ohulchanskyy, T. Y.; Ding, Y.; Wang, Z. L.; Swihart, M.; Prasad, P. N. *Nano Lett.* **2006,** *6*, 875-881.

25. Yu, H.; Chen, M.; Rice, P. M.; Wang, S. X.; White, R. L.; Sun, S. H. *Nano Lett.* **2005,** *5*, 379-382.

26. Alivisatos, A. P. *Nat. Biotechnol.* **2004,** *22*, 47-52.

27. Durr, N. J.; Larson, T.; Smith, D. K.; Korgel, B. A.; Sokolov, K.; Ben-Yakar, A. *Nano Lett.* **2007,** *7*, 941-945.

28. Lee, J. H.; Huh, Y. M.; Jun, Y.; Seo, J.; Jang, J.; Song, H. T.; Kim, S.; Cho, E. J.; Yoon, H. G.; Suh, J. S.; Cheon, J. *Nat. Med.* **2007,** *13*, 95-99.

29. Michalet, X.; Pinaud, F. F.; Bentolila, L. A.; Tsay, J. M.; Doose, S.; Li, J. J.; Sundaresan, G.; Wu, A. M.; Gambhir, S. S.; Weiss, S. *Science* **2005,** *307*, 538-544.

30. Zeng, H.; Li, J.; Liu, J. P.; Wang, Z. L.; Sun, S. *Nature* **2002,** *420*, 395-398.

31. Gur, I.; Fromer, N. A.; Geier, M. L.; Alivisatos, A. P. *Science* **2005,** *310*, 462-465.

32. Rogach, A. L. *Angew. Chem., Int. Ed.* **2004,** *43*, 148-149.

33. Cheon, J.; Park, J. I.; Choi, J. S.; Jun, Y. W.; Kim, S.; Kim, M. G.; Kim, Y. M.; Kim, Y. J. *Proc. Natl. Acad. Sci.* **2006,** *103*, 3023-3027.

34. Collier, C. P.; Vossmeyer, T.; Heath, J. R. *Annu. Rev. Phys. Chem.* **1998,** *49*, 371-404.

35. For example, the maximum packing fractions for superlattices with cub-AB (rock salt) and sh-AB_2 (AlB_2) structures are 0.793 and 0.778, respectively; whereas, the maximum packing fractions of the ico-AB_{13}, cub-AB_{13} and $CaCu_5$ structures are 0.738, 0.7 and 0.7, respectively. A face center cubic lattice of monodisperse nanocrystals has a packing fraction of 0.74, which is more dense than the ico-AB_{13}, cub-AB_{13} and $CaCu_5$ lattices that would be formed by a bidisperse mixture of nanocrystals. The packing fractions also depend on the actual particle size ratio and are maximized when the smaller nanocrystals fit perfectly into the interstitial spaces within a lattice composed of the larger nanocrystals—i.e., 0.414 for cub-AB and 0.53 for sh-AB_2.

36. Korgel, B. A.; Fullam, S.; Connolly, S.; Fitzmaurice, D. *J. Phys. Chem. B* **1998,** *102*, 8379-8388.

37. Korgel, B. A.; Fitzmaurice, D. *Phys. Rev. B* **1999**, *59*, 14191-14201.

38. Luedtke, W. D.; Landman, U. *J. Phys. Chem.* **1996**, *100*, 13323-13329.

39. Rabideau, B. D.; Bonnecaze, R. T. *Langmuir* **2004,** *20*, 9408-9414.

40. The issue of how subtle forces and packing density influence superlattice structure is a rich topic. For example, the packing density, coordination number and local packing geometry are equivalent for face-centered cubic (fcc) and hexagonal close-packed (hcp) structures, yet fcc superlattices tend to be favored because there is a small entropy increase when the close packed planes of the superlattice stack into a cubic structure with *ABC* stacking instead of the *ABAB* stacking of an hcp lattice. Relatively slight differences in interparticle interactions have been shown to lead to changes in superlattice structure; for example, by increasing the ratio of the ligand length to the radius of the inorganic core, the superlattice changes from fcc to body-center cubic (bcc).[37,61]

41. Sigman, M. B.; Saunders, A. E.; Korgel, B. A. *Langmuir* **2004,** *20*, 978-983.

42. Brust, M.; Walker, M.; Bethell, D.; Schiffrin, D. J.; Whyman, R. *Chem. Commun.* **1994**, 801-802.

43. Murray, C. B.; Norris, D. J.; Bawendi, M. G. *J. Am. Chem. Soc.* **1993,** *115*, 8706-8715.

44. Hyeon, T.; Lee, S. S.; Park, J.; Chung, Y.; Bin Na, H. *J. Am. Chem. Soc.* **2001,** *123*, 12798-12801.

45. Gruner, S. M.; Tate, M. W.; Eikenberry, E. F. *Rev. Sci. Instrum.* **2002,** *73*, 2815-2842.

46. Hammersley, A.P. ESRF Internal Report, **1997,** *ESRF97HA02T*.

47. Tate, M. P.; Urade, V. N.; Kowalski, J. D.; Wei, T. C.; Hamilton, B. D.; Eggiman, B. W.; Hillhouse, H. W. *J. Phys. Chem. B* **2006,** *110*, 9882-9892.

48. Smilgies, D.-M.; Blasini, D. R. *J. Appl. Crystallogr.* **2007**, 40, 716–718.

49. Bosworth, J. K.; M. Y. Paik; Ruiz, R.; Schwartz, E. L.; Huang, J. Q.; Ko, A. W.; Smilgies, D. M.; Black, C. T.; Ober, C. K. *ACS Nano* **2008**, *2*, 1396-1402.

50. Ruland, W.; Smarsly, B. M.; *J. Appl. Crystallogr.* **2007**, *40*, 409-417.

51. Dunphy, D.; Fan, H.; Li, X.; Wang, J.; Brinker, C. J. *Langmuir* **2008**; *24*, 10575-10578.

52. Cottin, X.; Monson, P. A. *J. Chem. Phys.* **1995,** *102*, 3354-3360.

53. Murray, M. J.; Sanders, J. V. *Philos. Mag. A* **1980,** *42*, 721-740.

54. Schofield, A. B.; Pusey, P. N.; Radcliffe, P. *Phys. Rev. E* **2005,** *72*, 031407.

55. Bartlett, P.; Ottewill, R. H.; Pusey, P. N. *Phys. Rev. Lett.* **1992,** *68*, 3801-3804.

56. Gelbart, W. M.; Ben-Shaul, A. *J. Phys. Chem.* **1996**, *100*, 13169-13189.

57. From TEM, the inorganic Au and Fe_2O_3 cores are 6.1 nm and 11.5 nm in diameter. Since the unit cell contains one Fe_2O_3 and two Au nanocrystals, the volume taken up by the inorganic cores of the Au and Fe_2O_3 nanocrystals in the unit cell is 1034.02 nm^3. The total unit cell volume determined from GISAXS is 2552.32 nm^3. Assuming that the Au and Fe_2O_3 nanocrystals are coated with a monolayer of ligands, the ligands have total excluded volumes of 233 nm^3 and 1209 nm^3, respectively. These values are calculated by using the relation, $v = (27.4 + 26.9n) \times 10^{-3} \left(\mathrm{nm}^3\right)$ for the excluded volume v, of each ligand molecule,[62] and estimating the number of ligands bound to each nanocrystal by taking a circular molecular "footprint" of 16 $Å^2$/molecule and assuming a close-packed monolayer with 91% surface coverage (the surface coverage of a hexagonal close-packed layer of disks).[36] From the GISAXS measurements of the BSL unit cell dimensions inorganic core sizes measured by TEM, the ligands must occupy (1990.81 nm^3 + 561.51 nm^3) - 1034.02 nm^3 = 1518.30 nm^3, which is very close to the estimated excluded volume of the ligands assuming close-packed capping ligand monolayers on the nanocrystals, which is 1209 nm^3 + (2×233 nm^3) = 1675 nm^3—a difference of ~9%.

58. The term, "nearly ideal," is used here to refer to the fact that the BSLs do not strictly have the simple hexagonal lattice symmetry because of their uniaxial lattice shrinkage perpendicular to the substrate that results during the late drying process when residual solvent entrained in the ligands evaporates after the BSL has formed and deposited on the substrate. This slight lattice distortion to an orthorhombic lattice itself is not predicted from simple sphere packing arguments, but easily understood in terms of how the substrate pins the nanocrystals and prevents their restructuring during this late stage of the drying process.

59. Asakura, S.; Oosawa, F., *J. Chem. Phys.* **1954**, *22*, 1255-1256.

60. Bigioni, T. P.; Lin, X. M.; Nguyen, T. T.; Corwin, E. I.; Witten, T. A.; Jaeger, H. M. *Nat. Mater.* **2006,** *5*, 265-270.

61. Whetten, R. L.; Shafigullin, M. N.; Khoury, J. T.; Schaaff, T. G.; Vezmar, I.; Alvarez, M. M.; Wilkinson, A. *Acct. Chem. Res.* **1999**, *32*, 397-406.

62. Israelachvili, J. *Intermolecular & Surface Forces* (2nd ed., Academic Press, San Diego, CA, 1992).

Chapter 3: The Role of Ligand Packing Frustration in the Formation of Body Centered Cubic (BCC) Nanocrystal Superlattices

3.1 INTRODUCTION

Colloidal sterically-stabilized nanocrystals of a wide range of materials, from metals and semiconductors to oxides, can be synthesized with controlled size and shape.[1] The nanocrystals consist of an inorganic, crystalline core typically ranging between 1 and 10 nm, coated by a relatively thin—between 0.5 and 3 nm thick—monolayer of adsorbed organic molecules. Nanocrystals in this size range exhibit unique size-dependent properties[1-4] and their self-assembly into ordered arrays, or superlattices, provides one means of obtaining spatially complex nanostructures with relative ease.[5, 6] Therefore, there has been a tremendous amount of effort to understand the fundamentals of nanocrystal self-assembly and superlattice formation with a goal of developing new technologies.

Due to the small diameter of the inorganic nanocrystal core, the chemically-tethered organic molecules can provide an effective physical barrier to irreversible aggregation and good dispersibility in compatible solvents. In a good solvent, the steric repulsion between particles outweighs the van der Waals attraction between inorganic cores and typical interparticle attractions are much less than the thermal energy, kT.[7] Brownian motion of the nanocrystals is also significant. The nanocrystals do not settle due to gravity and their diffusion is as fast as the typical rate of solvent evaporation.[7] Therefore, nanocrystals can be assembled into thermodynamically-favored structures by simply evaporating the solvent.[7, 8] A monodisperse collection of sterically-stabilized

nanocrystals tends to self-assemble into 2D hexagonal close-packed monolayers[9] or 3D face centered cubic (fcc) superlattices.[5]

Nanocrystal superlattice assembly is typically treated as a sphere-packing problem. In the absence of energetic interactions between particles, entropy dictates the structure of the assemblies and always favors the densest possible packing of the particles.[10, 11] For hard sphere particles, this is an fcc lattice.[12] Since non-close-packed superlattice structures are commonly observed, the ligand-stabilized nanocrystals are clearly not simple hard spheres.[7] The ligand coating creates a much softer interaction potential due to steric repulsion that depends on the size of the particle, ligand layer thickness, and the quality of the solvent. In addition to van der Waals attraction and steric repulsion, a variety of other influences to the interaction potential have been proposed to account for deviations from hard sphere behavior, including faceting, non-uniform ligand coverage, electrostatic and dipolar interactions, and depletion attractions.[13] Here, we argue that ligand packing frustration is primarily responsible for the formation of non-close-packed bcc superlattices.

3.2 Experimental Methods

3.2.1 Materials

Tetraoctylammonium bromide (TOAB, 98%), gold(III) chloride trihydrate ($HAuCl_4$-$3H_2O$, >99.9%), 1-dodecanethiol (>98%), and sodium borohydride (98%), lead oxide (99.9%), oleic acid (OA, >99%), 1-octadecene (tech, 90%), lead acetate trihydrate ($Pb(ac)_2 \cdot H_2O$, 99.999%), diphenyl ether (Fluka, >99.9%), selenium powder (Se, 100 mesh, 99.99%), and trioctylphosphine (TOP, tech., 90%) were obtained from Sigma Aldrich and used as received. Toluene (99.9%), methanol (99.9%), chloroform (99.9%

with 0.75% ethanol preservative), were obtained from Fisher Scientific and used as received. Bis(trimethylsilyl sulfide) (98%) was obtained from Alfa Aesar and used as received. Ethanol (99.5%) was obtained from Pharmco-Aaper. Deionized (DI) water with 18 megaohm resistance was obtained from a Barnstead Nanopure Ultrapure filtration system and passed through a 200 nm filter.

3.2.2 Au Nanocrystal Synthesis and Purification

Sub-2 nm diameter Au nanocrystals were synthesized at ambient temperature and pressure using the same arrested precipitation procedure previously reported in detail by Rasch et al.[30] Briefly, 0.833 mmol of gold(III) chloride trihydrate was dissolved in 20 mL of DI water. 12.0 mmol of TOAB dissolved in 80 mL of toluene was added to the aqueous solution and the two-phase mixture was stirred for 1h. The aqueous phase was then discarded. Then, 2.50 mmol of 1-dodecanethiol was injected into the organic solution and continued to stir for 15 minutes. 10.0 mmol of sodium borohydride dissolved in 20 mL of chilled DI water (4 °C) was then rapidly poured into the organic solution and the mixture continued to stir for 12 hours. The aqueous phase was then discarded. The nanocrystals were precipitated using ethanol antisolvent and high speed centrifugation. The nanocrystals were redispersed in toluene at a concentration of 50 mg/mL.

3.2.3 PbS Nanocrystal Synthesis and Purification

PbS nanocrystals with 3.7 nm diameter were synthesized following an adaptation of a procedure previously described by Konstantatos et. al.[31] Briefly, 450 mg of lead oxide, 1.5 mL of oleic acid, and 16.5 mL of octadecene were added to a reaction flask. The flask was then connected to a Schlenk line and degassed under vacuum at 120 °C. The flask was then purged with nitrogen and 3.5 mL of a 0.28 M solution of

bis(trimethylsilyl sulfide) in octadecene was injected into the flask. The heating mantle immediacy turned off but left in place so that the reaction flask cooled slowly. After cooling to room temperature, the nanocrystals were precipitated using acetone antisolvent and high speed centrifugation. After further purifying the nanocrystals with a chloroform/acetone solvent/antisolvent pair and high speed centrifugation, the nanocrystals were redispersed in toluene at a concentration of 50 mg/mL.

3.2.4 PbSe Nanocrystal Synthesis and Purification

PbSe nanocrystals with 7.9 nm diameter were prepared following an adaptation of a procedure previously described by Goodfellow et.al.[20] Briefly, 0.76 g of lead acetate trihydrate, 2.5 mL of oleic acid, and 10 mL phenyl ether were added to a reaction flask. The flask was then connected to a Schlenk line and degassed under vacuum at 75 °C for 1 hour. The flask was then purged with nitrogen, heated to 150 °C, left for 30 minutes, and then cooled to 60 °C. Then, 6 mL of a 1 M solution of Se in trioctylphosphine was injected into the flask. The solution in the flask was then rapidly injected into 15 mL of hot phenyl ether (which had been heated to 150 °C under nitrogen after being degassed under vacuum for 1 hour at 75 °C). The reaction proceeded for 10 minutes, at which point the heating mantel was removed and the flask was cooled to room temperature. The nanocrystals were precipitated using ethanol antisolvent and high speed centrifugation. After further purifying the nanocrystals with a toluene/ethanol solvent/antisolvent pair and high speed centrifugation, the nanocrystals were redispersed in toluene at a concentration of 4 mg/mL.

3.2.5 Nanocrystal Film Preparation

All nanocrystal dispersions aged for at least 2 weeks in the dark under an ambient atmosphere before use. In some cases, nanocrystal dispersions aged for over a year.

GISAXS samples were prepared by drop-casting 20 μL of the nanocrystal dispersion in toluene onto a silicon wafer (7 mm x 7 mm square with a native oxide) and allowing the solvent to evaporate. Samples for TEM imaging were prepared by drop-casting either 2 μL of a 10 mg/mL dispersion of Au or PbS nanocrystals in toluene or 5 μL of a 4 mg/mL dispersion of PbSe nanocrystals in toluene onto a TEM grid (carbon-coated copper 200 mesh, Electron Microscopy Sciences) and allowing the solvent to evaporate.

3.2.6 GISAXS of Nanocrystal Films

GISAXS measurements were performed at the CHESS D1 beamline as previously described by Smith et al.[26] Briefly, GISAXS measurements were performed using monochromatic radiation with wavelength, $\lambda = 1.265$ Å and a sample-to-detector distance of either 554 mm for Au nanocrystal and PbS nanocrystal samples or 880 mm for PbSe nanocrystal samples. The incident angle of the x-ray beam was 0.25°. Images were collected with exposure times of either 0.5 seconds or 1 second. Scattering images were calibrated using a silver behenate standard and image processing was performed with Fit2D software.[32] The GISAXS spot overlays were simulated using the "indexGISX" software package.[33]

3.2.7 Solution SAXS of Nanocrystal Dispersions

Nanocrystal dispersions were diluted with toluene to a concentration of approximately 1-3 mg/mL and were inserted into glass capillary tubes. These capillary tubes were placed into the CHESS D1 beamline and SAXS measurements were performed a previously described by Goodfellow et al.[20] Briefly, SAXS measurements were performed using monochromatic radiation with wavelength, $\lambda = 1.265$ Å and a sample-to-detector distance of either 554 mm for Au nanocrystal and PbS nanocrystal samples or 880 mm for PbSe nanocrystal samples. Images were collected with exposure

times ranging from 4 to 30 seconds. Scattering images were calibrated using a silver behenate standard; radial integrations and image processing was performed with Fit2D software.[32] Background scattering of the toluene solvent and experimental setup were subtracted from the data.

3.3 RESULTS AND DISCUSSION

3.3.1 Size Distribution of Nanocrystal Cores

The size distribution of the Au, PbS, and PbSe nanocrystal cores was determined by measuring the SAXS profile of a dispersion of the nanocrystals in toluene. The resulting SAXS data was fit to a model in which the scattering intensity, $I(q)$, was calculated for a dilute dispersion of non-interacting spherical particles by,[20]

$$I(q) \propto \int_0^\infty N(R)P(qR)R^6 dR \qquad (3.1)$$

where q is the scattering vector, which depends on the x-ray wavelength, λ, and the scattering angle θ: $q = (4\pi/\lambda)\sin(\theta/2)$; $N(R)$ is the number fraction of nanocrystals of radius R, which is assumed to be Gaussian with an average nanocrystal radius $\overline{R}$ and standard deviation of σ about the mean such that

$$N(R) = \frac{1}{\sigma\sqrt{2\pi}} \exp\left[\frac{-(R-\overline{R})^2}{2\sigma^2}\right], \qquad (3.2)$$

and $P(qR)$ is the form factor for a solid homogeneous sphere,

$$P(qR) = \left[3\frac{\sin(qR) - qR\cos(qR)}{(qR)^3} \right]^2 . \qquad (3.3)$$

Figures 3.1, 3.2, and 3.3 show that the distribution of nanocrystal core radii of Au, PbS, and PbSe nanocrystal samples is 0.885 nm ± 0.106 nm (12% polydispersity), 1.85 nm ± 0.167 nm (9% polydispersity), and 3.95 nm ± 0.356 nm (9% polydispersity), respectively, as measured by solution SAXS.

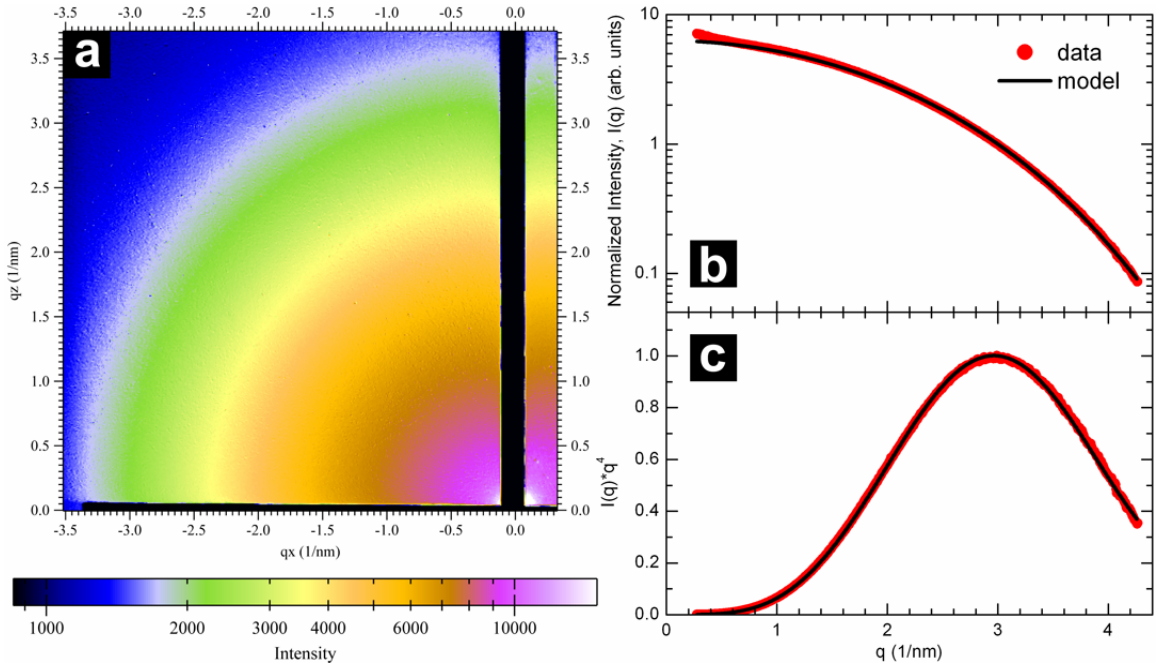

Figure 3.1: (a) 2D SAXS image of a dispersion of dodecanethiol-capped Au nanocrystals in toluene. (b) radially integrated scattering intensity $I(q)$ plotted vs q. (c) Porod plot ($I(q) \times q^4$ vs. q) of the data in (b). The data (red dots) in (b) and (c) are normalized by the value at q = 3.00 nm^{-1} (the position of the first maximum of the Porod plot). The black lines in (b) and (c) show the best fit to Eqn. (S1) which results when the average nanocrystal radius, $\overline{R}$, is 0.885 nm and the standard deviation, σ, is 0.106 nm (12% polydispersity).

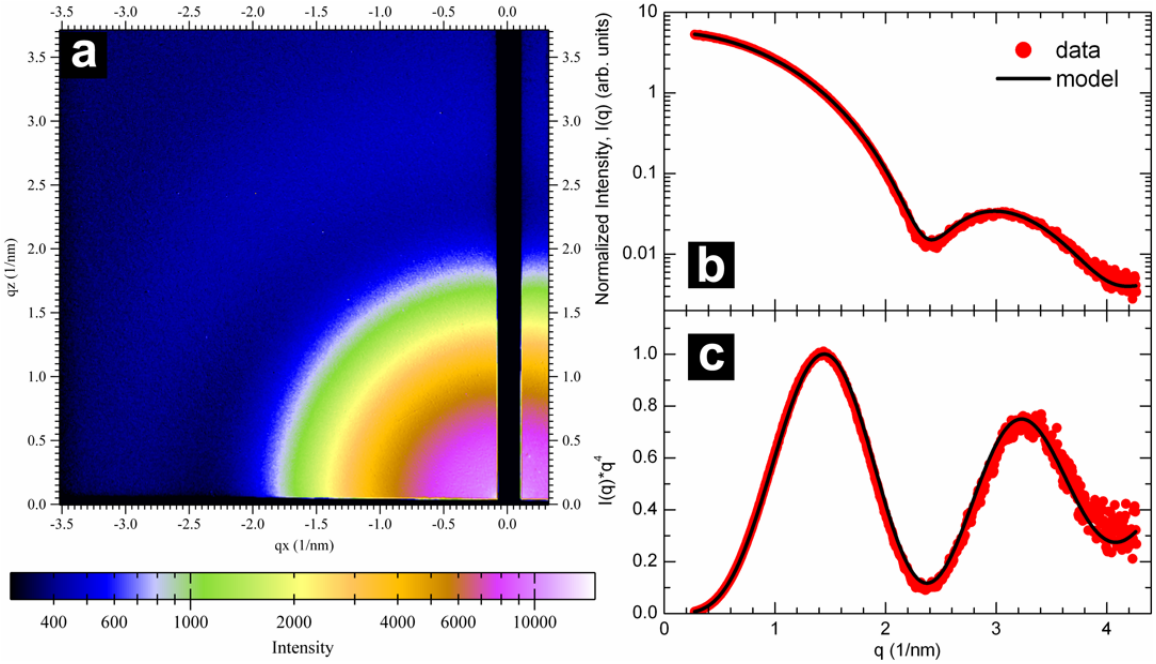

Figure 3.2: (a) 2D SAXS image of a dispersion of oleic acid-capped PbS nanocrystals in toluene. (b) radially integrated scattering intensity $I(q)$ plotted vs q. (c) Porod plot ($I(q) \times q^4$ vs. q) of the data in (b). The data (red dots) in (b) and (c) are normalized by the value at q = 1.43 nm^{-1} (the position of the first maximum of the Porod plot). The black lines in (b) and (c) show the best fit to Eqn. (S1) which results when the average nanocrystal radius, $\overline{R}$, is 1.85 nm and the standard deviation, σ, is 0.167 nm (9% polydispersity).

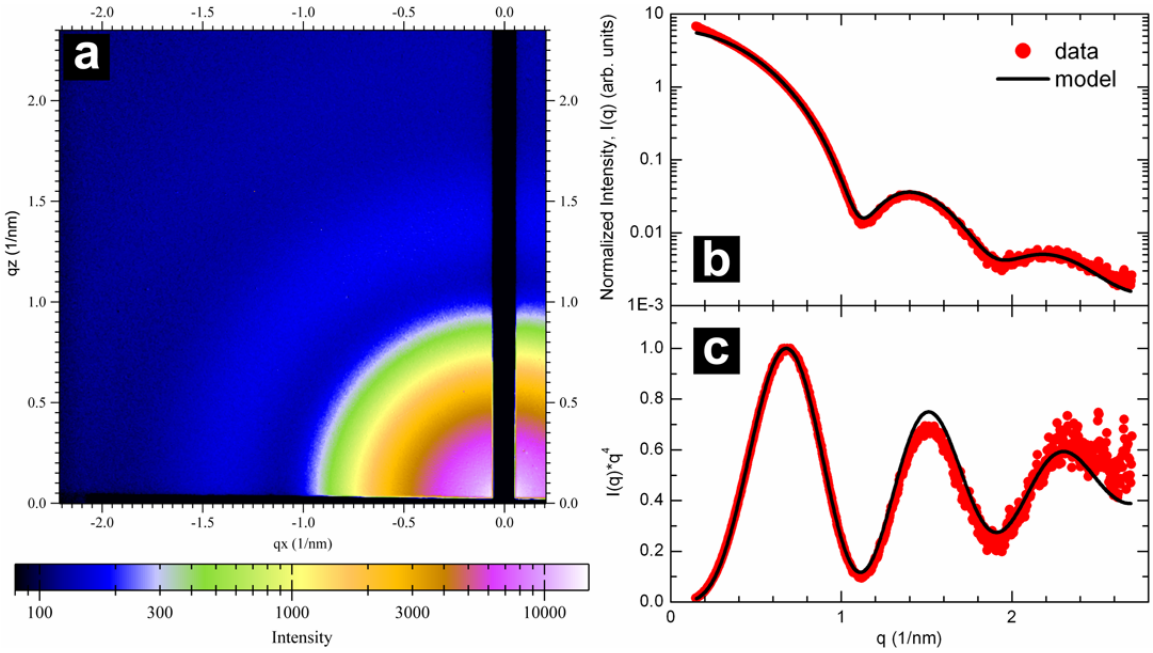

Figure 3.3: (a) 2D SAXS image of a dispersion of oleic acid-capped PbSe nanocrystals in toluene. (b) radially integrated scattering intensity $I(q)$ plotted vs q. (c) Porod plot ($I(q) \times q^4$ vs. q) of the data in (b). The data (red dots) in (b) and (c) are normalized by the value at q = 0.68 nm^{-1} (the position of the first maximum of the Porod plot). The black lines in (b) and (c) show the best fit to Eqn. (S1) which results when the average nanocrystal radius, $\overline{R}$, is 3.95 nm and the standard deviation, σ, is 0.356 nm (9% polydispersity).

3.3.2 GISAXS and TEM characterization BCC Superlattices

Figure 3.4 shows GISAXS and TEM data of bcc superlattices of three different kinds of nanocrystals: 1.8 nm dodecanethiol-capped Au nanocrystals, 3.7 nm oleic acid-capped PbS nanocrystals, and 7.9 nm oleic-acid capped PbSe nanocrystals. In all of these cases, GISAXS and TEM showed that the bcc nanocrystal superlattices are primarily oriented with the (110) plane parallel to the substrate. The (110) plane has the highest plane density in the bcc lattice and is very similar to the (111) plane of an fcc lattice, with a slight in-plane distortion. Solution SAXS, as shown in the previous section, was used

to measure the average radius of the inorganic nanocrystal cores (R) and GISAXS was used to determine the lattice constants of the bcc superlattices (a_{bcc}). These measurements were used to calculate the nearest neighbor spacings (r_{NN}) and the characteristic ligand lengths (L_o). These values are summarized in Table 3.1.

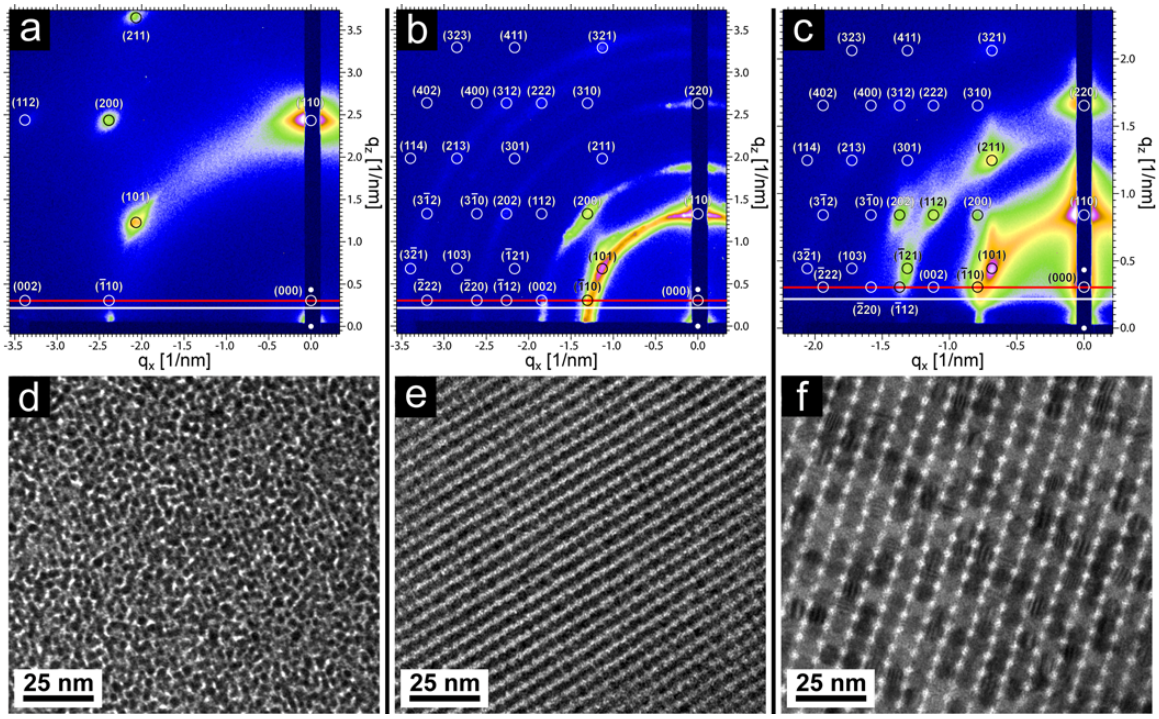

Figure 3.4: (a-c) GISAXS patterns and (d-f) TEM images of bcc superlattices of various nanocrystals: (a,d) 1.8 nm diameter dodecanethiol-capped Au nanocrystals, (b,e) 3.7 nm diameter oleic acid-capped PbS nanocrystals, and (c,f) 7.9 nm diameter oleic acid-capped PbSe nanocrystals. The spot indexing (open circles) of the GISAXS patterns correspond to a (110) oriented bcc superlattice with a lattice constant, a_{bcc}, of (a) 3.72 nm, (b) 6.80 nm, and (c) 11.2 nm. The solid white dots indicate the direct and reflected x-ray beam positions and the horizontal lines indicate the sample horizon (white) and the Yoneda peak for the film (red).

Table 3.1: Measurements of nanocrystal sizes and superlattice parameters.

core material	capping ligand	core radius[a] (R ; nm)	bcc superlattice constant[b] (a_{bcc} ; nm)	nearest-neighbor spacing[c] (r_{NN} ; nm)	characteristic ligand length[d] (L_o ; nm)
Au	dodecanethiol	0.90	3.72	3.22	0.93
PbS	oleic acid	1.85	6.80	5.89	1.50
PbSe	oleic acid	3.95	11.20	9.70	1.56

[a]Determined from solution SAXS (see Figures 3.1, 3.2, and 3.3)
[b]Determined from GISAXS
[c] $r_{NN} = a_{bcc}\sqrt{3}/2$
[d] $L_o = a_{bcc}\left(\frac{3}{8\pi}\right)^{1/3} - R$ (see Equations 3.7, 3.8, and 3.9 below)

Nanocrystal superlattices with bcc structure have been reported previously. Whetten et al. first reported bcc superlattices of alkanethiol-capped gold nanocrystals in 1996.[14] Korgel et al. and Henry et al. later observed bcc superlattices of alkanethiol-capped silver nanocrystals.[15, 16] Whetten observed that bcc superlattices formed when a critical ratio of the fully-extended capping ligand chain length $\langle L \rangle$ to the inorganic core radius R, $\langle L \rangle / R$, of 0.7 (for alkanethiol-capped gold nanocrystals) was exceeded.[17] Korgel and Fitzmaurice observed a slightly lower critical ratio of 0.6 for alkanethiol-capped silver nanocrystals.[15] Similar structural transitions from fcc to bcc superlattices with increased interparticle separation are in fact well-known to occur in colloidal dispersions of charge-stabilized particles.[18] Luedtke and Landman employed a purely geometrical optimal packing model for alkanethiol-capped Au nanocrystals and calculated a critical $\langle L \rangle / R$ ratio of 0.664 with the condition that the capping-ligand chains of one nanocrystal touch that of its next nearest neighbor.[19] While the $\langle L \rangle / R$ ratio has been useful in predicting bcc superlattices of alkanethiol-capped metal nanocrystals, it fails with other nanocrystal systems. Indeed, we observe a range of $\langle L \rangle / R$ values for

the bcc superlattices reported here: 1.73 for the Au nanocrystals, 1.23 for the PbS nanocrystals and 0.58 for the PbSe nanocrystals given that the fully extended chain lengths,[17] $\langle L \rangle = 0.12(m+1)$, for dodecanethiol and oleic acid are 1.56 nm and 2.28 nm, respectively.

Recently, there have been several reports of bcc superlattices of oleic acid-capped lead chalcogenide nanocrystals.[20-22] Choi et al. suggested that a bcc superlattice of PbSe nanocrystals formed due to shape anisotropy of the inorganic core and variable ligand coverage.[21] Later, Bain et al. showed that a PbS nanocrystal superlattice could be reversibly switched from bcc to fcc by swelling the ligand with solvent vapor.[22] Interestingly, this report suggested that greater interparticle separations favored fcc structure while previous studies on alkanethiol-capped nanocrystals suggested that increased interparticle separations favored a bcc superlattice. We recently suggested that the structure of a nanocrystal superlattice should be sensitive to the fact that the conformational entropy of the ligands is frustrated by packing in the superlattice.[10] The extent of this ligand packing frustration depends on the superlattice structure. In the case of sphere-forming block copolymers, chain packing constraints are very influential and are largely responsible for the preferential formation spherical morphologies with bcc structure over fcc.[23]

3.3.3 Space-Filling Polyhedra Considerations

The ligands tethered to the nanocrystal cores behave like identical springs that would prefer to distribute uniformly around the nanocrystal cores. Perfect uniformity is not possible in a superlattice because all of the free volume must be filled and spheres are not perfect space-filling structures. To maintain a uniform ligand density between inorganic cores in the superlattice, the ligands must conform to the available volume of

space-filling polyhedra. Figure 3.5 shows the space-filling polyhedra, or Wigner-Seitz (W-S) cells of fcc and bcc lattices. The W-S cells are Voronoi polygons which represent the set of space that is closer to one particular lattice point than all other lattice points. W-S cells are truncated octahedra and rhombic dodecahedra in the bcc and fcc lattices, respectively, as shown in Figure 3.5. The sphericity, a quantitative measure of how spherical a shape is (a perfect sphere having a sphericity of 1), is 0.9099 and 0.9047 for the W-S cells of bcc and fcc superlattices, respectively. Therefore, bcc superlattices of nanocrystals are more spherically symmetric and allow for a more uniform thickness of the ligand shell.

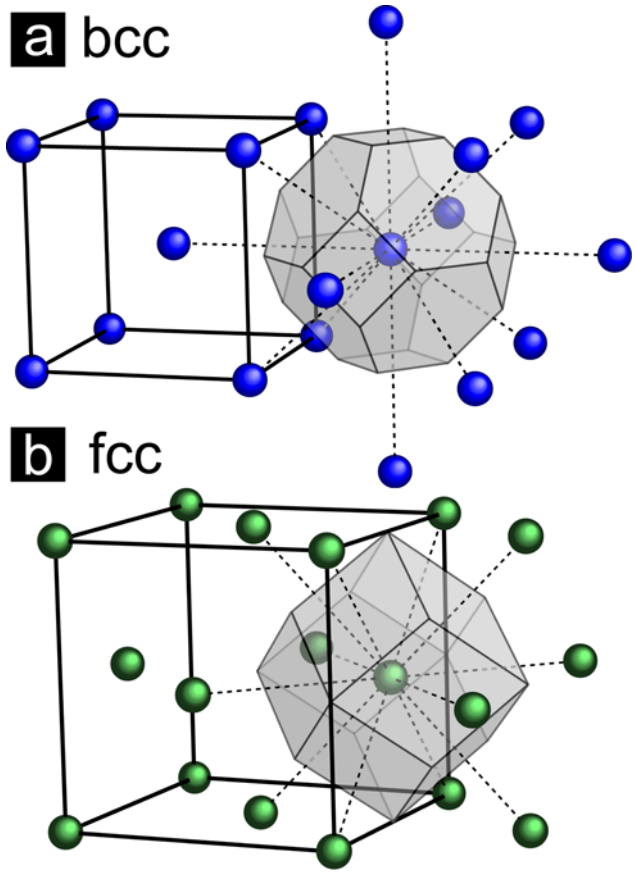

Figure 3.5: Unit cells and Wigner-Seitz cells for (a) bcc and (b) fcc lattices. The W-S cell is more spherically symmetric for bcc than for fcc, resulting in a more uniform thickness of the ligand shell.

While the sphericities show that the W-S cell for bcc is more spherically symmetric than the W-S cell for fcc, a more detailed analysis of the distribution of ligand lengths in each case is useful. The surface area of the W-S cells consist of 6 square and 8 hexagon faces for bcc and 12 rhombic faces for fcc as shown in Figure 3.6. These faces can be further reduced to right-triangles whose edge lengths can be related to the cubic unit cell parameter, a, as shown in Figure 3.6. The surface area of the Wigner-Seitz cell at a particular distance, $R + L$ from the center of the Wigner-Seitz cell (where R is the

nanocrystal core radius and L is the length of the ligand from the surface of the nanocrystal core to the surface of the W-S cell) is labeled dA in Figure 3.7.

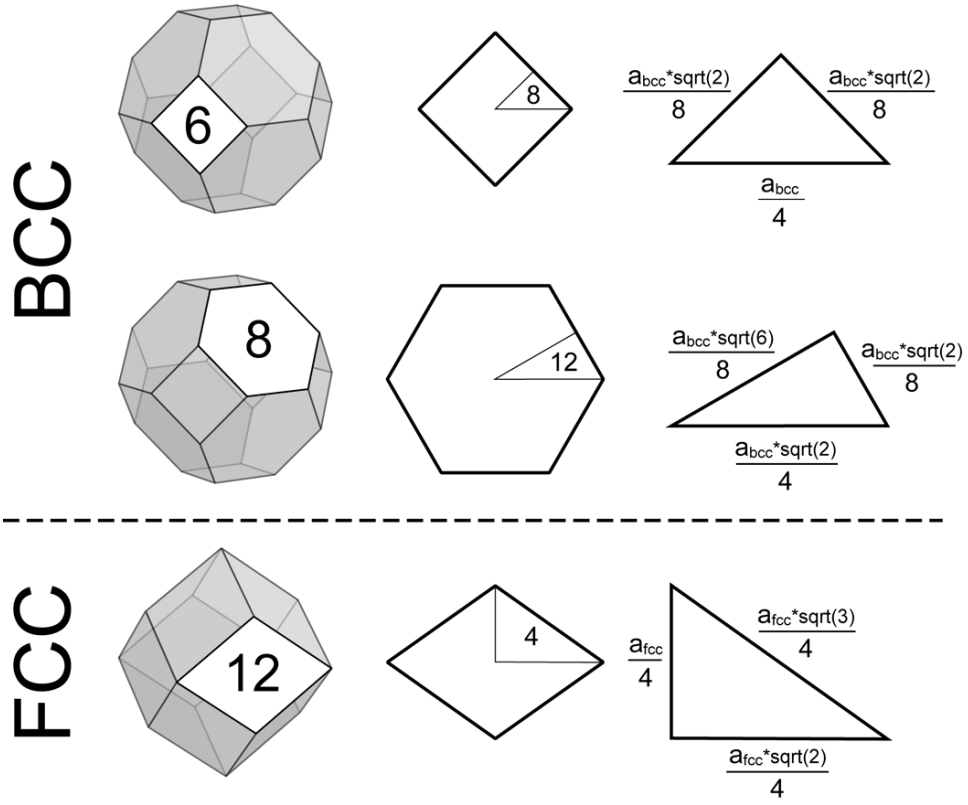

Figure 3.6: Schematic showing that the surface of bcc and fcc Wigner-Seitz cells can be reduced to right triangles which can tessellate the entire surface area.

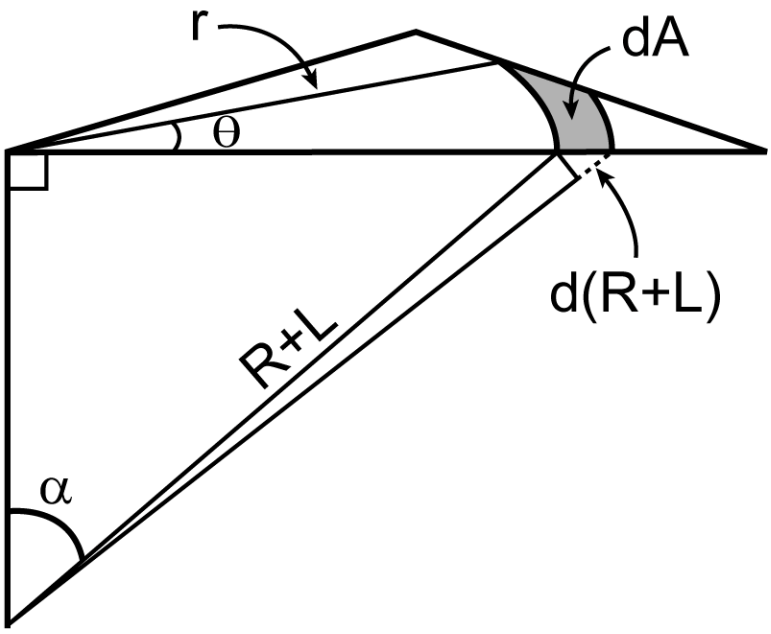

Figure 3.7: Schematic showing the area dA on the Wigner-Seitz surface that is at a distance $R + L$ from the center of the Wigner-Seitz cell.

From Figure 3.7, an expression for dA can be deduced:

$$dA = \theta * r * \frac{d(R+L)}{\sin\alpha}. \tag{3.1}$$

Also, the relationship of the angle α with *r*, *R*, and *L* can be expressed by

$$\sin\alpha = \frac{r}{R+L}. \tag{3.2}$$

By combining Equations (3.1) and (3.2), an expression for dA in terms of θ, *R*, and *L* can be found:

$$dA = \theta * (R+L) * d(R+L) \tag{3.3}$$

Since the radius of the nanocrystal, *R*, is a constant, $d(R+L) = dL$. With this and rearrangement of Equation (3.3), an expression for dA/dL is found:

$$dA/dL = \theta * (R + L) \tag{3.4}$$

Expressions for θ for the Wigner-Seitz cells of bcc and fcc are given below:

Body Centered Cubic:

$$\theta_{bcc}(R+L) = \begin{cases} 16\pi, & 0 < r_h \le \frac{a_{\text{bcc}}}{4} \\ 28\pi, & \frac{a_{bcc}}{4} < r_h \le \frac{a_{bcc}\sqrt{6}}{8}; 0 < r_s \le \frac{a_{bcc}\sqrt{2}}{8} \\ 96\left[\frac{\pi}{6} - \arccos\left(\frac{a_{bcc}\sqrt{6}}{8r_h}\right)\right] + 48\left[\frac{\pi}{4} - \arccos\left(\frac{a_{bcc}\sqrt{2}}{8r_s}\right)\right], & \frac{a_{bcc}\sqrt{6}}{8} < r_h \le \frac{a_{bcc}\sqrt{2}}{4}; \frac{a_{bcc}\sqrt{2}}{8} < r_s \le \frac{a_{bcc}}{4} \\ 0, & else \end{cases} \tag{3.5}$$

where, $\mathrm{r_h} = \sqrt{(R+L)^2 - \left(\frac{a_{bcc}\sqrt{3}}{4}\right)^2}$ and $r_s = \sqrt{(R+L)^2 - \left(\frac{a_{bcc}}{2}\right)^2}$

Face Centered Cubic:

$$\theta_{fcc}(R+L) = \begin{cases} 24\pi, & 0 < r \le \frac{a_{fcc}\sqrt{6}}{12} \\ 48[\frac{\pi}{2} - 2\arccos(\frac{a_{fcc}\sqrt{6}}{12r})], & \frac{a_{fcc}\sqrt{6}}{12} < r \le \frac{a_{fcc}}{4} \\ 48[\arctan(\sqrt{2}) - \arccos(\frac{a_{fcc}\sqrt{6}}{12r})], & \frac{a_{fcc}}{4} < r \le \frac{a_{fcc}\sqrt{2}}{4} \\ 0 & else \end{cases} \tag{3.6}$$

where, $\mathrm{r} = \sqrt{(R+L)^2 - \left(\frac{a_{fcc}\sqrt{2}}{4}\right)^2}$

In order to compare the distribution of ligand lengths for each case, the available volume per nanocrystal, v, was kept constant. The Wigner-Seitz radius, Rs, can then be defined by

$$R_s = \left(\frac{3v}{4\pi} \right)^{1/3}. \tag{3.7}$$

By considering an isolated nanocrystal, it is clear that $R_s = R + L_o$ where L_o is the characteristic length of the ligand. Since there are 2 nanocrystals in each bcc unit cell and 4 nanocrystals in each fcc unit cell,

$$v = \frac{a_{bcc}^{\ 3}}{2} = \frac{a_{fcc}^{\ 3}}{4}. \tag{3.8}$$

By combining Equations (3.7) and (3.8) and the relationship $R_s = R + L_o$, the characteristic ligand length, L_o, can be expressed in terms of the inorganic nanocrystal core radius, R, and the cubic lattice constant, a,

$$L_o = a_{bcc}\left(\frac{3}{8\pi} \right)^{1/3} - R = a_{fcc}\left(\frac{3}{16\pi} \right)^{1/3} - R \tag{3.9}$$

both of which can be experimentally determined by SAXS. Table 3.1 summarizes measurements of R and a_{bcc} for various bcc superlattices and the resulting values of L_o. We find that L_o is 0.93 nm for dodecanethiol and 1.53 nm for oleic acid.

Figure 3.8 shows the normalized probability density that an element of the W-S cell surface area is at a distance, $R + L$, from the center of the nanocrystal. By assuming

each ligand terminates at the surface the W-S cell, the curves in Figure 3.8 also show the distribution of ligand lengths when a nanocrystal is isolated or in a bcc or fcc superlattice. The distribution of ligand lengths in the W-S cell is significantly different for bcc and fcc arrangements as can be seen in Figure 3.8. In particular there is more significant compression of ligand chains in a bcc superlattice while there is more significant extension of ligand chains in an fcc lattice. Additionally, the standard deviation of the distribution of ligand lengths can also be calculated by

$$\sigma = \sqrt{\int_L \left[\mu - (R+L)\right]^2 * \frac{\theta(R+L)*(R+L)}{A_o} dL} \tag{3.10}$$

where,

$$\mu = \int_L \frac{\theta(R+L)*(R+L)^2}{A_o} dL \tag{3.11}$$

and were found to be $0.063(R + L_o)$ for bcc and $0.070(R + L_o)$ for fcc (11% greater than bcc). Indeed, the thickness of the ligand shell is more uniform in a bcc superlattice than in an fcc superlattice.

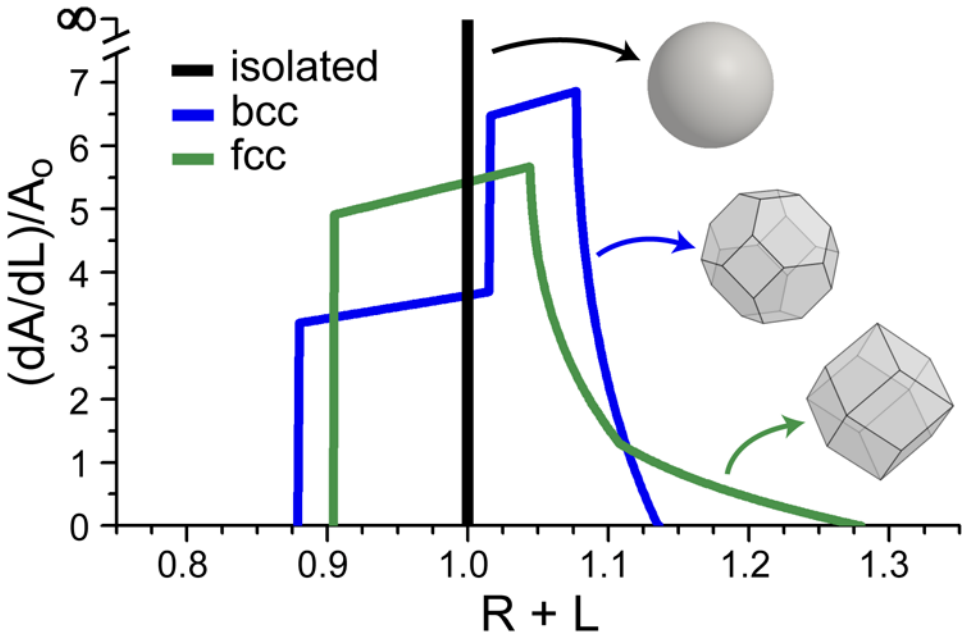

Figure 3.8: Plot of the normalized probability density ($[dA/dL]/A_o$) that an element of the W-S cell surface exists at a distance, $R+L$, from the center of the W-S cell. The total surface area of the W-S cell is denoted by A_o. The volume of each W-S cell is normalized so that $R+L_o=1$ and $V_{iso}=V_{bcc}=V_{fcc}=\frac{4}{3}\pi$.

3.3.4 Ligand Conformational Entropy Considerations

The extent of chain packing frustration can be expressed more quantitatively in terms of the conformational entropy of the adsorbed ligands. To fill the space in the superlattice unoccupied by inorganic cores, the ligands cannot be uniformly stretched, as they would be in the case of isolated nanocrystals and must deform from their equilibrium lengths. Since the W-S cells are space filling polyhedra, one may consider that the ligands extend from the nanocrystal surface to the surface of the W-S cell (Figure 3.5). Figure 3.8 shows the distribution of ligand lengths for an isolated nanocrystal and nanocrystals packed in a bcc and fcc superlattice. For an isolated nanocrystal, the ligand shell has a uniform thickness of L_o which corresponds to the equilibrium length of the

capping ligand molecule. When nanocrystals assemble into an ordered superlattice, the ligands must compress and stretch in order to fill the corresponding W-S cell.

Any compression or extension of the organic ligand chains from the equilibrium length leads to a decrease in conformational entropy. The ligand chains can be modeled with a freely-jointed chain model to calculate the change in entropy associated with their compression or extension. The relative number of conformations as a function of the ligand length, L, can be expressed by:

$$P(L) = 4\pi\left(\frac{\beta}{\sqrt{\pi}}\right)^3 L^2 e^{-\beta^2 L^2} \tag{3.12}$$

where $\beta = 1/L_o$ and L_o is the length of ligand that maximizes the number of confirmations. The conformational entropy of a ligand as a function of L can then be computed:

$$S(L) = k_B \ln(P(L)) \tag{3.13}$$

where k_B is the Boltzmann constant. The total entropy of the organic ligand layer can then be computed by summing the entropy of all ligand chains on the nanocrystal surface:

$$S_{lig} = \sum_L S(L)n(L) \tag{3.14}$$

where $n(L)$, the number of chains that have a length L, depends on whether the nanocrystal is isolated or in an ordered bcc or fcc superlattice. In order to compare the conformational entropy of the ligands in various environments, the number of ligand chains in the ligand shell of one nanocrystal, N, and the volume of the bounding cells,

V, were kept constant. N was determined from the size of the inorganic nanocrystal core:

$$N = \frac{4\pi R^2 \phi_s}{A_{lig}} \tag{3.15}$$

where ϕ_s is the packing fraction of ligands on the nanocrystal surface and A_{lig} is the footprint of a single ligand molecule on the nanocrystal surface.

The total conformational entropy of the ligand shell per nanocrystal is calculated for three cases: an isolated nanocrystal, a nanocrystal in a bcc superlattice, and a nanocrystal in an fcc superlattice. The conformational entropy of the ligand layer is maximized when the nanocrystal is isolated and all ligand chains can extend to a length L_o. For this case, the conformational entropy of the ligand layer can be simply expressed:

$$S_{lig,iso} = S(L_o)N \tag{3.16}$$

In an ordered bcc or fcc superlattice, the ligands can not all have a length of L_o as some must stretch or compress to fill the W-S cell. Thus, the conformational entropy of the ligand layer of a nanocrystal in a superlattice, $S_{lig,NCSL}$, is less than $S_{lig,iso}$. In Figures 3.9b and 3.9c, we plot the change in conformational entropy per mole of ligands as a collection of isolated nanocrystals assemble into superlattice:

$$\Delta S_{lig} = \frac{N_A}{N}(S_{lig,NCSL} - S_{lig,iso}) \tag{3.17}$$

where N_A is the Avogadro constant.

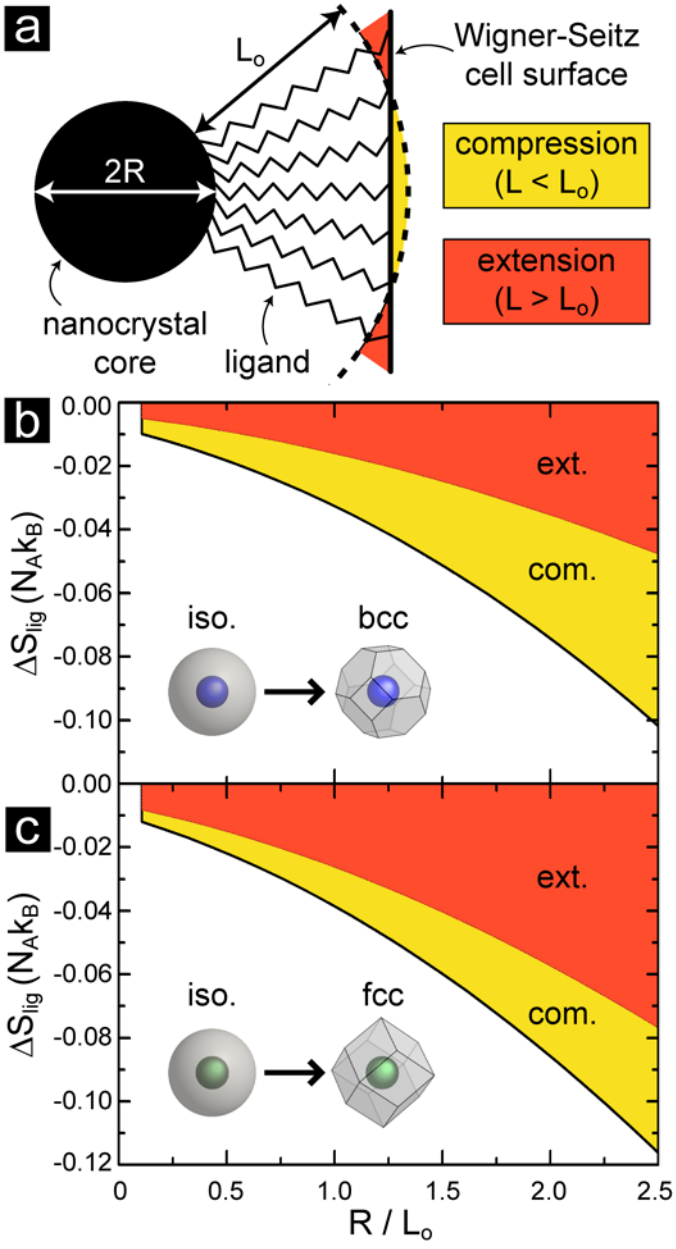
a
L_o
Wigner-Seitz
cell surface
2R
compression
($L < L_o$)
extension
($L > L_o$)
nanocrystal
core
ligand
b
0.00
-0.02
-0.04
-0.06
-0.08
-0.10
ΔS_{lig} ($N_A k_B$)
ext.
com.
iso.
bcc
c
0.00
-0.02
-0.04
-0.06
-0.08
-0.10
-0.12
ΔS_{lig} ($N_A k_B$)
ext.
com.
iso.
fcc
0
0.5
1.0
1.5
2.0
2.5
R / L_o

Figure 3.9: (a) Illustration of a nanocrystal with inorganic core radius, *R*, coated with capping ligands that span a length, L, from the nanocrystal core to the surface of the W-S cell. To fill the space in the W-S cell, the ligands must extend or compress from their equilibrium length, L_o. (b-c) Plots of the change in ligand conformational entropy per mole of ligands (ΔS_{lig}) in units of the gas constant ($N_A k_B$) vs. R / L_o as a population of isolated nanocrystals are arranged into (b) a bcc and (c) an fcc superlattice. The contributions of ligand compression and extension to the conformational entropy have been shaded. Only the contribution due to ligand compression can be mitigated by the ability of ligands to interpenetrate with ligands from a neighboring nanocrystal.

One important observation is that the entropic penalty to fill the W-S cell is less for a bcc superlattice than for an fcc superlattice. This difference, however, is not particularly large as can be seen in Figures 3.9b and 3.9c. To fully appreciate the entropic advantages of the bcc superlattice, one must consider the possibility of interpenetration of the ligands with those from neighboring nanocrystals. As can be seen in Figure 3.8, the fcc superlattice requires ligands that are significantly more extended when than those in the bcc superlattice. Interpenetration can relieve only compression of ligands since any relaxation of an extended ligand would lead to void space in the nanocrystal superlattice. By assuming the compressed ligand chains ($L < L_o$) can relax to a length of L_o when interpenetration is possible, the component of ΔS_{lig} related to compression (shaded yellow in Figures 3.9b and 3.9c) can be eliminated. By comparing Figures 3.9b and 3.9c, it is clear that the conformational entropy of the ligand layer significantly favors a bcc superlattice over an fcc superlattice when interpenetration is considered.

Based on ligand packing frustration, it appears that there can be a strong driving force for nanocrystals to assemble into a bcc superlattice instead of an fcc superlattice when significant interpenetration of the ligand is possible. This idea is consistent with previously observed bcc nanocrystal superlattices. For alkanethiol-capped metal nanocrystals, a $\langle L \rangle / R$ ratio larger than 0.6-0.7 resulted in a bcc superlattice.[15, 17] For small nanocrystal cores with high-curvature surfaces, the ligands are less densely packed away from the nanocrystal surface and the possibility in interpenetration increases as R decreases. Oleic acid-capped lead chalcogenide nanocrystals have a ligand layer that is less densely packed due to the double bond in the oleic acid molecule. Furthermore, the surface of PbS and PbSe nanocrystals can easily oxidize leading to ligand desorption—further decreasing the ligand shell density.[21] Therefore, significant interpenetration of the

ligands can occur with oleic acid-capped PbS and PbSe nanocrystals and assembly can favor bcc superlattices at lower $\langle L \rangle / R$ values than alkanethiol-capped metal nanocrystals.[20-22]

3.3.5 Monolayer-to-Multilayer Structural Transitions

Figure 3.10 shows a TEM image of 9.5 nm diameter oleic acid coated PbSe nanocrystals that have assembled into a 2D hexagonally-packed monolayer next to a thicker region of a 3D bcc superlattice. The structure of a hexagonal monolayer does not correspond to any bcc lattice plane. The assembly of sphere-forming diblock copolymer into hexagonally-packed monolayers in 2D and bcc superlattices in 3D is also well-known.[23] This kind of structural transition also results from chain packing frustration and is readily appreciated by considering the difference in 2D W-S cells between a hexagonal monolayer and a bcc (110) plane, which is the crystallographic plane with the structure that is closest to a hexagonally packed monolayer. Figure 3.10 compares the 2D W-S cell of a hexagonal monolayer and the bcc (110) plane. The 2D W-S cell is more spherically symmetric for a hexagonal monolayer than for any of the individual planes of a bcc superlattice resulting in less packing frustration of the ligands. Therefore, even though a nanocrystal system assembles into 3D bcc superlattice, monolayers of the same nanocrystals prefer to organize into a 2D hexagonal structure due to ligand packing frustration.

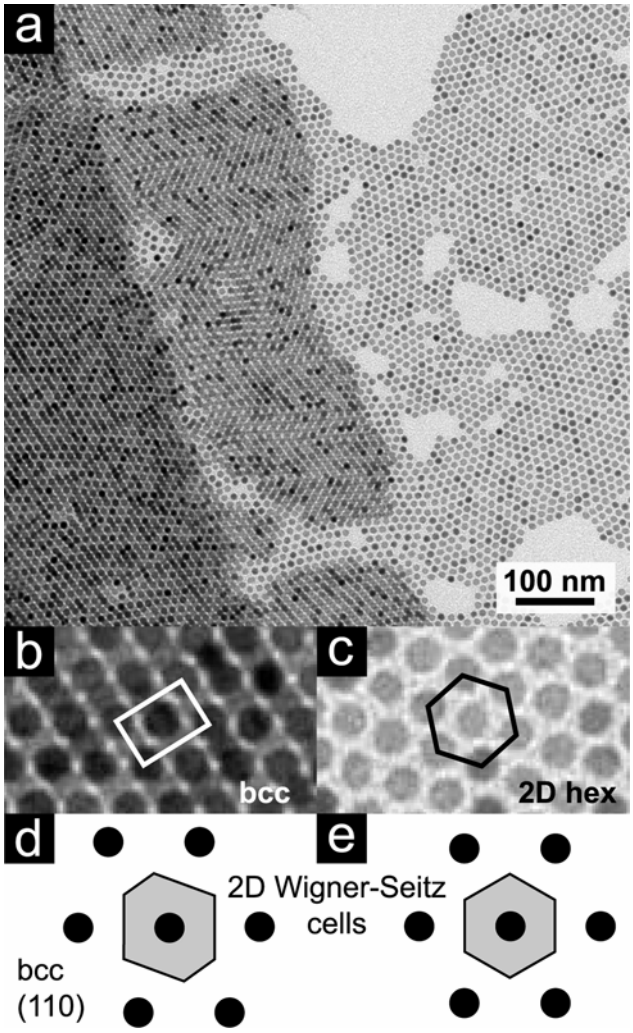

Figure 3.10: (a) TEM image of 9.5 nm PbSe nanocrystals showing the transition from a 2D hexagonally packed monolayer to a 3D bcc superlattice assembly. (b) and (c) show higher magnification images of the different structures in (a) and the corresponding unit cells. (d) and (e) illustrate the 2D W-S cells of the bcc (110) plane and the fcc (111) (or hexagonally-packed monolayer) plane. The 2D W-S cell for a hexagonally packed cell is more geometrically symmetric than the 2D W-S cell for the bcc (110) plane which minimizes the energetically unfavorable stretching and compression of organic ligand chains.

3.3.6 Twinning in BCC Nanocrystal Superlattices

Twin planes are often observed in bcc superlattices of nanocrystals. For example, Whetten et al. observed twinning in bcc superlattices of Au nanocrystals in 1996.[14] Ye et al. recently reported twin planes in bcc AB_6 binary superlattices of Au and Fe_3O_4 nanocrystals.[24] Figure 3.11 shows twin boundaries in bcc superlattices of 3.7 nm PbS and 7.9 nm PbSe nanocrystals. In all of these cases, the twinned bcc domains share common {112} planes.

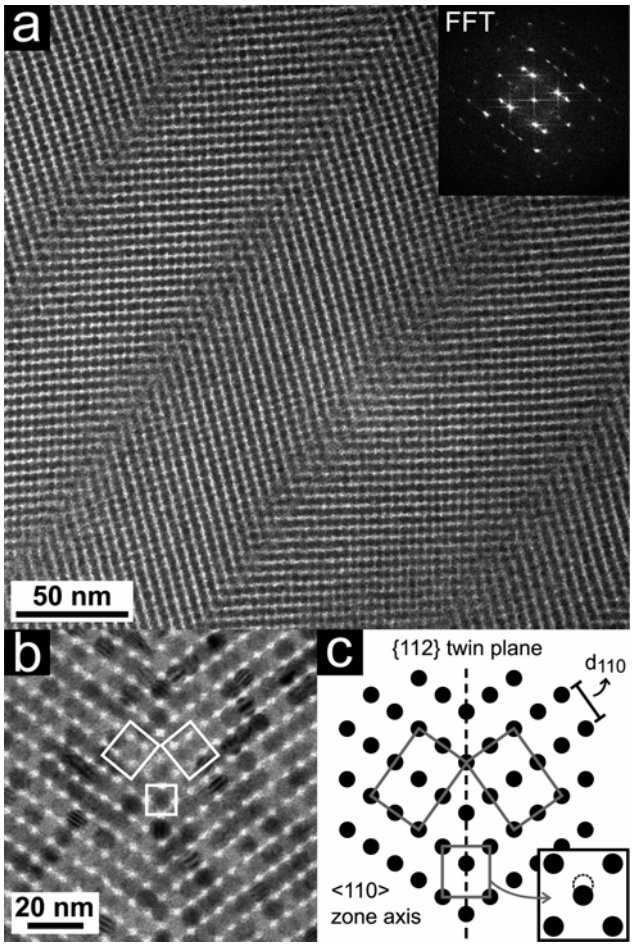

Figure 3.11: (a) TEM image and corresponding FTT of parallel {112} twin planes in a {110} oriented bcc superlattice of 3.7 nm PbS nanocrystals. A detailed view of a single twin plane in a bcc superlattice of 7.9 nm PbSe nanocrystals is shown in (b) and represented in the schematic in (c). The upper 2 rectangles show 2 bcc unit cells reflected across the twin plane and the lower rectangle highlights that the positions of the atoms along the twin plane are shifted slightly along the <111> direction from where they are crystallographically expected.

Twin boundaries can form during crystal formation or when a crystal plastically deforms due to an applied stress. For nanocrystal superlattices, twinning appears to be very common in bcc superlattices but is only rarely observed in fcc superlattices. In one

case, Rupich et al. showed that twinning occurs in large fcc superlattice crystals carefully grown over long periods of time.[25] The large superlattice crystals had multiple intersecting twin planes that allowed certain low surface-energy shapes of the macroscopic superlattice crystal. In contrast, the striations in Figure 3.11a, with parallel alignment of the twin boundaries, are common in plastically deformed crystals as a result of an applied shear stress. Nanocrystal films formed by solvent-evaporation methods tend to crack in response to appreciable lateral stresses due to the deposition and drying process. In addition to fracture, nanocrystal superlattices have also been shown to dissipate mechanical stress through elastic[26, 27] and plastic[27] deformation and by forming dislocations.[8, 26]

Plastic deformation in atomic crystals can be achieved by either defect-mediated slip involving dislocation motion or coordinated movements of atoms (e.g. twinning). In crystal systems with many available slip systems, like fcc, plastic deformation is achieved primarily by slip; in crystal systems with few slip systems, like hcp, twinning is more commonly observed. Based on the comparison of the number of slip systems in fcc and bcc, bcc is expected to exhibit a higher tendency to form twins. While there are several observations of dislocations in nanocrystal superlattices,[8, 26] dislocation motion due to an applied stress has not been explicitly demonstrated. Instead of dislocation motion, perhaps coordinated movements—where crystallographic planes slide past one another—are more common deformation mechanisms for nanocrystal superlattices. Indeed, such mechanisms are commonly accepted for shear-induced plastic deformation in ordered assemblies of polymer micelles[28] and colloidal particles.[29]

Nanocrystal superlattices tend to orient themselves such that the highest density plane—(111) for fcc and (110) for bcc—is parallel to the substrate. A lateral shear stress can thus result in relative motion of these highest density planes. In fcc lattices, relative

motion of close-packed (111) planes can result in stacking faults that can transform the pure fcc lattice into a structure that is intermediate to fcc and hcp which would not be easily detectable by TEM. The observation of twinning in bcc nanocrystal superlattices is consistent with ordered assemblies of polymer micelles[28] and colloidal particles[29] and suggests that the bcc (110) planes can not easily slide past one another. Instead, a continuous deformation of the superlattice by small coordinated movements of nanocrystals in the <111> direction in response to the lateral shear stress results in {112} twin planes as shown in Figure 3.11. We note that the highest density plane spacings, d_{111}^{fcc} and d_{110}^{bcc}, are both equal to $D_{eff}\sqrt{2/3}$ where D_{eff} is the effective sphere diameter and this can not be used to explain the observation that $\{111\}_{\text{fcc}}$ planes slide past one another and $\{110\}_{\text{bcc}}$ planes do not. However, the difference in plane density, 0.91 for $\{111\}_{\text{fcc}}$ and 0.83 for $\{110\}_{\text{bcc}}$, may play a significant role in the ability of these planes to slide past one another and explain the tendency for bcc nanocrystal superlattices to form twins.

3.4 CONCLUSIONS

Body-centered cubic nanocrystal superlattices of 1.8 nm dodecanethiol-capped Au nanocrystals, 3.7 nm oleic acid-capped PbS nanocrystals, and 7.9 nm oleic acid-capped PbSe nanocrystals were studied by TEM and GISAXS. By considering the Wigner-Seitz cells for bcc and fcc, we show that ligand packing frustration can lead to a tendency for spherical nanocrystals to assemble into bcc superlattices over fcc. A calculation of the change in conformational entropy of the ligand chains when a collection of nanocrystals organize into an ordered superlattice reviled that a bcc arrangement was significantly favored over fcc when the ligands were allowed to interpenetrate with ligands from a neighboring nanocrystals. The observation that

nanocrystals which form 3D bcc superlattices also form monolayers with 2D hexagonal close-packed symmetry is consistent with the role of ligand packing frustration in their assembly. Additionally, it was found that bcc nanocrystal superlattices tend to exhibit {112} twin planes after drying on a substrate. We propose that these twin planes form in response to lateral shear forces that arise due to the evaporation of solvent and that a difference in the density of the highest-density planes of bcc and fcc may be responsible for the tendency for bcc nanocrystal superlattices to undergo twinning when fcc superlattices do not.

3.5 REFERENCES AND NOTES

1. Burda, C.; Chen, X.; Narayanan, R.; El-Sayed, M. A., Chemistry and Properties of Nanocrystals of Different Shapes. *Chemical Reviews* **2005,** 105, (4), 1025-1102.
2. Alivisatos, A. P., Perspectives on the Physical Chemistry of Semiconductor Nanocrystals. *The Journal of Physical Chemistry* **1996,** 100, (31), 13226-13239.
3. Leslie-Pelecky, D. L.; Rieke, R. D., Magnetic Properties of Nanostructured Materials. *Chemistry of Materials* **1996,** 8, (8), 1770-1783.
4. Chen, C.-C.; Herhold, A. B.; Johnson, C. S.; Alivisatos, A. P., Size Dependence of Structural Metastability in Semiconductor Nanocrystals. *Science* **1997,** 276, (5311), 398-401.
5. Murray, C. B.; Kagan, C. R.; Bawendi, M. G., Self-Organization of CdSe Nanocrystallites into Three-Dimensional Quantum Dot Superlattices. *Science* **1995,** 270, (5240), 1335-1338.
6. Shevchenko, E. V.; Talapin, D. V.; Kotov, N. A.; O'Brien, S.; Murray, C. B., Structural diversity in binary nanoparticle superlattices. *Nature* **2006,** 439, (7072), 55-59.
7. Korgel, B. A.; Fullam, S.; Connolly, S.; Fitzmaurice, D., Assembly and Self-Organization of Silver Nanocrystal Superlattices: Ordered "Soft Spheres". *The Journal of Physical Chemistry B* **1998,** 102, (43), 8379-8388.
8. Sigman, M. B.; Saunders, A. E.; Korgel, B. A., Metal Nanocrystal Superlattice Nucleation and Growth. *Langmuir* **2004,** 20, (3), 978-983.

9. Giersig, M.; Mulvaney, P., Preparation of ordered colloid monolayers by electrophoretic deposition. *Langmuir* **1993,** 9, (12), 3408-3413.

10. Goodfellow, B. W.; Korgel, B. A., Reversible Solvent Vapor-Mediated Phase Changes in Nanocrystal Superlattices. *ACS Nano* **2011,** 5, (4), 2419-2424.

11. Alder, B. J.; Wainwright, T. E., Phase Transition for a Hard Sphere System. *The Journal of Chemical Physics* **1957,** 27, (5), 1208-1208.

12. Pusey, P. N.; van Megen, W.; Bartlett, P.; Ackerson, B. J.; Rarity, J. G.; Underwood, S. M., Structure of crystals of hard colloidal spheres. *Physical Review Letters* **1989,** 63, (25), 2753-2753.

13. Podsiadlo, P.; Krylova, G. V.; Demortière, A.; Shevchenko, E. V., Multicomponent periodic nanoparticle superlattices. *Journal of Nanoparticle Research* **2011,** 13, (1), 15-32.

14. Whetten, R. L.; Khoury, J. T.; Alvarez, M. M.; Murthy, S.; Vezmar, I.; Wang, Z. L.; Stephens, P. W.; Cleveland, C. L.; Luedtke, W. D.; Landman, U., Nanocrystal gold molecules. *Advanced Materials* **1996,** 8, (5), 428-433.

15. Korgel, B. A.; Fitzmaurice, D., Small-angle x-ray-scattering study of silver-nanocrystal disorder-order phase transitions. *Physical Review B* **1999,** 59, (22), 14191-14191.

16. Henry, A. I.; Courty, A.; Pileni, M. P.; Albouy, P. A.; Israelachvili, J., Tuning of Solid Phase in Supracrystals Made of Silver Nanocrystals. *Nano Letters* **2008,** 8, (7), 2000-2005.

17. Whetten, R. L.; Shafigullin, M. N.; Khoury, J. T.; Schaaff, T. G.; Vezmar, I.; Alvarez, M. M.; Wilkinson, A., Crystal Structures of Molecular Gold Nanocrystal Arrays. *Accounts of Chemical Research* **1999,** 32, (5), 397-406.

18. Kremer, K.; Robbins, M. O.; Grest, G. S., Phase Diagram of Yukawa Systems: Model for Charge-Stabilized Colloids. *Physical Review Letters* **1986,** 57, (21), 2694-2694.

19. Landman, U.; Luedtke, W. D., Small is different: energetic, structural, thermal, and mechanical properties of passivated nanocluster assemblies. *Faraday Discussions* **2004,** 125, 1-1.

20. Goodfellow, B. W.; Patel, R. N.; Panthani, M. G.; Smilgies, D.-M.; Korgel, B. A., Melting and Sintering of a Body-Centered Cubic Superlattice of PbSe Nanocrystals Followed by Small Angle X-ray Scattering. *The Journal of Physical Chemistry C* **2011,** 115, (14), 6397-6404.

21. Choi, J. J.; Bealing, C. R.; Bian, K.; Hughes, K. J.; Zhang, W.; Smilgies, D.-M.; Hennig, R. G.; Engstrom, J. R.; Hanrath, T., Controlling Nanocrystal Superlattice Symmetry and Shape-Anisotropic Interactions through Variable Ligand Surface Coverage. *Journal of the American Chemical Society* **2011,** 133, (9), 3131-3138.

22. Bian, K.; Choi, J. J.; Kaushik, A.; Clancy, P.; Smilgies, D.-M.; Hanrath, T., Shape-Anisotropy Driven Symmetry Transformations in Nanocrystal Superlattice Polymorphs. *ACS Nano* **2011,** 5, (4), 2815-2823.

23. Thomas, E. L.; Kinning, D. J.; Alward, D. B.; Henkee, C. S., Ordered packing arrangements of spherical micelles of diblock copolymers in two and three dimensions. *Macromolecules* **1987,** 20, (11), 2934-2939.

24. Ye, X.; Chen, J.; Murray, C. B., Polymorphism in Self-Assembled AB6 Binary Nanocrystal Superlattices. *Journal of the American Chemical Society* **2011,** 133, (8), 2613-2620.

25. Rupich, S. M.; Shevchenko, E. V.; Bodnarchuk, M. I.; Lee, B.; Talapin, D. V., Size-Dependent Multiple Twinning in Nanocrystal Superlattices. *Journal of the American Chemical Society* **2010,** 132, (1), 289-296.

26. Smith, D. K.; Goodfellow, B.; Smilgies, D.-M.; Korgel, B. A., Self-Assembled Simple Hexagonal AB2 Binary Nanocrystal Superlattices: SEM, GISAXS, and Defects. *Journal of the American Chemical Society* **2009,** 131, (9), 3281-3290.

27. Tam, E.; Podsiadlo, P.; Shevchenko, E.; Ogletree, D. F.; Delplancke-Ogletree, M.-P.; Ashby, P. D., Mechanical Properties of Face-Centered Cubic Supercrystals of Nanocrystals. *Nano Letters* **2010,** 10, (7), 2363-2367.

28. McConnell, G. A.; Lin, M. Y.; Gast, A. P., Long Range Order in Polymeric Micelles under Steady Shear. *Macromolecules* **1995,** 28, (20), 6754-6764.

29. Ackerson, B. J.; Clark, N. A., Shear-induced partial translational ordering of a colloidal solid. *Physical Review A* **1984,** 30, (2), 906-906.

30. Rasch, M. R.; Rossinyon, E.; Hueso, J. L.; Goodfellow, B. W.; Arbiol, J.; Korgel, B. A., Hydrophobic Gold Nanoparticle Self-Assembly with Phosphatidylcholine Lipid: Membrane-Loaded and Janus Vesicles. *Nano Letters* **2010**, 10, (9), 3733-3739.

31. Konstantatos, G.; Levina, L.; Fischer, A.; Sargent, E. H., Engineering the Temporal Response of Photoconductive Photodetectors via Selective Introduction of Surface Trap States. *Nano Letters* **2008,** *8* (5), 1446-1450.

32. Hammersley, A. P. ESRF Internal Report. ESRF97HA02T, **1997**.

33. Smilgies, D.-M.; Blasini, D. R.; Indexation scheme for oriented molecular thin films studied with grazing-incidence reciprocal-space mapping. *J. App. Cryst.* **2007,** 40, 716-718.

Chapter 4: Melting and Sintering of a Body-Centered Cubic Superlattice of PbSe Nanocrystals Characterized In Situ by Small Angle X-ray Scattering†

4.1 INTRODUCTION

Colloidal nanocrystals with precisely controlled size and shape represent a unique class of materials with significantly different properties than their bulk analogs.[1,2] Nanocrystal assemblies have been explored for a variety of applications, including solar cells,[3-14] field effect transistors,[8, 15-18] light emitting diodes,[19-22] thermoelectric devices,[17, 23, 24] photodetectors,[13, 25] and chemical sensors.[26] The deposition of nanocrystals on substrates by solution-based processes also provides a low-cost route to forming inorganic films without the use of high temperature or vacuum.[3,14,27,28] Lead chalcogenide (i.e. PbS, PbSe, PbTe) nanocrystals, in particular, have received considerable attention,[29-41] due in part to a large Bohr exciton radius, a narrow and size-tunable[29-31] band gap, symmetric conduction and valence bands,[42] and significant electronic coupling between neighboring nanocrystals in superlattices due to their relatively low effective electron and hole masses.[43] These properties make them interesting candidates for a variety of electronic and optoelectronic applications.[6-13,17,18,22-25]

Many applications of nanocrystal films will require device operation or processing at elevated temperature. The impacts of nanocrystal size,[12,44,45] arrangement,[15,46] surface chemistry,[13,18,47-50] and separation[18,44,48,49] on the electronic and optoelectronic properties of lead chalcogenide nanocrystal thin films have been

† Portions of this chapter appear in Goodfellow, Brian W.; Patel, Reken N.; Panthani, Matthew G.; Smilgies, Detlef-M.; Korgel, Brian A., "Melting and Sintering of a Body-Centered Cubic Superlattice of PbSe Nanocrystals Followed by Small Angle X-ray Scattering." *Journal of Physical Chemistry C* (2011), 115(14), 6397-6404.

extensively studied; however, the influence of heating on the structure and composition of the nanocrystal films has largely been overlooked. Several reports have shown that thermal processing can change significantly the electronic properties of PbSe nanocrystal films. For example, Law et. al.[49] observed a dramatic increase in the electrical conductivity of PbSe nanocrystal films, of nearly 10 orders of magnitude, after heating above 250°C. Based on scanning electron microscopy (SEM), small angle x-ray scattering (SAXS), and wide angle x-ray scattering (WAXS) data, they suggested that this was due to nanocrystal sintering; however, a detailed analysis of the structural changes of the heated PbSe nanocrystal assemblies was not provided. Similarly, Baik et. al.[51] reported significant increases in the electrical conductivity of ethanedithiol-treated PbSe and PbS nanocrystals when heated to an even lower temperature of 170°C, and Klem et. al.[52] observed improvements in both electrical conductivity and mobility of ethanedithiol-treated PbS nanocrystal films annealed at still lower temperature of only 90°C in air, which they attributed to surface oxidation and corresponding increases in hole concentration. Van Huis et. al.[53] directly observed nanocrystal fusion in PbSe nanocrystal assemblies by in situ high resolution transmission electron microscopy (TEM) of hexylamine-capped PbSe nanocrystal monolayers heated just above 100°C. One of the problems, however, with in situ TEM to study the structural changes of a heated superlattice is the presence of the energetic electron beam. The beam can induce melting of the inorganic cores, which may prematurely destabilize the superlattice, or decompose the hydrocarbon ligands into a graphitic carbon layer between particles that stabilizes the superlattice to unusually high temperature.[54,55] Clearly, there is still much uncertainty about how heating changes the structure of PbSe nanocrystal superlattices.

Here, we report a detailed study of how the structure and composition of a body-centered cubic (bcc) superlattice of oleic acid-capped PbSe nanocrystals changes as it is

heated in air to 350°C, relying on real time SAXS measurements with synchrotron radiation to provide statistically-appropriate structural data with sub-Ångstrom spatial resolution. Complementary X-ray diffraction (XRD), TEM, and SEM measurements of the heated superlattices were also carried out to provide additional information about the structural transitions observed by SAXS. In the cases of Ag[56,57] and Au[58,59] nanocrystal superlattices, in situ SAXS measurements of heated superlattices have provided new insight, for example, revealing that the temperature-dependence of the structural transitions can be quite complicated and interesting.[60-63] In the case here of a PbSe nanocrystal superlattice, the SAXS data show that the bcc superlattice is stable up to only 110°C, and then above this temperature the periodic superlattice order collapses. There is first a loss of long-range translational order between 110°C and 150°C and then a loss of local positional order at 168°C. Above 168°C, the nanocrystals undergo a gradual sintering process accompanied by an oxidative conversion of the PbSe nanocrystals to $PbSeO_3$ nanorods, which has not been previously observed.

4.2 Experimental Methods

4.2.1 Chemicals

Lead acetate trihydrate ($Pb(ac)_2 \cdot H_2O$, 99.999%), oleic acid (OA, >99%), diphenyl ether (Fluka, >99.9%), selenium powder (Se, 100 mesh, 99.99%), and trioctylphosphine (TOP, tech., 90%) were purchased from Aldrich and used as received. TOP was stored in a N_2-filled glovebox. A stock solution of 1M Se in TOP was prepared by dissolving 20 mmol Se powder in 20 mL TOP overnight in a glovebox.

4.2.2 PbSe Nanocrystal Synthesis and Purification

PbSe nanocrystals were prepared following an adaptation of a procedure described by Cho et.al.[32] In a 25 mL 3-neck flask, 10 mL phenyl ether, 2.5 mL oleic acid, and 0.76 g $Pb(ac)_2 \cdot H_2O$ were combined. The flask was attached to a Schlenk line, heated to 75°C under vacuum, and held there for one hour to begin the formation of a lead oleate precursor and to completely remove the acetic acid and water byproducts from the reaction flask. The flask was then heated to 150°C under a N_2 atmosphere and held there for 30 minutes to complete the formation of the lead oleate complex. The flask was then cooled to 60°C and 6 mL of the TOP-Se stock solution was injected into the flask. Separately, in a 50 mL three neck flask, 15 mL of phenyl ether was dried and degassed by heating to 75°C under vacuum for one hour. This flask was then heated to 150°C under N_2 flow. At this point, 13 mL of the lead-oleate and TOP-Se mixture in phenyl ether was rapidly injected into the hot flask. Once the temperature in the flask regained 120°C, the remaining 5.5 mL was injected dropwise over the course of 4 minutes. The temperature was then increased to 150°C, where it was allowed to react for 10 minutes. The heating mantle was then removed and the flask was allowed to cool to room temperature.

Excess ligand and unreacted precursors were removed from the crude reaction product by redispersion and precipitation of the nanocrystals using toluene and ethanol as a solvent/antisolvent pair. Initially, ethanol was added to the crude reaction solution to precipitate the nanocrystals. The mixture was centrifuged at 8000 rpm for 5 min to isolate the nanocrystals as a precipitate. The supernatant was discarded and the precipitate was redispersed in toluene. This procedure was repeated once more. After redispersing the nanocrystals in toluene, the dispersion was centrifuged at 8000 rpm for 5

minutes to separate any poorly-capped nanocrystals or agglomerates. The precipitate was discarded and the supernatant was collected and used for the experiments in this study.

4.2.3 PbSe Nanocrystal Film Preparation

PbSe nanocrystals were dispersed in hexane and then diluted with an equal volume of toluene. It is important to point out that the choice of solvent used for deposition can significantly affect the microstructure of the nanocrystal film.[64,65] The dispersion was drop-cast onto a TEM grid (carbon-coated copper 200 mesh, Electron Microscopy Sciences) for TEM imaging or a soda-lime glass cover slide (Fisherfinest Premium, 25mm x 25mm, 0.13 to 0.17mm thick, Fisher Scientific) for SAXS. The nanocrystal films were stored under ambient atmosphere at room temperature for approximately 5 days prior to characterization by in situ SAXS.

4.2.4 Materials Characterization

TEM was performed on a Phillips EM208 TEM with 80 kV accelerating voltage. Images were acquired digitally. Small angle x-ray scattering (SAXS) was performed on dilute dispersions (~0.5 mg/mL) of PbSe nanocrystals in hexane in a stainless steel cell with kapton windows using a Molecular Metrology instrument with a rotating copper anode X-ray generator (Bruker Nonius; λ = 1.54 Å) operating at 3.0 kW. The scattered X-rays were collected on a 2D multiwire gas-filled detector (Molecular Metrology, Inc.). A silver behenate ($CH_3(CH_2)_{20}COOAg$) standard was used to calibrate the scattering angle of scattered photons. Radial integrations of scattering intensity were performed using Datasqueeze.[66] Background scattering of the hexane solvent and the experimental setup were subtracted from the data.

4.2.5 In Situ SAXS of a Heated PbSe Film

A glass cover slide containing a PbSe nanocrystal film was placed into a Mettler Toledo FP82HT hot stage between 2 aluminum spacers specifically fabricated for this experiment. The hot stage was then placed into the D1 beam line at the Cornell High Energy Synchrotron (CHESS) in transmission mode with the side containing the nanocrystal film facing the detector. While much of the beamline is under vaccum or helium atmosphere, the x-ray beam transmits though a 10 cm section of ambient atmosphere and that this section was used to mount the hot stage. The hot stage was controlled with a Mettler Toledo FP80 processing unit to heat the sample from 28°C to 350°C at a rate of 3°C/min. SAXS measurements were performed using monochromatic radiation of wavelength λ=1.252 Å with a bandwidth $\Delta\lambda/\lambda$ of 1.5%. The x-ray beam was produced by a hard-bent dipole magnet in the Cornell storage ring and monochromatized with Mo:B_4C multilayers with a period of 30 Å. The D1 area detector (MedOptics) is a fiber coupled CCD camera with a pixel size of 46.9 μm by 46.9 μm and a total of 1024 x 1024 pixels with a 14-bit dynamical range per pixel. Typical read-out time per image was below 5 sec. The images were dark current corrected, distortion-corrected, and flat-field corrected by the acquisition software. The sample to detector distance was 852 mm, as determined using a silver behenate powder standard. The exposure time for each collected scattering image was 4 seconds and was followed by a 16 second delay (including detector readout). Considering the heating rate, this resulted in the collection of a scattering image about every 1°C. Scattering images were calibrated and integrated using the Fit2D software.[67]

4.3 Results and Discussion

4.3.1 PbSe Nanocrystals and BCC Superlattice Formation

Figure 4.1 shows TEM images of oleic acid-capped PbSe nanocrystals drop-cast from 1:1 hexane:toluene dispersions. The nanocrystals are sufficiently monodisperse to order into superlattices. The inorganic PbSe cores of the nanocrystals remain separated by the oleic acid capping ligand layer coating each particle. The superlattice structure was observed to vary depending on the concentration of the nanocrystals in the dispersion deposited on the substrate. Nanocrystals deposited from relatively dilute dispersions to form monolayers assembled with hexagonal order as shown in Figure 4.1a. In contrast, nanocrystals deposited from more concentrated dispersions as thicker superlattice films—as in Figure 4.1b—assembled into superlattices with bcc structure. Some regions of the sample showed the coexistence of thin monolayers with hexagonal order and thicker superlattices with bcc structure. The origin of this difference in superlattice symmetry and its dependence on the layer thickness is presently not understood and is under investigation. The thicker nanocrystal superlattice films with bcc structure were the focus of this study and were heated and probed by in situ SAXS.

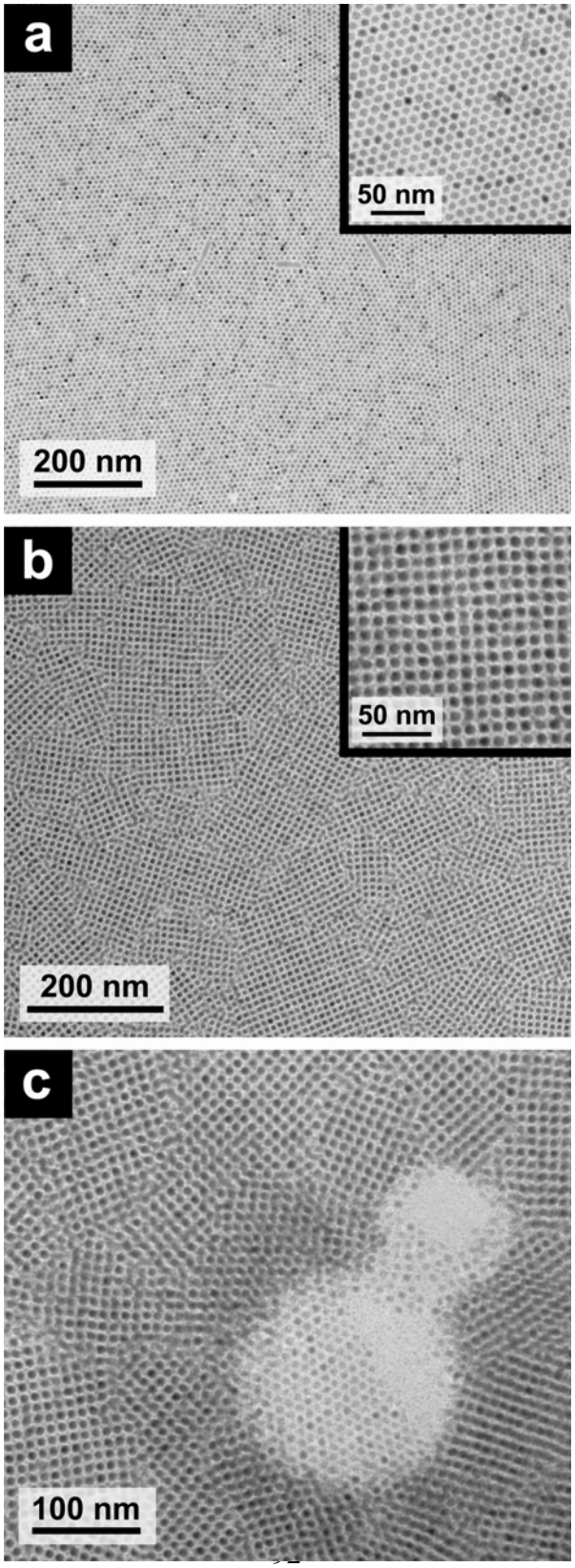
a
50 nm
200 nm
b
50 nm
200 nm
c
100 nm

Figure 4.1: TEM images of PbSe nanocrystals drop-cast from relatively (a) dilute or (b-c) concentrated dispersions in 1:1 mixture by volume of hexane and toluene. (a) A monolayer of PbSe nanocrystals with hexagonal order; (b) a PbSe nanocrystal superlattice film of several nanocrystals thick (~20 nm) with bcc symmetry. (c) A region of sample with the coexistence of thicker bcc superlattice films and monolayers of hexagonally ordered nanocrystals.

Figure 4.2 shows transmission SAXS data for a sample of PbSe nanocrystal superlattice. The radial X-ray scattering intensity profile is obtained by integrating the experimentally-measured 2D scattering pattern in the inset. The observation of relatively sharp Bragg peaks confirms that there is long-range periodic superlattice ordering of the nanocrystals, as was observed by TEM. Most commonly, monodisperse nanocrystals have been observed to assemble into superlattices with face centered cubic (fcc) structure;[68,69] however, in this case, the diffraction peaks appear with relative positions of $q/q^* = \sqrt{1} : \sqrt{2} : \sqrt{3} : \sqrt{4}$, where $q^* = 0.825\,\mathrm{nm}^{-1}$ is the location of the lowest order reflection, indicating that the superlattice has either bcc or simple cubic (sc) symmetry. An independent measure of the superlattice *d*-spacings by TEM confirmed that the superlattice is bcc and not sc. As illustrated in Figure 4.3, the *d*-spacings observed by TEM between (100), (110), and (210) planes of 10.57 nm, 7.63 nm, and 4.71 nm, respectively, correspond to an average lattice constant of $a_{bcc,TEM} = 10.63\,\mathrm{nm}$, which is very close to the bcc lattice constant determined from SAXS of $a_{bcc,SAXS} = 10.79\,\mathrm{nm}$. If the superlattice had sc symmetry, the lattice constant determined by SAXS would be $a_{sc,SAXS} = 7.63\,\mathrm{nm}$, which is not consistent with the lattice constant determined by TEM—i.e., $a_{sc,TEM} = 10.63\,\mathrm{nm}$. A full comparison of the *d*-spacings measured by SAXS and TEM is provided in Table 4.1.

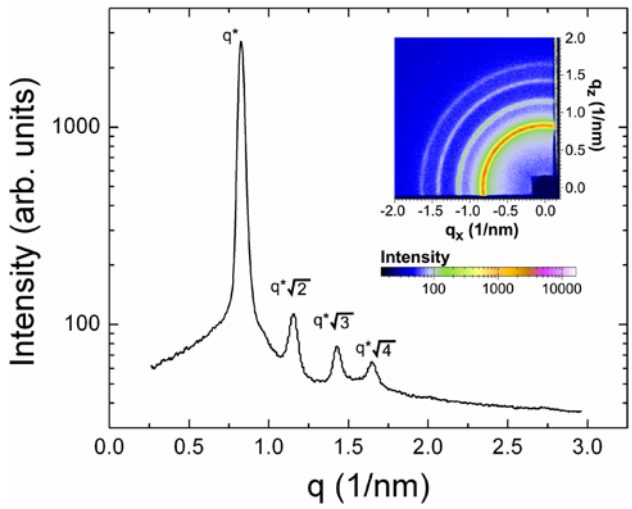

Figure 4.2: Transmission SAXS of a PbSe nanocrystal superlattice. The peak positions $q/q^* = \sqrt{1}, \sqrt{2}, \sqrt{3}, \sqrt{4}$ are consistent with reflections from the (110), (200), (211), and (220) lattice planes of a bcc superlattice. The inset shows the experimentally measured 2D scattering pattern. The *d*-spacings of the first four diffraction peaks correspond to $d = 2\pi / q = 7.61$ nm, 5.44 nm, 4.40 nm and 3.80 nm, for an average lattice constant of $a_{bcc,SAXS} = 10.79$ nm.

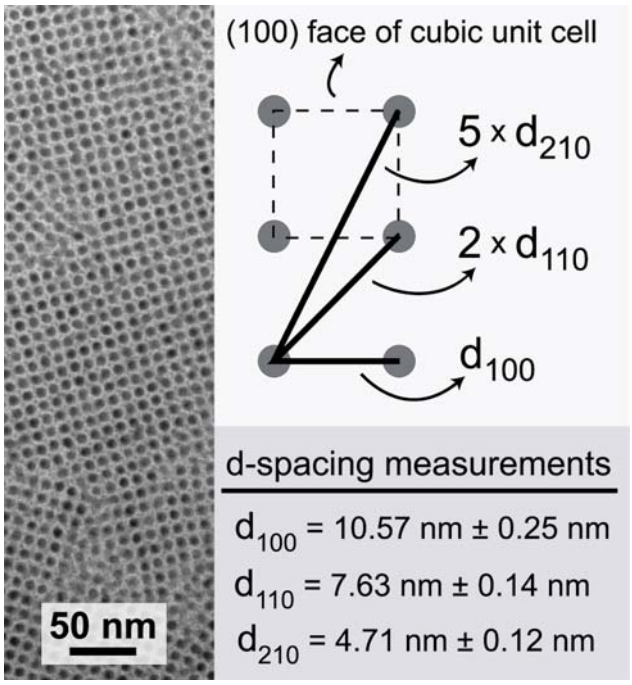

Figure 4.3: (Left) TEM image of a PbSe nanocrystal superlattice. A (100) superlattice plane has been imaged. The body-centered positions were also observed at different focal depths with high-resolution TEM, as shown in Figure 4.4. (Right) Schematic that shows how certain d-spacings can be directly measured from the TEM image. The measured lattice spacings of 10.57 nm, 7.63 nm, and 4.71 nm, correspond to the (100), (110), and (210) d-spacings of a bcc superlattice. The corresponding lattice constant of $a_{TEM} = 10.63\,\text{nm}$ is close to that measured by SAXS, $a_{\text{SAXS}} = 10.79\,\text{nm}$.

Table 4.1: Comparison of bcc superlattice *d*-spacings determined by TEM and SAXS.

	d(hkl) (nm)	
(hkl)	**from TEM**	**from SAXS**
(100)	10.57	
(110)	7.63	7.61
(111)	6.14*	
(200)	5.32*	5.44
(210)	4.71	
(211)	4.34*	4.40
(220)	3.76*	3.80
(300),(221)	3.54*	

* These values were calculated from the average lattice constant of $a_{bcc,TEM} = 10.63\,\text{nm}$ determined from the *d*(100), *d*(110), and *d*(210) spacings observed by TEM.

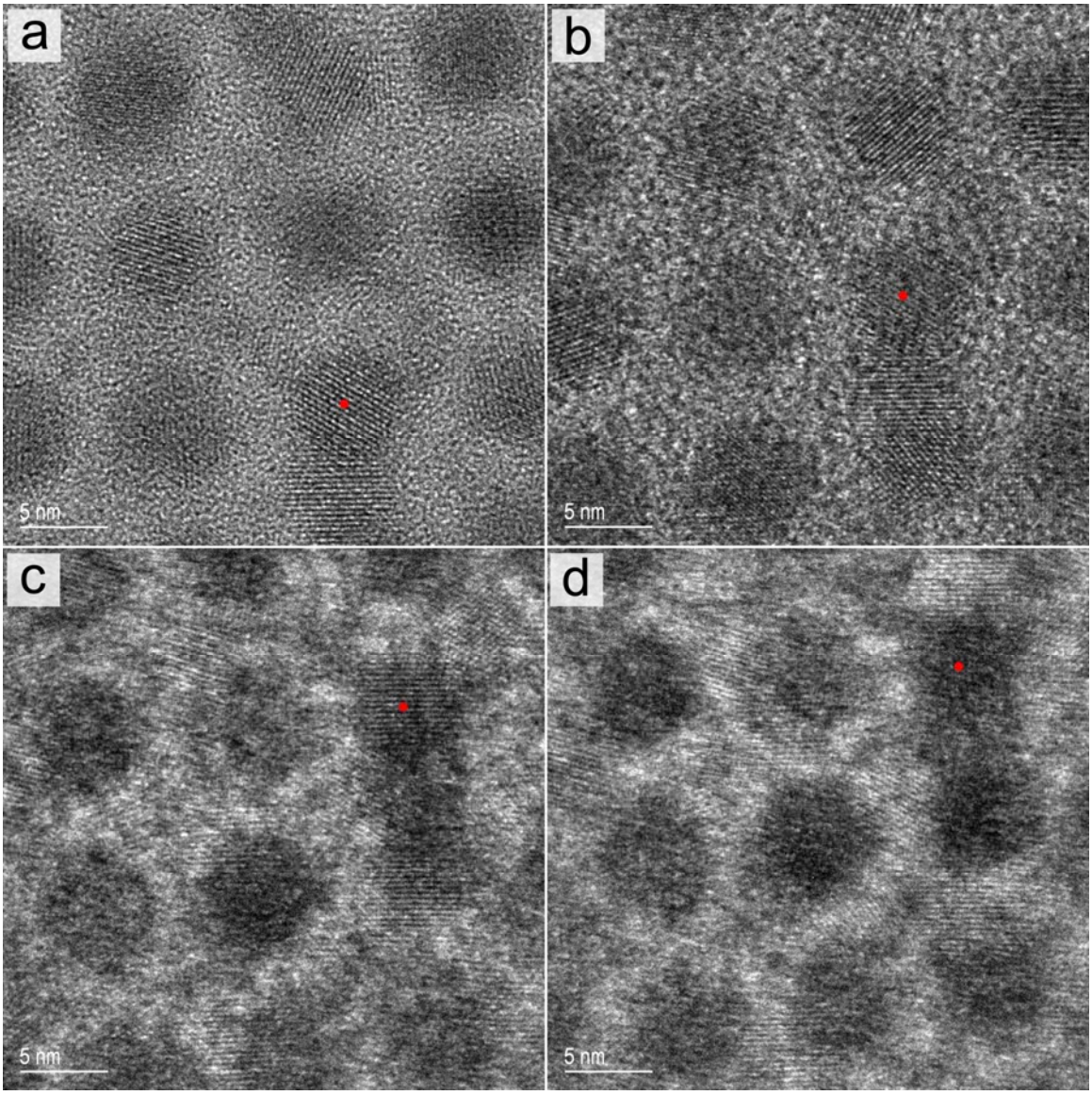

Figure 4.4: High resolution TEM images of a bcc superlattice of 6.6 nm diameter oleic acid-capped PbSe nanocrystals as the focal depth was increased. Beginning with the focused image in (a), the focal depth was gradually increased in the images (b-d), revealing lattice fringes of the underlying nanocrystal layers. The red dots in the images mark the same spot in the superlattice.

The center-to-center interparticle separation between nearest neighbor PbSe nanocrystals in the bcc superlattice measured by SAXS and TEM are $D_{eff,SAXS} = 9.34\,\text{nm}$

and $D_{eff,TEM} = 9.21\,\text{nm}$. This separation corresponds to a "soft sphere" nanocrystal diameter that includes the inorganic PbSe core of the nanocrystals and part of the ligand shell.[70] To obtain an estimate of the volume that is excluded in the superlattice by the ligands, the diameter of the inorganic PbSe cores was determined independently from solution SAXS measurements of the nanocrystals dispersed in hexane, shown in Figure 4.5. By fitting the data to a model for the X-ray scattering intensity, $I(q)$, from a dilute dispersion of non-interacting spherical particles,[69,70]

$$I(q) \propto \int_0^\infty N(R)P(qR)R^6 dR \tag{4.1}$$

the average radius of the inorganic PbSe cores $\overline{R}$, can be determined. In Eqn (4.1), q is the scattering vector, which depends on the X-ray wavelength (λ = 1.54 Å) and the scattering angle θ: $q = (4\pi/\lambda)\sin(\theta/2)$. Since the scattering intensity depends on the nanocrystal radius R, the data are very sensitive to the size distribution, $N(R)$, which is the number fraction of nanocrystals of radius R, in the sample. $P(qR)$ is the form factor for a solid homogeneous sphere:[71, 72]

$$P(qR) = \left[3\frac{\sin(qR) - qR\cos(qR)}{(qR)^3} \right]^2 . \tag{4.2}$$

Relatively monodisperse nanocrystals prepared by arrested precipitation, such as the PbSe nanocrystals studied here, typically exhibit a Gaussian size distribution with an average nanocrystal radius $\overline{R}$ and standard deviation of σ about the mean,[70]

$$N(R) = \frac{1}{\sigma\sqrt{2\pi}} \exp\left[\frac{-(R-\overline{R})^2}{2\sigma^2} \right] . \tag{4.3}$$

The average diameter (i.e., $2\overline{R}$) of the crystalline PbSe cores of the nanocrystals determined by fitting Eqns (4.1-4.3) to the data in Figure 4.5 is $D_{core,SAXS} = 6.60\,\text{nm} \pm 0.79\,\text{nm}\,(\pm 12\%)$. Therefore, the corresponding "soft sphere" ligand shell thickness is $\delta = \frac{1}{2}(D_{eff,SAXS} - D_{core,SAXS}) = 1.37\,\text{nm}$.

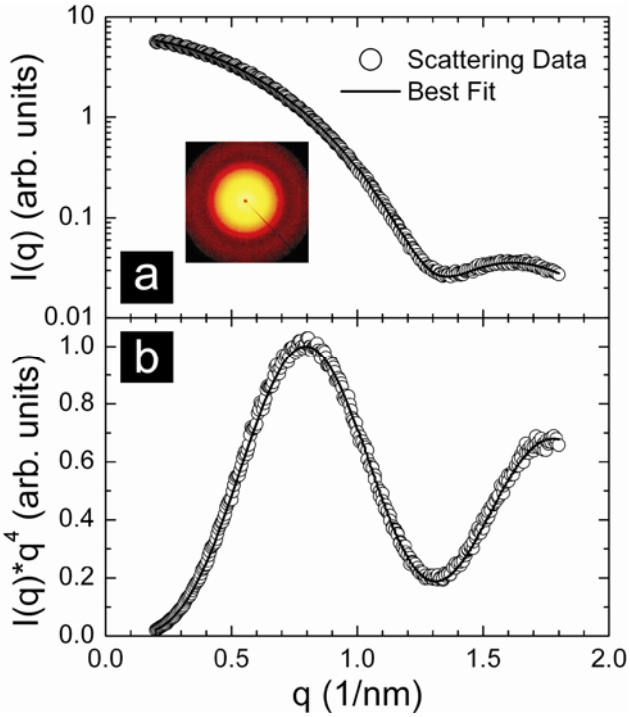

Figure 4.5: SAXS of PbSe nanocrystals dispersed in hexane. The radially integrated 2D scattering intensity (inset) is plotted as (a) $I(q)$ vs. q and (b) $I(q) \times q^4$ vs. q (Porod plot), with the data normalized to the scattering intensity of the first peak maximum in the Porod plot at q = 0.81 nm^{-1}. The best fit of Eqn (4.1) (solid line) to the scattering data (○) gives an average diameter of 6.60 nm ± 0.79 nm.

The interstitial void space between the soft sphere particles in the superlattice—corresponding to 32% of the total volume for a bcc superlattice—is also filled by ligand. Therefore, by knowing the lattice constant of the bcc unit cell and the PbSe core diameter independently, the total volume in the superlattice that must be occupied by the capping

ligands can be compared to the ligand excluded volume that is expected for each nanocrystal. The total volume excluded by the adsorbed oleic acid chains on each nanocrystal can be estimated by assuming that each ligand molecule attaches to the PbSe surface with a circular footprint of 0.16 nm^2 with a close-packed density on the surface of 91%, and taking an excluded volume of 0.5116 nm^3 for each oleic acid molecule.[65] Based on the total surface area of a 6.6 nm diameter PbSe nanocrystals, the total volume excluded by the capping ligand layer around each nanocrystals is $V_{ligand/particle} = 398\,\mathrm{nm}^3$. There are two nanocrystals per bcc unit cell, where the volume of the bcc unit cell is $V_{cell} = a_{bcc,SAXS}{}^3 = 1256\,\mathrm{nm}^3$. The inorganic PbSe cores occupy only $2 \times V_{core} = 301\,\mathrm{nm}^3$, or 24% of the unit cell. The remaining volume in the superlattice of 955 nm^3 is higher than the estimated excluded volume occupied by the capping ligands ($2 \times V_{ligand/particle} = 796\,\mathrm{nm}^3$). This leaves a remainder of 159 nm^3, or 13% of the unit cell, that is not accounted for by the nanocrystal cores or their capping ligands. This space is most likely occupied by unbound oleic acid or trapped solvent, as discussed later.

4.3.2 In Situ SAXS of the Heated Superlattice

Figure 4.6 shows in situ transmission SAXS data collected from a bcc superlattice of PbSe nanocrystals as it was heated at 3°C/min from 28°C to 350°C. Figure 4.7 shows a radial integration of the data at select temperatures. The data reveal four predominant transitions as the superlattice was heated from room temperature: (1) a contraction of the superlattice until reaching about 140°C; (2) a loss of long-range translational order (i.e. amorphization) between about 110°C and 150°C; (3) a loss of local, short-range, positional order at around 168°C; and (4) nanocrystal sintering above 168°C.

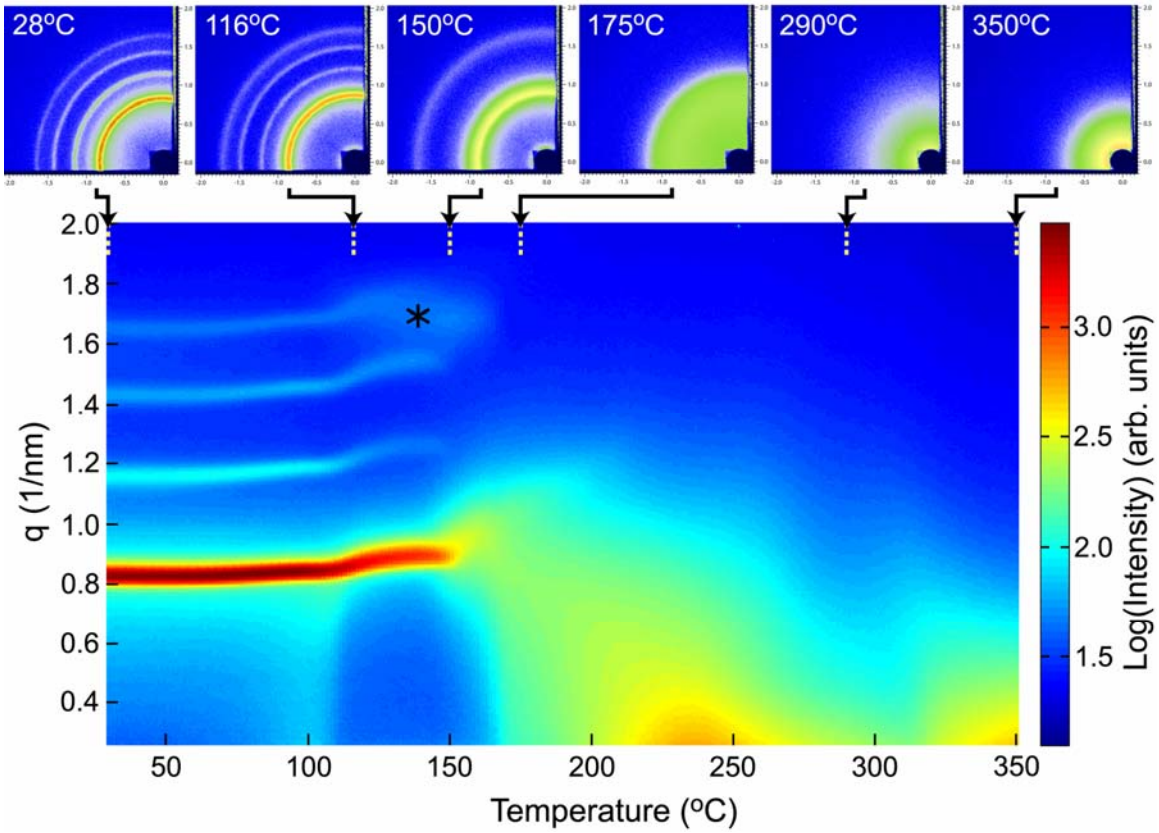

Figure 4.6: Contour plot of the SAXS intensity obtained from a PbSe nanocrystal superlattice with an initial bcc structure as it was heated from 28°C to 350°C. Each slice of the contour plot is a radial integration of 2D scattering profiles (representative patterns shown in upper panel). Between 25°C and 110°C, the superlattice exhibits bcc structure, with the diffraction peaks shifting to slighter larger q—indicating a slight lattice contraction upon heating. Above 110°C, the superlattice contracts more significantly with a gradual loss of order as indicated by the appearance of a second order diffraction peak (denoted by star) associated with an amorphous assembly. At 150°C, the superlattice structure has completely disappeared as indicated by the loss of the bcc (200), (211) and (220) diffraction peaks. At 168°C, all of the diffraction rings have disappeared, indicating the complete loss of local positional order and the onset of sintering. Above 168°C, sintered grains grow in size, as indicated by the shift in scattering intensity to lower q. Between 200°C and 250°C, the scattering intensity increases at low q values, which is consistent with oxidation of the PbSe nanocrystals into $PbSeO_3$ nanorods.

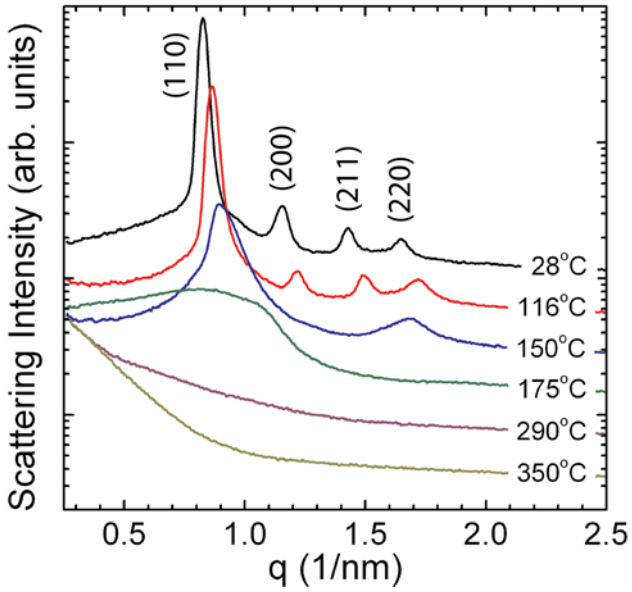

Figure 4.7: Radial integration of the 2D scattering profiles in Figure 4.6 of the PbSe nanocrystal superlattice at selected temperatures. The bcc peak indexing is provided. The two diffraction peaks in the blue curve at 150°C indicate that the superlattice has disordered to an amorphous structure.

Figure 4.8 shows the center-to-center nearest neighbor spacing in the superlattice determined from SAXS as it was heated from room temperature up to 160°C. In this temperature range, the superlattice contracts upon heating, while maintaining the bcc structure. The data in Figure 4.8 show that the lattice contraction became more significant when the temperature reached the boiling points of hexane (69°C) and toluene (110°C)—the solvents used to disperse the nanocrystals. Therefore, it would appear that the superlattice contraction is related to the evaporation of solvent trapped in the superlattice after deposition. In previous reports of heated superlattices, heating has either increased,[56,73] decreased,[8,59,73] or left unaffected,[59] the interparticle spacing; the lattice expansion or contraction of a nanocrystal superlattice in this temperature range appears to depend on the details of the system, such as the presence of trapped solvent and the thermal expansion of the ligands. In our case, TGA of a sample of oleic acid-

capped PbSe nanocrystals (9 nm diameter) confirmed that there was indeed significant solvent trapped in the superlattice, equivalent to about 2% of the total sample weight after heating from room temperature to 190°C, as shown in Figure 4.9. The amount of superlattice contraction that is actually observed corresponds to an amount of trapped solvent that would be about 4-5 times higher than this.[74] Therefore, it appears that solvent evaporation is indeed partly responsible for the superlattice contraction, but cannot completely explain it. Perhaps there is a cooperative effect between the ligand packing density (i.e. conformational changes or interdigitation) in the superlattice and the amount of residual solvent between particles. This issue requires further study, but it is clear that in this case of oleic acid-capped PbSe nanocrystals, the superlattice contracts significantly as it is heated from room temperature to its disordering transition, by more than 20%, and that this is somehow related to solvent trapped in the superlattice during solvent deposition.

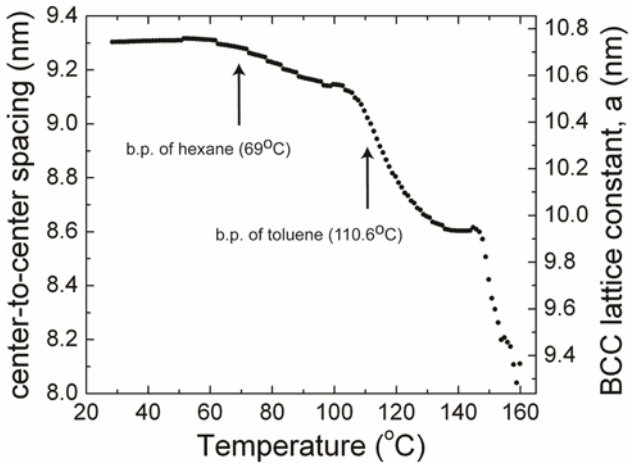

Figure 4.8: Center-to-center nearest-neighbor spacing and the bcc superlattice constant *a*, calculated from the bcc (110) Bragg ring plotted as a function of temperature. The boiling temperatures (b.p.) of hexane and toluene are indicated. Note that when the temperature exceeds 110°C, the superlattice begins to lose order.

When the temperature is increased to just above 110°C, a broad diffraction ring begins to appear at slightly lower q than the position of the bcc (220) Bragg ring (labeled in Figure 4.6 by a star). This diffraction ring is a second order reflection corresponding to an average nearest neighbor distance in an amorphous assembly and signifies the loss of long-range translational order of the superlattice. As shown in Figure 4.7, the Bragg peaks have disappeared completely by 150°C and the diffraction pattern consists of two broad diffraction peaks characteristic of an amorphous assembly of nanocrystals.[69] The two diffraction rings associated with the amorphous assembly are present in the scattering data up to 168°C, indicating that the nanocrystals have not sintered and remain intact, but are no longer ordered in a periodic superlattice.

At 168°C, the scattering rings disappear, which indicates that complete disordering of the nanocrystals has occurred and marks the onset of the sintering process. Thermogravimetric analysis (TGA) (Figure 4.9) and differential scanning calorimetry (DSC) (Figure 4.10) of oleic acid-capped PbSe nanocrystals showed no observable transitions below 168°C aside from the evaporation of some residual solvent. This suggests that structural transformations of the PbSe nanocrystal superlattice below 168°C are not directly influenced by the thermal behavior of the capping ligand. However, TGA of pure oleic acid showed that oleic acid begins to evaporate at around 150°C, so it is possible that superlattice disordering and nanocrystal sintering may be related to the evaporation of "free", or unbound, oleic acid from the superlattice.

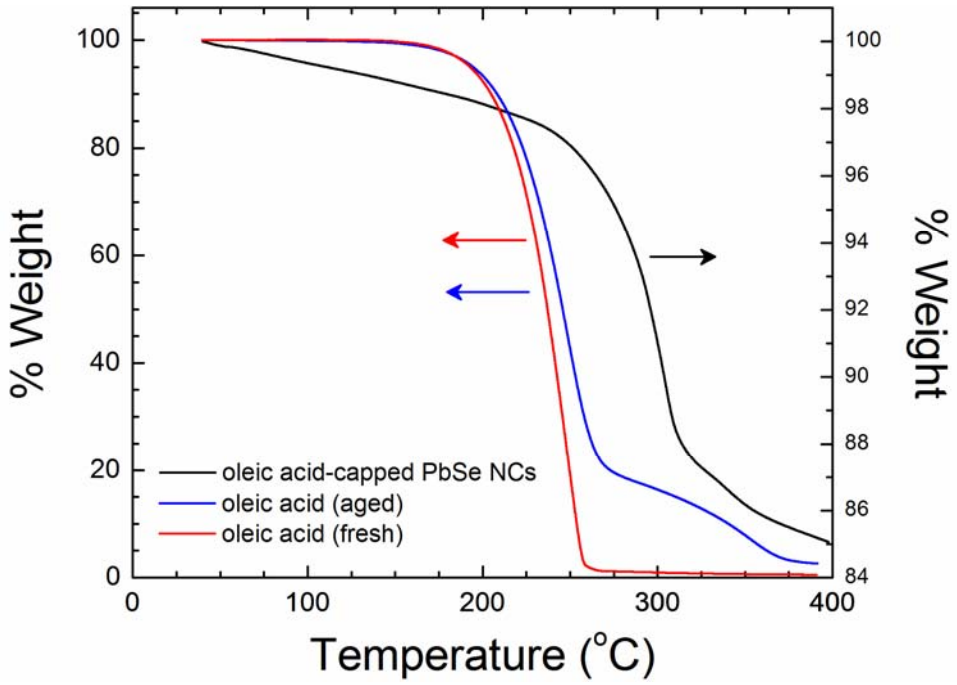

Figure 4.9: Thermogravimetric analysis (TGA) of oleic acid-capped 9 nm diameter PbSe nanocrystals and pure oleic acid. Data were collected for oleic acid immediately after receiving it from the supplier and after storing for one month in the laboratory at room temperature in ambient atmosphere. A ramp rate of 3°C/min was used, which was identical to that used in the in situ SAXS experiments.

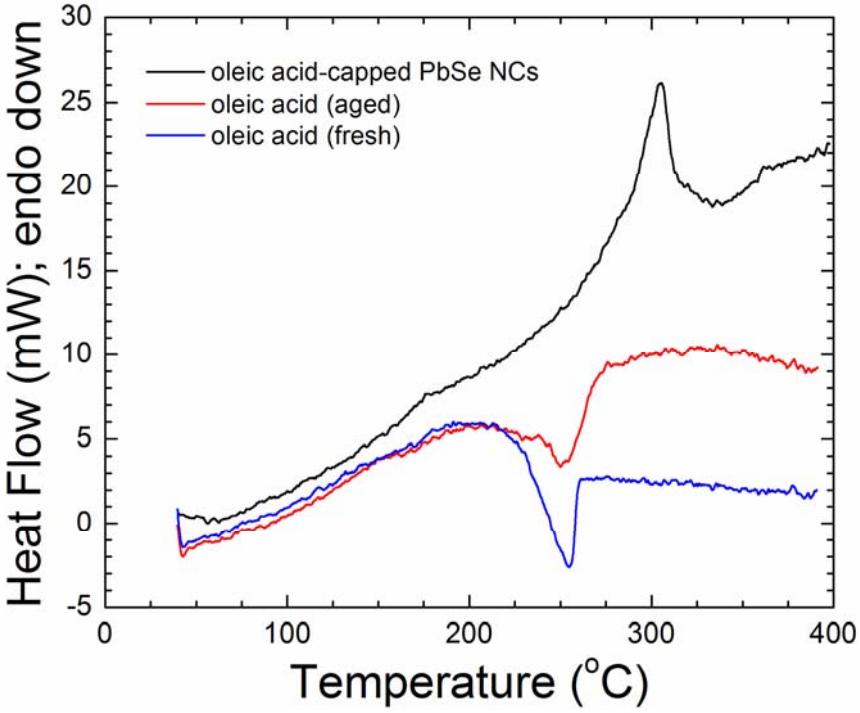

Figure 4.10: Differential Scanning Calorimetry (DSC) curves for oleic acid-capped PbSe nanocrystals and pure oleic acid. The oleic acid curves exhibit an endothermic peak near 250°C associated with the evaporation of oleic acid. The PbSe nanocrystals exhibit an exothermic peak at 300°C attributed to sintering and oxidation.

There is also a noticeable increase in scattering intensity at lower *q*-values as the temperature increased above 168°C. This is a signature of sintering and grain growth. We found that heating PbSe nanocrystals in air led to oxidation and the formation of lead selenite ($PbSeO_3$) nanorods (see Supporting Information). Figure 4.11 shows XRD profiles and Figure 4.12 shows TEM images of PbSe nanocrystal films heated in air. There is no evidence of $PbSeO_3$ in the initial sample, but at 200°C, a mixture of PbSe and $PbSeO_3$ is clearly present. By 300°C, all of the PbSe has oxidized to $PbSeO_3$. TEM of PbSe nanocrystal films heated to 300°C in air revealed that the PbSe nanocrystals had transformed into $PbSeO_3$ nanorods. A transformation from spherical nanocrystals into

nanorods, with an elongation of the nanocrystal size in one direction, is consistent with the observed increase in scattering intensity at low q after the temperature was increased from 200°C to 250°C. Micrometer-size PbSe particles have also been observed to oxidize to $PbSeO_3$ when annealed in an oxygen-containing atmosphere.[75]

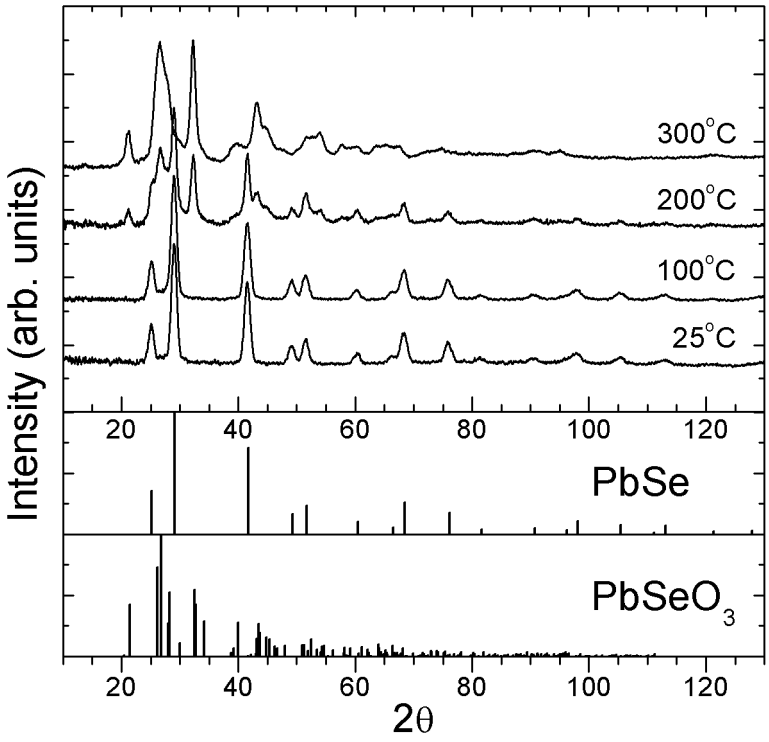

Figure 4.11: a) XRD profiles of 9 nm PbSe nanocrystal films heated in air from room temperature to the indicated temperature. Oxidation of the PbSe nanocrystals to $PbSeO_3$ begins to occur at around 200°C. Complete transformation of PbSe to $PbSeO_3$ has occurred after heating to 300°C in air.

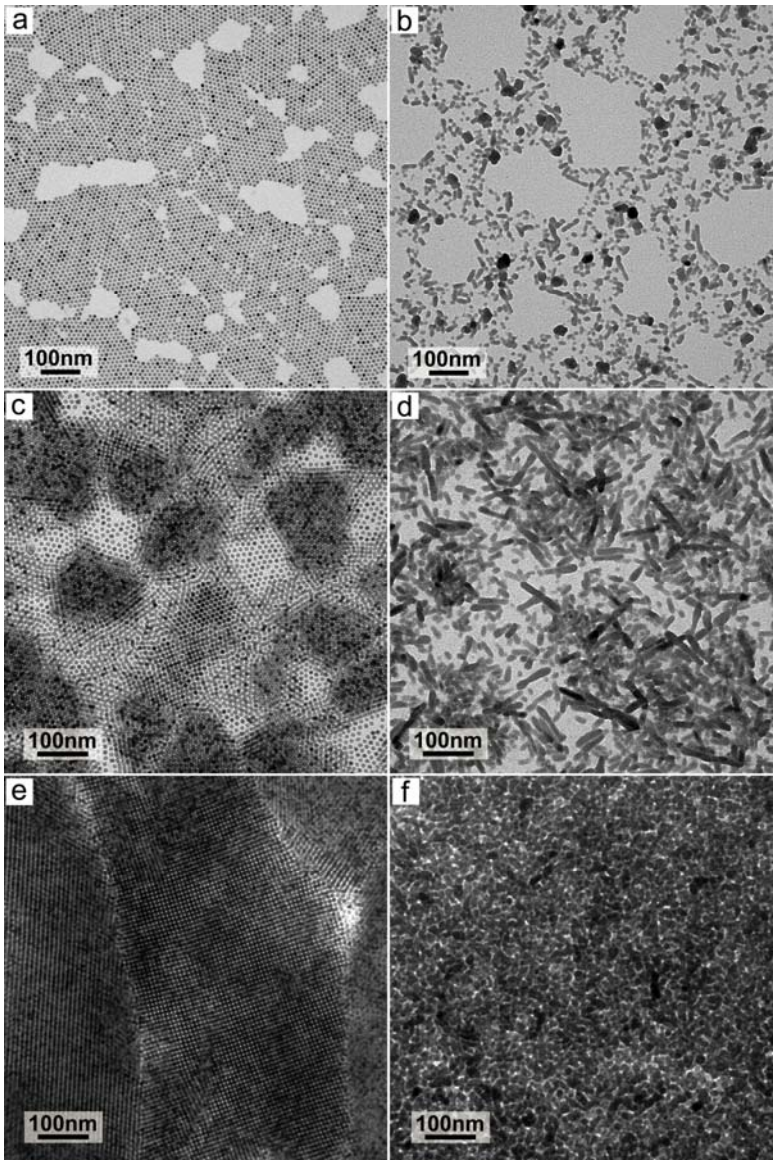

Figure 4.12: TEM images of 9 nm diameter oleic acid-capped PbSe nanocrystal superlattices at room temperature (a,c,e) and after heating to 300°C in air (b,d,f). The PbSe nanocrystals oxidize and convert to $PbSeO_3$ nanorods when heated to 300°C in air.

4.4 CONCLUSIONS

The heating-induced structural changes of a PbSe nanocrystal superlattice with bcc structure were followed by in situ SAXS. The bcc superlattice is stable up to a temperature of 110°C with a slight lattice contraction. At 110°C, the lattice contraction becomes more pronounced and is accompanied by disordering of the superlattice. By 150°C, the nanocrystal film has lost long-range translational order and is completely amorphous. The amorphous assembly of nanocrystals persists to a temperature of 168°C, at which point the weak diffraction peaks from the amorphous nanocrystal assembly disappear, indicating loss of local, short-range, positional order. Above 168°C, the nanocrystals sinter. XRD revealed that the sintering of neighboring nanocrystals is accompanied by the oxidative transformation of the PbSe nanocrystals to $PbSeO_3$ nanorods when the superlattice is heated in air. These results are valuable as many practical applications of semiconductor nanocrystal superlattices will require operation at elevated temperatures.

4.5 REFERENCES AND NOTES

1. Brus, L. Appl. Phys. A: Mater. Sci. Process. **1991**, 53, 465-474.
2. Alivisatos, A. P. J. Phys. Chem. **1996**, 100, 13226-13239.
3. Gur, I.; Fromer, N. A.; Geier, M. L.; Alivisatos, A. P. Science **2005**, 310, 462-465.
4. Wu, Y.; Wadia, C.; Ma, W.; Sadtler, B.; Alivisatos, A. P. Nano Lett. **2008**, 8, 2551-2555.
5. Panthani, M. G.; Akhavan, V.; Goodfellow, B.; Schmidtke, J. P.; Dunn, L.; Dodabalapur, A.; Barbara, P. F.; Korgel, B. A. J. Am. Chem. Soc. **2008**, 130, 16770-16777.
6. Zhao, N.; Osedach, T. P.; Chang, L.-Y.; Geyer, S. M.; Wanger, D.; Binda, M. T.; Arango, A. C.; Bawendi, M. G.; Bulovic, V. ACS Nano **2010**, 4, 3743-3752.

7. Johnston, K. W.; Pattantyus-Abraham, A. G.; Clifford, J. P.; Myrskog, S. H.; MacNeil, D. D.; Levina, L.; Sargent, E. H. Appl. Phys. Lett. **2008**, 92, 151115.

8. Mentzel, T. S.; Porter, V. J.; Geyer, S.; MacLean, K.; Bawendi, M. G.; Kastner, M. A. Phys. Rev. B **2008**, 77, 075316.

9. Choi, J. J.; Lim, Y.-F.; Santiago-Berrios, M. E. B.; Oh, M.; Hyun, B.-R.; Sun, L.; Bartnik, A. C.; Goedhart, A.; Malliaras, G. G.; Abruña, H. D.; Wise, F. W.; Hanrath, T. Nano Lett. **2009**, 9, 3749-3755.

10. Ma, W.; Luther, J. M.; Zheng, H.; Wu, Y.; Alivisatos, A. P. Nano Lett. **2009**, 9, 1699-1703.

11. Luther, J. M.; Law, M.; Beard, M. C.; Song, Q.; Reese, M. O.; Ellingson, R. J.; Nozik, A. J. Nano Lett. **2008**, 8, 3488-3492.

12. Leschkies, K. S.; Beatty, T. J.; Kang, M. S.; Norris, D. J.; Aydil, E. S. ACS Nano **2009**, 3, 3638-3648.

13. McDonald, S. A.; Konstantatos, G.; Zhang, S.; Cyr, P. W.; Klem, E. J. D.; Levina, L.; Sargent, E. H. Nature Mater. **2005**, 4, 138-142.

14. Akhavan, V. A.; Goodfellow, B. W.; Panthani, M. G.; Reid, D. K.; Hellebusch, D. J.; Adachi, T.; Korgel, B. A. Energy Environ. Sci. **2010**, 3, 1600-1606.

15. Urban, J. J.; Talapin, D. V.; Shevchenko, E. V.; Kagan, C. R.; Murray, C. B. Nature Mater. **2007**, 6, 115-121.

16. Sun, B.; Sirringhaus, H. Nano Lett. **2005**, 5, 2408-2413.

17. Lin, Y.-M.; Dresselhaus, M. S. Phys. Rev. B **2003**, 68, 075304.

18. Talapin, D. V.; Murray, C. B. Science **2005**, 310, 86-89.

19. Coe, S.; Woo, W.-K.; Bawendi, M.; Bulovic, V. Nature **2002**, 420, 800-803.

20. Cho, K.-S.; Lee, E. K.; Joo, W.-J.; Jang, E.; Kim, T.-H.; Lee, S. J.; Kwon, S.-J.; Han, J. Y.; Kim, B.-K.; Choi, B. L.; Kim, J. M. Nature Photon. **2009**, 3, 341-345.

21. Mueller, A. H.; Petruska, M. A.; Achermann, M.; Werder, D. J.; Akhadov, E. A.; Koleske, D. D.; Hoffbauer, M. A.; Klimov, V. I. Nano Lett. **2005**, 5, 1039-1044.

22. Steckel, J. S.; Coe-Sullivan, S.; Bulovic, V.; Bawendi, M. G. Adv. Mater. **2003**, 15, 1862-1866.

23. Harman, T. C.; Taylor, P. J.; Walsh, M. P.; LaForge, B. E. Science **2002**, 297, 2229-2232.

24. Wang, R. Y.; Feser, J. P.; Lee, J.-S.; Talapin, D. V.; Segalman, R.; Majumdar, A. Nano Lett. **2008**, 8, 2283-2288.

25. Sarasqueta, G.; Choudhury, K. R.; So, F. Chem. Mat. **2010**, 22, 3496-3501.

26. Shipway, A. N.; Katz, E.; Willner, I. ChemPhysChem **2000**, 1, 18-52.

27. Ridley, B. A.; Nivi, B.; Jacobson, J. M. Science **1999**, 286, 746-749.

28. Akhavan, V. A.; Goodfellow, B. W.; Panthani, M. G.; Korgel, B. A. Modern Energy Review **2010**, 2, 25-27.

29. Murray, C. B.; Sun, S.; Gaschler, W.; Doyle, H.; Betley, T. A.; Kagan, C. R. IBM J. Res. & Dev. **2001**, 45, 47-56.

30. Du, H.; Chen, C.; Krishnan, R.; Krauss, T. D.; Harbold, J. M.; Wise, F. W.; Thomas, M. G.; Silcox, J. Nano Lett. **2002**, 2, 1321-1324.

31. Wehrenberg, B. L.; Wang, C.; Guyot-Sionnest, P. J. Phys. Chem. B **2002**, 106, 10634-10640.

32. Cho, K.-S.; Talapin, D. V.; Gaschler, W.; Murray, C. B. J. Am. Chem. Soc. **2005**, 127, 7140-7147.

33. Wang, N.; Cao, X.; Guo, L.; Yang, S.; Wu, Z. ACS Nano **2008**, 2, 184-190.

34. Talapin, D. V.; Yu, H.; Shevchenko, E. V.; Lobo, A.; Murray, C. B. J. Phys. Chem. C **2007**, 111, 14049-14054.

35. Hines, M. A.; Scholes, G. D. Adv. Mater. **2003**, 15, 1844-1849.

36. Lifshitz, E.; Bashouti, M.; Kloper, V.; Kigel, A.; Eisen, M. S.; Berger, S. Nano Lett. **2003**, 3, 857-862.

37. Houtepen, A. J.; Koole, R.; Vanmaekelbergh, D.; Meeldijk, J.; Hickey, S. G. J. Am. Chem. Soc. **2006**, 128, 6792-6793.

38. Lu, W.; Fang, J.; Ding, Y.; Wang, Z. L. J. Phys. Chem. B **2005**, 109, 19219-19222.

39. Lee, S.-M.; Jun, Y.-w.; Cho, S.-N.; Cheon, J. J. Am. Chem. Soc. **2002**, 124, 11244-11245.

40. Zhao, Z.; Zhang, K.; Zhang, J.; Yang, K.; He, C.; Dong, F.; Yang, B. Colloids Surf., A **2010**, 355, 114-120.

41. Smith, D. K.; Luther, J. M.; Semonin, O. E.; Nozik, A. J.; Beard, M. C. ACS Nano **2011**, 5, 183-190.

42. Kang, I.; Wise, F. W. J. Opt. Soc. Am. B **1997**, 14, 1632-1646.

43. Liljeroth, P.; Overgaag, K.; Urbieta, A.; Grandidier, B.; Hickey, S. G.; Vanmaekelbergh, D. Phys. Rev. Lett. **2006**, 97, 096803.

44. Liu, Y.; Gibbs, M.; Puthussery, J.; Gaik, S.; Ihly, R.; Hillhouse, H. W.; Law, M. Nano Lett. **2010**, 10, 1960-1969.

45. Kigel, A.; Brumer, M.; Maikov, G.; Sashchiuk, A.; Lifshitz, E. Superlattices Microstruct. **2009**, 46, 272-276.

46. Fischbein, M. D.; Puster, M.; Drndic, M. Nano Lett. **2010**, 10, 2155-2161.

47. Sykora, M.; Koposov, A. Y.; McGuire, J. A.; Schulze, R. K.; Tretiak, O.; Pietryga, J. M.; Klimov, V. I. ACS Nano **2010**, 4, 2021-2034.

48. Choi, J. J.; Luria, J.; Hyun, B.-R.; Bartnik, A. C.; Sun, L.; Lim, Y.-F.; Marohn, J. A.; Wise, F. W.; Hanrath, T. Nano Lett. **2010**, 10, 1805-1811.

49. Law, M.; Luther, J. M.; Song, Q.; Hughes, B. K.; Perkins, C. L.; Nozik, A. J. J. Am. Chem. Soc. **2008**, 130, 5974-5985.

50. Barkhouse, D. A. R.; Pattantyus-Abraham, A. G.; Levina, L.; Sargent, E. H. ACS Nano **2008**, 2, 2356-2362.

51. Baik, S. J.; Kim, K.; Lim, K. S.; Jung, S.; Park, Y.-C.; Han, D. G.; Lim, S.; Yoo, S.; Jeong, S. J. Phys. Chem. C **2011**, 115, 607-612.

52. Klem, E. J. D.; Shukla, H.; Hinds, S.; MacNeil, D. D.; Levina, L.; Sargent, E. H. Appl. Phys. Lett. **2008**, 92, 212105.

53. van Huis, M. A.; Kunneman, L. T.; Overgaag, K.; Xu, Q.; Pandraud, G.; Zandbergen, H. W.; Vanmaekelbergh, D. Nano Lett. **2008**, 8, 3959-3963.

54. Xu, B. S.; Tanaka, S. I. Acta Mater. **1998**, 46, 5249-5257.

55. Sutter, E.; Sutter, P.; Zhu, Y. Nano Lett. **2005**, 5, 2092-2096.

56. Korgel, B. A.; Zaccheroni, N.; Fitzmaurice, D. J. Am. Chem. Soc. **1999**, 121, 3533-3534.

57. Sandhyarani, N.; Antony, M. P.; Selvam, G. P.; Pradeep, T. J. Chem. Phys. **2000**, 113, 9794-9794.

58. Constantinides, M. G.; Jaeger, H. M.; Li, X.; Wang, J.; Lin, X.-M. Z. Kristallogr. **2007**, 222, 595-600.

59. Robel, I.; Lin, X.-M.; Sprung, M.; Wang, J. J. Phys.: Condens. Matter **2009**, 21, 264011-264011.

60. Luedtke, W. D.; Landman, U. J. Phys. Chem. **1996**, 100, 13323-13329.

61. Pérez-Dieste, V.; Castellini, O. M.; Crain, J. N.; Eriksson, M. A.; Kirakosian, A.; Lin, J. L.; McChesney, J. L.; Himpsel, F. J.; Black, C. T.; Murray, C. B. Appl. Phys. Lett. **2003**, 83, 5053-5053.

62. Takagi, M. J. Phys. Soc. Jpn. **1954**, 9, 359-363.

63. Goldstein, A. N.; Echer, C. M.; Alivisatos, A. P. Science **1992**, 256, 1425-1427.

64. Sigman, M. B.; Saunders, A. E.; Korgel, B. A. Langmuir **2004**, 20, 978-983.

65. Smith, D. K.; Goodfellow, B.; Smilgies, D.-M.; Korgel, B. A. J. Am. Chem. Soc. **2009**, 131, 3281-3290.

66. Heiney, P. Datasqueeze Software. http://www.datasqueezesoftware.com/

67. Hammersley, A. P. ESRF Internal Report; ESRF97HA02T; **1997**.

68. Murray, C. B.; Kagan, C. R.; Bawendi, M. G. Science **1995**, 270, 1335-1338.

69. Korgel, B. A.; Fitzmaurice, D. Phys. Rev. B **1999**, 59, 14191-14191.

70. Korgel, B. A.; Fullam, S.; Connolly, S.; Fitzmaurice, D. J. Phys. Chem. B **1998**, 102, 8379-8388.

71. Guinier, A.; Fournet, G. Small-Angle Scattering of X-Rays. Wiley: New York, **1955**.

72. Glatter, O.; Kratky, O. Small-Angle X-Ray Scattering. Academic Press Inc.: New York, **1982**.

73. Lee, B.; Podsiadlo, P.; Rupich, S.; Talapin, D. V.; Rajh, T.; Shevchenko, E. V. J. Am. Chem. Soc. **2009**, 131, 16386-16388.

74. The density of PbSe, oleic acid, hexane, and toluene are 8.27 g/cm^3, 0.895 g/cm^3, 0.6548 g/cm^3, and 0.8669 g/cm^3, respectively. The relative weight fractions of PbSe, oleic acid, and solvent in the bcc superlattice at room temperature were calculated by assuming that the volume (and weight) of 6.6 nm diameter PbSe nanocrystal cores is fixed in the bcc unit cell and that the volume contraction of the superlattice as it was heated to 140°C was due to the evaporation of the solvent ($V_{bcc}^{RT} = (a_{bcc,SAXS}^{RT})^3 = 1256\ \mathrm{nm}^3$; $V_{bcc}^{140C} = (a_{bcc,SAXS}^{140C})^3 = 979\ \mathrm{nm}^3$). The remainder of the unit cell volume (e.g. $V_{bcc,cell} - V_{cores} - V_{solvent}$) was assumed to be filled by a constant volume of ligands. The exact ratio of hexane to toluene trapped in the superlattice is not known, so the expected weight fraction of solvent in the superlattice at room temperature was calculated for the two extreme cases of pure hexane and pure toluene, expecting that the actual case lies somewhere in between. If all of the trapped solvent is hexane, the superlattice at room temperature would consist of 76.0 wt% PbSe, 18.5 wt% oleic acid, and 5.5 wt% hexane. If all the trapped solvent is toluene, the superlattice would consist of 74.6 wt% PbSe, 18.2 wt% oleic acid, and 7.2 wt% toluene.

75. Tomaev, V. V.; Makarov, L. L.; Tikhonov, P. A.; Solomennikov, A. A. Glass Phys. Chem. **2004**, 30, 349-355.

Chapter 5: Phase Transitions in Heated Gold Nanocrystal Superlattices†

5.1 INTRODUCTION

Materials respond to changes in environmental conditions, like temperature, pressure, mechanical force, electric fields, etc., by changing structure. Relatively minor environmental differences may lead to subtle effects, like an expansion or contraction without a change in packing symmetry or geometrical arrangement of the atoms. More extreme environmental variations can weaken bonds and lead to a phase transition. Phase transitions of solids can involve a change in state, to a liquid or a gas for example, or from one crystal structure to another. Most solids exhibit structural polymorphism and solid-solid phase transitions. For example, graphite and diamond are well-known polymorphs of carbon; iron can exist with body-centered cubic (bcc) or face-centered cubic (fcc) crystal structure depending on temperature and pressure. Soft molecular materials, like amphiphilic diblock copolymers and surfactants, will assemble into various ordered structures under various conditions, ranging from micellar cubic, to hexagonal (cylindrical), to bicontinuous cubic to lamellar structures, to name a few.[1,2] Dense colloidal dispersions of charge-stabilized particles and spherical block copolymer micelles can also exhibit structural polymorphism, forming either fcc and bcc lattices depending on temperature and solvent parameters.[3,4] Here, we report that ordered assemblies of ligand-stabilized nanocrystals can also exhibit temperature-dependent solid-solid phase transitions.

Ordered assemblies of ligand-stabilized nanocrystals, or *superlattices*, are interesting because of their unique optical and electronic properties. Nanocrystals in the quantum size regime, i.e., less than about 10 nm in diameter, can be produced with very

† Portions of this chapter have been submitted for publication

monodisperse size distributions, exhibiting physical properties that are fundamentally different from their bulk counterparts and can be tuned synthetically by manipulating the particle size.[5] In the assemblies, collective electronic coupling between neighboring nanocrystals can give rise to new physical properties that depend on their superlattice structure.[6] These self-assembled materials have therefore been called "artificial solids" or "metamaterials" since the fundamental "building blocks" are nanocrystals instead of atoms. These superlattices can also exhibit structural polymorphism like atomic and molecular solids. This contrasts the solvent-free colloidal crystals of sub-micrometer hard-sphere particles (similar to opals) that are like collections of rigid marbles, forming only the thermodynamically favored close-packed lattices (like fcc) at high density.[7,8] The soft organic ligand coating of the nanocrystals occupies a significant volume of the superlattice—up to 90% in the case of dodecanethiol-coated sub-2 nm diameter Au nanocrystals—and responds rather sensitively to environmental factors. For example, exposure of oleic acid-coated PbSe and PbS nanocrystal superlattices to the vapor of a solvent that swells the ligands has been shown to reversibly change the superlattice structure from bcc to fcc.[9] Different superlattice structures—i.e., packing polymorphism—has been observed in *binary* nanocrystal superlattices composed of the same large and small nanocrystals formed under different deposition conditions.[10-13] However, temperature-dependent phase transitions in nanocrystal superlattices have never been observed. This remains surprising, as theoretical and computer simulations have anticipated thermally driven structural transformations—including melting—of nanocrystal superlattices.[14]

The issue relates to the fact that the ligand-stabilized nanocrystals of the superlattices are generally considered as robust, discrete self-assembled units. For example, nanocrystals in a superlattice readily redisperse in solvent and then recrystallize

when the solvent is removed. The superlattice structure is reversibly restored without a change in the nanocrystals—this process of recrystallization is entirely reversible. Therefore, self-assembly of ligand-stabilized nanocrystals has typically been viewed as a close-packing of spheres composed of a rigid inorganic core with a chemisorbed layer of flexible, yet incompressible, ligands that fill space as efficiently as possible in the superlattice.[15,16] However, under more extreme conditions, the ligand shell will in fact desorb. This is why temperature-dependent phase transitions have never been observed for ligand-stabilized nanocrystal superlattices: organic ligand-coated nanocrystals have simply not been thermally stable. Heating has led to the coalescence of inorganic material within a matrix of organic material[17,18] or in some cases, chemical transformation or decomposition of the superlattice composition.[19] Therefore, the observation of order-order phase transitions of dodecanethiol-coated Au nanocrystal superlattices at elevated temperature, reported here, was quite unexpected.

5.2 Experimental Methods

5.2.1 Materials

Tetraoctylammonium bromide (TOAB, 98%), gold(III) chloride trihydrate (HAuCl4-3H2O, >99.9%), 1-dodecanethiol (>98%), and sodium borohydride (98%) were obtained from Sigma Aldrich and used as received. Toluene (99.9%), methanol (99.9%), chloroform (99.9% with 0.75% ethanol preservative), hydrochloric acid, and nitric acid were purchased from Fisher Scientific and used as received. Ethanol (99.5%) was purchased from Pharmco-Aaper. Deionized (DI) water with 18 megaohm resistance was obtained from a Barnstead Nanopure Ultrapure filtration system and passed through a

200 nm filter. Glassware and Teflon stir bars were cleaned with aqua regia, rinsed five times with DI water, and dried in an oven prior to use.

5.2.2 Au Nanocrystal Synthesis and Purification

Au nanocrystals were synthesized using the same arrested precipitation procedure described in detail in Rasch et al.[28] The purified nanocrystals were redispersed in toluene at a concentration of 50 mg/mL and stored under ambient conditions for at least 5 weeks prior to use in the SAXS experiments. In some cases, the nanocrystal dispersions had been stored for more than a year prior to use.

5.2.3 Nanocrystal Superlattice Film Preparation

Transmission SAXS samples were prepared by drop-casing approximately 100 μL of a 50 mg/mL dispersion of Au nanocrystals in toluene onto a glass cover slide (Fisherfinest Premium, 25 mm x 25 mm, 0.13 to 0.17 mm thick, Fisher Scientific) and allowing the solvent to evaporate. GISAXS samples were prepared by drop-casting 20 μL of a 50 mg/mL dispersion of Au nanocrystals in toluene onto a silicon wafer (7 mm x 7 mm square with a native oxide) and allowing the solvent to evaporate. Samples for TEM imaging were prepared by drop-casting 2 μL of a 10 mg/mL dispersion of Au nanocrystals in toluene onto a TEM grid (carbon-coated copper 200 mesh, Electron Microscopy Sciences) and allowing the solvent to evaporate.

5.2.4 In situ SAXS of Heated Nanocrystal Films

Transmission SAXS and GISAXS measurements were performed as previously reported.[16,19] Transmission SAXS samples were placed into a Mettler-Toledo FP82HT hot stage between 2 aluminum spacers specifically fabricated for this experiment. The hot stage was then placed into the D1 beam line at the Cornell High Energy Synchrotron (CHESS) in transmission mode with the side of the sample containing the nanocrystal

film facing the detector. The hot stage was controlled with a Mettler Toledo FP80 processing unit to heat the sample from 30 °C to 215 °C at a rate of 3 °C/min. GISAXS samples were placed on a brass heating block with an electric rod heater and thermocouple inserted into holes that had been bored into the heating block. The temperature and heating rate of the brass block was maintained by a temperature controller and a variac. Transmission SAXS measurements were performed using monochromatic radiation of wavelength $\lambda = 1.230$ Å and a sample-to-detector distance of 691 mm; images were collected with exposure times ranging from 0.1 sec to 6 sec in order to maximize the intensity resolution of the detector. GISAXS measurements were performed using monochromatic radiation of wavelength $\lambda = 1.265$ Å and a sample-to-detector distance of 554 mm; images were collected with exposure times ranging from 0.1 sec to 1 sec. Scattering images were calibrated with a silver behenate standard; image processing and radial integrations were performed with Fit2D software.[29]

5.2.5 Additional X-ray Scattering Characterization

In situ GIWAXS measurements were performed by placing a Fuji image plate into the scattered x-ray beam at various times during the in situ GISAXS experiment. The image plates were exposed for either 1 or 2 sec and were read by a GE Typhoon FLA 7000 imager. The scattering images were calibrated using a CeO2 standard. Solution SAXS samples were prepared by heating an Au nanocrystal film to various temperatures, cooling the sample back to room temperature, and then redispersing the nanocrystals in toluene to a concentration of approximately 1-5 mg/mL. These dispersions were inserted into glass capillary tubes and placed into the CHESS D1 beamline. In situ GIWAXS measurements were performed using monochromatic radiation of wavelength $\lambda = 1.222$ Å and a sample-to-detector distance of 151 mm. Solution SAXS measurements were

performed using monochromatic radiation of wavelength λ = 1.265 Å and a sample-to-detector distance of 554 mm with exposure times ranging from 8 sec to 30 sec. Solution SAXS data was calibrated with a silver behenate standard, background subtracted using scattering data from pure toluene, and fit to a model as previously reported.[19]. All image processing and radial integrations were performed with Fit2D software.[29]

5.2.6 Additional Materials Characterization

Low-resolution TEM images were acquired digitally using a FEI Tecnai Spirit Bio Twin operated at 80 kV. Scion Image software (Scion Corporation) was used to measure the diameters of 765 nanocrystals in three 300kx magnification TEM images for each temperature studied. Optical images of the nanocrystal films were acquired during the in situ GISAXS experiments using a Navitar motorized zoom and focus module with on-axis lighting and a Sony CCD camera.

5.3 Results and Discussion

A marked series of structural transitions were observed in the in situ SAXS measurements of Au nanocrystal superlattices heated to increasing temperature. A dodecanethiol-coated sub-2 nm diameter Au nanocrystal superlattice heated from room temperature to 213°C progressed through at least four different structures before finally decomposing at high temperature. These transitions were not reversible and transmission electron microscopy (TEM) showed that the nanocrystals were ripening as the temperature increased, but in a surprisingly controlled way. The changing Au core size was then accommodated by changes in superlattice symmetry, maintaining positional order of a superlattice. These observations suggest that ligand-stabilized nanocrystals have much in common with amphiphilic diblock copolymer assemblies, as the structure

appears to be closely related to the micro-phase separation of inorganic and organic domains evolving with increasing temperature.

5.3.1 In Situ SAXS and Temperature-Induced Superlattice Phase Transitions

The SAXS data in Fig. 5.1 shows a series of temperature-induced structural phase transitions of the Au nanocrystal assembly. Initially, the 1.8 nm dodecanethiol-capped Au nanocrystals are organized into a bcc superlattice with a cubic lattice constant, a_{bcc}, of 3.72 nm. As the bcc superlattice was heated from room temperature, there was a slight thermal expansion, with the diffraction peaks shifting to slightly lower q (q is inversely related to the d-spacing: $q = 2\pi/d$). The linear coefficient of thermal expansion of the bcc superlattice was found to be approximately 3×10^{-4} $°C^{-1}$ between 30°C and 120°C. This is consistent with the thermal expansion of the ligands, as shown previously for dodecanethiol-coated silver nanocrystal superlattices.[17]

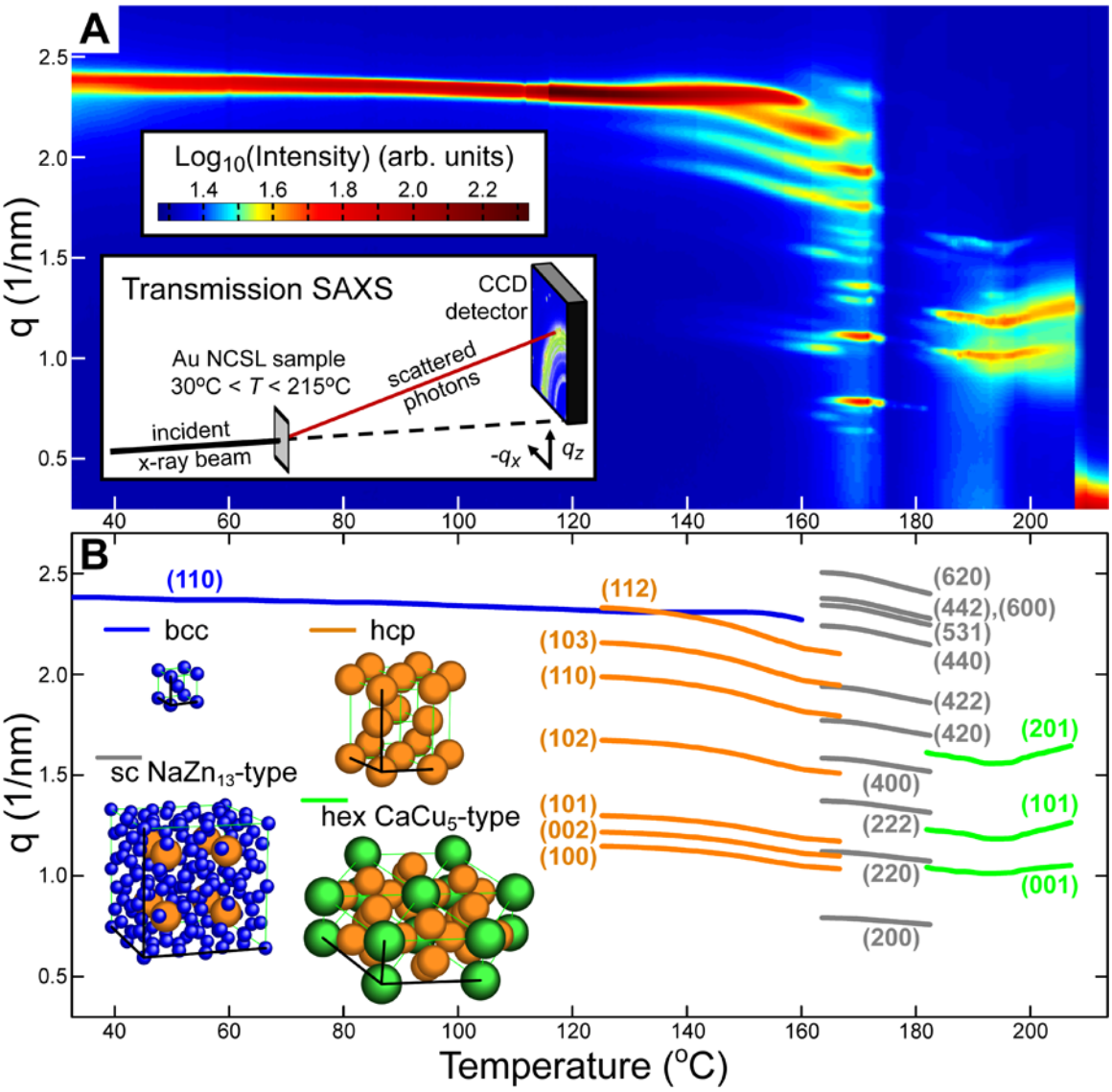

Figure 5.1: (A) Contour plot of the radially integrated scattering intensity as a function of q ($q = \sqrt{q_x^{\,2} + q_z^{\,2}}$) and temperature during in situ transmission SAXS of a nanocrystal superlattice of sub-2 nm dodecanethiol-capped Au nanocrystals heated from room temperature to 213°C. (B) Indexing of the simulated diffraction peak positions and schematics of the unit cells of the observed structures.

At 125°C, extra Bragg rings appear in the diffraction patterns. These new features index to an hcp superlattice structure with hexagonal lattice constants a_{hcp} = 6.32 nm and c_{hcp} = 10.3 nm. The ratio c_{hcp}/a_{hcp} is equal to $\sqrt{8/3}$ which is the expected ratio for a hcp arrangement of perfect spheres. Initially, the spacing of the hcp (112) planes is identical to the spacing of the bcc (110) planes (i.e. $d(112)_{hcp} = d(110)_{bcc}$ = 2.31 nm). As the nanocrystals are heated further, the hcp superlattice expands faster than the bcc superlattice. The linear coefficient of thermal expansion of the hcp lattice was found to be approximately 2.7×10^{-3} °C^{-1} (about 9 times larger than for bcc) between 130°C and 160°C. The bcc and hcp superlattice structures coexisted until reaching 160°C, at which point, the bcc superlattice peaks disappeared.

At 167 °C, the hcp structure disappeared and another new superlattice structure emerged. Indexing of the SAXS data showed that this new superlattice structure is in fact an ordered array of nanocrystals with two different sizes—a binary nanocrystal superlattice (BNSL)—with an icosahedral AB_{13} (ico-AB_{13}) structure with simple cubic symmetry (isostructural with $NaZn_{13}$ (PDF#01-071-9884); space group 226; Wyckoff sequence: iba) and a large cubic unit cell (a = 16 nm). One distinguishing feature of the ico-AB_{13} structure in the SAXS data is the strong (531) diffraction peak at q = 2.3 nm^{-1} which is typically forbidden for simple cubic symmetry.[8] The ico-AB_{13} structure is a well-known BNSL assembled by solvent evaporation and observed by TEM,[20] but is very surprising in this case because the Au nanocrystals have an initially monodisperse size distribution which then evolves into a collection of nanocrystals with two specific sizes at elevated temperature. Like the bcc and hcp superlattices, the ico-AB_{13} superlattice expands as it is heated. The linear coefficient of thermal expansion of the ico-AB_{13} superlattices was found to be 2.4×10^{-3} °C^{-1} which is comparable with the hcp superlattice and about 8 times greater than the value for the bcc superlattice.

At 177 °C, the superlattice structure changed yet again and the new Bragg reflections index to a structure with hexagonal symmetry. At 181 °C a structurally similar yet slightly more compact hexagonal superlattice appears whose Bragg reflections outshine those from the original hexagonal structure. These superlattices are also BNSLs, but with AB_5 structure (isostructural with $CaCu_5$; space group 191; Wyckoff sequence: gca). The superlattice structure finally collapses at 208 °C. The scattering signal shifted rapidly to low q at 208 °C, characteristic of spinodal decomposition and phase separation between Au and the organic ligands.

5.3.2 Minor Superlattice Structures Observed During Heating

Figure 5.2 shows a zoomed-in region of Figure 5.1 with temperature-dependent SAXS intensity profiles between 155 °C and 185 °C. Simulated Bragg peaks have been overlaid onto the image to show where the peaks associated with the 4 primary superlattice structures (bcc, hcp, ico-AB_{13}, and hex-AB_5) occur. In this temperature range, several relatively week Bragg peaks occur which cannot be attributed to the previously described superlattice structures.

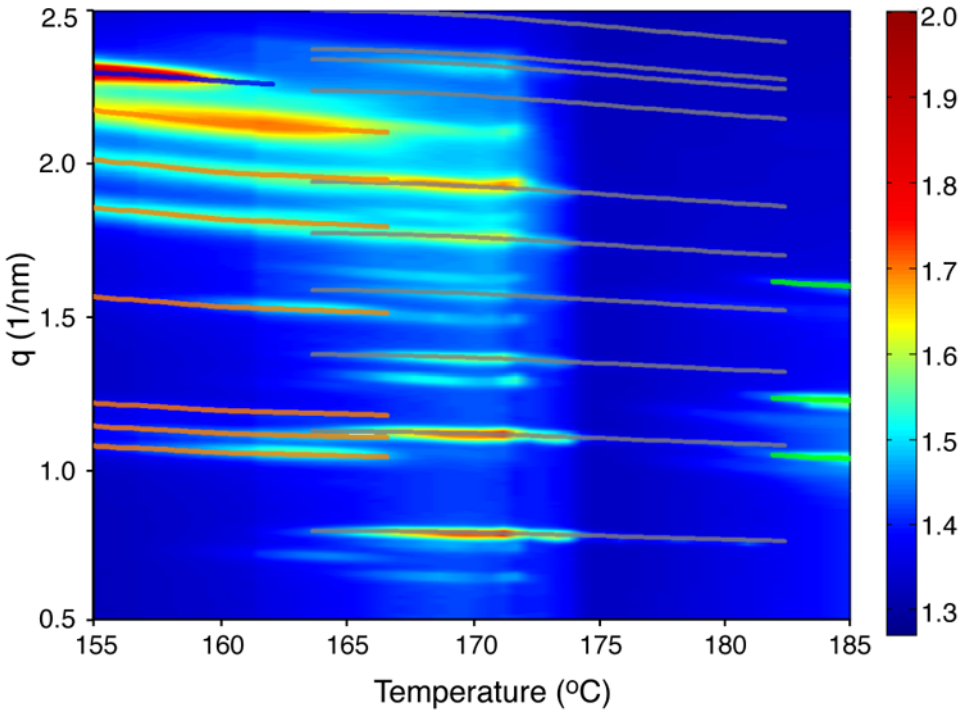

Figure 5.2: Contour plot of temperature-dependent SAXS profiles of an Au nanocrystal superlattice zoomed into the temperature range 155 °C – 185 °C. The color scale relates to $\log_{10}$(Intensity). Overlays represent simulated diffraction peak positions from the 4 primary superlattice structures (blue: bcc; orange: hcp; grey: ico-AB_{13}; green: hex-AB_5).

At 158°C, an additional diffraction peak emerges at q = 0.73 nm^{-1} (Figure 5.2). This peak does not correspond to either the hcp or the ico-AB_{13} superlattices. Interestingly, this peak disappears at approximately 167°C along with the peaks that are associated with the hcp lattice. This suggests that the minor structure that generated the diffraction peak at q = 0.73 nm^{-1} is somehow *related* to the hcp structure. Because there are few peaks associated with this minor superlattice and the intensity of these peaks is relatively low, it is difficult to determine exactly the structure of this superlattice. One possibility is that the additional diffraction peak at q = 0.73 nm^{-1} can be explained by the

introduction of periodic $(001)_{hcp}$ stacking faults in the hcp superlattice (Figure 5.3). The resulting structure depicted in Figure 5.3 is isostructural with Samarium (Sm, space group 166) and is a hexagonal structure consisting of a repeat stacking of nine close-packed planes with stacking sequence ABABCBCACA and commonly called *R9*. The spacing of the (001) close-packed planes is nearly identical to those in the more dominate hcp structure. The extra peak at q = 0.73 nm^{-1} is then the (006) reflection for the *R9* superlattice structure, as shown in Figure 5.3.

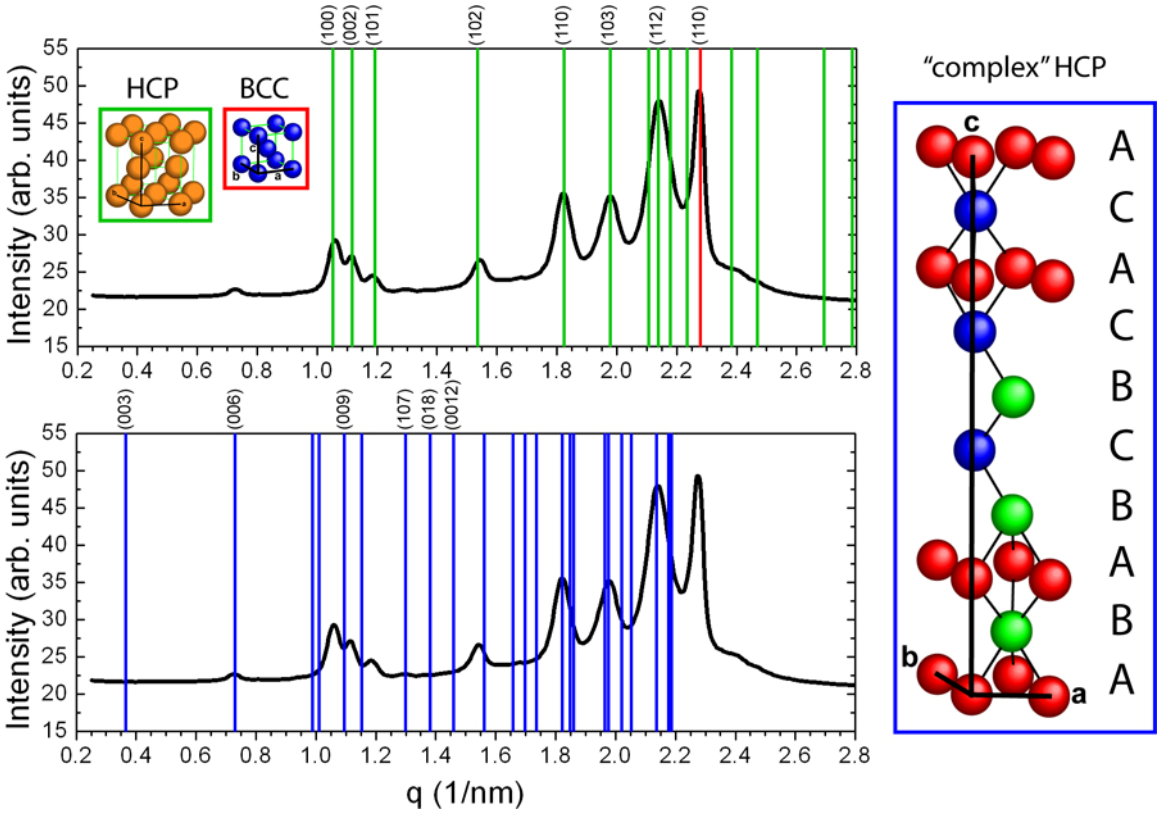

Figure 5.3: Indexing of the transmission SAXS profile collected from a superlattice of sub-2 nm dodecanethiol-capped Au nanocrystals heated to 159 °C. The black curves are a radial integration of the 2D transmission SAXS pattern. Several diffraction peaks cannot be indexed to the hcp or bcc superlattices (e.g. at q = 0.73 nm^{-1}). The extra diffraction peaks can, however, be explained by the introduction of periodic $(001)_{hcp}$ stacking faults into the hcp lattice such that the stacking sequence of the close-packed planes is 'ABABCBCAC'. The green lines correspond to an hcp superlattice with a = b = 6.89 nm and c = 11.25 nm. The red line corresponds to a bcc superlattice with a = b = c = 3.9 nm. The blue lines correspond to a "complex" hcp superlattice (right panel; isostructural with Sm; space group 166) with a = b = 7.4 nm and c = 51.7 nm. The lattice constant, c, for the "complex" hcp structure is nearly 4.5 times as large as it is for the original hcp structure, which is expected based on the stacking sequence of close-packed planes in the "complex" hcp superlattice.

The $NaZn_{13}$-type ico-AB_{13} BNSL exists between 163 °C and 182 °C as can be seen in Figure 5.1 and 5.2. The ico-AB_{13} structure consists of cubic sub-cells where the

large nanocrystals sit on the corners of the sub-cells and a cluster of 13 small nanocrystals resides in the center of the sub-cell, as shown in Figure 5.4. This cluster of 13 small nanocrystals is arranged as if 12 of the nanocrystals sit on the corners of an icosahedron and the 13th small nanocrystal resides at the center of the icosahedron. Other arrangements of the B_{13} clusters in the cubic sub-cells have also been observed.[11] To distinguish the $NaZn_{13}$-type BNSL structure from other AB_{13} BNSLs, it is typically referred to by the term "ico-AB_{13}." In the ico-AB_{13} structure, the B_{13} clusters are rotated by 90° with respect to the B_{13} clusters in adjacent cubic sub-cells. Thus, the full unit cell must include 8 sub-cells to fully capture the symmetry structure. The unit cell for ico-AB_{13} crystals is conventionally defined such that that the "A" components reside at the positions (1/4, 1/4, 1/4), (3/4, 1/4, 1/4), (1/4, 3/4, 1/4), (3/4, 3/4, 1/4), (1/4, 1/4, 3/4), (3/4, 1/4, 3/4), (1/4, 3/4, 3/4), and (3/4, 3/4, 3/4) in the unit cell as shown in Figure 5.4.

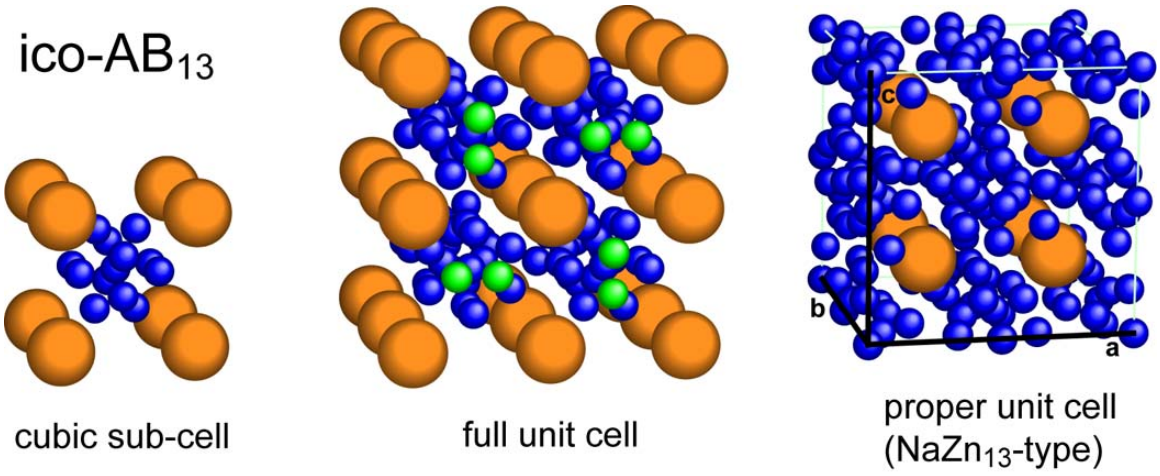

Figure 5.4: Schematic of the ico-AB_{13} structure. Large nanocrystals (orange) sit on the corners of cubic sub-cells (left) and 13 small nanocrystals (blue) reside in the center of the sub-cells with Pm-3n symmetry. Each B_{13} cluster is rotated by 90° with respect to the B_{13} cluster in adjacent cells (illustrated by green coloring) such that the full unit cell (middle) must be composed of 8 cubic sub-cells. While it is convenient for illustration purposes to define the unit cell as shown in the middle panel, the unit cell for ico-AB_{13} crystals is conventionally defined as shown in the right panel.

As can be seen in Figure 5.2, there are several diffraction peaks that exist between 167 °C and 177 °C that cannot be indexed to the ico-AB_{13} BNSL. These extra reflections can be explained by considering systematic replacements of the small nanocrystals at the centers of the B_{13} clusters with larger nanocrystals (see Figure 5.5). In particular, the replacement of the small nanocrystals at the corners and face centers of the unit cell (i.e. positions (0, 0, 0), (1/2, 1/2, 0), (1/2, 0, 1/2), and (0, 1/2, 1/2)) transforms the superlattice symmetry from sc to fcc. Additional replacements of the small nanocrystals on the edges and at the center of the unit cell (i.e. positions (1/2, 0, 0), (0, 1/2, 0), (0, 0, 1/2), and (1/2, 1/2, 1/2)) transform the superlattice symmetry from fcc to bcc. Similar replacements of small nanocrystals for larger nanocrystals in very thin BNSLs have been previously reported.[16]

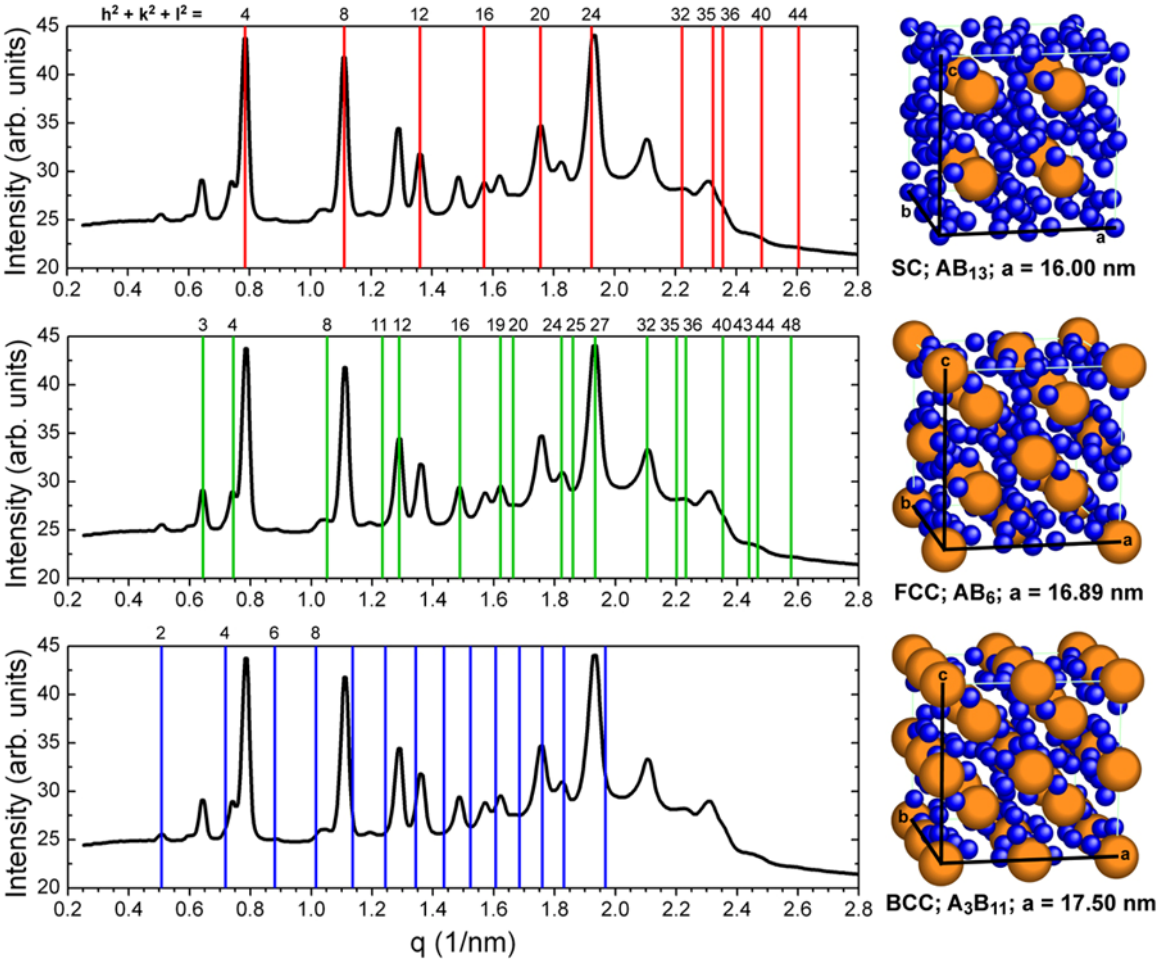

Figure 5.5: Indexing of the transmission SAXS profile collected from a superlattice of sub-2 nm dodecanethiol-capped Au nanocrystals heated to 172 °C. The black curves are a radial integration of the 2D transmission SAXS pattern and show a coexistence of 3 different superlattice symmetries: the ico-AB_{13} BNSL and 2 others resulting from systematic replacement of small nanocrystals at the center of the B_{13} clusters with a larger nanocrystal. Schematics of these structures are shown in the panels to the right. Red lines (top) indicate the expected diffraction peaks for a simple cubic ico-AB_{13} structure with a = b = c = 16.00 nm. Replacement of the small nanocrystals with larger nanocrystals at the corners and face centers of the unit cell transforms the superlattice symmetry and thus the expected diffraction peaks. The green lines (middle) correspond to the fcc symmetry with a = b = c = 16.89 nm. Additional replacement of the small nanocrystals on the edges and at the center of the unit cell transforms the superlattice symmetry from fcc to bcc. The blue lines (bottom) show the expected diffraction peaks for the bcc symmetry with a = b = c = 17.50 nm.

5.3.3 TEM Characterization of Heated Superlattices

The nanocrystal superlattices observed by SAXS during the heating of a film of 1.8 nm dodecanethiol-capped nanocrystals were also studied by TEM. Figures 5.6, 5.7, 5.8, and 5.9 show TEM images of the bcc, hcp, ico-AB_{13}, and hex-AB_5 nanocrystal superlattice, respectively.

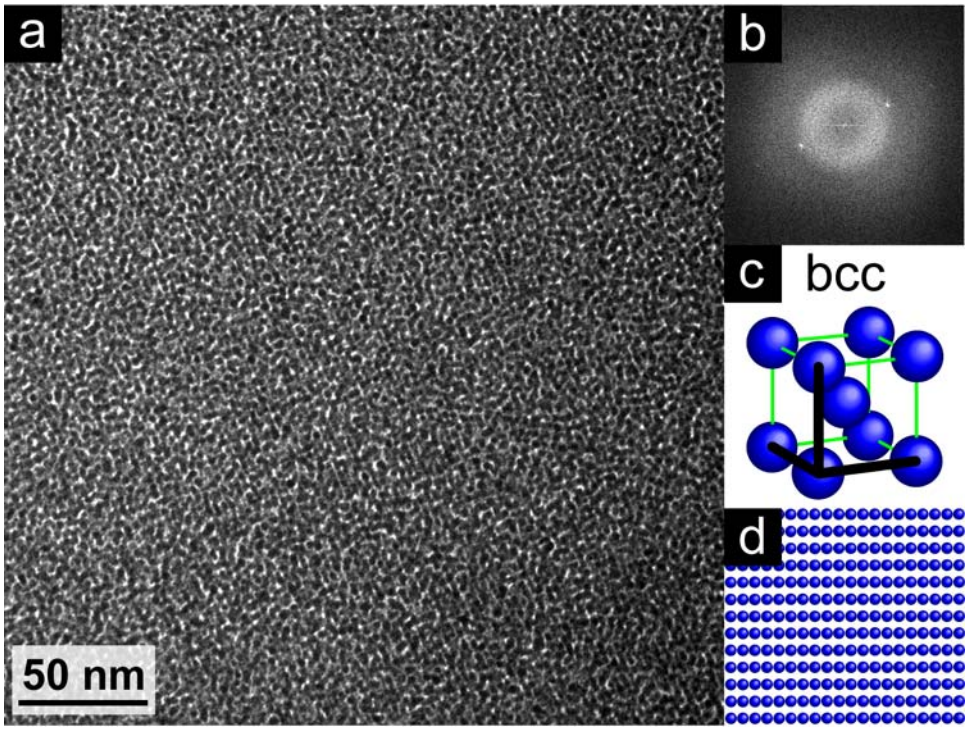

Figure 5.6: (a) TEM image and (b) FFT of a bcc superlattice of sub-2 nm dodecanethiol-capped Au nanocrystals. The nanocrystal superlattice is oriented with the (110) plane parallel to the substrate and results in the observation of (110) "superlattice fringes." (c) Illustration of the bcc superlattice and (d) projection of the superlattice along the <110> zone axis.

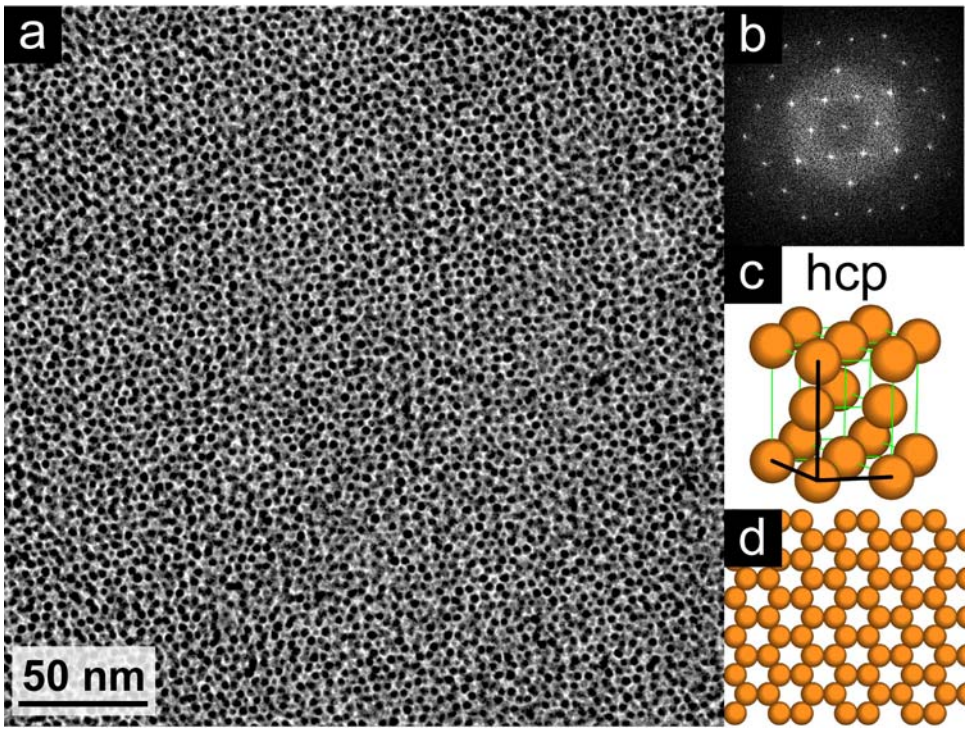

Figure 5.7: (a) TEM image and (b) FFT of an hcp superlattice of heated dodecanethiol-capped Au nanocrystals. The nanocrystal superlattice is oriented with the (001) plane parallel to the substrate. (c) Illustration of the hcp superlattice and (d) projection of the superlattice along the <001> zone axis.

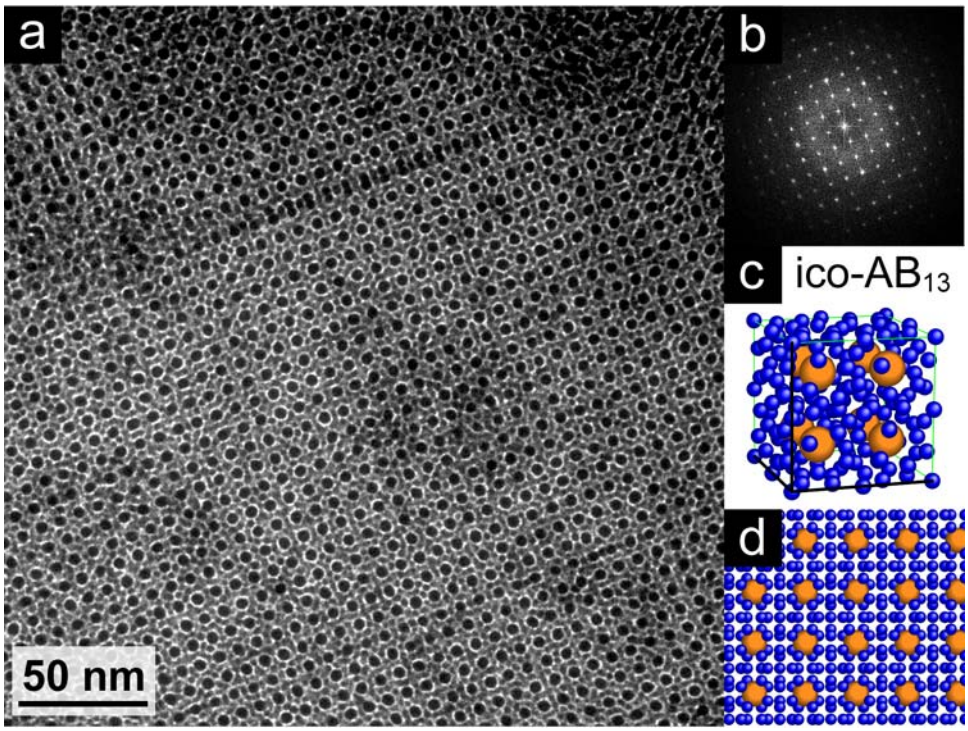

Figure 5.8: (a) TEM image and (b) FFT of an ico-AB_{13} ($NaZn_{13}$-type) superlattice of heated dodecanethiol-capped Au nanocrystals. The heated nanocrystals have a bimodal distribution and form a BNSL. The nanocrystal superlattice is oriented with the (001) plane parallel to the substrate. (c) Illustration of the ico-AB_{13} superlattice and (d) projection of the superlattice along the <001> zone axis.

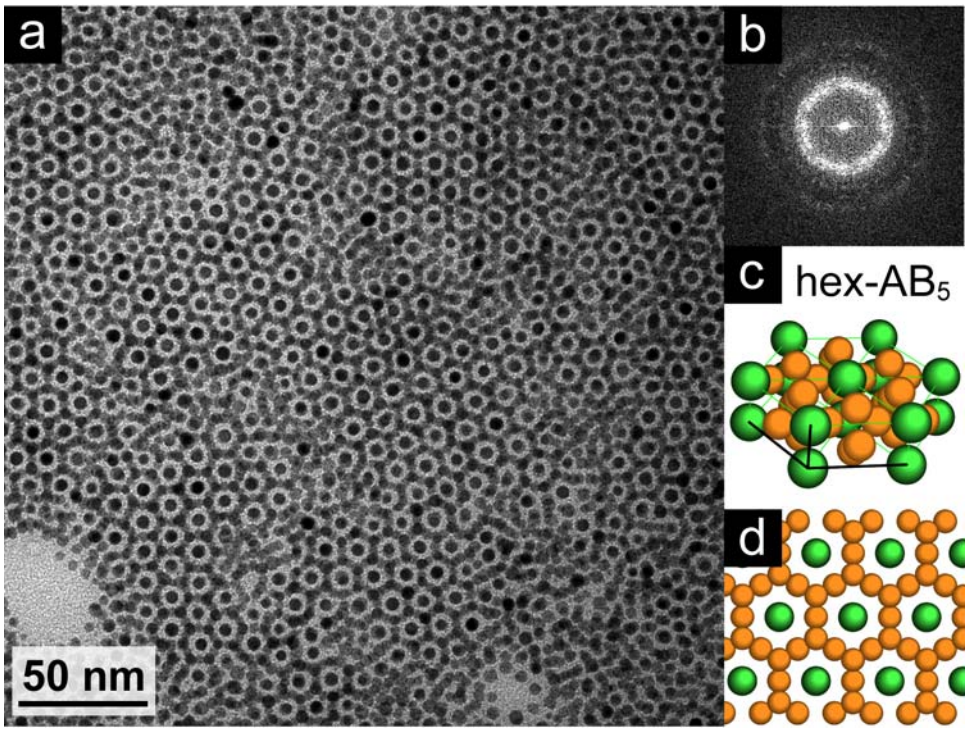

Figure 5.9: (a) TEM image and (b) FFT of a hex-AB_5 (CuC_5-type) superlattice of heated dodecanethiol-capped Au nanocrystals. The heated nanocrystals have a bimodal distribution and form a BNSL. The nanocrystal superlattice is oriented with the (001) plane parallel to the substrate. (c) Illustration of the AB_5 superlattice and (d) projection of the superlattice along the <001> zone axis.

While the SAXS data showed clearly that the 1.8 nm dodecanethiol-capped Au nanocrystals were initially organized into a bcc superlattice, the positions of the nanocrystals in the bcc superlattices are difficult resolve, as shown in Figure 5.6. Instead, superlattice "fringes" corresponding to the bcc (110) planes can be observed in the TEM image resulting in the spots shown in the FFT. As shown in Figure 5.9, the hex-AB_5 superlattice did not appear to form large grains on the TEM grid. However, grains as large as 2 μm were observed by TEM for the hcp and ico-AB_5 superlattices. Figure 5.10 shows low magnification TEM images of large superlattice grains from the heated Au nanocrystals.

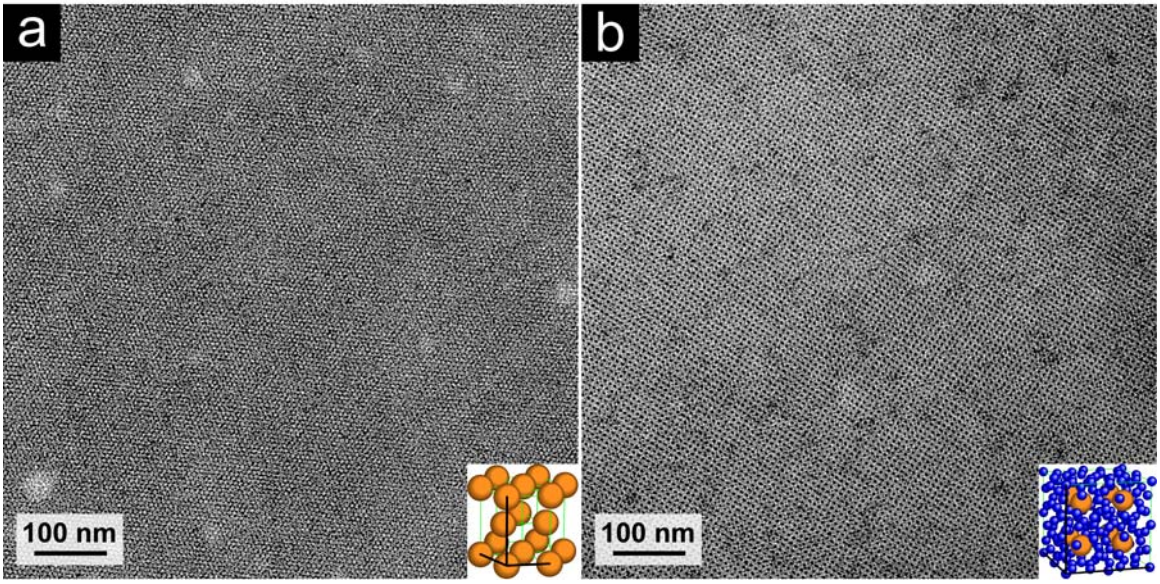

Figure 5.10: Low magnification TEM images of (a) an hcp and (b) an ico-AB_{13} superlattice of heated dodecanethiol-capped Au nanocrystals. In each case the superlattice grain extends approximately 2 μm on the TEM grid.

At 208 °C, the scattering intensity from the superlattices disappeared and the scattering signal rapidly shifts to low angles. This is due to the rapid phase separation of the inorganic and organic material in the film. The bicontinuous network of coalesced Au and organic is clear in the TEM image of a film of Au nanocrystals heated above 208 °C shown in Figure 5.11.

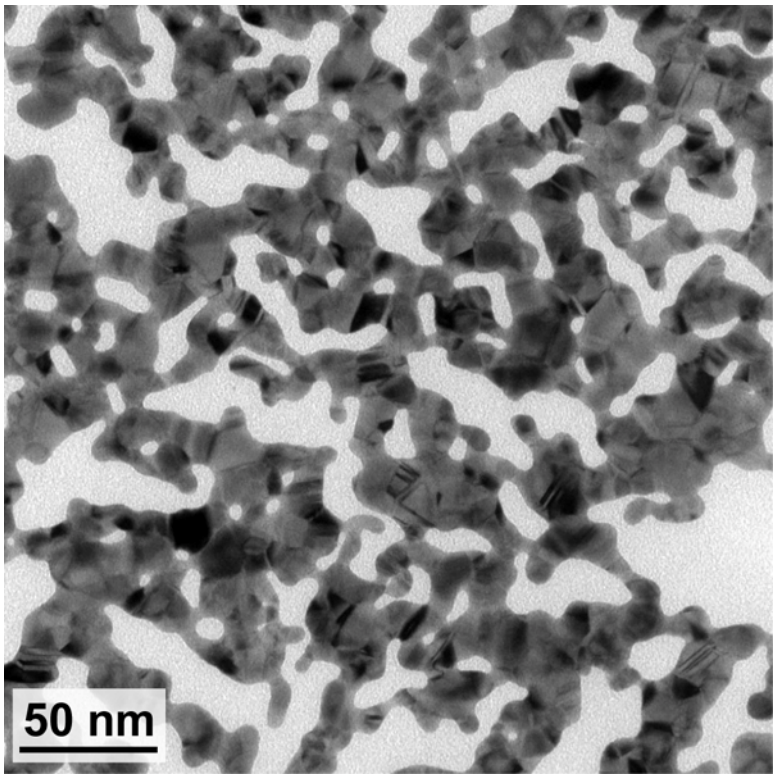

Figure 5.11: TEM image of a film of Au nanocrystals heated above 208 °C. The inorganic gold cores and organic ligand have undergone a phase segregation resulting in the bicontinuous structure shown in the TEM image.

5.3.4 GISAXS Characterization of Heated Superlattices

Transmission-mode small angle x-ray scattering (SAXS) was used to probe the structural transformations of heated nanocrystal superlattices for a number of reasons: 1) the temperature and heating rate can be precisely controlled with commercially available instrumentation, 2) thermal expansion of the experimental apparatus during heating does not result in misalignment of the sample with the incident x-ray beam, 3) since the x-ray beam only probes an area of the sample equal to the beam cross-section, an accurate picture of the transition kinetics can be obtained, and 4) radial integrations of 2D

transmission SAXS data can be used to observe weak diffraction peaks that would otherwise be lost in the detector noise.

While grazing incidence small angle x-ray scattering (GISAXS) requires a more complicated experimental approach and data interpretation, it can provide crystallographic detail not accessible with the transmission SAXS geometry including, but not limited to, preferential orientation of the superlattice with the substrate and distortions of the superlattice along the direction normal to the substrate. Figures 5.12 through 5.16 show GISAXS patterns from the nanocrystal superlattice structures that are observed during the heating a film of sub-2 nm Au nanocrystals. The GISAXS patterns are overlaid with spot patterns that were simulated with the "indexGIXS" software package.[30]

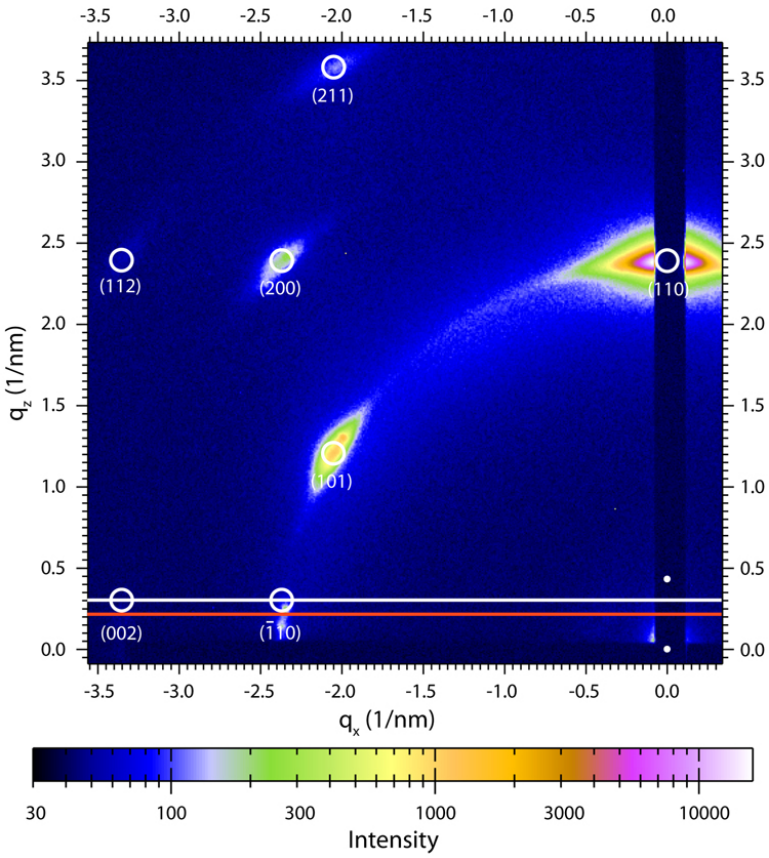

Figure 5.12: GISAXS pattern resulting from a body-centered cubic (bcc) superlattice of sub-2 nm dodecanethiol-capped nanocrystals. The spot overlay was simulated using the following parameters: a = b = c = 3.75 nm, $\alpha = \beta = \gamma = 90°$, (110) plane parallel to the substrate, incident angle $\alpha_i = 0.25°$, critical angle for the substrate $\alpha_s = 0.18°$, and the critical angle for the film $\alpha f = 0.10°$. The open white circles show the expected positions of the Bragg spots with the indicated indexes. The white dots denote the direct and reflected beam positions. The horizontal lines indicate the sample horizon (red) and the Yoneda peak for the film (white).

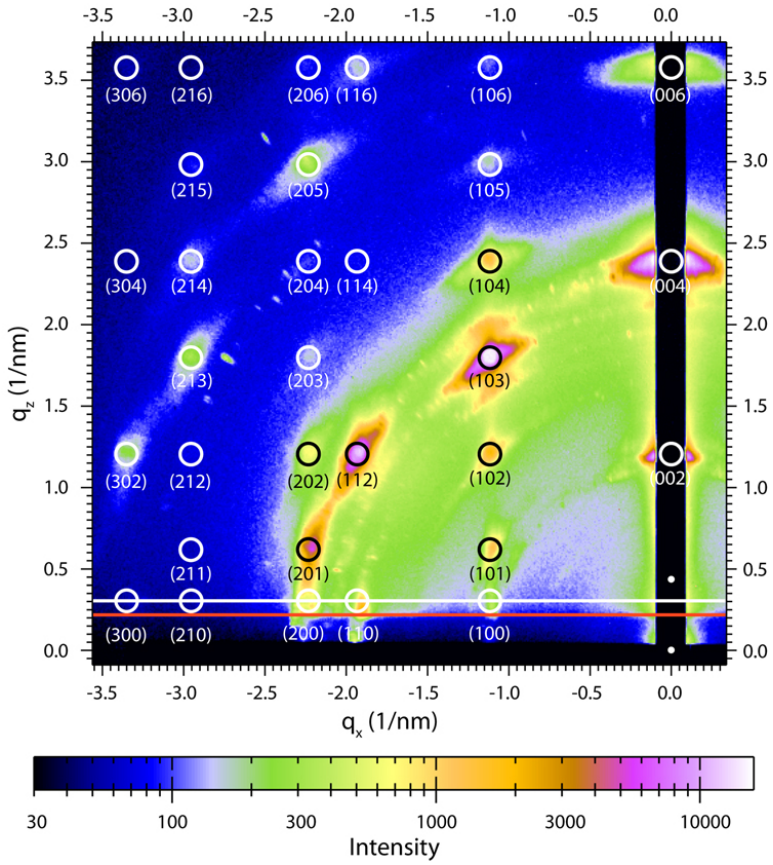

Figure 5.13: GISAXS pattern resulting from a hexagonal close-packed (hcp) superlattice of dodecanethiol-capped Au nanocrystals. The spot overlay was simulated with the following parameters: a = b = 6.5 nm, c = 10.61 nm, $\alpha = \beta = 90°$, $\gamma = 120°$, (001) plane parallel to the substrate, incident angle $\alpha_i = 0.25°$, critical angle for the substrate $\alpha_s = 0.18°$, and the critical angle for the film $\alpha_f = 0.10°$.

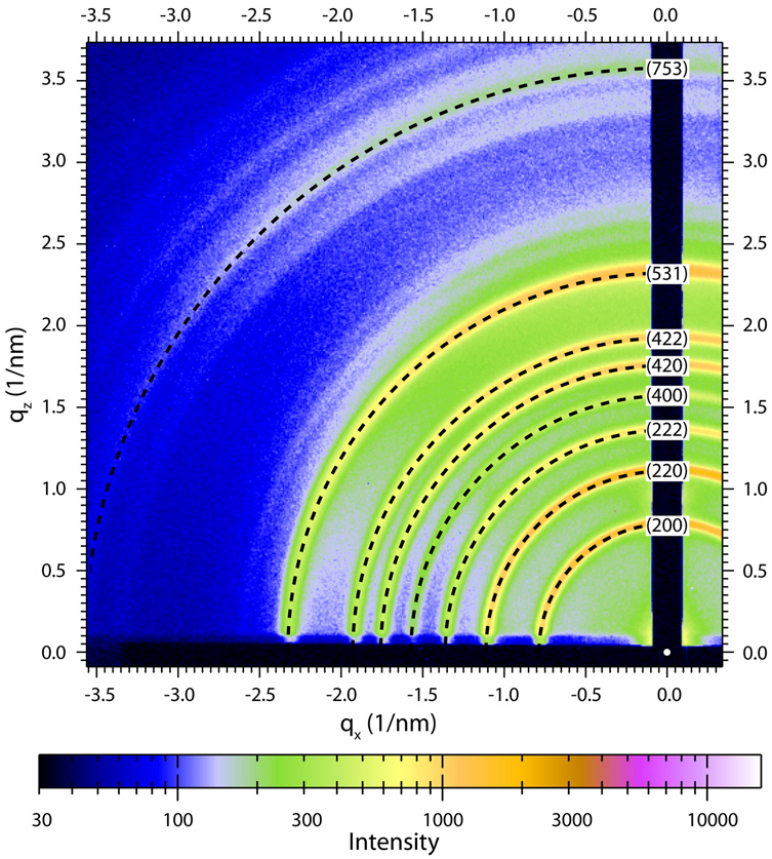

Figure 5.14: GISAXS pattern resulting from a simple cubic (sc) $NaZn_{13}$-type ico-AB_{13} binary nanocrystal superlattice (BNSL) of dodecanethiol-capped Au nanocrystals. The dashed black rings show the expected positions of the diffraction rings with the indicated indexes from a cubic $NaZn_{13}$-type structure with a = b = c = 16.0 nm. The appearance of powder rings in the GISAXS pattern indicates that there is no preferential orientation of the superlattice with the substrate. The appearance of strong (531) and (753) reflections is characteristic of diffraction patterns from $NaZn_{13}$-type structures.

The GISAXS patterns for the hexagonal $CaCu_5$-type AB_5 BNSL could not be indexed such that all observed Bragg spots were accounted for with no additional expected spots. We explored 2 different simulation schemes, one with the hexagonal lattice parameters a = b = 2c (which can be inferred from the TEM image of the AB_5 BSNL; Figure 5.9) and the other with a = b = c. In the first case (Figure 5.15), nearly all

Bragg spots can be accounted for but many additional spots are also expected and not observed. In the second case (Figure 5.16), not all spots can be explained using common crystallographic orientations of the superlattice and several high index orientations are presented to account for the other spots. It is important to note that our simulation only predicts whether a spot is expected or not and does not calculate the relative strengths of the reflections. Thus, it is possible that many spots that are expected from our simulations may be too weak to observe in the data. In considering a $CuCu_5$-type structure (space group 191; Wyckoff sequence: gca) with a = b = 2c, it is interesting to note that if the nanocrystals in the 2c Wyckoff were similar in size to those in the 1a Wyckoff positions (and thus possessed a similar scattering factor) then the structure would resemble a simple hexagonal structure with a = b = c.

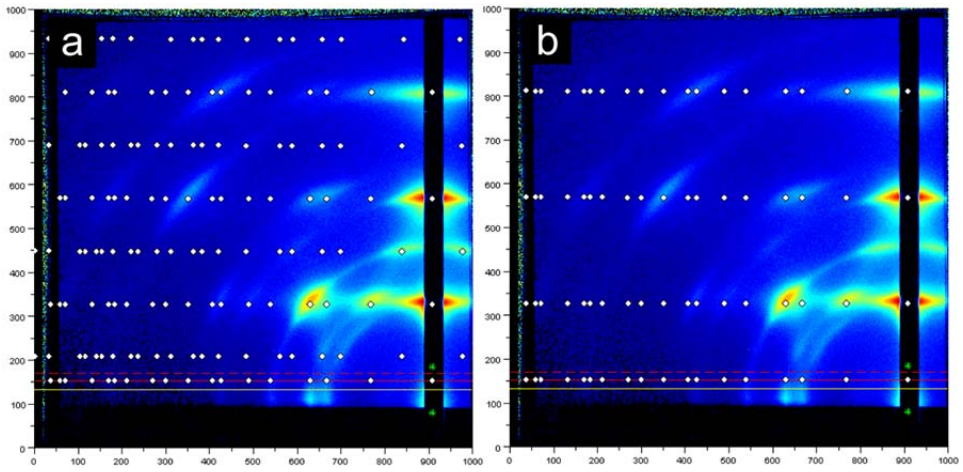

Figure 5.15: GISAXS pattern resulting from a hexagonal $CaCu_5$-type AB_5 BNSL of dodecanethiol-capped Au nanocrystals. The spot overlays in (a) and (b) were simulated with the following parameters: a = b = 12.4 nm, c = 6.2 nm, $\alpha = \beta = 90°$, $\gamma = 120°$, incident angle $\alpha_i = 0.25°$, critical angle for the substrate $\alpha_s = 0.18°$, and the critical angle for the film $\alpha_f = 0.10°$. The plane parallel to the substrate was (110) in (a) and (001) in (b). The green stars denote the positions of the direct and reflected beam. The horizontal lines represent the sample horizon (white), the Yoneda peak for the film (solid red), and the Yoneda peak for the substrate (dashed red). The simulation in (a) accounts for all the observed Bragg spots but also predicts many other spots which are not observed in the GISAXS pattern.

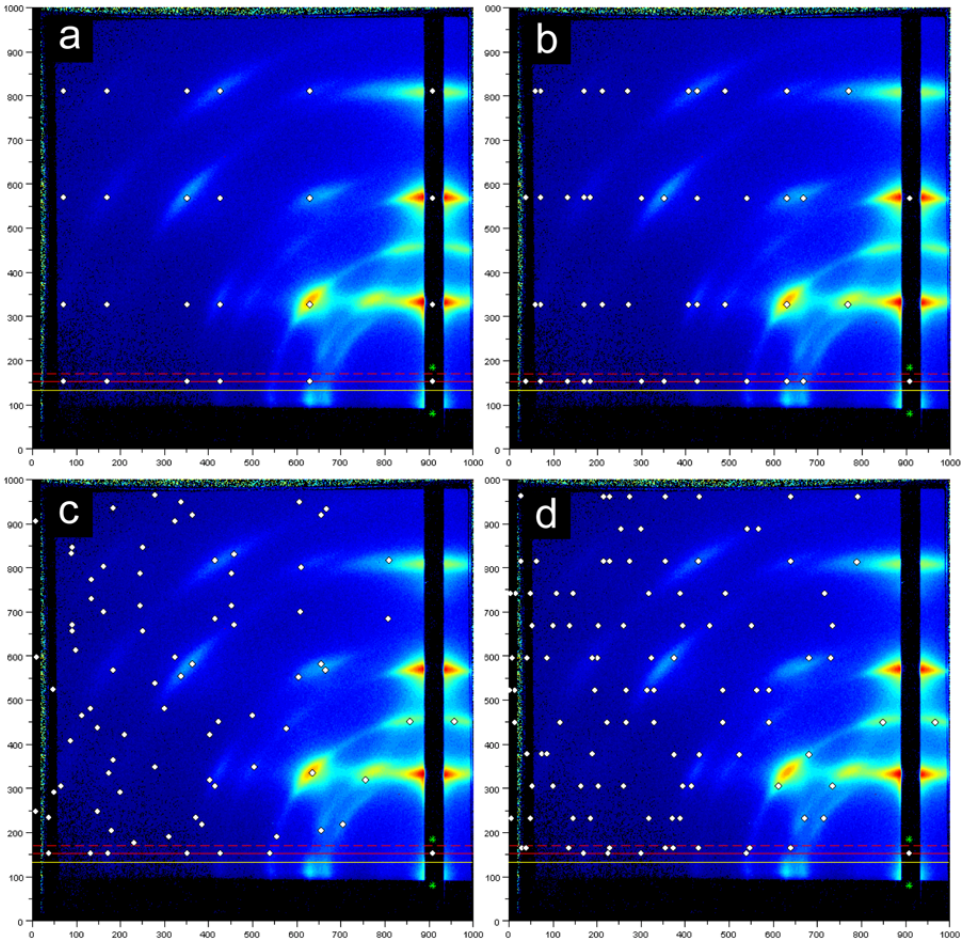

Figure 5.16: GISAXS pattern resulting from a hexagonal $CaCu_5$-type AB_5 BNSL of dodecanethiol-capped Au nanocrystals. The spot overlays in all images were simulated with the following parameters: a = b = c = 6.2 nm, $\alpha = \beta = 90°$, $\gamma = 120°$, incident angle $\alpha_i = 0.25°$, critical angle for the substrate $\alpha_s = 0.18°$, and the critical angle for the film $\alpha_f = 0.10°$. The plane parallel to the substrate was (001) in (a) and (110) in (b). Not all observed Bragg spots are accounted for in (a) and (b), but have the same q-values as identified reflections in (a) and (b) so several other superlattice orientations were explored that simulate them. In particular, simulations with the (c) (043) and (d) (144) superlattice planes parallel to the substrate are shown. A unique characterization of these minority orientations cannot be given, as in each case only one diffraction spot was strong enough to observe.

5.3.5 Temperature-Induced Growth of Nanocrystals

The temperature-dependent phase transitions of the Au nanocrystal superlattice derive from the growth of the Au nanocrystal cores, the accompanying partial desorption of the ligand shell, and the tendency towards Au-organic phase segregation (that is frustrated at lower temperature due to bonding). It was very surprising to find that the nanocrystal size distribution changes with increasing temperature while remaining sufficiently well-defined to retain order during this ripening process. Figure 5.17 shows TEM, SAXS, grazing-incidence wide angle X-ray scattering (GIWAXS) and optical absorbance spectra of the Au nanocrystals after being heated to various temperatures. All of the data confirm the increased nanocrystal size that was observed in TEM and SAXS data from the heated superlattices. This kind of "controlled" ripening of alkanethiol-coated Au nanocrystals, however, is not unprecedented, as Shimizu *et al.* has observed similar ripening behavior[21] in heated films of Au nanocrystals. The nanocrystal assembly retains a high degree of order, but changes symmetry to accommodate the difference in interfacial curvature at the interface between the inorganic nanocrystal cores and the ligand shell. Additionally, there is a decrease in the total nanocrystal surface area in the system as the nanocrystal cores grow; thus, a change in the relative amount of "bound" to "unbound" ligand is also potentially important. These observations suggest similarities between nanocrystal superlattices and microphase-segregating diblock copolymers.[1,22]

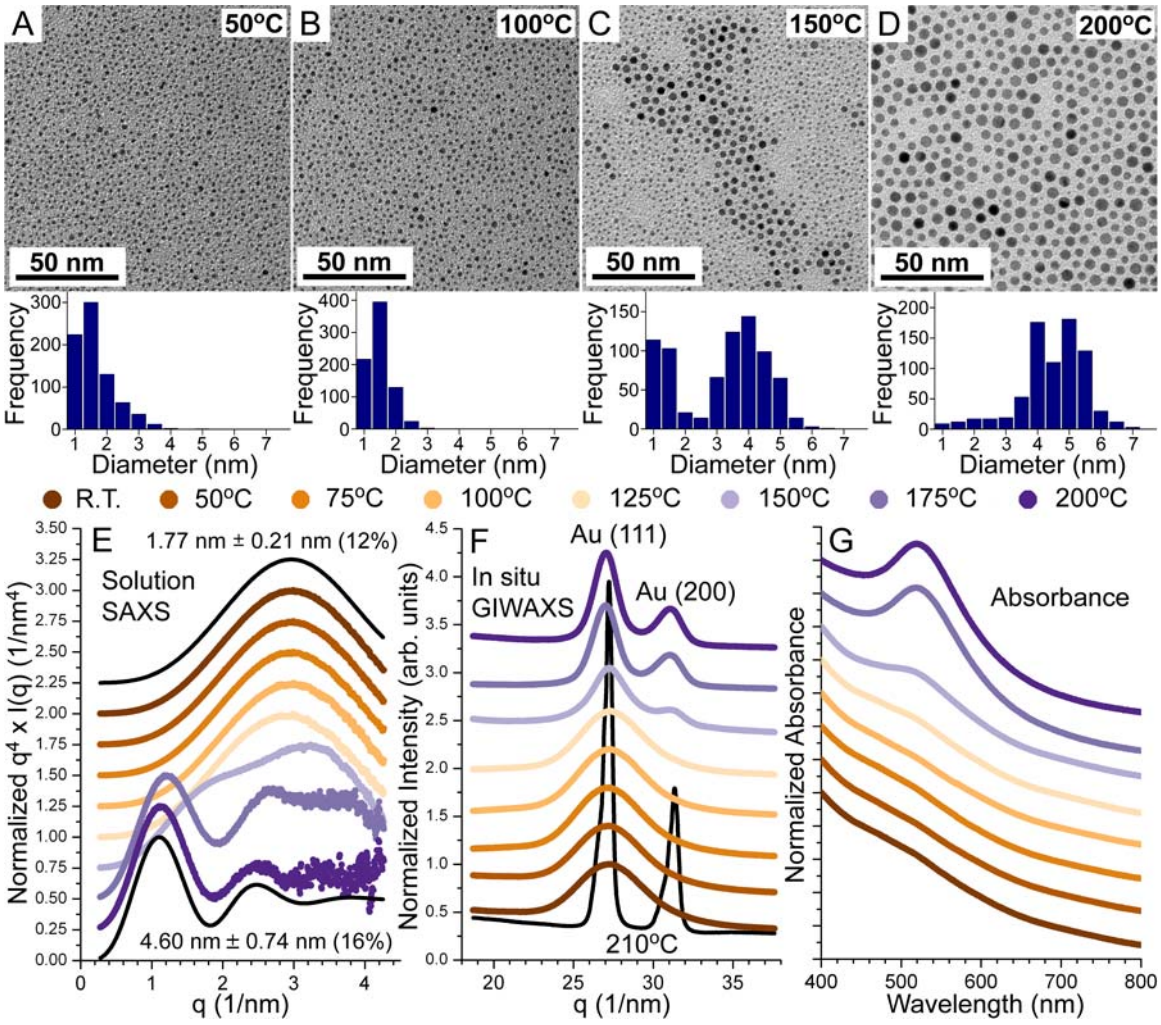

Figure 5.17: (A-D) TEM images of a single layer of nanocrystals heated to the indicated temperatures and the corresponding nanocrystal core size distributions measured from TEM images. (E) Porod plots of solution SAXS data with simulated intensity profiles (solid black lines), (F) in situ GIWAXS, and (G) absorbance spectra of Au nanocrystals after heating to the indicated temperature and being redispersed in toluene. The data show that the growth of the Au nanocrystal cores begins around 125°C, which corresponds to the appearance of the hcp superlattice structure as shown in Figure 5.1.

5.3.6 Influence of Nanophase-Separation

Typically, the assembly of ligand-stabilized nanocrystals into superlattices is considered similar to hard-sphere packing whereby the constituents assemble into the most efficient space-filling structure in order to maximize free volume entropy. The densest arrangement of hard spheres are fcc and hcp, both having a space filling fraction of 0.74. However, fcc is observed significantly more than hcp in assemblies of micrometer-sized colloidal particles and ligand-stabalized nanocrystals—presumably due to the very small (about 10^{-3} k_BT) difference in free energy.[31] It is interesting, then, that none of the four ordered structures observed in this heated nanocrystal system were fcc. The structures must be influenced by something besides packing fraction considerations.

In fact, there is a distinct similarity between the Au nanocrystal superlattice structures and those of microphase-separated diblock copolymers. As illustrated in Figure 5.18, columns of ligand extend from the substrate in a 2D hexagonal array in an hcp superlattice (Figure 5.18F) like the cylindrical (or hexagonal) morphology of diblock copolymer melts. The ligand network in the simple cubic ico-AB_{13} $NaZn_{13}$-type superlattice is similar to the cubic bicontinuous "plumber's nightmare," which is triply periodic.[23] In the case of the BNSL, the three domains correspond to the large nanocrystals, the small nanocrystals, and the ligand (Figure 5.18I). In the hexagonal $CaCu_5$-type superlattice (Figure 5.18K), the ligands have a 2D hexagonal arrangement of hollow tubes extending up from the substrate (Figure 5.18L). While this topology is closely related to inverse hexagonal morphology for diblock copolymers, the simple hexagonal nanocrystal superlattice[24] is the direct analog of the inverse hexagonal morphology of diblock copolymers. Strong evidence of this nanophase separation is the spinodal decomposition that occurs at 208 °C. As the dodecanethiol ligand desorbs from the nanocrystal surface, the Au cores phase segregate from the organic ligand as shown in

Figure 5.18M. The phase segregation occurs rapidly, as shown in the TGA and DSC data in Figure 5.19. While the DSC data shows a very narrow peak that corresponds to the rapid coalescence of the Au nanocrystals, the TGA data shows that the organic ligand does not evaporate in such a narrow timeframe. In fact, only about 2 % of the ligand has evaporated at the time when the Au nanocrystal cores coalesce (the ligand makes up about 25% of the sample weight).

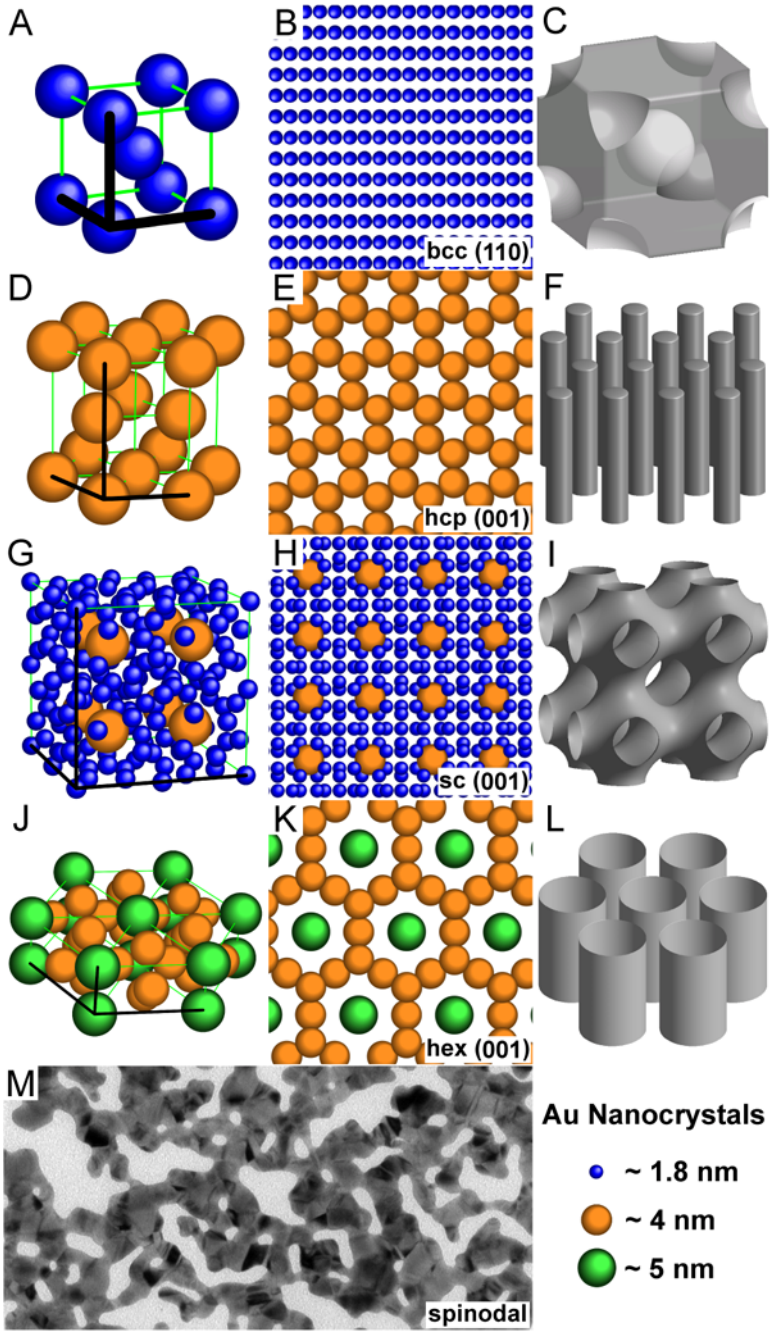
A
B
C
bcc (110)
D
E
F
hcp (001)
G
H
I
sc (001)
J
K
L
hex (001)
M
spinodal
Au Nanocrystals
~ 1.8 nm
~ 4 nm
~ 5 nm

Figure 5.18: (A, D, G, J) Model representations, (B, E, H, K) superlattice projections with the noted orientations, and (C, F, I, L) simplified ligand domains for observed nanocrystal superlattice structures: (A-C) bcc, (D-F) hcp, (G-I), binary sc ico-AB_{13}, and (J-L) binary hex AB_5. The simplified ligand domains mimic microphase-separated morphologies for amphiphilic organic molecules: (C) bcc (spherical), (F) hexagonal (cylindrical), (I) cubic bicontinuous (plumber's nightmare), and (L) inverse hexagonal. (M) TEM image of a nanocrystal superlattice that has been heated above 200°C. Spinodal decomposition of the superlattice occurs as the ligand completely desorbs from the nanocrystal surface.

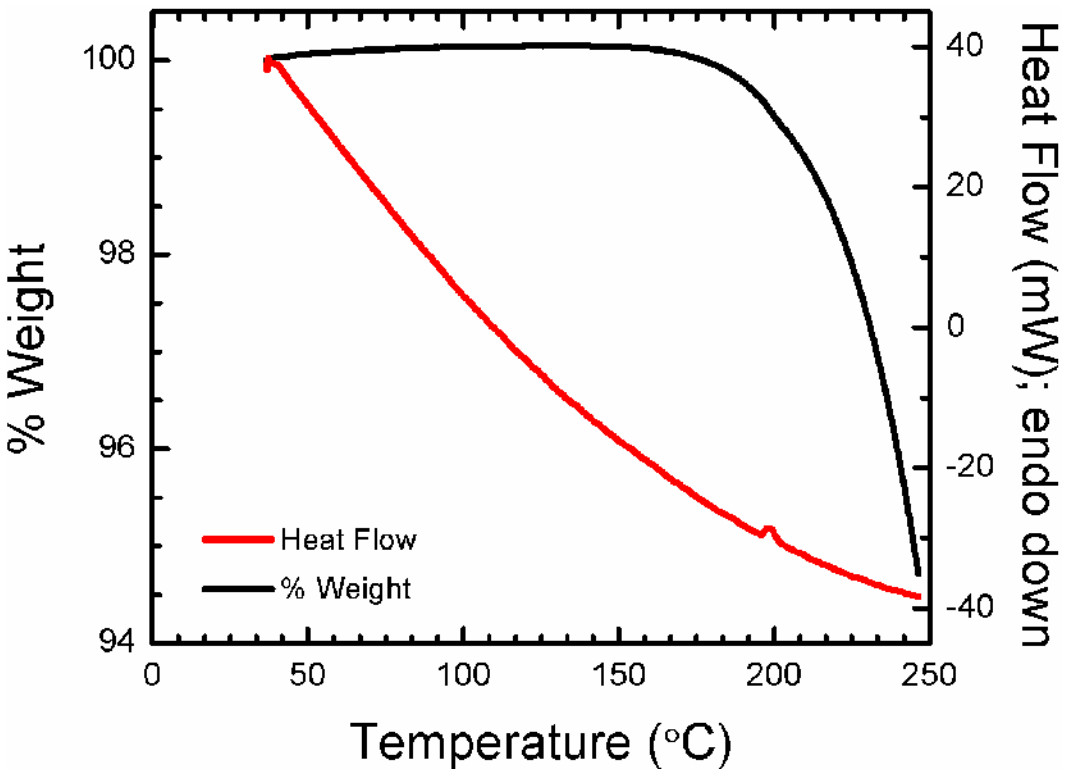

Figure 5.19: TGA data (black curve) and DSC data (red curve) collected simultaneously for sub-2 nm dodecanethiol-capped Au nanocrystals. The TGA shows that evaporation of the ligand occurs gradually over a large temperature range. The DSC data shows a narrow exothermic peak around 200 °C which can be attributed to the rapid coalescence of the Au nanocrystal cores as they phase separate from the organic ligand.

The phase separation of the inorganic cores and the organic ligand dictates the nanostructure of the dodecanethiol-capped Au nanocrystal film as it is heated. Initially, all the ligand is bound to the nanocrystal surface and the nanocrystal cores are unable to phase segregate from the organic ligand. The chemical bond between the ligand and the nanocrystal core frustrates the system and the nanocrystals arrange into a bcc superlattice as do amphiphilic sphere-forming block copolymers. As the nanocrystals are heated, the nanocrystals grow which reduces the surface area in the system and liberates some of the

ligand from the nanocrystal core. This decreases the frustration in the system and the nanocrystals rearrange to in order to further segregate the inorganic and organic material.

5.4 CONCLUSION

Our findings show a strong conceptual link between the self-assembly of nanocrystal superlattices and microphase-separated amphiphilic soft materials like diblock copolymers. Indeed, there are analogs of some of the most complex nanocrystal superlattice structures[25] in diblock copolymers.[26] This work also shows that nanocrystal superlattices can undergo a surprisingly diverse range of structural transitions with only subtle changes in nanocrystal size and ligand content. An initial bcc superlattice transformed to a hexagonal close-packed (hcp) lattice, then to binary superlattices with simple cubic (sc) symmetry (isostructural with $NaZn_{13}$) and hexagonal (hex) structure (isostructural with $CaCu_5$). The phase transitions were not reversible and resulted from changes in nanocrystal size. One common perception of nanocrystal superlattices is that they are assemblies of discrete units—i.e., "artificial atoms"—yet, here we show that nanocrystal superlattices are essentially metastable nanophase-separated ordered arrays of inorganic and organic domains. The self-assembly of soft materials is well understood based on microphase-separation and molecular packing constraints.[27] There is opportunity to leverage the extensive theoretical understanding of microphase-separated organic systems to enable greater understanding of nanocrystal self-assembly. Additionally, nanocrystals can offer a unique fundamental test bed for exploring the self-organization of microphase separated systems, since nanocrystals assemble on rapid time scales and several parameters like interfacial curvature and the "block" volume fraction can be independently controlled.

5.5 REFERENCES AND NOTES

1. I. W. Hamley, *The Physics of Block Copolymers* (Oxford Univ. Press, Oxford, 1998).
2. J. M. Seddon, R. H. Templer, in *Structure and Dynamics of Membranes* (Eds. R. Lipowsky, E. Sackmann) 97-160 (North-Holland, Amsterdam, 1995).
3. K. Kremer, M. O. Robbins, G. S. Grest, Phase Diagram of Yukawa Systems: Model for Charge-Stabilized Colloids. *Phys. Rev. Lett.* **57**, 2694– 2697 (1986).
4. G. A. McConnell, A. P. Gast, Predicting Disorder–Order Phase Transitions in Polymeric Micelles. *Phys. Rev. E* **54**, 5447-5455 (1996).
5. A. P. Alivisatos, Perspectives on the Physical Chemistry of Semiconductor Nanocrystals. *J. Phys. Chem.* **100**, 13226-13239 (1996).
6. J. J. Urban, D. V. Talapin, E. V. Shevchenko, C. R. Kagan, C. B. Murray, Synergism in binary nanocrystal superlattices leads to enhanced p-type conductivity in self-assembled PbTe/Ag2Te thin films. *Nature Mater.* **6**, 115-121 (2007).
7. M. J. Murray, J. V. Sanders, Close-packed structures of spheres of two different sizes II. The packing densities of likely arrangements. *Philos. Mag. A* **42**, 721-721 (1980).
8. P. Bartlett, R. H. Ottewill, P. N. Pusey, Superlattice formation in binary mixtures of hard-sphere colloids. *Phys. Rev. Lett.* **68**, 3801-3801 (1992).
9. K. Bian, J. J. Choi, A. Kaushik, P. Clancy, D.-M. Smilgies, T. Hanrath, Shape-Anisotropy Driven Symmetry Transformations in Nanocrystal Superlattice Polymorphs. *ACS Nano* **5,** 2815-2823 (2011).
10. E. V. Shevchenko, D. V. Talapin, C. B. Murray, S. O'Brien, Structural Characterization of Self-Assembled Multifunctional Binary Nanoparticle Superlattices. *J. Am. Chem. Soc.* **128**, 3620-3637 (2006).
11. E. V. Shevchenko, D. V. Talapin, S. O'Brien, C. B. Murray, Polymorphism in AB13 Nanoparticle Superlattices: An Example of Semiconductor−Metal Metamaterials. *J. Am. Chem. Soc.* **127**, 8741-8747 (2005).
12. X. Ye, J. Chen, C. B. Murray, Polymorphism in Self-Assembled AB6 Binary Nanocrystal Superlattices. *J. Am. Chem. Soc.* **133**, 2613-2620 (2011).
13. M. I. Bodnarchuk, M. V. Kovalenko, W. Heiss, D. V. Talapin, Energetic and Entropic Contributions to Self-Assembly of Binary Nanocrystal Superlattices: Temperature as the Structure-Directing Factor. *J. Am. Chem. Soc.* **132**, 11967-11977 (2010).

14. J. C. Pàmies, A. Cacciuto, D. Frenkel, Phase diagram of Hertzian spheres. *The Journal of Chemical Physics* **131**, 044514 (2009).

15. B. A. Korgel, S. Fullam, S. Connolly, D. Fitzmaurice, Assembly and Self-Organization of Silver Nanocrystal Superlattices: Ordered "Soft Spheres". *J. Phys. Chem. B* **102**, 8379-8388 (1998).

16. D. K. Smith, B. Goodfellow, D.-M. Smilgies, B. A. Korgel, Self-Assembled Simple Hexagonal AB2 Binary Nanocrystal Superlattices: SEM, GISAXS, and Defects. *J. Am. Chem. Soc.* **131**, 3281-3290 (2009).

17. B. A. Korgel, N. Zaccheroni, D. Fitzmaurice, "Melting Transition" of a Quantum Dot Solid: Collective Interactions Influence the Thermally-Induced Order−Disorder Transition of a Silver Nanocrystal Superlattice. *J. Am. Chem. Soc.* **121**, 3533-3534 (1999).

18. B. A. Korgel, Correlated Membrane Fluctuations in Nanocrystal Superlattices. *Phys. Rev. Lett.* **86**, 127-127 (2001).

19. B. W. Goodfellow, R. N. Patel, M. G. Panthani, D.-M. Smilgies, B. A. Korgel, Melting and Sintering of a Body-Centered Cubic Superlattice of PbSe Nanocrystals Followed by Small Angle X-ray Scattering. *J. Phys. Chem.* C **115**, 6397-6404 (2011).

20. F. X. Redl, K. S. Cho, C. B. Murray, S. O'Brien, Three-dimensional binary superlattices of magnetic nanocrystals and semiconductor quantum dots. *Nature* **423**, 968-971 (2003).

21. T. Shimizu, T. Teranishi, S. Hasegawa, M. Miyake, Size Evolution of Alkanethiol-Protected Gold Nanoparticles by Heat Treatment in the Solid State. *J. Phys. Chem. B* **107**, 2719-2724 (2003).

22. K. I. Winey, E. L. Thomas, L. J. Fetters, Ordered morphologies in binary blends of diblock copolymer and homopolymer and characterization of their intermaterial dividing surfaces. *J. Chem. Phys.* **95**, 9367-9367 (1991).

23. A. C. Finnefrock, R. Ulrich, G. E. S. Toombes, S. M. Gruner, U. Wiesner, The Plumber's Nightmare: A New Morphology in Block Copolymer−Ceramic Nanocomposites and Mesoporous Aluminosilicates. *J. Am. Chem. Soc.* **125**, 13084-13093 (2003).

24. D. V. Talapin, E. V. Shevchenko, C. B. Murray, A. V. Titov, P. Král, Dipole−Dipole Interactions in Nanoparticle Superlattices. *Nano Lett.* **7**, 1213-1219 (2007).

25. D. V. Talapin *et al.* Quasicrystalline order in self-assembled binary nanoparticle superlattices. *Nature* **461**, 964-967 (2009).

26. S. Lee, M. J. Bluemle, F. S. Bates, Discovery of a Frank-Kasper σ Phase in Sphere-Forming Block Copolymer Melts. *Science* **330**, 349-353 (2010).

27. M. W. Matsen, F. S. Bates, Unifying Weak- and Strong-Segregation Block Copolymer Theories. *Macromolecules* **29**, 1091-1098 (1996).

28. M. R. Rasch, *et al.* Hydrophobic Gold Nanoparticle Self-Assembly with Phosphatidylcholine Lipid: Membrane-Loaded and Janus Vesicles. *Nano Lett.* **10**, 3733-3739 (2010).

29. Hammersley, A. P. *ESRF Internal Report.* ESRF97HA02T, 1997.

30. D.-M. Smilgies, D. R. Blasini, Indexation scheme for oriented molecular thin films studied with grazing-incidence reciprocal-space mapping. *J. App. Cryst.* **40**, 716-718 (2007).

31. P. G. Bolhuis, D. Frenkel, S.-C. Mau and D. A. Huse, Entropy difference between crystal phases. *Nature*, **388** 235-236 (1997)

Chapter 6: Copper Chalcogenide Nanocrystal Inks for Low-Cost Printable Photovoltaics†

6.1 INTRODUCTION

I-III-VI_2 chalcopyrite compounds, particularly copper indium gallium selenide ($Cu(In_xGa_{1-x})Se_2$; CIGS), are effective light-absorbing materials in thin film solar cells.[1] These materials possess advantageous properties for solar applications, including that their band gap energy at the red edge of the solar spectrum; they are direct band gap semiconductors with correspondingly high optical absorption coefficients;[2,3] and CIGS materials, in contrast to other candidate materials for thin-film solar cells such as CdTe and amorphous silicon (a-Si), are stable under long-term excitation.[4] High efficiency CIGS-based devices are typically fabricated using polycrystalline films,[5] and single-junction CIGS solar cells have demonstrated nearly 20% solar energy conversion efficiency,[6] which is significantly higher than either CdTe or a-Si based devices.[7] Furthermore, CIGS devices and manufacturing processes may provide have less environmental impact than those with thin film materials with large amounts of Cd and Pb, like CdTe and PbSe based solar cells, although to date the highest efficiency CIGS PV devices have nonetheless required CdS buffer layers.[8]

One of the hurdles currently impeding widespread commercialization of CIGS-based solar cells is the difficulty in achieving controlled stoichiometry over large device

† Portions of this chapter appear in Panthani, Matthew G.; Akhavan, Vahid; Goodfellow, Brian; Schmidtke, Johanna P.; Dunn, Lawrence; Dodabalapur, Ananth; Barbara, Paul F.; Korgel, Brian A., "Synthesis of $CuInS_2$, $CuInSe_2$, and $Cu(In_xGa_{1-x})Se_2$ (CIGS) Nanocrystal "Inks" for Printable Photovoltaics.", Steinhagen, Chet; Panthani, Matthew G.; Akhavan, Vahid; Goodfellow, Brian; Koo, Bonil; Korgel, Brian A., "Synthesis of Cu_2ZnSnS_4 Nanocrystals for Use in Low-Cost Photovoltaics." *Journal of the American Chemical Society* (2009), 131(35), 12554-12555., Akhavan, Vahid A.; Goodfellow, Brian W.; Panthani, Matthew G.; Reid, Dariya K; Hellebusch, Danny J.; Adachi, Takuji; Korgel, Brian A., "Spray-deposited $CuInSe_2$ Nanocrystal Photovoltaics." *Energy and Environmental Science* (2010), 3, 1600-1606., and Akhavan, Vahid A.; Panthani, Matthew G.; Goodfellow, Brian W.; Reid, Dariya K; Korgel, Brian A., Thickness-limited Performance of $CuInSe_2$ Nanocrystal Photovoltaic Devices. *Optics Express* (2010), 18(S3), A411-A420.

areas, leading to high manufacturing costs and poor device yield.[9] CIGS layers in state-of-the-art devices are deposited by a multi-stage co-evaporation of depositing alternate copper, indium, and gallium layers followed by reacting with a selenium source, Se or H_2Se gas, in the chamber.[10,11] This process is time-consuming and the CIGS stoichiometry is difficult to control—intermetallic phases can form and the Se content can vary significantly in the films.[9,12] Large materials losses on the deposition chamber walls also increases cost. For all of these reasons, alternative CIGS layer deposition strategies are desired.

One approach with the potential to produce CIGS layers with controlled stoichiometry without the need for high temperature annealing is to chemically synthesize CIGS nanocrystals with controlled stoichiometry and crystal phase and disperse them in solvents, creating a paint or ink. Such an approach—of printable CIGS inks—make accessible a range of solution-based processing techniques and may lead to inexpensive fabrication routes for CIGS light-absorbing layers.[13] A chemical, solution-based approach alleviates the need for a high temperature annealing step under selenium atmosphere and may solve the CIGS "selenium problem"—i.e., avoiding Se loss and achieving the correct CIGS stoichiometry in films covering large substrate areas.[14] Photovoltaic devices incorporating nanocrystalline-based CdSe/CdTe[15] and CuS[16] absorber layers have been reported and demonstrated solar energy conversion efficiencies as high as 2.9%, although a high temperature anneal at 400°C was required. Semiconductor nanocrystals have also been combined with polymers to produce solution-processed photovoltaics, such as hybrid CdSe nanocrystal/poly-3(hexylthiophene) solar cells, which yield reported efficiencies of up to 1.7%.[17] Many different semiconductor nanocrystals can be synthesized by colloidal routes, including Groups II-VI[18], III-V,[19] I-VI.[20-22] IV-VI,[23] and IV[24-26] semiconductors, but the synthesis of I-III-VI_2 nanocrystals is

much less developed. Nonetheless, there are literature reports of the synthesis of ternary chalcopyrite compound nanocrystals, such as $CuInS_2$, $CuInSe_2$, and other I-II-VI_2 semiconductor nanocrystals such as $AgInS_2$.[27-32] These nanocrystals, however, generally suffer from relatively low yields, and poor crystallinity[33] and poor uniformity in composition and phase.[3,34] This is not surprising considering that many of these systems have very complicated phase diagrams and nanocrystals can exhibit greater phase complexity than the corresponding bulk materials, which furthermore can depend on how the nanocrystals are made.[22]

6.2 EXPERIMENTAL SECTION

6.2.1 Materials

All chemicals were used as received without further purification unless otherwise noted. Copper(II) acetylacetonate ($Cu(acac)_2$; 99.99+%), copper(I) chloride (CuCl; 99.995+%), indium(III) chloride ($InCl_3$; anyhydrous 99.99%), indium(III) acetylacetonate ($In(acac)_3$; 99.99+%), zinc acetate ($Zn(O_2CCH_3)_2$, 99.99%), tin(II) chloride dihydrate ($SnCl_2 \bullet 2H_2O$, 99.99+%), elemental sulfur (99.98%), tributylphosphine (TBP; 97%), *o*-dichlorobenzene (DCB; 99%), and cadmium sulfate ($CdSO_4$, 99.999%) were obtained from Aldrich Chemical Co.; elemental selenium (99.99%) was obtained from Aldrich Chemical Co. or Strem Chemicals; gallium(III) chloride ($GaCl_3$; 99.9999%) was obtained from Strem Chemicals; oleylamine (OLA; >70%) was obtained from Aldrich Chemical Co. or Fluka and, in some cases, was degassed by three cycles of freeze-pump-thaw; thiourea (99.999%) was obtained from Fluka; chloroform (99.99%), toluene (99.99%), ethanol (absolute), tetrachloroethylene (TCE; spectrophotometric grade 99+%), and ammonium hydroxide (18M NH_4OH, ACS certified) were obtained from Fisher

Scientific; N_2 and forming gas (7% H_2, 93%N_2) were received from Matheson Tri-Gas. Copper(I) chloride, indium(III) chloride, and gallium(III) chloride, TBP and degassed OLA were stored in a nitrogen-filled glovebox to prevent degradation.

Soda lime glass (25 x 25 x 1.1 mm polished float glass) was obtained from Delta Technologies; kapton was obtained from DuPont; chromium (Cr 99.999%) and gold (Au, 99.95%) and aluminum (Al, 99.99%) metal for thermal evaporation and molybdenum (Mo, 99.999%), zinc oxide (ZnO, 99.9%) and indium tin oxide (ITO, 99.99% In_2O_3:SnO_2 90:10) sputtering targets were obtained from Kurt J. Lesker Co.; ultrapure Ar gas (99.999%) and 0.5% O_2 in Ar gas (99.95%) were obtained from Praxair.

6.2.2 $CuInS_2$ Nanocrystal Synthesis

0.26 g (1 mmol) of $Cu(acac)_2$ and 0.41 g (1 mmol) of $In(acac)_3$ are added to 7 mL of DCB in a 25 mL three-neck flask in air In a separate 25-mL three-neck flask, 0.064 g (2 mmol) of elemental sulfur is dissolved in 3 mL of DCB in air. Both flasks are then attached to a Schlenk line and purged of oxygen and water by pulling vacuum at room temperature for 30 minutes, followed by N_2 bubbling at 60°C for 30 minutes. Between 0.5 and 2 mL (1.5 to 6 mmol) of OLA are added to the (Cu, In)-DCB mixture and both flasks are heated to 110°C and combined, maintaining a N_2 flow. The reaction mixture is refluxed (~182°C) for one hour under N_2 flow. The reaction is allowed to cool to room temperature, and the nanocrystals are separated by adding excess ethanol. The yield of solution-stable nanocrystals after purification was ~90%.

6.2.3 $CuInSe_2$ Nanocrystal Synthesis

6.2.3.1 One-Pot Synthesis

In a nitrogen-filled glove box, 1 mmol of CuCl (0.099 g), 1 mmol of $InCl_3$ (0.221 g), and 2 mmol of elemental Se (0.158 g) are combined in a 25-mL three-neck flask with

an attached condenser and stopcock valve. The stopcock valve is closed before removing the flask from the glove box, where it is attached to a Schlenk line and placed on a heating mantle. 10 mL of OLA stored in air is injected into the flask. The flask is purged of oxygen and water by pulling vacuum at 60°C for one hour, followed by N_2 bubbling at 110°C for one hour while stirring. The mixture is then heated to 240°C and the reaction proceeds for 4 hr under vigorous stirring. The reaction is cooled to ~100°C, where ~10 mL of chloroform is added to quench the reaction, and ~5 mL of ethanol is added to precipitate the nanocrystals. After adding the ethanol, the reaction mixture is immediately removed and placed in a centrifuge tube. Reactions carried out for less than four hours yielded nanocrystals with a larger size distribution and more agglomeration when dispersed after purification. A significant amount of poorly-capped and large (up to 200 nm diameter) nanocrystals are found in the crude reaction product, which is separated from the well-capped nanocrystals. The typical product yield of the well-dispersed $CuInSe_2$ nanocrystals was ~15%.

6.2.3.2 Hot-Injection Synthesis

In a nitrogen-filled glove box, 5 mmol of CuCl (0.45 g) and 5 mmol of $InCl_3$ (1.11 g), 50 ml of degassed OLA and a magnetic stir bar are sealed in a 100-mL three-neck flask with septa, and an attached condenser-stopcock valve combination. The reaction flask is taken outside the glovebox and mounted on a conventional Schlenk line setup. The flask is purged of oxygen and water by pulling vacuum at 110 °C for 30 min, followed by N_2 bubbling at 110 °C for 5 min while stirring.

A 1M TBP:Se solution is separately prepared in the glovebox by dissolving 10 mmol of Se (0.79 g) in 10 ml TBP in a 25 ml vial under magnetic stirring. The resulting Se reactant solution is drawn into a syringe and taken outside the glovebox in preparation

for injection into the reaction flask on the Schlenk line. At this point, the temperature of the reaction flask is raised to 240 °C at a heating rate of approximately 50˚C/min. When the temperature in the flask reaches 180^{o}C, the TBP:Se stock solution is injected into the flask. The reaction mixture is then maintained at 240^{o}C for 10 minutes. The heating mantle is removed and the reaction is allowed to cool to room temperature. The contents of the reaction vessel and 10 ml of ethanol are mixed in a glass centrifuge tube, and the nanocrystal product is precipitated by centrifugation at 4000 rpm for 5 minutes. The supernatant is discarded. The nanocrystal product is redispersed in 5 mL of toluene and centrifuged at 4000 rpm for 5 minutes to remove the larger and poorly capped product. The supernatant is added to a new glass centrifuge tube and the precipitate is discarded. Ethanol is then slowly added to the nanocrystal dispersion until the mixture becomes slightly turbid. The mixture is centrifuged at 4000 rpm for 5 minutes to again precipitate the nanocrystal product. The supernatant is discarded, and the solid product is redispersed in toluene to a final concentration of 20 mg/ml.

6.2.4 $Cu(In_xGa_{1-x})Se_2$ (CIGS) Nanocrystal Synthesis

A typical reaction is carried about by adding 1 mmol of CuCl (0.099 g), 2 mmol of elemental Se (0.158 g), and 1 mmol total of $InCl_3$ (0.00 to 0.221 g) and $GaCl_3$ (0.00 to 0.111 g), to a 25-mL three-neck flask with attached condenser and stopcock valve in a nitrogen-filled glove box. The stopcock valve is closed before removing the flask from the glove box, where it is attached to a Schlenk line and placed on a heating mantle. 10 mL of OLA is injected into the flask. The flask is purged of oxygen and water by pulling vacuum at 60°C for one hour, followed by N_2 bubbling at 110°C for one hour while stirring. The mixture is then heated to 240°C and the reaction proceeds for 4 hr under

vigorous stirring. The product yield of $CuIn_xGa_{1-x}Se_2$ nanocrystals with $x < 1$ ranged from 20%-60% after purification.

6.2.5 Cu_2ZnSnS_4 (CZTS) Nanocrystal Synthesis

In a typical reaction, 0.52 g of $Cu(acac)_2$, 0.29 g of zinc acetate, 0.18 g of $SnCl_2$, 0.13 g of elemental S are added to 40 mL of oleylamine in a 100 mL three-neck flask on a Schlenk line. After degassing under vacuum for 2 hours and purging with N_2 for 30 min at 110 °C, the reaction mixture is heated to 280 °C for 1 hr. After cooling to room temperature, the nanocrystals are isolated by precipitation with ethanol, followed by centrifugation. Solid reaction byproducts and poorly capped nanocrystals are removed by redispersion in chloroform and centrifugation at 8,000 rpm for 2 min. The nanocrystals are washed three more times by solvent/antisolvent precipitation with chloroform/ethanol. A typical reaction yields approximately 200 mg of nanocrystals.

6.2.6 Materials Characterization

The nanocrystals were characterized using a range of analytical techniques, including transmission electron microscopy (TEM), energy-dispersive x-ray spectroscopy (EDS), inductively coupled plasma mass spectrometry (ICP-MS), scanning electron microscopy (SEM), X-ray diffraction (XRD), and UV-Vis-NIR absorbance spectroscopy.

TEM imaging was performed on nanocrystals drop-cast from chloroform, hexane, or toluene dispersions on carbon-coated 200 mesh copper or nickel TEM grids (Electron Microscopy Sciences). TEM images were acquired on either a Phillips 208 TEM with 80 kV accelerating voltage or a JEOL 2010F TEM operating at 200 keV. EDS was carried out using an Oxford INCA EDS detector mounted on the JEOL2010F TEM or a Bruker Quantax 200 detector mounted on a Hitachi S-5500 STEM. The nanocrystal composition was also measured using inductively coupled mass-spectrometry (ICPMS) for

nanocrystal films and powders using a GBC Optimass 8000 ICP-TOF-MS. The ICPMS samples were prepared by digesting a dried nanocrystal powder or thin film in concentrated HNO3. SEM images were acquired using either a LEO 1530 or Zeiss Supra 40 VP SEM operated between 1 and 10 keV. Images were collected through the in-lens or SE2 detector. SEM samples were prepared by depositing a thin layer of the nanocrystals on a conductive surface and were grounded to the SEM base using a strip of copper tape to prevent charging of sample surface. XRD data was acquired using a Bruker-Nonius D8 Advance θ-2θ Powder Diffractometer equipped with a Bruker Sol-X Si(Li) solid-state detector and a rotating stage. Cu Kα (λ= 1.54 Å) radiation was used. For XRD, the nanocrystals were evaporated from concentrated dispersions onto quartz (0001) substrates as ~0.5 mm thick films. Diffraction data was collected by scanning for 4 to 12 hours with an angle increment of 0.01° or 0.02° at a scan rate of 6°/min or 12°/min and a sample rotation speed of 15 rpm. UV-vis-NIR absorbance spectra were obtained with a Varian Cary 500 UV-Vis-NIR spectrophotometer using hexane-dispersed nanocrystals in a quartz cuvette. Film thicknesses were found using a Veeco Dektak 6M stylus profiler. Absorbance was also measured for thin, optically transparent nanocrystal films deposited by spray coating on a quartz substrate.

6.2.7 Nanocrystal Film Deposition

6.2.7.1 Drop-Casting

Thick films (~1 μm) of nanocrystals were deposited onto 12 x 25 mm glass or Mo-coated glass substrates by dropping 150 μL of TCE dispersions with nanocrystal concentrations of 5 mg/mL. The film was fully dried by placing the substrate in a vacuum chamber at room temperature for 12 hours.

6.2.7.2 Spray-Deposition

Nanocrystal films were deposited onto substrates by spray deposition of 20 mg/mL nanocrystal dispersions in toluene using a commercial spray gun (Iwata Eclipse HP-CS) operated at 50 psig head pressure. The gun head was held approximately 10 cm from the substrates.

6.2.8 Photovoltaic Device Fabrication

Conductive back contacts (Mo, Au, or ITO) were deposited on polished soda lime float glass (25 mm x 25 mm x 1.1 mm) or kapton using conventional vapor deposition techniques. Mo and ITO were deposited using radio frequency (RF) sputtering in ultrapure Ar at 5mTorr. RF sputtering was used instead of DC sputtering because it has been reported to provide a film with a better combination of substrate adhesion and good conductivity.[35] Back contact layers of a 5 nm Cr adhesion layer with 60 nm of Au were deposited by thermal evaporation from a tungsten boat. Nanocrystals films were deposited onto the conductive back contacts as described in sections 6.2.7.1 and 6.2.7.2. In a typical deposition, a 20 mg/ml dispersion of nanocrystals were prepared for spray deposition and nanocrystal layers were spray-deposited with a commercial airbrush operated at 50 psig of head pressure. A CdS buffer layer was then deposited from solution following procedures and parameters described by McCandless and Shafarman.[36] Stock aqueous solutions of 0.015 M cadmium sulfate, 1.5 M thiourea, and 14.28 M ammonium hydroxide were made and used in preparation of working solutions by mixing 1.25 mL of the $CdSO_4$ solution, 2.2 mL of the $CS(NH_2)_2$ solution, and 2.8 mL of the NH_4OH solution. Substrates were placed on a hot plate for 10 min that had been preheated to 90°C, after which 0.5-1.0 mL of the working solution was deposited on each substrate. The substrates were immediately covered to reduce the loss of ammonia from the solution. After 2 minutes the substrates were removed from the hot plate, rinsed with

DI water, and dried in a clean air stream. i-ZnO/ITO top contacts were deposited by RF sputtering. First, a layer of i-ZnO approximately 50 nm thick was sputtered from a target of ZnO in an atmosphere of 0.5% O_2 in Ar. Then, a layer of ITO approximately 300 nm thick was sputtered from a target of ITO in an Ar atmosphere. The final active region of the device was 8 mm^2 (a 4 mm x 2 mm rectangle). Completed devices were placed in a vacuum oven at 200°C for up to 40 minutes to improve the device performance.

Stacked PV devices were made by placing the active areas directly on top of each other, and then connecting the stacked devices in parallel using conductive silver paint (SPI Supplies). There was less than 5% area offset between multiple stacked devices. Mott-Schottky measurements were performed on PV devices with slightly different architectures. Approximately 300 nm of sputtered ITO was used as a substrate to deposit $CuInSe_2$ nanocrystal films as described above in 6.2.7.2. A top contact layer of Al approximately 40 nm thick was thermally evaporated from an alumina-coated tungsten boat. The active device area was 8 mm^2.

6.2.9 Photovoltaic Device Testing

Current-potential (I-V) characteristics were collected using a Keithley 2400 General Purpose Sourcemeter and a Xenon Lamp Solar Simulator (Newport) equipped with an AM1.5 optical filter. The intensity of the light source was calibrated using a NIST calibrated Si photodiode (Hamamatsu, S1787-08). Different fractions of solar spectrum were generated by placing a colored glass, cutoff filters (Newport) directly in the path of light beam emanating from the solar simulator. Incident photon conversion efficiency (IPCE) measurements were performed at zero bias between 300 and 1100 nm in 10 nm steps using an in-house fabricated spectrophotometer. Monochromatic light was generated using a commercial monochromator (Newport Cornerstone 260 1/4M).

Generated light was chopped at 213 Hz and was focused to a spot size of 1 mm in diameter on the active region. The response of the device was recorded using a lock-in-amplifier (Stanford Research Systems, model SR830). The light intensity was calibrated using calibrated photodiodes of silicon (Hamamatsu) and germanium (Judson).

Impedance characteristics was measured by applying a 50 mV A-C waveform at frequencies between 0.1 Hz and 10^7 Hz with 5 steps per decade, using a Solartron 1260A Frequency Response Analyzer coupled with a Solartron 1296 Dielectric Interface.

6.3 RESULTS AND DISCUSSION

6.3.1 $CuInS_2$ Nanocrystals

$CuInS_2$ nanocrystals were synthesized using a variation of the procedure developed by Ghezelbash and Korgel[22] for CuS nanocrystals, by adding $In(acac)_3$ as an In source to the reaction:

$$Cu(acac)_2 + In(acac)_3 + 2S \xrightarrow[\text{oleylamine}]{o\text{-dichlorobenzene},\,180^\circ C} CuInS_2 \text{ nanocrystals} + \text{byproducts} \quad (6.1)$$

Elemental sulfur dissolves in dichlorobenzene and could be used directly as the sulfur source. Figure 6.1 shows TEM images of $CuInS_2$ nanocrystals synthesized using the reaction scheme in Eqn (6.1). The nanocrystal size could be roughly controlled by varying the OLA:metal ratio. Figure 6.1 shows $CuInS_2$ nanocrystals with two different average diameters obtained by varying the OLA:metal ratio in the reaction. The average nanocrystal diameter was increased from 6 to 12 nm as the OLA:metal ratio by decreasing the ratio from 6:1 to 3:1. The nanocrystal shape was not perfectly spherical, which contributed to the relatively broad size distributions of the nanocrystals. High

resolution TEM (Figure 6.2) showed the crystallinity of the nanocrystals, with lattice spacings corresponding to tetragonal $CuInS_2$. XRD (Figure 6.3) confirmed that the nanocrystals are chalcopyrite (tetragonal) $CuInS_2$ and that no other phases are produced in the reaction. EDS from fields of nanocrystals gave an average Cu:In:S composition of 0.29:0.25:0.46, which is near the target 0.25:0.25:0.5 ratio, considering the error of the EDS detector (approx. ±2 at. %) and that Cu is slightly overrepresented in the EDS spectra due to signal from the Cu sample holder. There was no compositional variation from particle to particle within the error of the EDS detector. The band gap energy determined from absorbance spectra (Figure 6.4) of optically-clear (i.e., non-scattering) dispersions of nanocrystals was found to be 1.29 eV (960 nm), which is within the range of the $CuInS_2$ band gap energy (which has been reported to lie between 1.2 and 1.5 eV) reported in literature.[3,37]

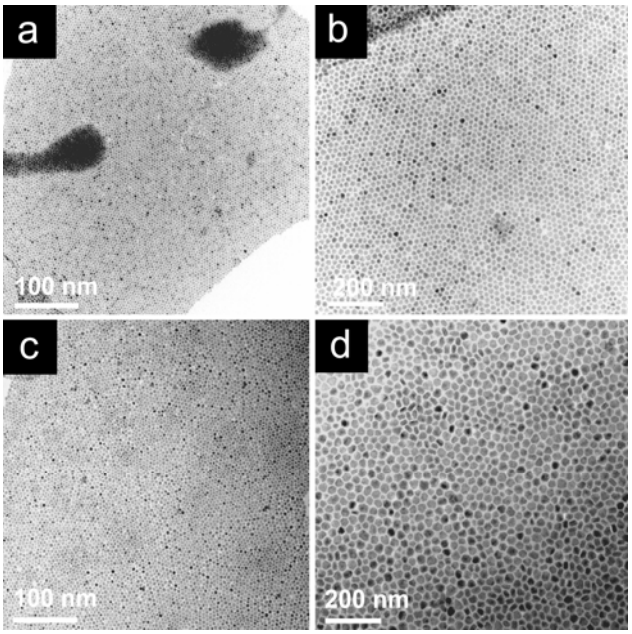

Figure 6.1: TEM images of $CuInS_2$ nanocrystals synthesized with varying OLA:(Cu+In) mole ratios: (a,b) 6:1, 8 nm diameter; (c,d) 3:1, 12 nm diameter.

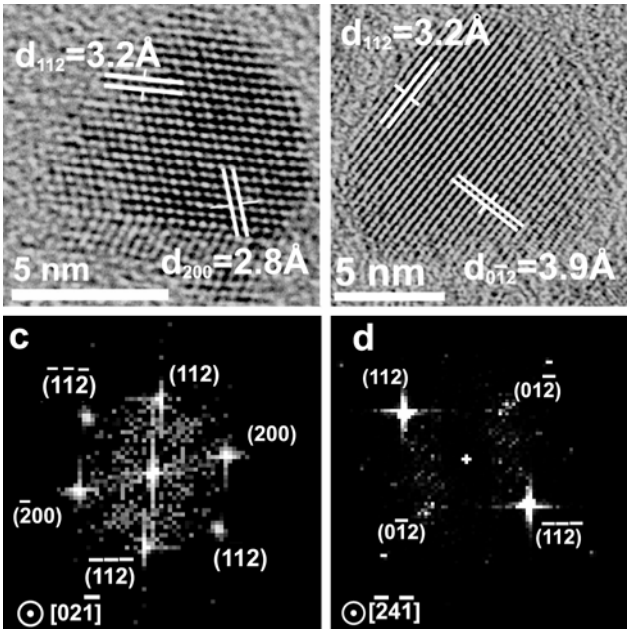

Figure 6.2: HRTEM images of a $CuInS_2$ nanocrystals (a,b) and their respective fast Fourier transforms (FFTs) (c,d). The d-spacings correspond to chalcopyrite (tetragonal) $CuInS_2$.

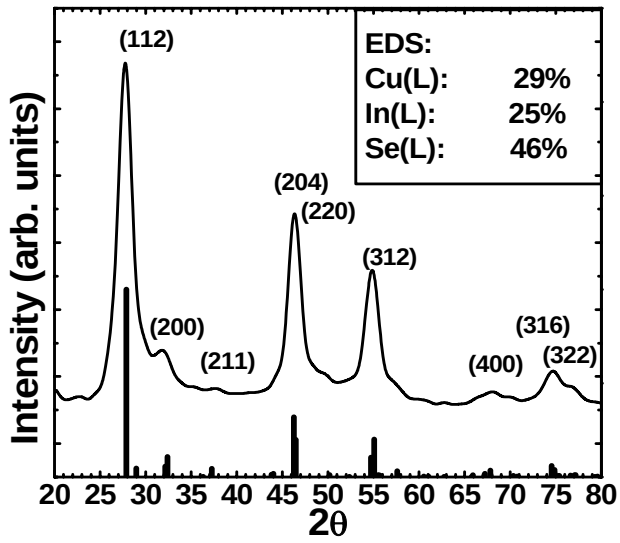

Figure 6.3: XRD and (inset) elemental composition measured by EDS of 8 nm diameter $CuInS_2$ nanocrystals. The peak labels correspond to those of chalcopyrite (tetragonal) $CuInS_2$ JCPDS#085-1575).

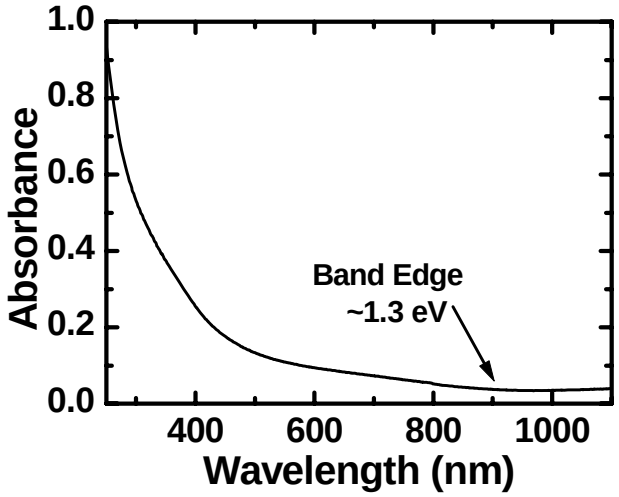

Figure 6.4: Room temperature absorbance spectrum of 8 nm diameter $CuInS_2$ nanocrystals dispersed in hexane.

6.3.2 $CuInSe_2$ Nanocrystals

6.3.2.1 Synthesized With One-Pot Method

$CuInSe_2$ nanocrystals could not be synthesized using an approach similar to $CuInS_2$ because unlike S, Se does not dissolve in dichlorobenzene. After exploring a variety of different reaction approaches, one effective route was a direct combination of Cu and In salts and solid Se in a flask with oleylamine followed by heating to 240°C for four hours (Equation (6.2)).

$$CuCl + InCl_3 + 2Se \xrightarrow[240^{o}\,C]{\text{oleylamine}} CuInSe_2 \text{ nanocrystals} + \text{byproducts} \qquad (6.2)$$

Figure 6.5 shows TEM images of a typical $CuInSe_2$ nanocrystal preparation. The nanocrystals are approximately 15 nm in diameter. Both high-resolution TEM (Figure 6.6) and XRD (Figure 6.7) confirmed that the nanocrystals are crystalline with tetragonal chalcopyrite $CuInSe_2$ structure. The *d*-spacings observed in TEM and the FFTs of the TEM images are also consistent with tetragonal $CuInSe_2$. No other crystal phases were observed in the XRD patterns of the product. Compositional analysis by ICPMS showed that the average composition of the nanocrystals in the sample has a molar Cu:In:Se ratio of 1:1:2 and the composition of individual particles measured by EDS was 1:1:2 with a variation from particle to particle less than the experimental error of approximately ±2 at.%.

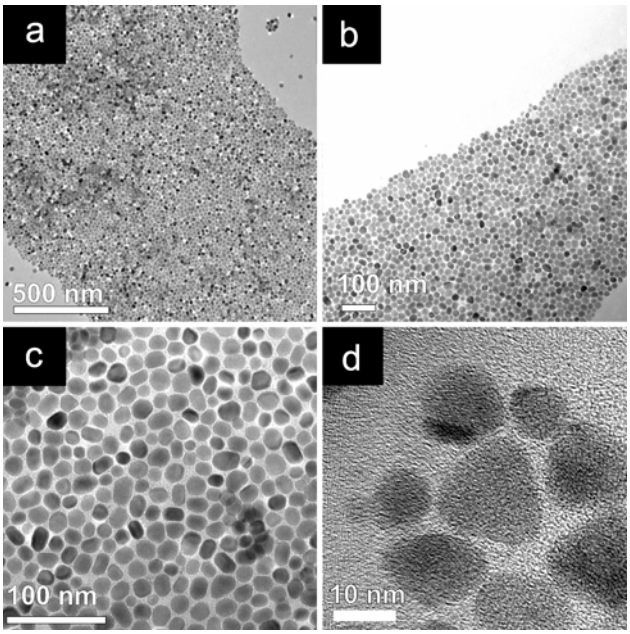

Figure 6.5: TEM images of $CuInSe_2$ nanocrystals with an average diameter of 15 nm.

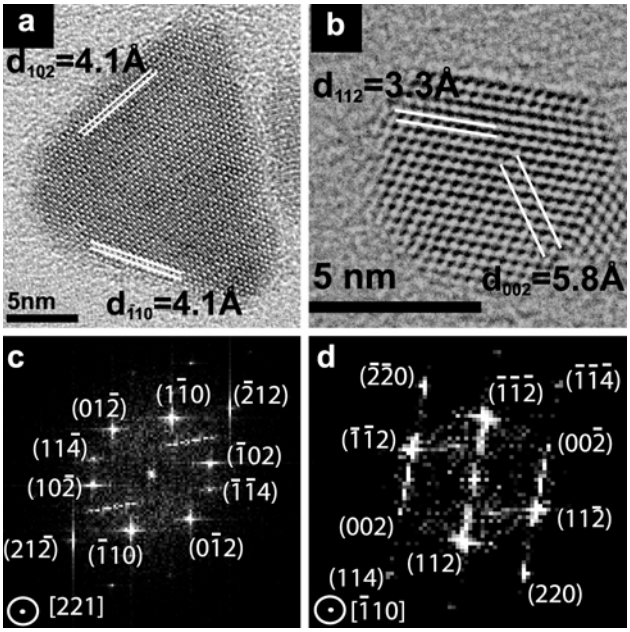

Figure 6.6: (a,b) HRTEM images of $CuInSe_2$ nanocrystals and (c,d) their FFTs. The observed d-spacings and the indexed FFTs are consistent with chalcopyrite (tetragonal) $CuInSe_2$.

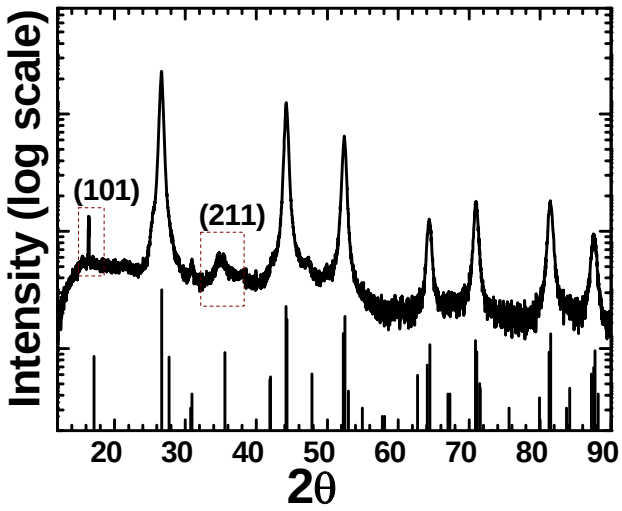

Figure 6.7: XRD pattern of chalcopyrite $CuInSe_2$ nanocrystals (JCPDS#00-040-1487). The scattering intensity is plotted on a logarithmic scale to elucidate the (211) peak. Dashed boxes indicate reflections that are unique to chalcopyrite ($CuInSe_2$).

Like the $CuInS_2$ nanocrystals, the $CuInSe_2$ nanocrystals are not spherical and exhibit significant faceting. The faceting has thus far been difficult to control, but this might be addressed by the optimization of several factors, including the capping ligand chemistry and the way reactants are added to the reaction. The relatively broad size distribution of the nanocrystals (ranging from as small as 5 nm to as large as 25 nm) is largely the result of this irregularity in particle shape.

6.3.2.2 Synthesized With Hot-Injection Method

Figure 6.8 shows TEM, SEM and XRD data for the oleylamine-capped CIS nanocrystals. The nanocrystals are composed of chalcopyrite CIS with an average diameter of 12 ± 4 nm, and a slightly irregular, faceted shape. The atomic ratio of Cu:In:Se in the nanocrystals determined by EDS is nearly 1:1:2, with a tendency to be slightly Cu rich, with a Cu/(Cu+In) ratio of 52%. Using the approach reported here for

nanocrystal synthesis, it has not been possible to vary the Cu:In ratio. The nanocrystals disperse in various organic solvents, including chloroform, hexane, toluene and acetone. Toluene was used as the dispersing solvent for the nanocrystal inks used to fabricate devices, as it provided the most uniform coatings of the solvents that were tested. An SEM image of a spray-deposited 300 nm thick nanocrystal film is shown in Figure 2c. The film has uniform thickness and is nearly free of drying cracks, which is crucial for obtaining functional PVs without electrical shorts. In practice, it is very difficult to completely eliminate drying cracks, and even the film in Figure 6.8c has some observable cracks. However, much thicker films were much more prone to cracking, and films thicker than about 800 nm tended to be electrically shorted due to significant cracking during the drying of the films. Film uniformity is still one aspect of the device fabrication process that requires further optimization.

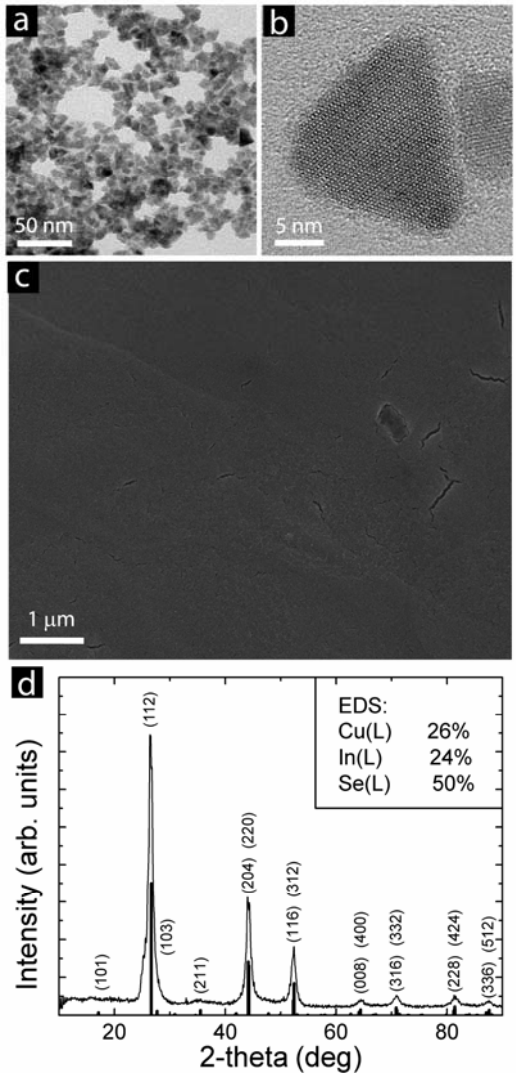

Figure 6.8: (a,b) TEM images of CIS nanocrystals; (c) an SEM image of a film of CIS nanocrystals spray-deposited from a toluene dispersion; (d) XRD pattern of CIS nanocrystals indexed to chalcopyrite CIS (PDF#97-006-8928). The inset in (d) is the average Cu, In and Se composition determined by EDS of a field of nanocrystals.

6.3.3 $Cu(In_xGa_{1-x})Se_2$ (CIGS) Nanocrystals

CIGS nanocrystals were synthesized following the approach developed for $CuInSe_2$ nanocrystals, but with the addition of $GaCl_3$ to the reaction mixture in the desired In:Ga mole ratio:

$$CuCl + xInCl_3 + (1-x)GaCl_3 + 2Se \xrightarrow[240^{o}C]{\text{oleylamine}} Cu(In_xGa_{1-x})Se_2 \text{ nanocrystals} + \text{byproducts} \quad (6.3)$$

The In:Ga ratio could be tuned across the entire stoichiometric range with x from 0 to 1 using this approach. Figure 6.11 shows TEM images of $CuIn_xGa_{1-x}Se_2$ with x ranging from 0.79 to 0. Figures 6.9 and 6.10 show XRD data of CIGS nanocrystals synthesized with Ga:In ratios varying from 0 to 1. All of the patterns are consistent with chalcopyrite (tetragonal) crystal structure and exhibit the expected amount of peak broadening due to their nanoscale crystal domain size. The diffraction peaks shift to higher 2θ with increasing Ga content, due to the decreased lattice spacing with smaller Ga atoms substituting for larger In atoms. The In:Ga ratio of the nanocrystals determined by ICPMS and EDS were consistent with the In:Ga mole ratio in the reaction mixture. Additionally, EDS measurements on different nanocrystals on the substrate did now show any noticeable variation in Cu:In:Ga ratio from particle to particle in the sample. Table 6.1 summarizes the synthesis results. The band gap energies of the $Cu(In_xGa_{1-x})Se_2$ nanocrystals determined from room temperature absorbance spectra (Figure 6.12) ($CuInSe_2$: 0.95 eV; $CuIn_{0.56}Ga_{0.44}Se_2$: 1.14 eV; $CuGaSe_2$: 1.51 eV) of nanocrystal dispersions were also consistent with energies of the corresponding bulk compounds: 0.95 eV, 1.23 eV, and 1.6 eV.[38] The only noticeable difference in the nanocrystals with varying In:Ga ratio was that nanocrystals with higher Ga content were more difficult to stabilize in solution without aggregation. Particularly the $CuGaSe_2$ nanocrystals were not easily dispersible after isolation from the reaction mixture. More effective capping approaches to Ga-rich nanocrystals are desirable.

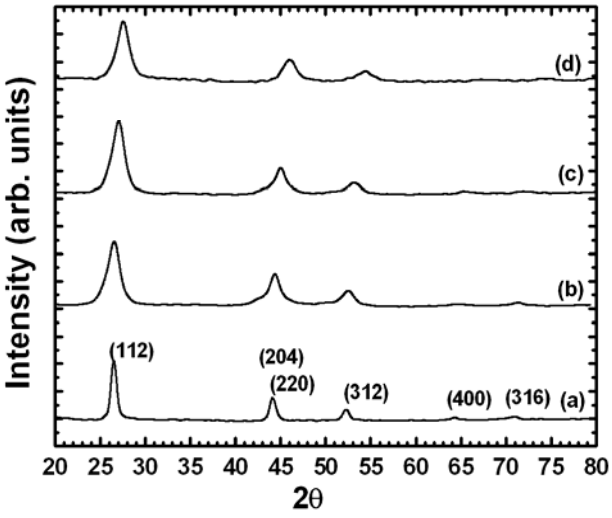

Figure 6.9: XRD patterns of CIGS nanocrystals synthesized with varying In:Ga ratios: (a) $CuInSe_2$ (b) $CuIn_{0.79}Ga_{0.21}Se_2$ (by EDS) (c) $CuIn_{0.51}Ga_{0.49}Se_2$ (by EDS) (d) $CuGaSe_2$ nanocrystals. The diffraction patterns correspond to those of the tetragonal chalcopyrite phases of the respective compounds. The indexing of the peaks noted in (a) correspond to the expected peaks positions of the chalcopyrite compounds.

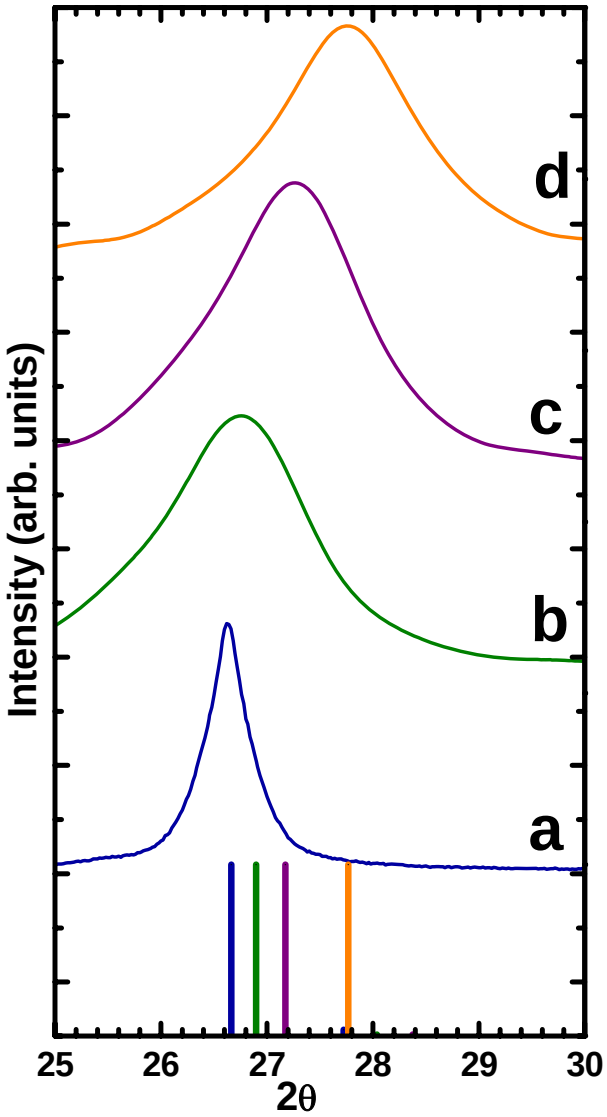

Figure 6.10: Magnification of the (112) XRD peaks from Figure 8 of the CIGS nanocrystals: (a) $CuInSe_2$ (b) $CuIn_{0.79}Ga_{0.21}Se_2$ (by EDS) (c) $CuIn_{0.51}Ga_{0.49}Se_2$ (by EDS) (d) $CuGaSe_2$ nanocrystals. The reference positions are for $CuInSe_2$ (JCPDS#00-040-1487), $CuIn_{07}Ga_{0.3}Se_2$ (JCPDS#00-035-1102), $CuIn_{0.5}Ga_{0.5}Se_2$ (JCPDS#00-040-1488), and $CuGaSe_2$ (JCPDS#00-031-0456).

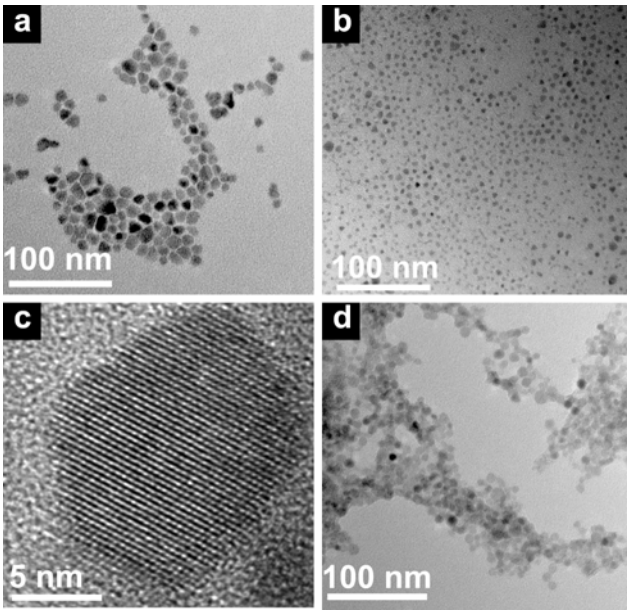

Figure 6.11: TEM images of $CuIn_xGa_{1-x}Se_2$ nanocrystals with (a) $x = 0.79$, (b) 0.56, (c) 0.21 and (d) 0.

Table 6.1: Measured CIGS nanocrystal composition.

Target Compound	Precursor Composition (at. Ratio % Cu:In:Ga:Se)	Composition measured by EDS[a] (at. Ratio % Cu:In:Ga:Se)	Composition measured by ICPMS[b] (at. Ratio % Cu:In:Ga:Se)
$CuInSe_2$	25:25:50	29:25:0:46	25:25:0:50
	(1:1:0:2)	(1.16:1.00:0:1.84)	(1:1:0:2)
$CuIn_{0.75}Ga_{0.25}Se_2$	25:19:6:50	25:18:5:52	26:15:9:50
	(1:0.76:0.24:2)	(1:0.72:0.20:2.08)	(1.04:0.60:0.36:2.00)
$CuIn_{0.50}Ga_{0.50}Se_2$	25:13:12:50	27:14:12:47	26:13:11:50
	(1:0.52:0.48:2)	(1.08:0.56:0.48:1.88)	(1.04:0.52:0.44:2.00)

[a] EDS measurements have an error of ~ ±2 at.%.
[b] ICPMS measurements have an error of ±0.1 at.% for Cu, ±0.2 at.% for In, ±0.1 at.% for Ga, ±0.5 at.% for Se

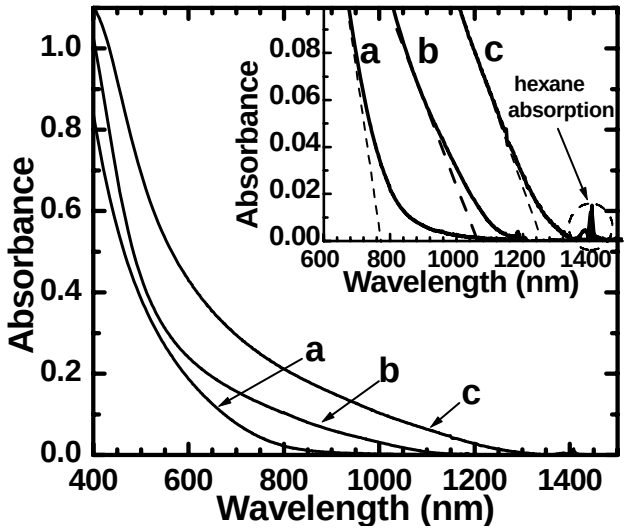

Figure 6.12: Room temperature absorbance spectra of $Cu(In_xGa_{1-x})Se_2$ nanocrystals dispersed in hexane. The curves correspond to In:Ga stoichiometries of (a) x=0, (b) x=0.56 and (c) x=1. An extrapolation of the spectra to identify the band edge is shown in the inset. The small feature at ~1400 nm is related to the absorbance of hexane.

6.3.4 Cu_2ZnSnS_4 (CZTS) Nanocrystals

Cu_2ZnSnS_4 (CZTS) is another promising new material for photovoltaics.[39,40] Its crystal structure and optical properties (~1.5 eV band gap energy; absorption coefficient of ~10^4 cm^{-1}) are similar to $Cu(In,Ga)Se_2$ (CIGS), but unlike CIGS, which requires relatively rare In and Ga, CZTS is composed of abundant elements.[39,40] Figure 6.13 shows transmission electron microscopy (TEM) and scanning electron microscopy (SEM) images of a typical CZTS nanocrystal sample. The particles are crystalline and have an average diameter of 10.6 ± 2.9 nm, with slightly irregular, faceted shape.

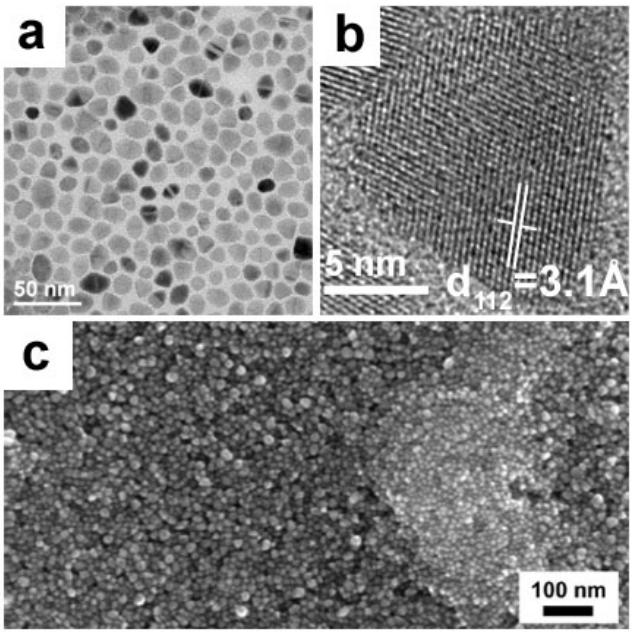

Figure 6.13: (a,b) TEM and (c) SEM images of CZTS nanocrystals. In (b), the nanocrystal is imaged down the [-1 1 0] crystallographic zone axis.

The average composition of the nanocrystals determined by energy dispersive X-ray spectroscopy (EDS) analysis of 225 nanocrystals was $Cu_{2.08}Zn_{1.01}Sn_{1.20}S_{3.70}$. The nanocrystals are slightly tin-rich and sulfur-deficient. Scanning transmission electron microscopy (STEM)-EDS elemental mapping of a field of nanocrystals (Figure 6.14) confirmed that Cu, Zn, Sn and S are evenly distributed among the nanocrystals and that there is no noticeable compositional distribution between the nanocrystals. The band gap energy determined from absorbance spectra of a nanocrystal dispersion (Figure 6.16, inset) is 1.3 eV, which is close to the bulk literature value of ~1.5 eV for CZTS.[19]

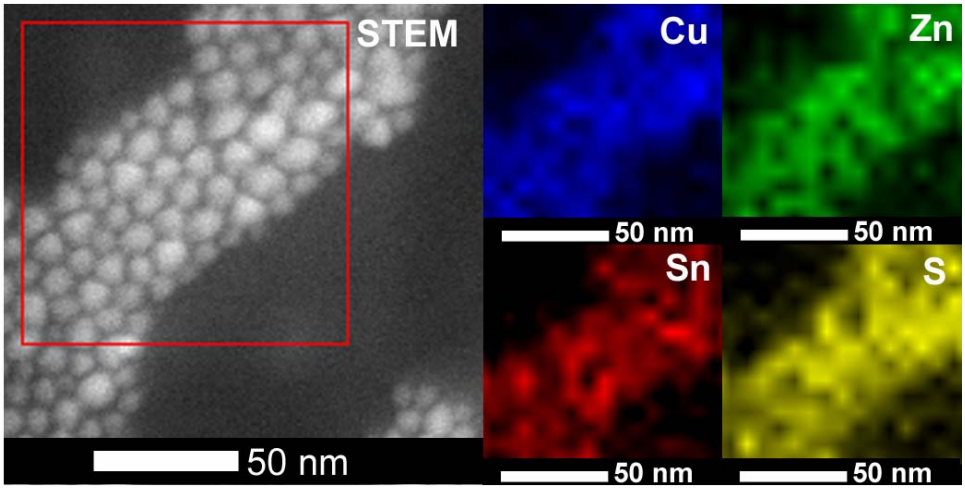

Figure 6.14: STEM-EDS elemental map of CZTS nanocrystals.

XRD (Figure 6.15) showed that the nanocrystals are composed of CZTS with kesterite structure.[41,42] Kesterite has a tetragonal unit cell, with sulfur atoms located in a face-center cubic sublattice. The Cu, Zn and Sn atoms occupy half the tetrahedral interstitial sites within the S sublattice, with compositional order.[41] Similar to chalcopyrite CIGS, kesterite CZTS exhibits diffraction peaks in addition to those observed from the compositionally disordered sphalerite compound, such as the (101) and (211) peaks.[41,43]

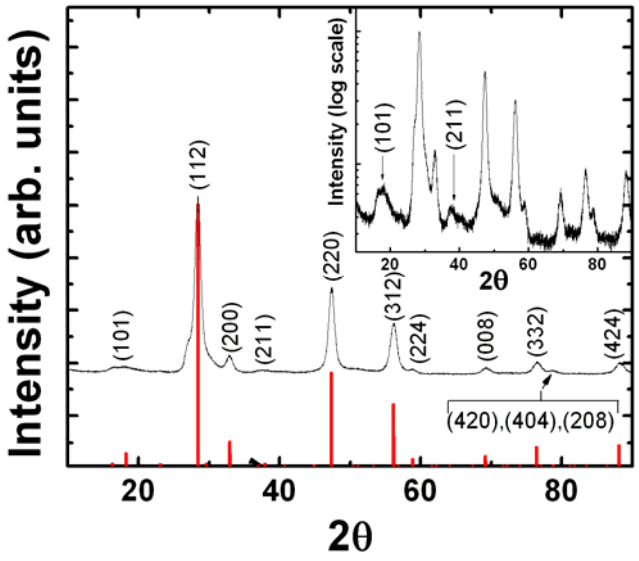

Figure 6.15: .XRD of CZTS nanocrystals. The red reference pattern was simulated using CaRIne Crystallography 3.1 software using space group I4 and lattice parameters a=b=5.427 Å and c=10.848 Å for kesterite CZTS (JCPDS #26-0575)

PV devices were fabricated with the CZTS nanocrystals. Like CIGS, CZTS films are typically p-type,[40] and test devices were fabricated with a layered structure composed of Au/CZTS/CdS/ZnO/indium tin oxide (ITO). The CZTS layer was deposited by spray coating of toluene dispersion. The nanocrystal layer was not annealed. Figure 6.16 shows the PV response of a typical device, having an open circuit voltage (V_{OC}) of 321 mV, a short circuit current density (J_{SC}) of 1.95 mA/cm^2, fill factor (FF) of 0.37, and a power conversion efficiency η, was 0.23% under AM 1.5 conditions.

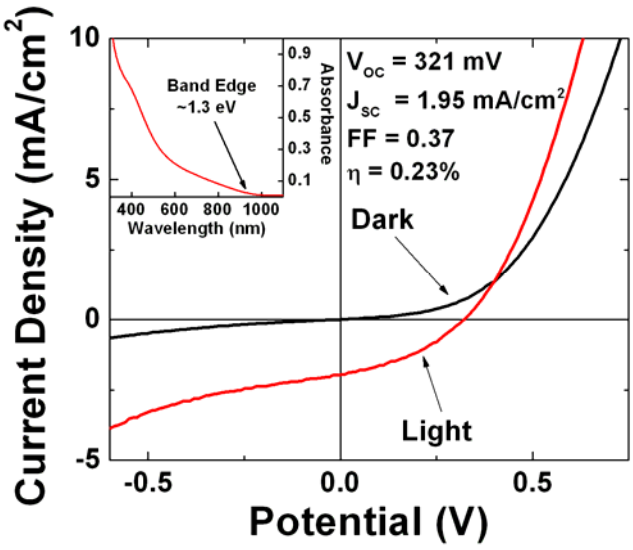

Figure 6.16: Current-Voltage characteristics of a CZTS nanocrystal PV device. (Inset) Room temperature UV-vis-NIR absorbance spectrum of CZTS nanocrystals dispersed in toluene.

While the efficiency of these devices is relatively low, the absorber layers were not processed after deposition with any high temperature or chemical means. Further optimization of the synthesis and device fabrication should lead to increases in PV efficiency.

6.3.5 Photovoltaic Devices From Drop-Cast $CuInSe_2$ Nanocrystal Films

As a proof-of-concept, films of OLA-coated 15 nm $CuInSe_2$ nanocrystals were tested as the absorber layer in PV devices fabricated with a conventional layered Mo/$CuInSe_2$/CdS/ZnO/ITO configuration. Figure 6.17 shows the device configuration. Typical PV devices require relatively thick absorber layers (>1 μm) and therefore a strategy was first developed to deposit uniform, crack-free nanocrystal films.

Dip-coating worked well to deposit uniform, crack-free nanocrystal films, but only up to a maximum thickness of ~300 nm. The maximum film thickness of ~300 nm appeared to be related to the thickness of the fluid layer that formed on the vertically

dipped substrate as it was pulled from the solvent. Multiple dipping steps could not improve the film thickness either as it appeared that previously deposited nanocrystals would redisperse as a new layer of particles was deposited. This fluid layer thickness depends on the substrate wettability and the dispersion viscosity and perhaps could be further improved with more study.

Uniform nanocrystal films in the appropriate thickness range could be formed by drop-casting from dispersions in high boiling point organic solvents. Nanocrystal films as thick as 3 μm could be deposited by drop-casting from concentrated TCE dispersions and the film thickness could be controlled by varying the nanocrystal concentration in the dispersions as shown in Figure 6.17. Figure 6.18 shows pictures of a TCE dispersion of $CuInSe_2$ nanocrystals and the deposition process used to make multiple films of $CuInSe_2$ nanocrystals on 12 mm X 25 mm soda-lime glass or Mo-coated glass substrates.

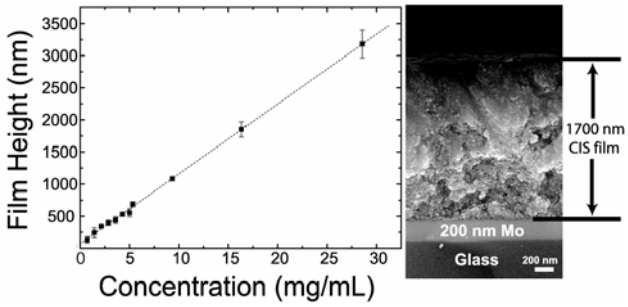

Figure 6.17: The thickness determined by profilometry of $CuInSe_2$ nanocrystal films drop-cast from TCE dispersions with different concentrations. The SEM image shows a cross-section of a 1.7 μm thick nanocrystal film on Mo-coated soda lime glass.

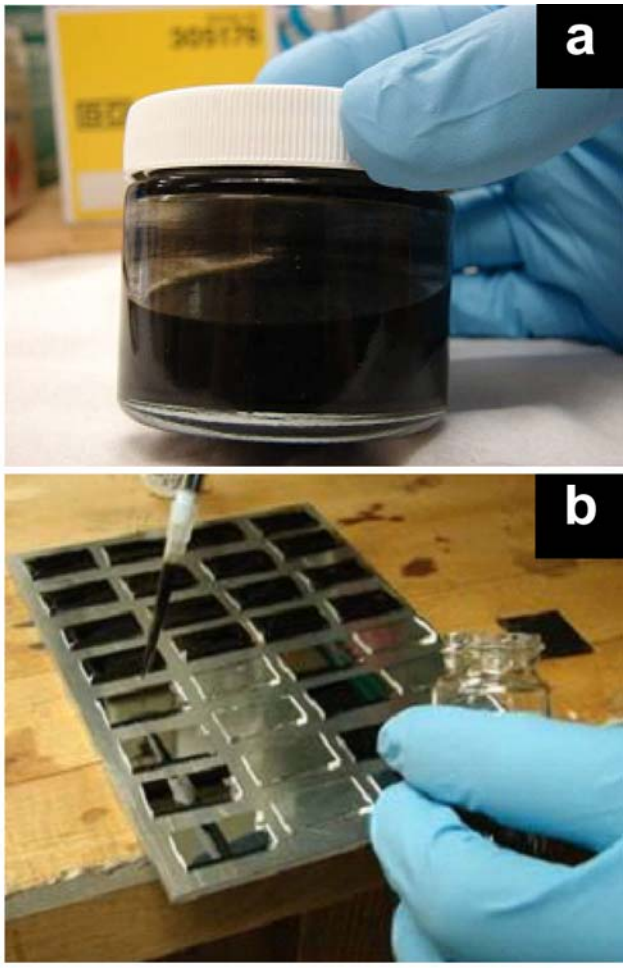

Figure 6.18: Photograph of (a) a $CuInSe_2$ nanocrystal dispersion and (b) the deposition of thin films on an array of glass substrates. After depositing the films, the substrates were placed in a vacuum oven at room temperature for 12 hours.

The current-voltage characteristics and the incident photon conversion efficiency (IPCE) of a typical PV device made with $CuInSe_2$ nanocrystals are shown in Figure 6.19. The measured power conversion efficiencies (η) of 32 devices ranged in value from 0.01 to 0.24%. The IPCE matches approximately the absorbance spectra of the $CuInSe_2$ nanocrystals (Figure 6.19b), confirming that the device response results from the nanocrystals. The relatively high IPCE of ~9% for wavelengths between 400 and 500 nm tails off at higher wavelengths. The long-wavelength IPCE cutoff at ~1050 nm

corresponds approximately to the optical gap of the $CuInSe_2$ nanocrystals as it should and the sharp drop in IPCE at wavelengths <400 nm is the result of ZnO light absorption—the ZnO layer is essentially serving as a photon cutoff filter in the device.

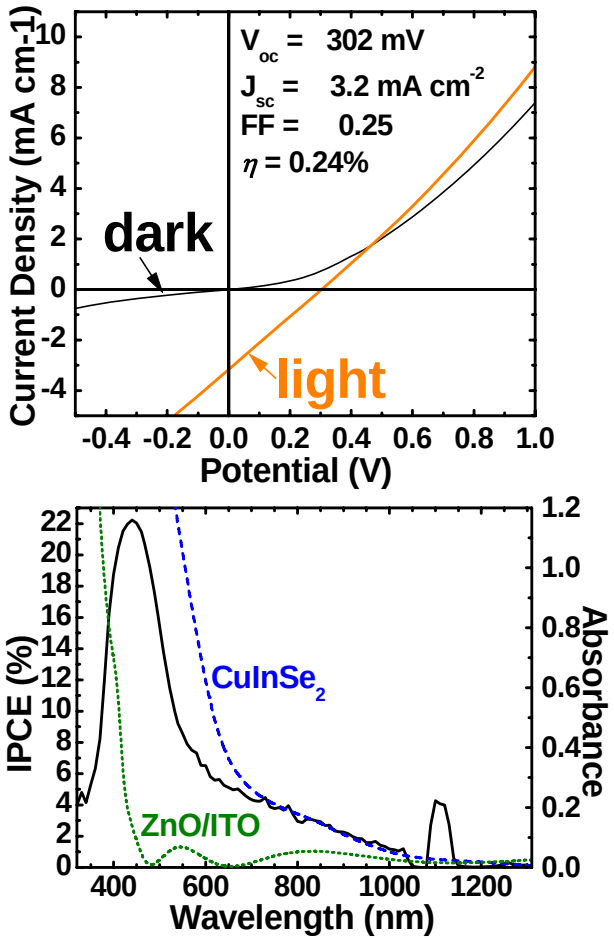

Figure 6.19: (a) Current-voltage characteristics and (b) IPCE spectra of a $CuInSe_2$ nanocrystal photovoltaic device (solid line) with absorbance curves of $CuInSe_2$ and ITO/ZnO layers (dashed). The IPCE spectrum was measured at zero bias. The nanocrystal absorber layer was 700 nm thick, consisting of oleylamine-capped $CuInSe_2$ nanocrystals with an average diameter of 15 nm. The measured short circuit current density in (a) corresponded to within a few percent of the integrated IPCE spectra in (b) multiplied by the AM 1.5 solar spectrum (i.e., the total number of photons converted to electrons by the device) as it should.

The photovoltaic response of devices made from $CuInSe_2$ nanocrystal layers was reproducible and demonstrated that these nanocrystals have potential as light absorbing materials in PVs. However, the PV efficiencies in these particular devices are relatively low and require significant improvement for practical applications. Device efficiencies might be improved increasing the $CuInSe_2$ film thickness to absorb more photons and the device structures themselves are relatively complicated with many factors that can decrease efficiency. The open circuit voltages (V_{oc}) of the $CuInSe_2$ nanocrystal devices were actually quite reasonable, typically near 300 mV, which is getting close to the high-efficiency vapor-deposited $CuInSe_2$ devices (typical V_{oc} values are ~400 mV).[44] The short circuit current densities (J_{sc}) and fill factors (FF), however, were quite low, with typical J_{sc} values of ~3 mA cm^{-2} (compared to J_{sc} of ~35 mA cm^{-2} for the highest efficiency (19%) vapor-deposited CIGS device)[10] and FF's close to 0.25. The diode response was also relatively poor, with an ideality factor (A) much larger than 1, revealing that the device has high series and low shunt resistances.[44] The high series resistance is partly attributed to high ITO sheet resistances (>300 Ω/□) and relatively resistive nanocrystal films—four-point probe measurements gave resistivities of approximately 1 kΩ·cm, which are about three orders of magnitude more resistive than conventional CIGS films with good photovoltaic efficiencies.[38] High shunt conductance (or low shunt resistance) in the devices can result from many factors, including holes or cracks in the nanocrystal film and penetration of the CBD CdS or sputtered ZnO layers to the back contact.

6.3.6 Photovoltaic Devices From Spray-Deposited $CuInSe_2$ Nanocrystal Films

6.3.6.1 Device Architecture Diversity

Figure 6.19 shows a cross-sectional SEM image of a PV device made by spray-depositing a CIS nanocrystal layer. The device has a similar architecture as those with the highest reported efficiency for CIGS,[3] consisting of layers of glass/Mo/CIS(nc)/CdS/ZnO/ITO. No high temperature annealing or selenization of this device was carried out. This particular device had a power conversion efficiency under AM 1.5 simulated sunlight of 1.18%.

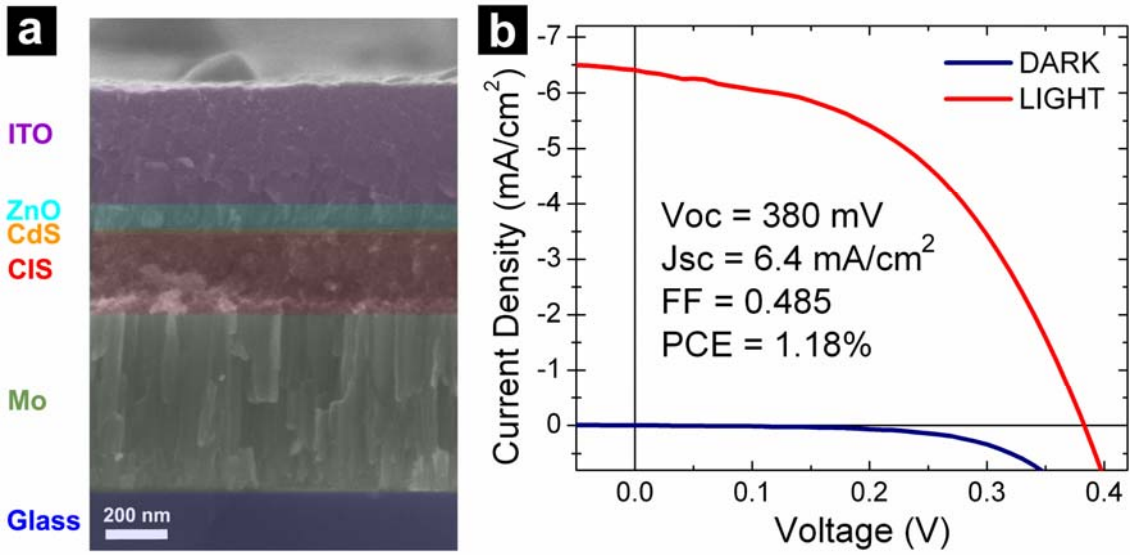

Figure 6.19: (a) SEM image of a cross-section of the PV device built using the conventional device architecture with spray coated CIS nanoparticle layer in place of vapor deposited CIS layer and (b) the I-V characteristics and power conversion efficiency of a typical PV device with this structure.

Since the absorber layers are not processed at high temperature, alternative substrates and contacts can be used, including transparent conductive ITO or mechanically flexible plastic. Figure 6.21 shows photographs of different kinds of PV

devices that could be prepared by spray-depositing CIS nanocrystal absorber layers. The devices generally consist of a sandwiched construction of the p-type light-absorbing nanocrystal layer interfaced with an n-type semiconductor (CdS, ZnO) positioned between two planar conducting contacts. The thin CdS layer (5-10 nm) also helps protect the CIS nanocrystal layer during sputtering of the window layer.

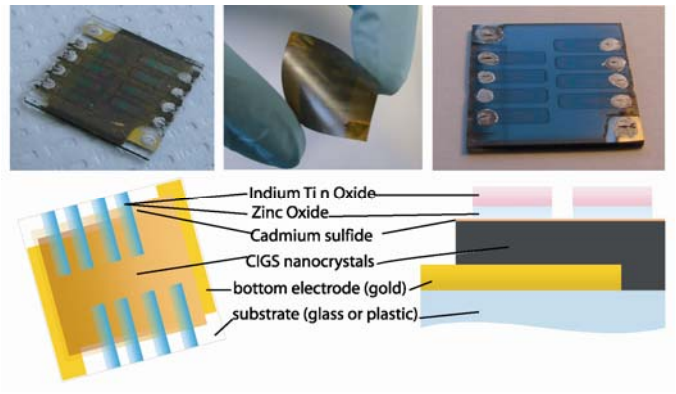

Figure 6.21: (Top) Photographs of PVs fabricated by spray depositing CIS nanocrystals on various substrates: (top left and right) glass and (top, middle) plastic (kapton). (Bottom) Illustration of the device layer structure as viewed from the top and from the side.

Conventional vapor-deposited CIGS PVs are fabricated on soda lime glass substrates with Mo back contacts because it can withstand the high selenization/annealing temperatures used to process the CIGS layer. The work function of Mo, however, is not well suited for the devices, as it creates a Schottky barrier with the CIS layer. During the selenization process, a thin $MoSe_2$ layer is created that provides ohmic contact to the CIGS layer, so this is not a problem.[45] However, without annealing, the Schottky barrier between Mo and CIS significantly limits device performance.

Gold (Au) has a higher work function than Mo and should make a better back contact metal for the p-type CIS nanocrystal layer. Au is not used in conventional CIGS

PVs because it cannot withstand the high temperature annealing conditions. We have found that CIS nanocrystal PVs made with Au contacts on glass outperform those made with Mo contacts. Au contacts are also easy to deposit on plastic substrates for flexible devices. Figure 6.22 shows device characteristics of PV devices made from spray-deposited CIS nanocrystal layers on Au contacts on (6.22a) glass and (6.22b) plastic substrates.

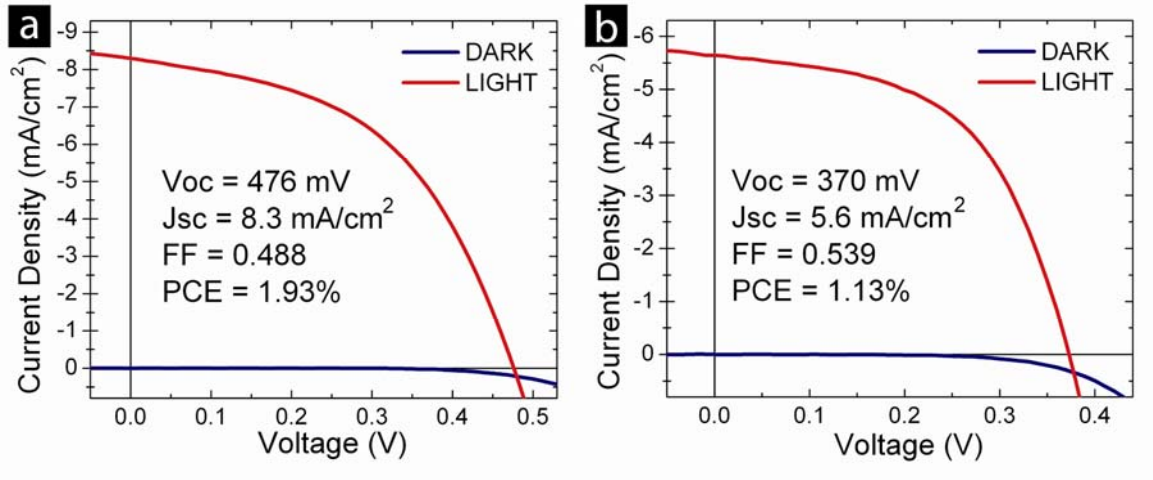

Figure 6.22: I-V characteristics of spray-deposited CIS nanocrystal PVs with gold back contacts on (a) soda lime glass and (b) plastic (kapton). The power conversion efficiencies (PCE) were measured under AM1.5 illumination.

6.3.6.2 Influence of CIS Layer Thickness on Device Efficiency

The relatively modest power conversion efficiency (up to 2% PCE under AM1.5 illumination) of the nanocrystal-based PVs is primarily related to the lower short circuit current (J_{sc}) compared to the conventional vapor-deposited devices. Vapor-deposited CIS layers are capable of producing J_{sc} in excess of 40 mA/cm^2;[10] whereas, we have not been able to achieve J_{sc} values greater than 10 mA/cm^2 from the CIS nanocrystal PVs. Interestingly, the nanocrystal PVs with the highest J_{sc} have been made with relatively thin

absorber layers that are less than 200 nm thick—far too thin to absorb all of the incident light. Incomplete absorption of the incident light leads to losses in the power conversion efficiency. Devices made with thicker nanocrystal layers absorb more light, but do not have improved efficiency. Figure 6.23 summarizes performance data for devices made with varying nanocrystal layer thickness, showing the trends in power conversion efficiency with nanocrystal layer thickness.

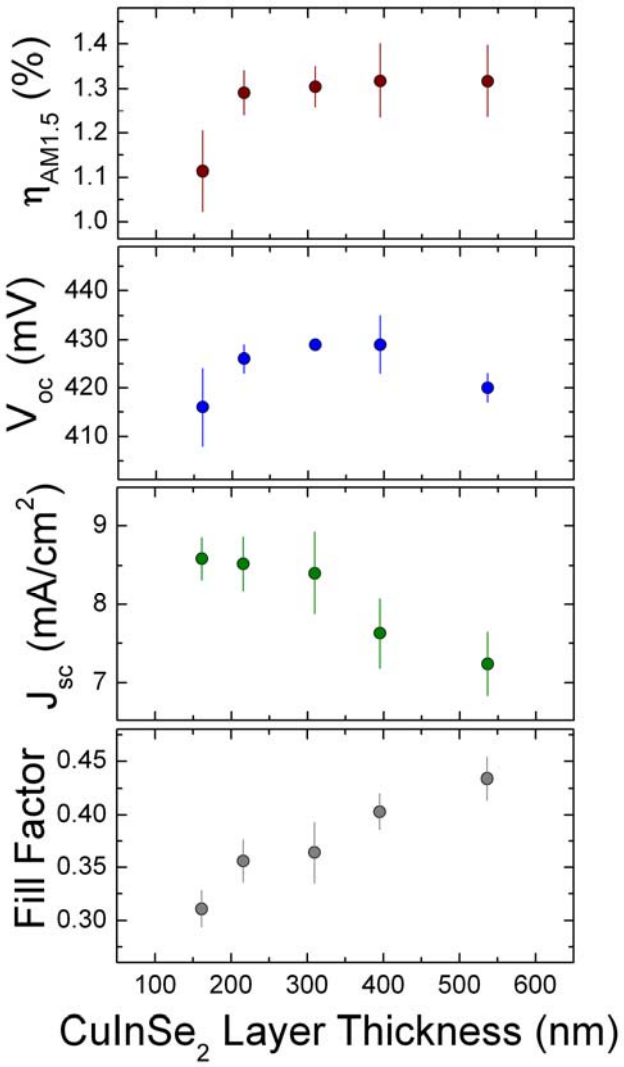

Figure 6.23: Device characteristics measured for PVs made with spray-deposited CIS nanocrystal layers of varying thickness. $\eta_{AM1.5}$ is the PCE under AM1.5 illumination, V_{OC} is the open circuit voltage, and J_{SC} is the short circuit current density.

Figure 6.24a shows the optical absorbance spectra for a 200 nm thick CIS nanocrystal film. The layer absorbs only a limited fraction of incident light, especially at the longer wavelengths near the band edge. It is also worth noting that the optical absorption of the nanocrystal layer is weaker than a dense CIS film due to the presence of

the ligands—approximately 30% of the volume in the film is occupied by ligands, which only absorb very short wavelength blue and UV light. Devices made with thicker nanocrystal films absorb proportionally more light, but do not perform better. In fact, J_{sc} was found to decrease with increasing CIS film thickness, as shown in Figure 6.24. This means that the nanocrystal films have a high charge carrier trap density with significant electron-hole recombination that lead to losses in efficiency.

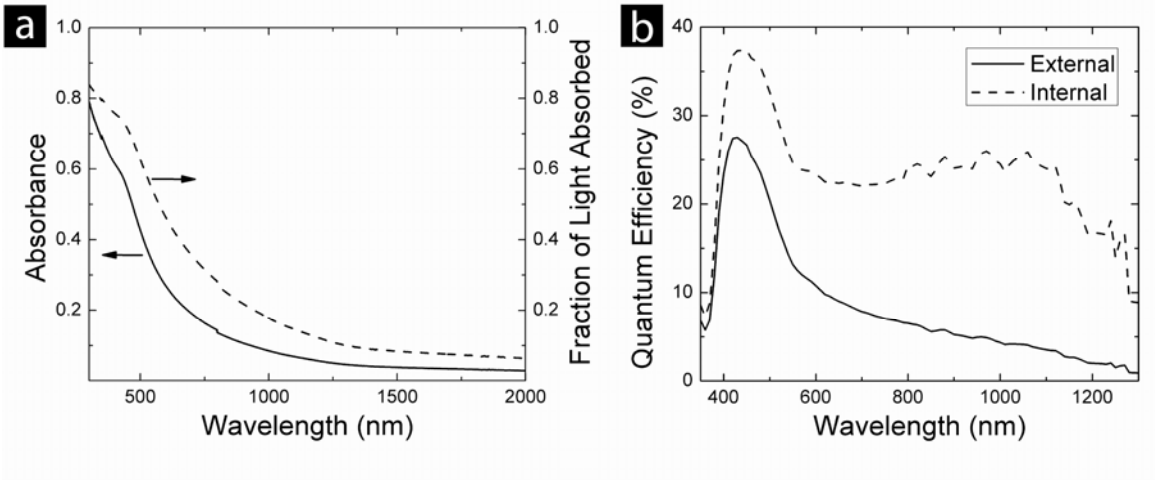

Figure 6.24: (a) UV-vis-NIR absorbance spectra of a 200 nm thick CIS nanoparticle film on a quartz substrate and the corresponding fraction of incident light that is absorbed. (b) External and internal quantum efficiency (EQE and IQE) of a PV device made with a spray-deposited CIS nanocrystal layer. EQE is determined from the incident photon conversion efficiency (IPCE) spectra, which is a measure of short circuit current as a function of light wavelength. The IQE is then determined from the EQE by accounting for the fraction of light that is absorbed by the CIS layer at each wavelength (i.e., the absorbance spectra). It should be noted that these IQE calculations do not account for additional absorption in the active layer that might occur due to internal reflections within the device, and the absorbance of light by CdS at wavelengths of 500 nm and less are also not accounted for in the IQE calculation.

Figure 6.24b shows the external and internal quantum efficiencies of a CIS nanocrystal device as a function of photon wavelength. The external quantum efficiency (EQE)—also known as incident photon conversion efficiency (IPCE) spectra—are determined by measuring the short circuit current (at zero bias) when the device is illuminated with varying photon wavelength. The EQE are not equivalent to power conversion efficiencies, but nonetheless provide revealing data about internal losses due to electron-hole recombination. The EQE is lowest near the CIS optical gap due to low light absorption, but extends across all visible wavelengths, indicating that the devices are functioning via light absorption by the nanocrystals.

Another way to examine the losses in the device due to electron-hole recombination is to calculate the internal quantum efficiency (IQE). The IQE is obtained by normalizing the EQE with the optical absorption in the nanocrystal layer and does not depend on how much light the layer absorbs. The devices made with thin nanocrystal layers had reasonably high values of IQE, of about 25% across the visible spectrum. The peak in IQE at about 450 nm is related to light absorption by the CdS buffer layer. Clearly, the PCE of the nanocrystal devices could be significantly improved if losses due to recombination could be reduced. Perhaps this could be accomplished by improving capping ligand passivation of traps on the nanocrystal surfaces and by reducing the energy barrier to interparticle charge transport with thinner ligand layers.

6.3.6.3 Improved Efficiency by Device Stacking

One other way to improve overall PCE, given the significant amount of recombination in the device is to stack multiple devices with thin absorber layers and transparent contacts to combine the efficiency of each device layer. Figure 6.25 shows the device characteristics of a spray-deposited CIS nanocrystal PV with ITO back

contacts. Such a device configuration is not possible with conventional vapor deposition due to the high temperature annealing and selenization. The CIS nanocrystal layer in this device absorbs less than 50% of the AM1.5 solar spectrum (Figure 6.25b).

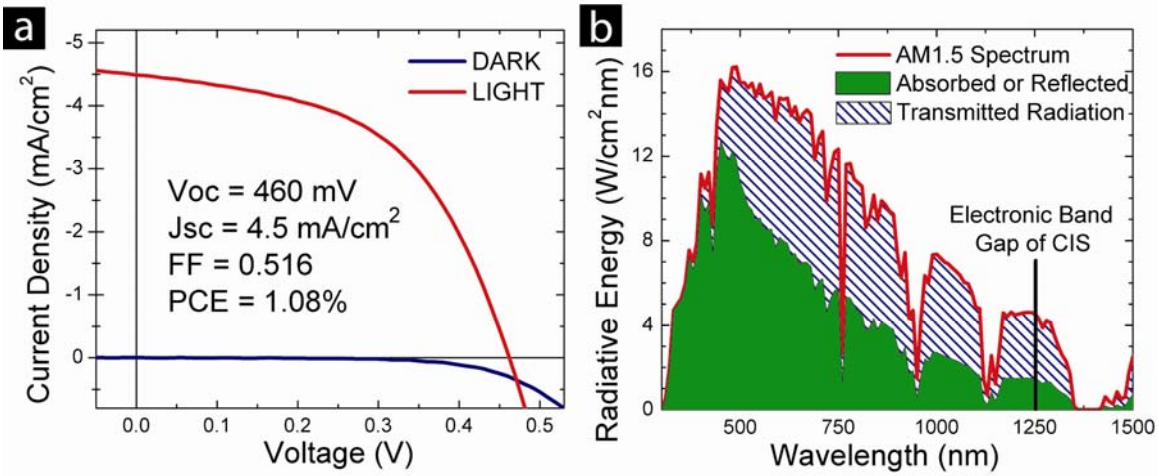

Figure 6.25: (a) I-V characteristics of a device prepared with a transparent ITO back contact, and (b) the fraction of the incident light absorbed and transmitted by the device on ITO determined from the UV-vis absorbance spectra of the device.

Figure 6.26 shows the device performance of stacked PV structures with two and three junctions compared to a single junction device. The stacked devices have enhanced J_{sc}. For example, the triple-stacked, spray-deposited CIS nanocrystal PV device had a 70% improvement in J_{sc} compared to a single junction device. However, in these particular devices, V_{oc} and the fill factor also decreased when the devices were stacked, reducing the gains in enhanced J_{sc} enough that the PCE did not increase. Nonetheless, stacked devices could be made that also exhibited higher PCE. Figure 6.27 shows a stacked PV device with significantly enhanced PCE compared to the single junction devices. This device was made by layering a semi-transparent device with ITO top and bottom contacts over a device with an ITO top contact and a Au bottom contact, which

yielded a power conversion efficiency of 2.1% under AM 1.5 simulated sunlight. Table 6.2 summarizes the device parameters for the two different stacked PV structures. Combining the Au back contact junction with an ITO back contact junction resulted in 20% improvement in PCE over the single junction devices (Figure 6.27).

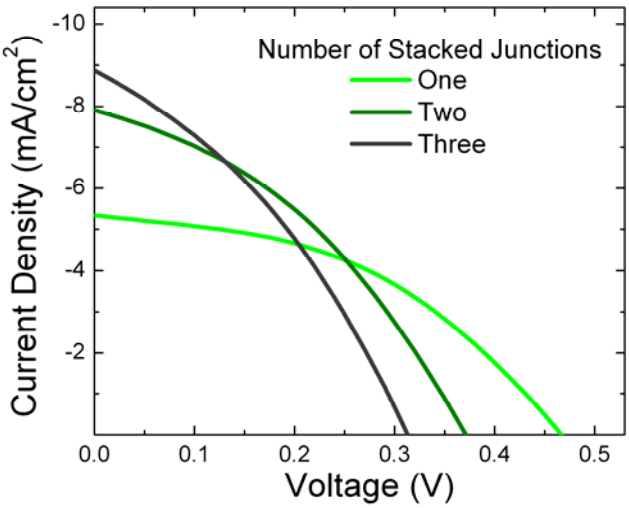

Figure 6.26: I-V characteristics of nearly transparent devices prepared with ITO back and top contacts placed in a stacked device configuration.

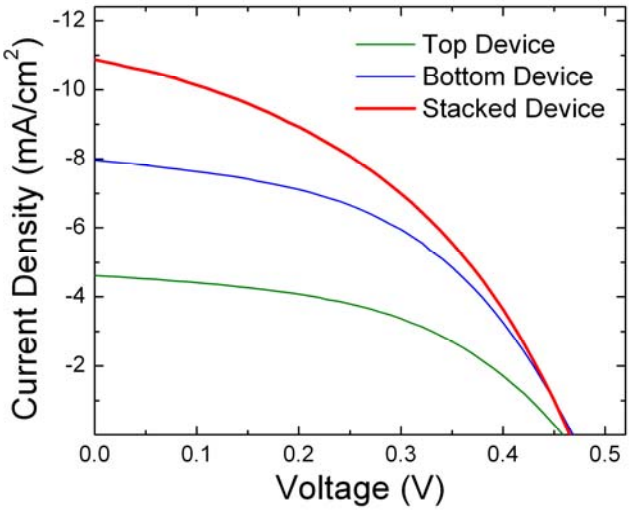

Figure 6.27: I-V characteristics of two CIS nanocrystal PVs measured independently and in a stacked configuration under AM1.5 illumination.

Table 6.2: Summary of device characteristics obtained from stacked junction spray-deposited CIS nanocrystal devices with transparent back contacts.

	Multiple Transparent Junctions			Highest Efficiency Stacked Device		
	One Junction	Two Junctions	Three Junctions	Bottom Device	Top Device	Stacked Device
$\eta_{AM1.5}$	1.1%	1.11%	0.97%	1.79%	1.01%	2.10%
J_{sc} (mA/cm^2)	5.34	7.907	8.87	7.96	4.62	10.88
V_{oc} (mV)	467	371	349	468	458	465
Fill Factor	0.442	0.379	0.349	0.479	0.478	0.414

The reason that all of the gains in J_{sc} have not translated directly into higher device efficiency is that the ITO contacts have suffered from a relatively low shunt resistance. Figure 6.28 shows a comparison of the dark I-V characteristics of CIS nanocrystal devices prepared with Au and ITO back contacts. The series resistance (R_s)

and shunt resistance (R_{sh}) of the devices were estimated by fitting the data to a diode equation,

$$I = J_0 A\left(e^{\frac{V-IR_s}{nkT}} + \frac{V-IR_s}{J_0 AR_{sh}} - 1 \right). \tag{6.4}$$

A is the area, J_0 is the saturation current density under reverse bias, and *n* is the ideality factor of the device, with *k* and *T* representing Boltzmann's constant and the temperature. Devices made with Au back contacts have significantly higher shunt resistance than the devices with ITO back contacts. Lower shunt resistance leads to reduced V_{oc} and FF and power conversion efficiency and must be improved in order to realize the full benefit of stacking the semi-transparent PVs. The stacked device structure used in Figure 6.27 is an example of a structure in which the use of lower performance ITO contacts is minimized by using a Au bottom contact, which also provides a reflective back contact to help increase the total amount of light absorption by the device.

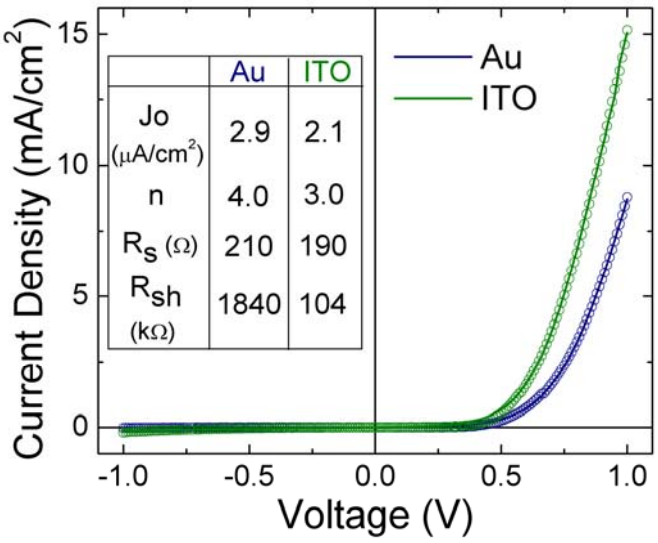

Figure 6.28: I-V characteristics of typical diodes used for the stacked structure devices that were prepared on Au and ITO back contacts. Measured data (open circles) were modeled (solid lines) using Eqn (6.4). The best fit of Eqn (6.4) to the data gives the diode parameters tabulated in the inset.

6.3.6.4 Diode Behavior in the Dark and Light

To date, the highest power conversion efficiencies from photovoltaic devices with $CuInSe_2$ nanocrystal absorber layers occur by spray-coating the $CuInSe_2$ nanocrystal ink onto Au back contacts on glass substrates. Spray-deposited nanocrystal films by spray-deposition have relatively uniform thickness with few pinholes or cracks and devices made from these films have demonstrated power conversation efficiencies under AM 1.5 illumination up to 3.1 %. Figure 6.29 shows the dark and light I-V curves for the device with highest power conversion efficiency (PCE).

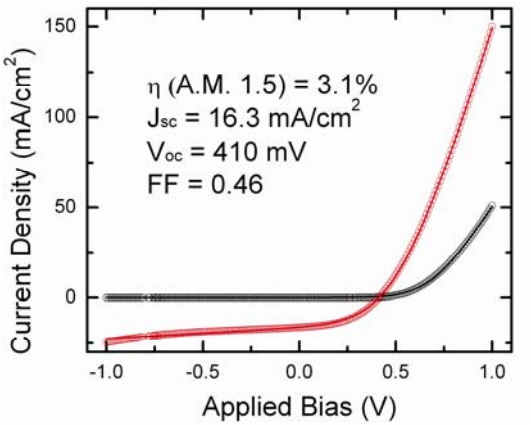

Figure 6.29: I-V characteristics of a device with power conversion efficiency of 3.1% under AM1.5 illumination. Dark conditions (black) and under AM1.5 irradiation (red). The device parameters are obtained by a best fit of Eqn (6.5) (solid lines) to the data (○). The parameters from the best fit are listed in table 1.

The device in Figure 6.29 exhibits a "crossover" between the dark and the light I-V curves at forward bias, which is commonly observed in our devices. This crossover is undesirable as it leads to a decrease in device efficiency, and ideally should be prevented. The reason for this crossover can be deduced by modeling the device current density, *J*, based on a single junction diode model:

$$J = J_0\left(e^{\frac{V-JAR_s}{nkT}} + \frac{V-JAR_s}{J_0AR_{sh}} - 1\right) - J_{ph} \qquad (6.5)$$

In Eqn (6.5), J_0 is the reverse bias saturation current density, A is the device area, n is the ideality factor of the diode, R_s is the series resistance of the diode, R_{sh} is the shunt resistance of the diode, J_{ph} is the photogenerated current density, k is Boltzmann's constant and T is temperature. Table 6.3 lists the device parameters obtained by fitting Eqn (6.5) to the device data in Figure 6.29. The large value of n, greater than 3, suggests that the devices are dominated by recombination current and illumination with light

increases the non-ideality of the diode. R_s and R_{sh} both decrease under illumination and J_0 increases by two orders of magnitude, indicating that the crossover is an outcome of photoconductivity of the materials in the device—mostly likely the CdS layer (see discussion in next paragraph). A reduction in R_s is desirable, as it lowers the barrier for current extraction, but reduced R_{sh} and increased J_0 are undesirable and result from higher recombination within the device.

Table 6.3: Diode performance parameters for the highest efficiency PVs

	Dark	AM1.5 illumination
J_0 ($\mu A/cm^2$)	3.2	200
n	3.1	3.8
R_s (Ω)	57	29
R_{sh} ($k\Omega$)	1300	2.0
J_{ph} (mA/cm^2)	---	16.5

The origin of the photoconductivity effect leading to the crossover of the light and dark curves in the devices discussed above was examined by shining light on the device with different ranges of wavelengths. The $CuInSe_2$ nanocrystals have a band gap of about 1 eV, corresponding to a wavelength of 1236 nm. ZnO and CdS have much wider band gaps of 3.3 eV and 2.4 eV, corresponding to wavelengths of 375 nm and 515 nm, respectively. Figure 6.30A shows the I-V response of the device when it was illuminated with light with the high energy photons filtered out, as shown in Figure 6.30B.

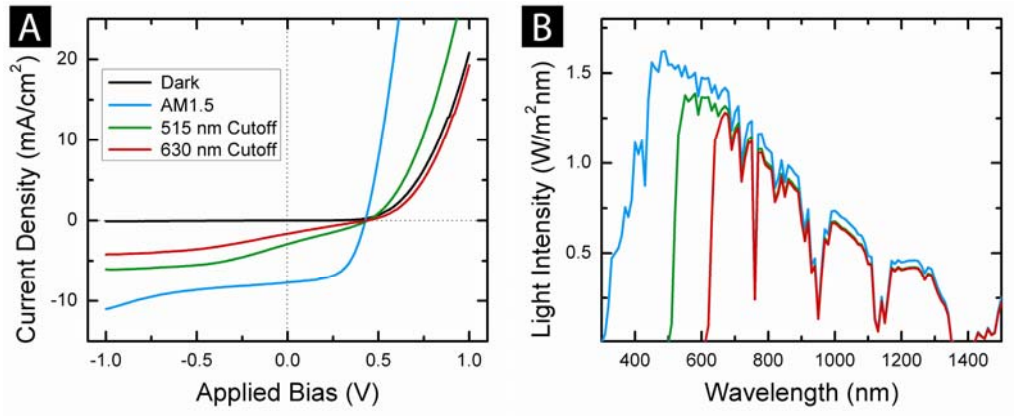

Figure 6.30: (A) I-V measurements of a $CuInSe_2$ nanocrystal PV device with a crossover between the light and the dark curves. Using light with wavelength higher than 515 nm, the crossover is still present. By using only low energy photons above 630 nm wavelength, however, the cross over between the dark and light curves is eliminated. (B) Spectra of light used for each illuminated measurement.

As shown in Figure 6.30A, the amount of crossover between the light and dark curves decreased when the shorter wavelength light was filtered, and it was completely eliminated when the illumination had wavelengths larger than the absorption edge of the CdS (515 nm) layer. Similarly, the shunt current in the reverse bias is reduced as longer wavelength light is used. These data show that it is the CdS buffer layer that leads to the high leakage current under illumination. .

Elimination of the shorter wavelength light and higher series resistance also significantly changed the fill factor of the device. The devices performed well under AM1.5 illumination, with a fill factor of 0.56. With a 515 nm cutoff filter, the fill factor decreased to 0.29, and with a 630 nm cutoff filter, it decreased to 0.24. Low fill factors in vapor-deposited $CuInSe_2$[46] have been attributed to type-I band alignment between the $CuInSe_2$ and CdS layers. Figure 6.31 shows the expected band alignment at the $CuInSe_2$/CdS/ZnO heterojunction.[45] The $CuInSe_2$ nanocrystals are p-type, and there is expected to be a "spike" in the conduction band alignment with the CdS buffer layer that

creates a barrier to electron extraction under forward bias. The CdS buffer layer has a significant concentration of low energy donors that lead to its n-type behavior. There are additional deep electron traps, however, that reduce the concentration of mobile carriers present in the n-type CdS layer. When excitons are generated in the CdS layer, the deep traps are compensated by "photo-doping",[47] which increases the number of mobile carriers, reduces the barrier to electron transport across the CdS layer and leads to an increased junction conductance (Figure 6.31).[46,48] Increased conductance is the reason for the observed crossover of the dark and light I-V curves. Additionally, as the concentration of mobile carriers in the CdS layer is increased, the Schottky barrier between the n-type CdS layer and the Au back contact is reduced, that can lead to higher leakage current through pinholes and cracks in the nanocrystal film when illuminated.

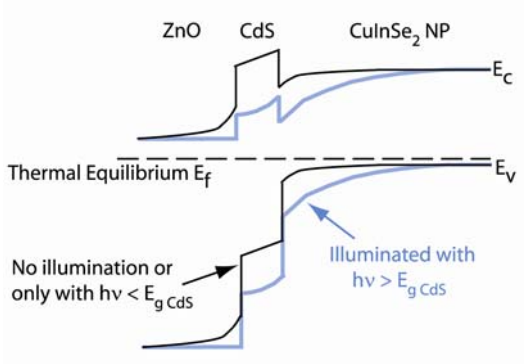

Figure 6.31: Band alignment of $CuInSe_2$/CdS/ZnO heterojunction with or without the photo-doping of the CdS buffer layer. Modified from Poduv, *et. al.* [2]

6.3.6.5 Device Performance Limitation

Device efficiencies of 3% are too low for commercialization and need to be improved.[49] The highest efficiency devices are actually composed of relatively thin nanocrystal layers that are only about 150 nm thick. We have found that increasing the nanocrystal layer thickness enhances light absorption but it does not improve device

efficiency. Figure 6.32 shows I-V characteristics of devices made with nanocrystal films of increasing thickness. J_{sc} actually decreased when the nanocrystal films were made thicker, even though more electrons and holes are being photogenerated. This indicates that the photogenerated carriers cannot be extracted from the nanocrystal layer unless they are relatively close to the junctions.

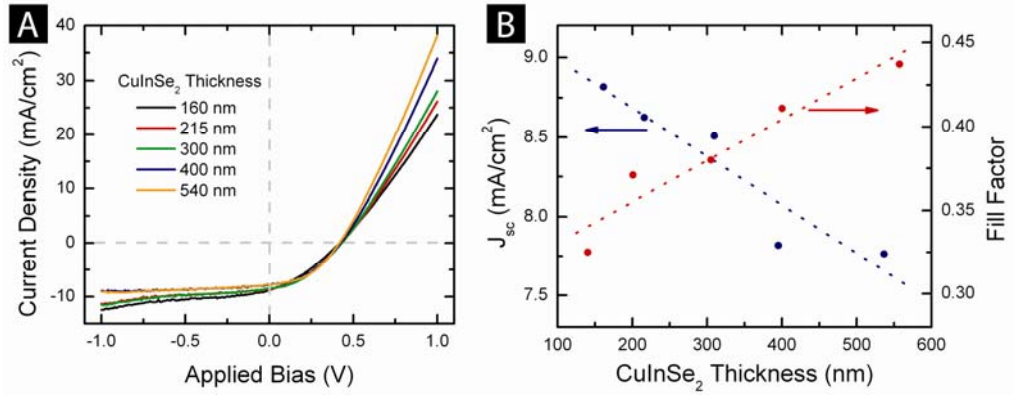

Figure 6.32: (A) I-V measurements of devices with varying thickness of spray deposited $CuInSe_2$ nanocrystal film and (B) calculated device parameters associated with these devices.

Measurements of the incident photon-to-electron conversion efficiency (IPCE) provide additional insight into how well the devices are performing and what the limiting factors are. In IPCE measurements, the short circuit current is measured as a function of the wavelength of the incident illumination. Figure 6.33 shows IPCE measurements for devices with varying nanocrystal layer thickness. The IPCE data is essentially an external quantum efficiency (at zero bias) that does not account for how much light is absorbed by the device—it is a measure of charge carriers extracted based on the number of photons that are illuminating the device. Another useful quantity is the internal quantum efficiency, which provides an accounting of the photon absorption and tells what fraction of the photogenerated carriers are actually extracted from the device.

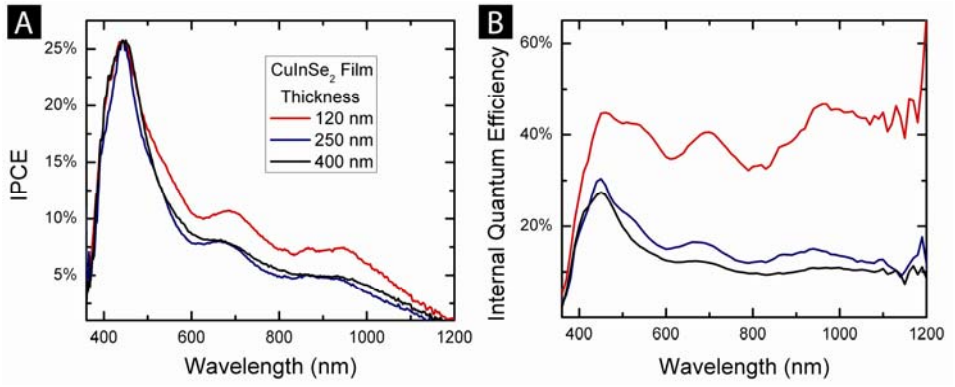

Figure 6.33: (A) IPCE measurements of a set of devices with different thicknesses of the CuInSe2 nanocrystal film thickness shows similar trend between the different thicknesses. (B) Internal quantum efficiency data of the same devices reveals how thinner devices extract photogenerated carriers at a better efficiency.

The internal quantum efficiency of the devices, *IQE(λ)*, is the ratio of the wavelength-dependent IPCE, *IPCE(λ)*, to the fraction of the incident light at that wavelength that is absorbed by the $CuInSe_2$ nanocrystal films, *f(λ)*. *f(λ)* is determined from the transmittance of the top window layer, $T_{top}(\lambda)$; the transmittance of the $CuInSe_2$ nanocrystals layer, $T_1(\lambda)$; and the reflectivity of the back contact, $R_{BC}(\lambda)$.

$$f(\lambda) \approx T_{top}(\lambda)\left[1 - T_1(\lambda)^2 R_{BC}(\lambda)\right] \tag{6.5}$$

It should be noted that this estimate of the *IQE(λ)* does not account for internal reflection or optical interference effects that may also contribute to *f(λ)* and represents an upper bound. Figure 6.33 shows the device *IQE(λ)* for devices with different nanocrystal layer thickness. Consistent with the reduced J_{sc} for devices with thicker nanocrystal films, the thinner devices have much higher IQE, indicating that they are much better at extracting photogenerated carriers, across a wide range of wavelength, than the thicker devices.

The higher IQE and more efficient device performance of the thinner devices is also enhanced by light reflection from the back contact. Especially, the thinner films benefit from a "second pass" of light reflected off the back contact. This is evident in the IPCE measurements at longer wavelegths (600 nm to 1200 nm) where only a very small fraction of the incident light is absorbed by the thinner layers on the first pass. As the films get thicker, a large fraction of the incident photons are absorbed deeper in the nanocrystals layer and the resulting photogenerated carriers are unable to be efficiently extracted. This data also indicates that the photogenerated carriers can only be extracted efficiently when they are generated close to the CuInSe2/CdS/ZnO heterojunction.

6.3.6.6 Impedance Spectroscopy

The thickness of the active region in the nanocrystal layer in the device was determined by measuring the impedance of the devices. Figure 6.34C shows typical impedance data on a $CuInSe_2$ nanocrystal PV device with slightly modified structure. The device geometry (shown in Figure 6.34A) was devised to ensure that carrier depletion was limited to the spray deposited $CuInSe_2$ film. The circuit model shown in Figure 6.34B was found to provide the best fit to the impedance data. The capacitance of the space charge region C_{sc}, was extracted to determine the majority carrier density and an effective depletion width in the nanocrystal layer using a Mott-Schottky analysis. C_{sc} is related to the doping level N_A, and applied voltage V:

$$\frac{1}{C_{sc}^{\ 2}} = \left(\frac{2}{qN_A \varepsilon_s \varepsilon_0 A^2} \right) \left(V - V_{bi} - \frac{kT}{q} \right) \tag{6.6}$$

In Eqn (6.6), V_{bi} is the built-in voltage of the junction, q is the elementary charge of an electron, ε_0 is the vacuum permittivity and ε_s is the relative permittivity of $CuInSe_2$ ($\approx$ 10). Figure 6.34D shows C_{sc}^{-2} plotted against V. Values of N_A and V_{bi} were

determined by fitting Eqn (6.6) to the data. The depletion layer width can be estimated from the relation:

$$V_{bi} = \frac{q}{2\varepsilon_s \varepsilon_0}\left[N_A x_p^{\,2} + N_D x_n^{\,2} \right] \tag{6.7}$$

N_A and N_D are acceptor and donor concentrations in the p-type and n-type layers, respectively, and x_p and x_n are the depletion layer widths of the p-type and n-type layers, respectively. With the device design shown in Figure 6.34A, depletion occurs only in the p-type nanocrystal layer, and Eqn (6.7) simplifies to

$$V_{bi} = \frac{qN_A x_p^{\,2}}{2\varepsilon_s \varepsilon_0} \tag{6.8}$$

In a typical device the depletion region thickness was found to be 55 nm in the dark. When the device was illuminated, the depletion region thickness was found to decrease to 45 nm (under AM1.5 illumination). The change in doping level in the CdS layer under light leads to a noticeable change in the device properties, as discussed above. Further work is underway to gain a more detailed understand about the band alignment between layers in the nanocrystal devices.

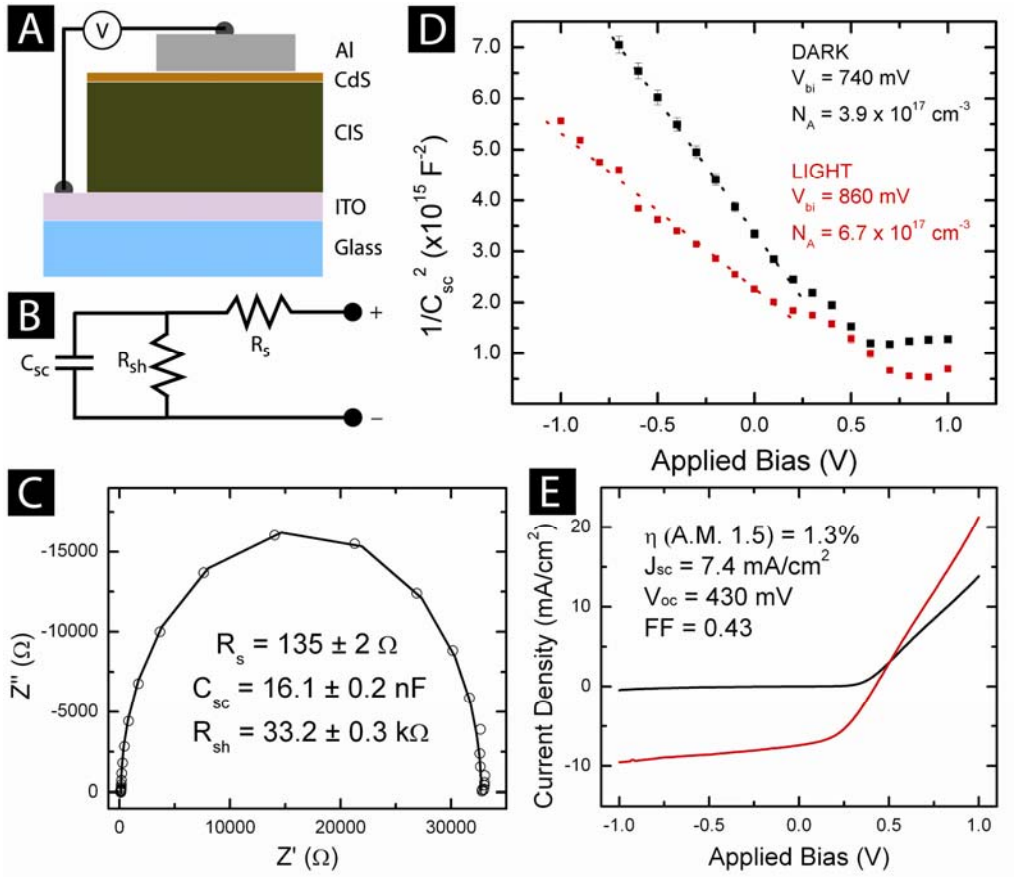

Figure 6.34: (A) Device architecture used for C-V measurements consists of a simplified junction. (B) One diode model considered for this type of junction to analyze the impedance data. (C) Sample Nyquist plot illustrating the response of the junction at a certain bias; inset provides the parameters gathered from the model fit (solid line) for the equivalent circuit to the raw data (marked by ○). (D) Linear plot of inverse square capacitance of the junction versus applied voltage across the junction, inset provides the gathered parameters based on Mott-Schottky approximation. Area of this device was isolated to 8 mm^2. (E) I-V characteristics of this junction show that it shows a very similar response to the more complex conventional devices, inset lists the device parameters.

6.4 CONCLUSIONS

Synthetic methods for producing $CuInS_2$, $CuInSe_2$, $Cu(In_xGa_{1-x})Se_2$, and Cu_2ZnSnS_4 nanocrystals by arrested precipitation in solution are described. Oleylamine was found to be an effective capping ligand for all these nanocrystals. $CuInSe_2$

nanocrystals were formulated into inks that could be spray-deposited into films. Photovoltaic devices with reproducible and reliable power output were fabricated by spray-coating $CuInSe_2$ nanocrystals without post-deposition annealing. Layered Au/CIS/CdS/ZnO/ITO devices exhibited power conversion efficiencies of up to 3.1% for single-junction devices. The device efficiency still requires significant improvement; however, it is similar to that of other nanocrystal devices that have been fabricated without post-deposition high temperature annealing. For example, Cd-containing, Pb-containing, and Cu_2S or Cu_2ZnSnS_4 nanocrystal devices have exhibited efficiencies as high as 3.6%,[15] 6%,[50-53] and 1.5%,[16,54,55] respectively. Nanocrystal-based devices in general have suffered to date from low J_{sc}. The extraction of photogenerated carriers from deep within the $CuInSe_2$ nanocrystal film remains a major challenge. The high concentration of crystal interfaces leads to high recombination. A Mott-Schottky analysis of the space-charge capacitance in the device revealed that the active region of the device is only about 50 nm thick, which is consistent with IPCE and IQE measurements on devices with varying nanocrystal film thickness. One approach to improving J_{sc} is to perform a post-deposition high temperature anneal to sinter the films and reduce the grain boundary density in the film, as Hillhouse and Agrawal have demonstrated for $CuIn_{1-x}Ga_x(S_{1-y}Se_y)_2$ PVs, in which they have achieved power conversion efficiency of more than 10%.[56,57] Stacking single-junction nanocrystal devices provides a potential route for improved light harvesting and increased J_{sc} for significantly improved power conversion efficiency without the need for high temperature annealing. For single-junction devices, future efforts must focus on increasing the thickness of the space charge region to extract carriers deeper in the nanocrystal layer in order to improve device efficiency.

A nanocrystal ink that could be used to fabricate high efficiency PVs without the need for high temperature processing would change the way PVs are made. New contact

and substrate combinations could be used, with high throughput roll-to-roll processing on lightweight, flexible plastic substrates. At the moment, however, nanocrystal-based PVs require higher efficiency. This means that a better understanding of how to passive defects and traps in the nanocrystal layers and at materials interfaces in the devices, without resorting to high temperature sintering, is needed and remains an ongoing topic of research.

6.5 REFERENCES AND NOTES

1. Miller, A.; Mackinnon, A.; Weaire, D. *Solid State Physics* **1981**, *36*, 119-175.
2. Devaney, W. E.; Chen, W. S.; Stewart, J. M.; Mickelsen, R. A. A.-M., R.A. *IEEE Trans. Electron Devices* **1990**, *37*, 428-433.
3. Scheer, R.; Walter, T.; Schock, H. W.; Fearheiley, M. L.; Lewerenz, H. J. *Appl. Phys. Lett.* **1993**, *63*, 3294-3296.
4. Guillemoles, J.-F.; Kronik, L.; Cahen, D.; Rau, U.; Jasenek, A.; Schock, H.-W. *J. Phys. Chem. B* **2000**, *104*, 4849-4862.
5. Rockett, A.; Birkmire, R. W. *J. App. Phys.* **1991**, *70*, R81-R97.
6. Contreras, Miguel A.; AbuShama, K. R., J.; =Hasoon, F.; Young, D. L.; Egaas, B.; Noufi, R. *Prog. Photovoltaics Res. Appl.* **2005**, *13*, 209-216.
7. Green, M.A.; Emery, K.; King, D.L.; Hishikawa, Y.; Warta, W. *Prog. Photovoltaics Res. Appl.* **2007**, *15*, 35-40.
8. Eberspacher, C.; Fthenakis, V. M.; Moskowitz, P. D. *25th IEEE Photovoltaic Specialist Conference, Washington, D.C., 1996*; pp 1417-1420.
9. Powalla, M.; Dimmler, B. *Thin Solid Films* **2000**, *361-362*, 540-546.
10. Repins, I.; Contreras, M. A.; Egaas, B.; DeHart, C.; Scharf, J.; Perkins, C. L.; To, B.; Noufi, R. *Prog. Photovoltaics Res. Appl.* **2008**, *16*, 235-239.
11. Contreras, M. A.; Egaas, B.; Ramanathan, K.; Hiltner, J.; Swartzlander, A.; Hasoon, F.; Noufi, R. *Prog. Photovoltaics Res. Appl.* **1999**, *7*, 311-316.
12. Schock, H.-W.; Noufi, R. *Prog. Photovoltaics Res. Appl.* **2000**, *8*, 151-160.
13. Eberspacher, C.; Pauls, K. L.; Serra, J. P. *Mat. Res. Soc. Symp. Proc.* **2003**, *763*, B8.27.21-26.

14. Kumar, A. P.; Reddy, K. V. *Thin Solid Films* **1997**, *304*, 365-370.

15. Gur, I.; Fromer, N. A.; Geier, M. L.; Alivisatos, A. P. *Science* **2005**, *310*, 462-465.

16. Wu, Y.; Wadia, C.; Ma, W.; Sadtler, B.; Alivisatos, A. P. *Nano Lett*. **2008**, *8*, 2551-2555.

17. Huynh, W. U.; Dittmer, J. J.; Alivisatos, A. P. *Science* **2002**, *295*, 2425-2427.

18. Murray, C. B.; Norris, D. J.; Bawendi, M. G. *J. Am. Chem. Soc.* **1993**, *115*, 8706-8715.

19. Micic, O. I.; Curtis, C. J.; Jones, K. M.; Sprague, J. R.; Nozik, A. J. *J. Phys. Chem.* **1994**, *98*, 4966-4969.

22. Motte, L.; Billoudet, F.; Pileni, M. P. *J. Phys. Chem.* **1995**, *99*, 16425-16429.

21. Larsen, T. H.; Sigman, M.; Ghezelbash, A.; Doty, R. C.; Korgel, B. A. *J. Am. Chem. Soc.* **2003**, *125*, 5638-5639.

22. Ghezelbash, A.; Korgel, B. A. *Langmuir* **2005**, *21*, 9451-9456.

23. Murray, C. B.; Sun, S.; Gaschler, W.; Doyle, H.; Betley, T. A.; Kagan, C. R. *IBM J. Res. Dev.* **2001**, *45*, 47.

24. Heath, J. R.; Shiang, J. J.; Alivisatos, A. P. *J. Chem. Phys.* **1994**, *101*, 1607-1615.

25. Holmes, J. D.; Ziegler, K. J.; Doty, R. C.; Pell, L. E.; Johnston, K. P.; Korgel, B. A. *J. Am. Chem. Soc.* **2001**, *123*, 3743-3748.

26. Lu, X.; Korgel, B. A.; Johnston, K. P. *Chem. Mater.* **2005**, *17*, 6479-6485.

27. Elim, H. I.; Ji, W.; Ng, M.-T.; Vittal, J. J. *Appl. Phys. Lett.* **2007**, *90*, 033106.

28. Castro, S. L.; Bailey, S. G.; Raffaelle, R. P.; Banger, K. K.; Hepp, A. F. *J. Phys. Chem. B* **2004**, *108*, 12429-12435.

29. Banger, K. K.; Jin, M. H.-C.; Harris, J. D.; Fanwick, P. E.; Hepp, A. F. *Inorg. Chem.* **2003**, *42*, 7713-7715.

30. Castro, S. L.; Bailey, S. G.; Raffaelle, R. P.; Banger, K. K.; Hepp, A. F. *Chem. Mater.* **2003**, *15*, 3142-3147.

31. E. Arici, N. S. S., D. Meissner, *Advanced Functional Materials* **2003**, *13*, 165-171.

32. Czekelius, C.; Hilgendorff, M.; Spanhel, L.; Bedja, I.; Lerch, M.; Müller, G.; Bloeck, U.; Su, D.-S.; Giersig, M. *Advanced Materials* **1999**, *11*, 643-646.

33. Eberspacher, C.; Pauls, K.; Serra, J. *28th IEEE Photovoltaic Specialist Conference, Anchorage, Alaska,* **2000**; pp 517-520.

34. Choi, S.-H.; Kim, E.-G.; Hyeon, T. *J. Am. Chem. Soc.* **2006**, *128*, 2520-2521.

35. Scofield, J. H.; Duda, A.; Albin, D.; Ballard, B. L.; Predecki, P. K. *Thin Solid Films* **1995**, *260*, 26-31.

36. McCandless, B. E. and Shafarman, W. N., U.S. Patent 6,537,845, 2003.

37. Berger, L. I. In *CRC Handbook of Chemistry and Physics*; 79 ed., 1999, pp 12-84.

38. Wei, S.-H.; Zhang, S. B.; Zunger, A. *Appl. Phys. Lett.* **1998**, *72*, 3199-3201.

39. Wadia, C.; Alivisatos, A. P.; Kammen, D. M. *Environmental Science & Technology* **2009**, *43*, 2072-2077.

40. Katagiri, H.; Jimbo, K.; Maw, W. S.; Oishi, K.; Yamazaki, M. ; Araki, H.; Takeuchi, A. *Thin Solid Films* **2009**, *517*, 2455-2460.

41. Paier, J.; Asahi, R.; Nagoya, A.; Kresse, G. *Phys. Rev. B* **2009**, *79*, 115126.

42. Stannite and kesterite CZTS have very similar structure,[41] and the presence of stannite CZTS cannot be ruled out based on the XRD data.

43. Koo, B.; Patel, R. N.; Korgel, B. A. *J. Am. Chem. Soc.* **2009**, *131*, 3134-3135.

44. van Dyk, E.E.; Meyer, E.L. *Renew. Energ.* **2004**, *29*, 333-344.

45. Rau, U. and Schock, H. W., *Appl. Phys. A,* **1999**, 69, 131–147.

46. Pudov,A. O.; Sites, J. R.; Contreras, M. A.; Nakada T. and Schock, H.–W. *Thin Solid Films* **2005**,480–481, 273–278.

47. Niemegeers, A.; Burgelman M. and De Vos, A., *Appl. Phys. Lett.* **1995**, 67 (6), 843–845.

48. Burgelman, M.; Engelhardt, F.; Guillemoles, J. F.; Herberholz, R.; Igalson, M.; Klenk, R.; Lampert, M.; Meyer, T.; Nadenau, V.; Niemegeers, A.; Parisi, J.; Rau, U.; Schock, H–W.; Schmitt, M.; Seifert, O.; Walter T. and Zott, S., *Progress in Photovoltaics: Res. And Appl.* **1997**, 5, 121–130.

49. Akhavan, V. A.; Goodfellow, B. W.; Panthani M. G. and Korgel, B. A. *Modern Energy Review* **2010**, 2, (2), 25-27.

50. Luther, J. M.; Law, M.; Beard, M. C.; Song, Q.; Reese, M. O.; Ellingson R. J. and Nozik, A. J. *Nano Lett.* **2008**, 8, 3488–3492.

51. Ma, W.; Luther, J. M.; Zheng, H.; Wu Y. and Alivisatos, A. P. *Nano Lett.* **2009**, 9, 1699–1703.

52. Koleilat, G. I.; Levina, L.; Shukla, H.; Myrskog, S. H.; Hinds, S.; Pattantyus-Abraham A. G. and Sargent, E. H. *ACS Nano* **2008**, 2,833–840.

53. Choi, J. J.; Lim, Y. F.; Santiago-Berrios, M. B.; Oh, M.; Hyun, B. R.; Sun, L.; Bartnik, A. C.; Goedhart, A.; Malliaras, G. G.; Abruna, H. D.; Wise F. W. and Hanrath, T. *Nano Lett.* **2009**, 9, 3749–3755.

54. Steinhagen, C.; Panthani, M. G.; Akhavan, V.; Goodfellow, B.; Koo B. and Korgel, B. A. *J. Am. Chem. Soc.*,**2009**, 131, 12554–12555.

55. Guo, Q.; Hillhouse H. W. and Agrawal, R. *J. Am. Chem. Soc.,* **2009**, 131, 11672–11673.

56. Guo, Q.; Ford, G. M.; Hillhouse H. W. and Agrawal, R. *Nano Lett.* **2009**, 9, 3060–3065.

57. Guo, Q.; Hillhouse H.W. and Agrawal, R. *2009 AIChE Annual Meeting*, Nashville, **2009**, 447C.

Chapter 7: Spatial Heterogeneity in $Cu(In_{1-x}Ga_x)Se_2$ (CIGS) Nanocrystal-Based Photovoltaics Mapped with Scanning Photocurrent and Fluorescence Microscopy†

7.1 INTRODUCTION

The widespread use of photovoltaic devices (PVs) to harvest energy from the sun requires significant reduction in the cost of solar cell technology.[1,2] One approach to lowering manufacturing cost is to use solution-processable materials that can be printed onto various substrates, including plastics, under ambient conditions with high throughput techniques like roll-to-roll printing.[3,4] While many soluble photovoltaic materials have been developed in recent years, the efficiency of these devices is still too low for commercial viability.[5-7] In order to improve efficiency, a more detailed understanding of PV performance is needed. One factor that can limit the performance of thin film PVs is structural, chemical and electronic heterogeneity in the device.[3,8-16] These variations can occur on the sub-micrometer length scale, thus requiring microscopic techniques that can examine functioning devices with sufficient resolution to observe these kinds of effects. Here, we present a microscopy technique, capable of studying as-fabricated PV devices, that allows local PV performance to be measured with sub-micron resolution and correlated with the optical properties of the materials. The technique is used here to examine PV devices fabricated with $Cu(In_{1-x}Ga_x)Se_2$ (CIGS) nanocrystal "inks".

Numerous microscopy techniques have been developed to study local variations in PV performance. Scanning-probe techniques, such as conductive probe atomic force

† Portions of this chapter appear in Ostrowski, David P.; Glaz, Micah S.; Goodfellow, Brian W.; Akhavan, Vahid A.; Panthani, Matthew G.; Korgel, Brian A.; Vanden Bout, David A., "Mapping Spatial Heterogeneity in $Cu(In_{1-x}Ga_x)Se_2$ Nanocrystal-Based Photovoltaics with Scanning Photocurrent and Fluorescence Microscopy." *Small* (2010), 6(24) 2832-2836.

microscopy (AFM) and kelvin force microscopy (KFM), have been used to relate morphology to local variations in properties, including photoresponse and surface potential.[9,17-25] Since these tools operate by monitoring tip-sample interaction, the measurements are localized to the region of the sample directly below the metalized cantilever. These techniques however cannot be applied to as-fabricated PV devices, and are instead useful for measuring the electrical properties of model thin films.

One way to probe the local photovoltaic response of devices, is to only illuminate small regions of a device with a microscopically focused beam of light. Only the light-induced electrical properties of the illuminated region contribute to the measured performance; this technique maps the induced photocurrent and is known as light beam induced current microscopy (LBIC).[24,26-31] The spatial resolution depends on the size of the illumination spot, which through focusing the incident light via a microscope objective can reach the diffraction limit and beyond with near-field techniques. By raster-scanning the focused light spot across the device, a map of local PV response can be generated, highlighting spatial heterogeneities in photocurrent generation present in the device.

LBIC measurements have been used primarily to test for both fabrication defects and performance quality in silicon-based PVs[27,32] and to study heterogeneity in organic bulk heterojunction PVs.[24,28-31,33] Most of these studies have utilized conventional microscopy; a few of studies achieved higher spatial resolution on the order of 200 nm utilizing near-field scanning optical microscopy.[28-30,33]

Here we report a novel approach of LBIC microscopy coupled with fluorescence microscopy that we apply to study the response of as-fabricated, functional PV devices. As this technique illuminates the PV through the transparent electrode, there is no need for constructing planar devices[33] or ones with a thin, semi-transparent metal electrode.[28-

[30] Simultaneous collection of fluorescence and PV response enables spatial correlation of the optical and electronic properties with the morphology of the device. It should also be possible to couple other optical microscopy techniques with the LBIC method, such as time-resolved fluorescence, polarized fluorescence, and absorption or reflection modes, which can yield valuable information into specific PV characteristics such as charge separation, molecular orientation, local crystallinity and absorption.[12,14-16,31] For example, LBIC coupled with Resonance Raman spectroscopy has recently been demonstrated.[31] In addition to imaging, the technique presented here is capable of collecting local voltage-dependent photocurrent data. Here, the technique is applied to a solution-processed CIGS nanocrystal-based PV device.

7.2 Experimental Section

7.2.1 Synthesis of CIGS Nanocrystal Inks

$Cu(In_{1-x}Ga_x)Se_2$ (x=0.25 targeted) nanocrystals were synthesized by arrested precipitation using standard Schlenk line techniques as previously reported.[34] The washed and purified CIGS NPs were dispersed in toluene at a concentration of 20 mg/mL to make the 'ink' used in device fabrication.

7.2.2 CIGS Nanocrystal-Based PV Device Fabrication

Polished float glass substrates with dimensions 25 x 25 x 1.1 mm (Delta Technologies, Ltd.) were cleaned by sonication in a 50/50 mixture of acetone and isopropanol followed by sonication in deionized water. Each sonication lasted 5 min and was followed by drying in a nitrogen stream. The glass substrates were then exposed to a 100 W oxygen plasma for 5 min to remove any organic residue on the surface. After cleaning, 5 nm of chromium and 60 nm of gold was thermally evaporated which served

as the metal back contact of the devices. A 600 nm CIGS nanocrystal absorber layer was then deposited by spray coating from an ink (described above) using a commercially available airbrush (iwata Eclipse HP-CS) operated at 50 psig of head pressure. A CdS buffer layer was deposited by a modified chemical bath deposition following procedures outlined by McCandless and Shafarman.[37] The device was placed on a hotplate at 90°C for 5 min after which an aqueous solution of 3 mM cadmium sulfate ($CdSO_4$, Aldrich, 99.999%), 0.53 M thiourea (Fluka, 99.999%), and 8.1 M ammonium hydroxide (NH_3, Fisher, ACS certified) was deposited onto the device which was then covered with a glass petri dish to prevent evaporation. After 2 min, the device was removed from the hotplate and rinsed with DI water and then left flat to dry. Next a window layer consisting of i-ZnO and ITO were deposited by RF sputtering. A 50 nm layer of ZnO (target 99.9%, Lesker) was first sputtered in an atmosphere of 0.5% O_2 in Ar (99.95%, Praxair) with a 150 W plasma. This was followed by a 300 nm of ITO (target 99.99% In_2O_3: SnO_2 90:10, Lesker) sputtered in an Ar atmosphere (research grade, Praxair) with a 180 W plasma. The final active area of the device was 8 mm^2 (a 4 x 2 mm rectangle). A small dab of conductive silver paint (SPI supplies) was placed on all contact pads to improve contact with the testing apparatus.

7.2.3 'Bulk' Photovoltaic Characterization

PV characterization was performed with a Keithley 2400 General Purpose Sourcemeter for current-voltage measurements using a Xenon Lamp Solar Simulator (Newport) equipped with an AM1.5 filter as an illumination source. External Quantum Efficiency (EQE) spectra were gathered using a chopper (Stanford Research Systems, model SR540), a lock-in amplifier (Stanford Research Systems, model SR830), a

monochromator (Newport Cornerstone 260 1/4M), and a Si photodiode calibrated by the manufacturer (Hamamatsu).

7.2.4 Morphological and Spectral Characterization

Scanning electron microscopy (SEM) images were acquired using a Zeiss Supra 40 VP SEM operating at 10 keV accelerating voltages and using an in-lens detector. Atomic force microcopy (AFM) images were acquired using a Digital Instruments multimode AFM (model MMAFM-2). UV-VIS spectra were collected using an Agilent 8453 UV-VIS.

7.2.5 Local Photocurrent and Fluorescence Characterization

Photocurrent and Fluorescence maps were obtained using a Coherent 408 nm diode laser as the excitation light source, which was focused through a 50x Olympus objective. The size of the focal spot was ~ 275 nm in diameter as determined by scanning across a step edge in a patterned metal film. The typical incident laser power was 1.5 μW, which yields a power density of ~ 2.53 kW/cm^2 after the light is focused through the objective. For sample scanning capabilities a Physik Instrumente (PI) piezoelectric stage (model E-501.00) was mounted onto a Nikon Diaphot 300 inverted microscope. The excitation beam was chopped at 174 Hz using a Digirad chopper (model C-980) and the photocurrent of the device was amplified 10^4 times using a transimpedance amplifier built in house. The fluorescence was collected using a Perkin Elmer APD (model SPCM-CD290) and the amplified current was collected using an EG&G DSP lock-in amplifier (model 7220). The LVPC curves were obtained by sweeping the applied voltage across the device, sourced from a serial digital to analog (D/A) converter built onto the circuit board of the pre-amplifier, and recording the output

signal from the lock-in with a Keithley 2400 General Purpose Sourcemeter. The serial D/A was controlled with LabVIEW.

7.3 RESULTS AND DISCUSSION

7.3.1 CIGS Nanocrystal PV Device and Bulk Photovoltaic Characterization

Figure 7.1A shows the structure of the CIGS nanocrystal PV device that was studied. The device consists of a light-absorbing layer of CIGS nanocrystals deposited on a gold back-contact. Cadmium sulfide (CdS) is added as a buffer layer on top of the nanocrystal layer by chemical bath deposition, followed by a 50 nm thick zinc oxide (ZnO) window layer and 300 nm of indium tin oxide (ITO) deposited by RF sputtering. Figure 7.1B shows the device response in the dark and under AM 1.5 illumination. The short-circuit current density (J_{sc}), open-circuit voltage (V_{oc}), fill factor (FF) and power conversion efficiency (PCE) were 3.5 mA/cm^2, 0.38 V, 0.41 and 0.51%, respectively. Figure 7.1C shows the wavelength-dependent external quantum efficiency (EQE) measured for the same device. The EQE is a measure of zero-bias current generated per incident photon on the device. The excitation source for the LBIC measurements had a wavelength of 408 nm, on the blue edge of the EQE spectrum. The shape of the EQE curve is a result of the optical characteristics of both the CIGS nanocrystal absorber layer and the ZnO/ITO window layer as previously discussed.[34]

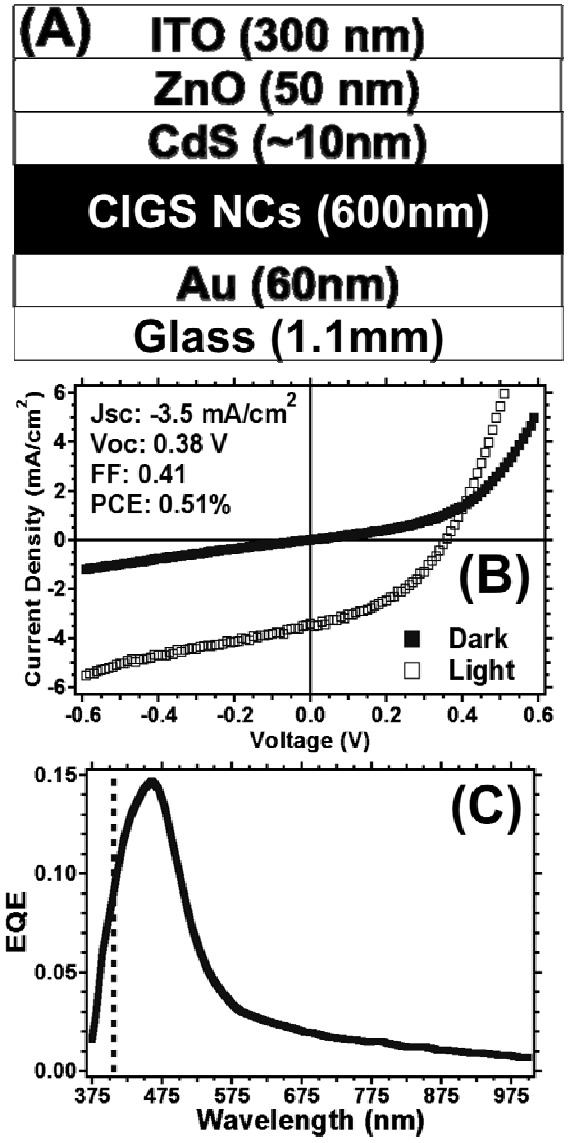

Figure 7.1: (A) Schematic of a CIGS nanocrystal (NC) based PV device. (B) J-V measurements performed under dark and AM1.5 illumination conditions. (C) External Quantum Efficiency (EQE) measured as a function of wavelength (vertical dotted line marks the laser excitation wavelength used for LBIC, 408 nm).

7.3.2 Local Photovoltaic Characterization

Figure 7.2 shows a schematic of the LBIC microscopy setup. The sample is illuminated with 408 nm laser-light focused to a 275 nm diameter spot size. The

photogenerated current is measured, along with fluorescence from the sample. As the illumination spot is raster-scanned across the sample, measurements are collected at each step to generate an image map of the measured, local properties.

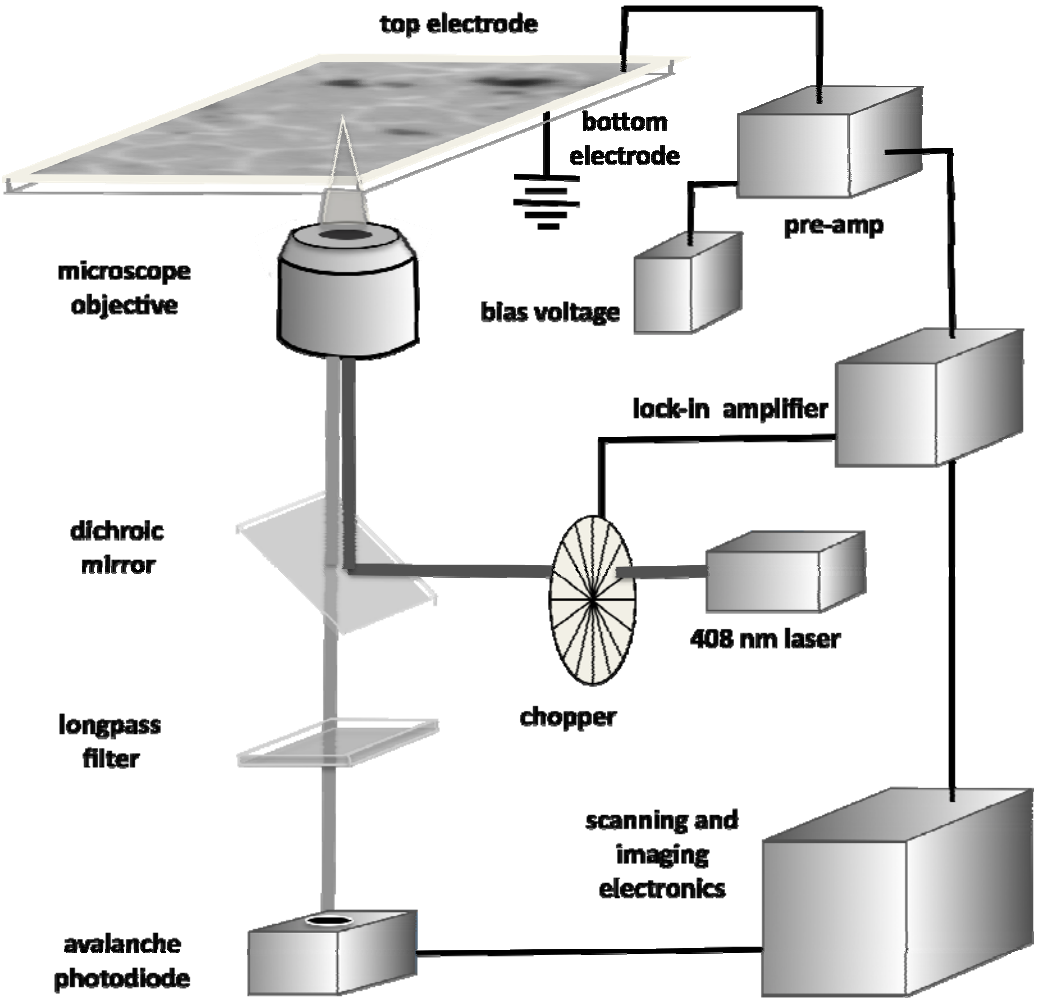

Figure 7.2: Schematic of the scanning Light Beam Induced Current (LBIC) and fluorescence microscopy experimental setup.

One challenge of mapping the photocurrent is that the entire device is active but only a microscopic region is being illuminated. The induced photocurrent (IPC) signals

from the focused laser spot are on the order of 1 and 40 nA. However, these signals are on top of a comparatively large background from the dark current of the full device, which also varies non-linearly with applied bias voltage. As such, current amplification and lock-in detection were necessary to obtain sufficient signal to noise. Signal amplification was accomplished with a transimpedance amplifier (or current to voltage converter) built in-house with a gain of 10,000x. For noise filtering, the incident light beam is chopped and output signal of the device is measured with a lock-in amplifier. Therefore, the IPC that is measured represents the difference between the current measured during illumination and the dark current.

An LBIC image map of a CIGS nanocrystal based PV is shown in Figure 7.3A. There is significant heterogeneity in device response, with micrometer-scale regions of both increased and decreased IPC generation compared to the average response of the device. The higher performance regions appear filamentary (Region B), while the lowest performance regions have a circular shape with typical diameters of 1-2 microns (Region C). These regions of high and low response are scattered throughout relatively homogeneous regions with average device response (Region A). From the image it is observed that regions A, B and C correspond to 75%, 20% and 5% of the device, as shown in Figure 7.4. Figure 7.3B shows the fluorescence microscopy image that was acquired simultaneously with the LBIC measurement. It is clear that the local variations in IPC have corresponding variations in fluorescence. The fluorescence intensity, which relates to the local chemical composition and the extent of radiative charge recombination, is inversely correlated with the IPC signal in the image. For instance, areas of the device like Region A have high fluorescence intensity with low IPC, and areas like Region B show lower fluorescence and exhibit higher IPC, as shown in Figure 7.5. This is consistent with what one would expect: regions with higher fluorescence

have higher radiative recombination and fewer charge carriers available for extraction as IPC.

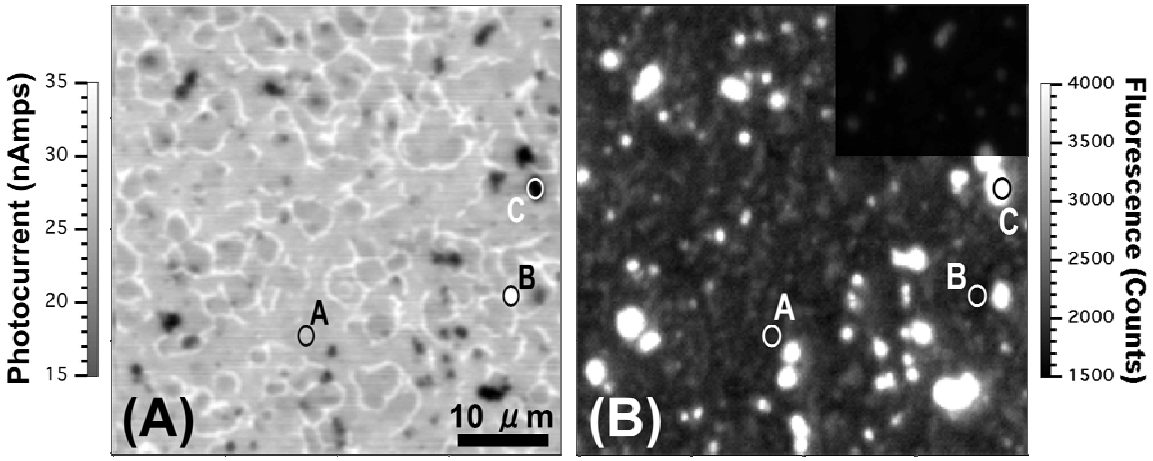

Figure 7.3: Image maps of (A) zero-bias induced photocurrent (IPC) and (B) fluorescence intensity for a CdS-capped CIGS nanocrystal PV device. Overlay in upper right corner of (B): that area of the fluorescence image shown at a different, non-saturated contrast scale of 1,500 to 27,000 counts.

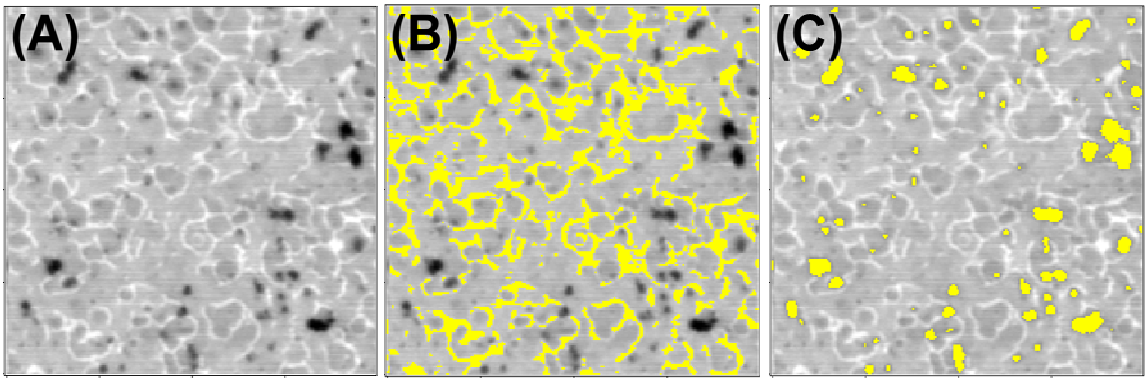

Figure 7.4: Image map of (A) zero-bias induced photocurrent (IPC) from Figure 7.3, and images with a threshold set to highlight areas of (B) high photocurrent and (C) low photocurrent and are 20% and 5% respectively of the image area.

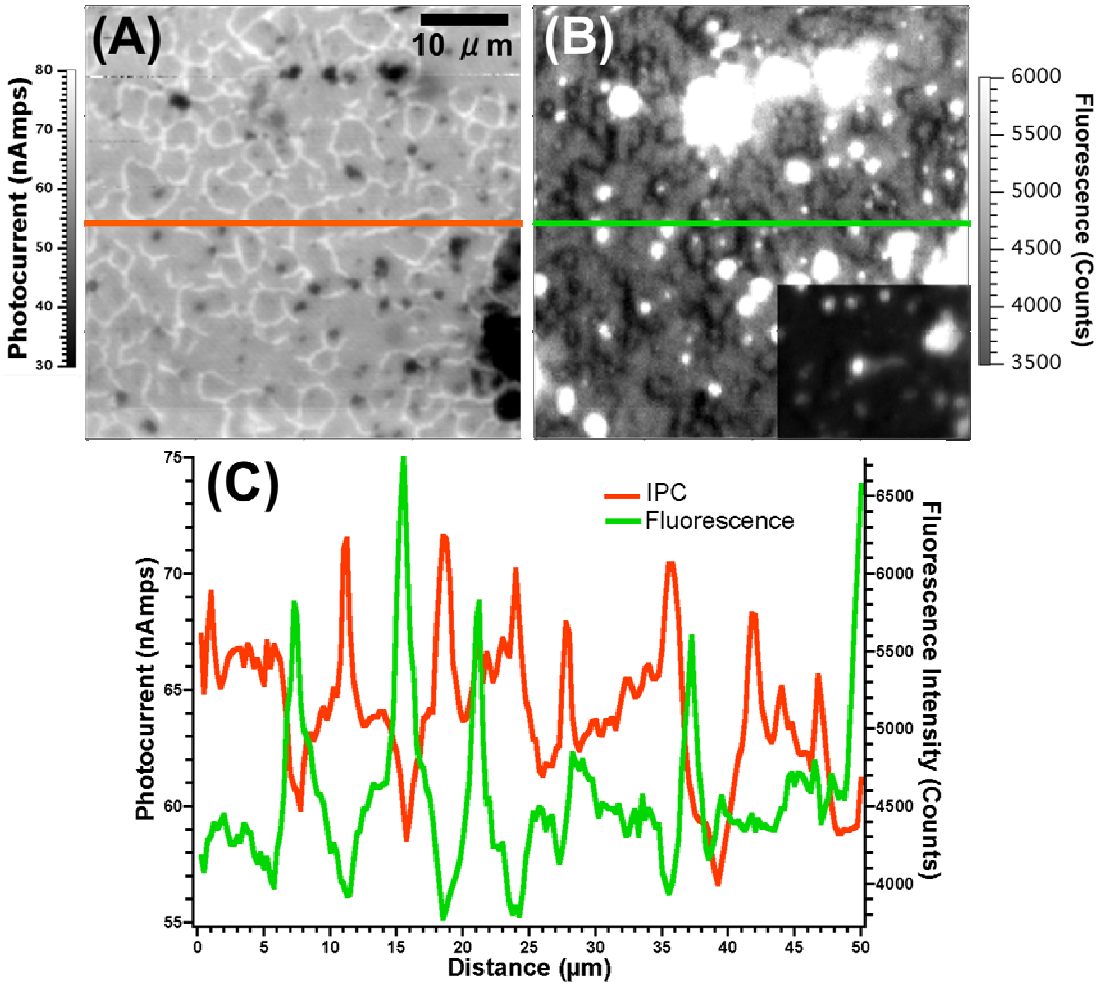

Figure 7.5: Image maps of (A) zero-bias induced photocurrent (IPC) and (B) fluorescence intensity for a CdS-capped CIGS nanocrystal PV device. Overlay in lower right corner of (B): that area of the fluorescence image shown at a different, non-saturated contrast scale of 3,500 to 20,000 counts. The units for image (A) are not exact due to use of non-calibrated lock-in amplifier. (C) Line scans of the IPC and fluorescence images taken at the location of the line shown on the images of (A) and (B), this analysis highlights the anti-correlation of IPC with fluorescence.

This technique provides another useful feature: after an image map is collected, the beam can be repositioned to illuminate a selected region of the sample to measure the

local voltage-dependent photocurrent (LVPC). Figure 7.6 shows the local photocurrent traces obtained at points labeled A, B, and C in Figure 7.3; the traces are representative of the three distinct types of regions found across the device. The main difference between regions is the magnitude of the photocurrent at zero bias. The general shape of the LVPC curve is similar for the three different regions. There is a slight decrease of ~0.06 V for region C in the bias at which the LVPC is zero, however, the decrease is close to the error in the voltage measurement of ±0.05 V. This difference may result from lower charge carrier densities in these regions as they have an associated high fluorescence intensity, which is shown to be from CdS (see further discussion below).

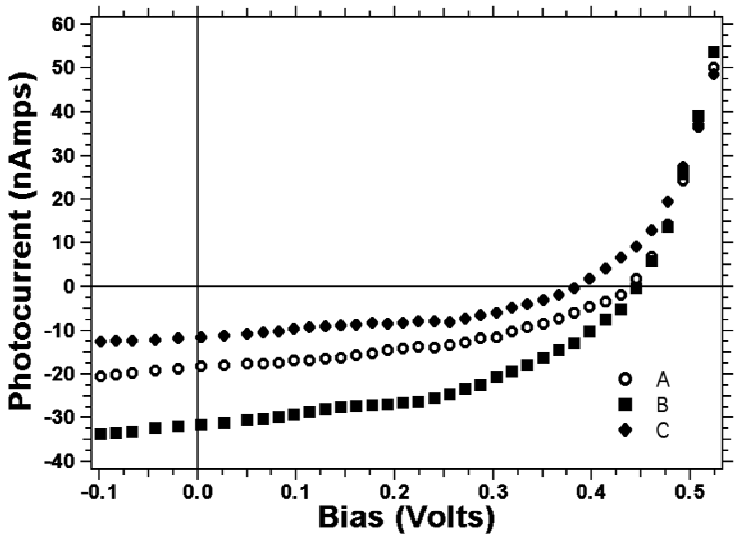

Figure 7.6: Local voltage-dependent photocurrent (LVPC) measured with the focused light beam positioned at locations A, B and C labeled on the images shown in Figure 7.3. These LVPC measurements are representative of the response from regions of the device with average, high and low IPC.

It is important to note the LVPC is not the same as the conventional I-V response measured with the device exposed to light. As a result of the lock-in detection, the

measured current reflects only the additional current induced by the local illumination since the dark current has been subtracted from the signal. This means that the bias at which the LVPC is zero (induced photocurrent is zero) is not the same as the V_{oc} (total current is zero). As a result, a local power conversion efficiency cannot be calculated. However, relative efficiencies can be estimated since the only significant difference between the LVPC response of the different regions is the current at zero bias.

From the data in Figure 7.6, the LVPC at zero bias in regions A, B and C are 18.3, 31.6 and 11.6 nA, respectively, with an error of ±1.5 nA. Thus, the regions of higher photocurrent are nearly a factor of two greater than the average, while the regions of low response are over one-third decreased from the average. It is interesting to consider that if the device was composed entirely of the regions of greatest photocurrent (region B), there would be more than 50% enhancement in the power conversion efficiency of the device. While this would still be far below other reported CIGS device efficiencies,[35] these results identify specific pathways for substantially improving the performance of this emerging, solution-deposited photovoltaic system.

7.3.3 Origins of Performance Heterogeneity

The high IPC regions in the device, regions B, have a filamentary morphology. As shown in Figure 7.7 and Figure 7.8A, cracks in the nanocrystal films observed by SEM have a similar morphology. Therefore, it appears that these cracked regions are giving rise to the observed increased photocurrent in the device. Higher IPC is most likely due to the fact that the nanocrystal film is thinner in this region and therefore, more of the photogenerated carriers can be extracted from the layer before being eliminated by recombination. Increased photocurrent could also stem from increased interfacial contact area between the CdS layer and CIGS nanocrystal film, as a result of CdS penetrating

into the cracks. This type of structure would also require shorter distances for minority charge carriers to travel to reach the interface. These regions also have lower fluorescence (see Figures 7.3 and 7.5), indicating that there is less radiative charge recombination.

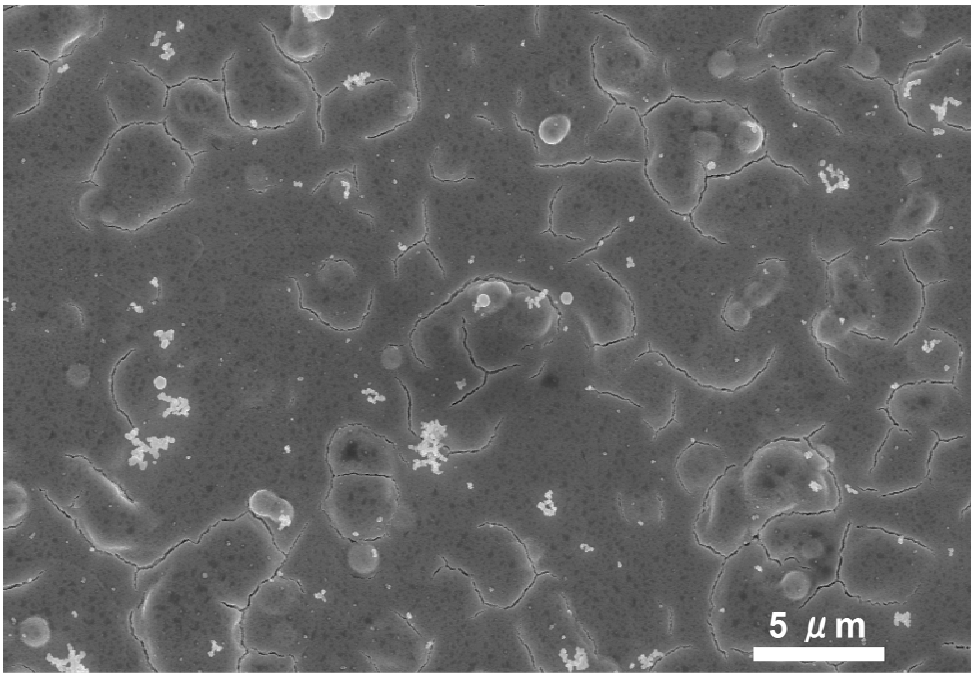

Figure 7.7: Scanning electron microscope image of the CIGS nanocrystal layer of the device capped with the CdS layer.

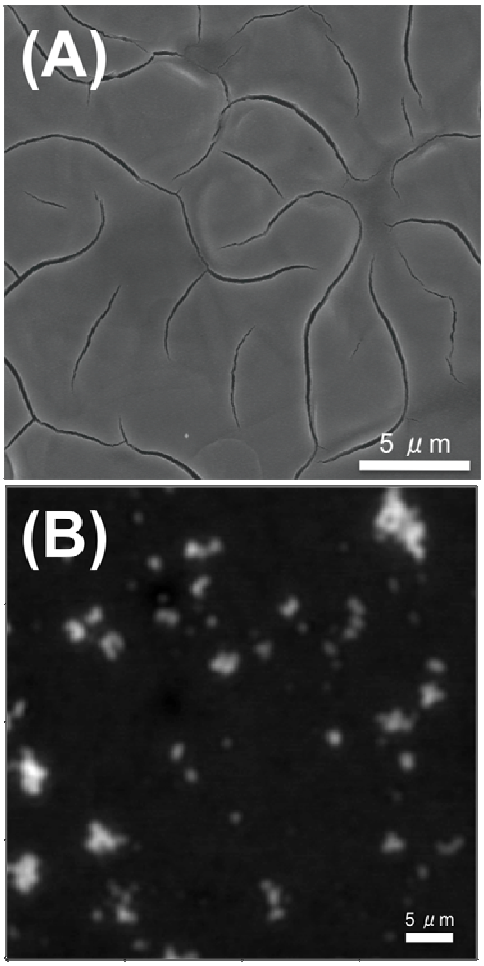

Figure 7.8: (A) Scanning electron microscope image of the CIGS nanocrystal layer of the device. (B) Fluorescence image of a CdS layer deposited on glass, intensity scale is 10,000 to 50,000 counts.

AFM images of the CdS buffer layer showed that occasionally large aggregates form in the thin film as a result of homogeneous nucleation in the deposited solution (Figure 7.9). To investigate if region C areas corresponded to CdS aggregates, fluorescence image maps were separately collected from each layer of the device on glass: ZnO/ITO, CdS, CIGS nanocrystal and blank glass. While the fluorescence image of the CdS showed highly fluorescent features, Figure 7.8B, none of the other layers

showed fluorescence contrast. The similarity between the fluorescence images of the CdS films (Figure 7.8B) and the fluorescence from the device (Figure 7.3B) confirms that regions C correspond to places in the device in which the CdS aggregates are present. As the illumination must pass through the CdS layer before reaching the photoactive layer, one possibility for the lower response of these regions is that the aggregate may absorb most of the incident light, limiting transmission to the photoactive CIGS nanocrystal layer. The thickness of the CdS aggregates was assessed with a height analysis of the AFM topography images and the aggregates were found to range from 250 nm to greater than 1000 nm in height. The transmission of the aggregates was estimated to be at most 1.7% for the 250 nm aggregates and even as low as 10^{-4}% transmission for aggregates at 1000 nm.[36] Thus, when the aggregates are present, essentially no light is reaching the photoactive CIGS nanocrystal layer and one may expect the IPC in these regions to drop to zero. However, the IPC in these regions fall by at most half the IPC from that of region A (average IPC). This could be a result of fluorescence from or incident light scattered off of the aggregates being reabsorbed by the CIGS nanocrystal layer and generated into IPC. Alternatively, light absorbed by the CdS layer may also generate current, albeit not as efficiently as the CIGS nanocrystal layer.

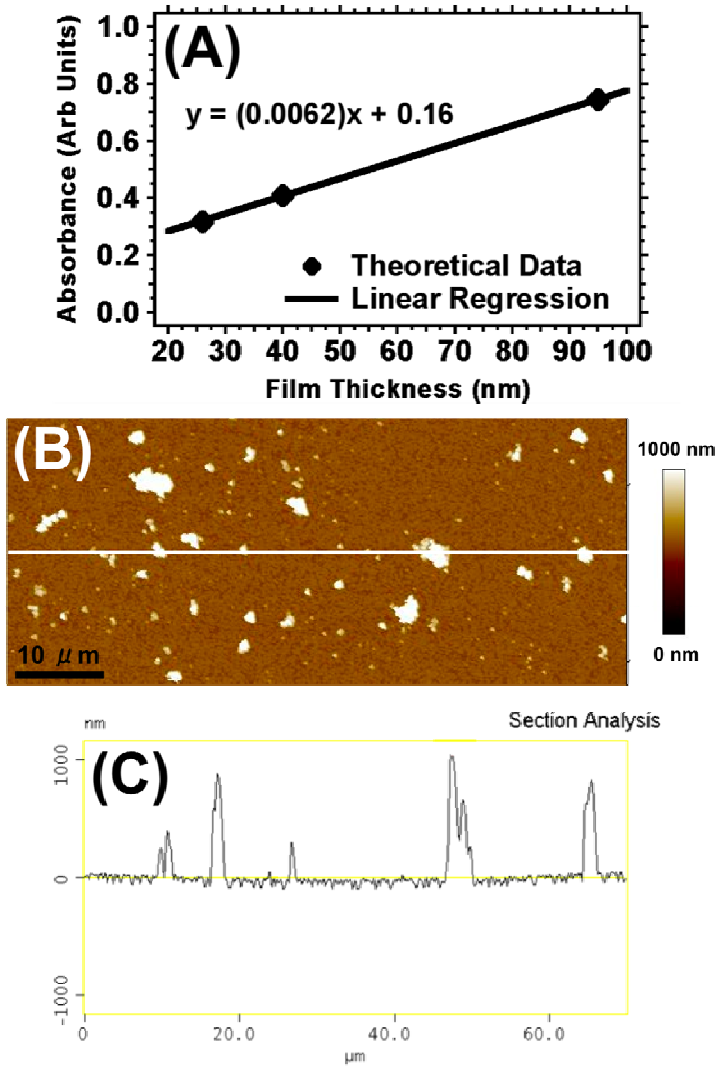

Figure 7.9: (A) Beer's Law plot of CdS absorbance at 408 nm wavelength light, constructed from theoretically calculated data from Derkaoui and co-workers.[36] (B) Topographic AFM image of CdS layer deposited on a glass substrate. (C) Line scan (section analysis) of the AFM topography taken along the white line in (B).

7.4 CONCLUSIONS

Microscopic imaging of a CIGS nanocrystal-based PV device has revealed substantial spatial heterogeneity in the photoresponse. Distinct regions of both higher and

lower photocurrent could be observed on a variety of length scales ranging from hundreds of nanometers to tens of microns. Two morphological features were found to cause the heterogeneity: CdS aggregates that lowered IPC and cracks in the CIGS nanocrystal absorber layer that produced higher IPC. The performance differences between regions could be quantified using LVPC measurements and show the cracked regions had a zero bias photocurrent that was nearly double that of an average region. This information along with the photocurrent maps allow for an estimation of efficiency from a theoretical device composed entirely of the high IPC regions; such a device would have an increase of more than 50% in power conversion efficiency compared to the device studied. Efforts are currently underway to leverage this information to design new fabrication techniques that will improve the device efficiency of CIGS nanocrystal PVs. The coupling of microscopy, spectroscopy and electrical characterization presented here is applicable not only to these systems but any PV device. As such, direct measurements of how morphology affects performance can be used to guide device design and fabrication in the development of future high efficiency PVs.

7.5 REFERENCES AND NOTES

1 Bredas, J.-L.; Durrant, J. R. *Acc. Chem. Res.* **2009**, *42*, 1689-1690.

2 Goetzberger, A.; Hebling, C.; Schock, H. W. *Mat. Sci. Eng. R* **2003**, *40*, 1-46.

3 Yang, X.; Loos, J. *Macromolecules* **2007**, *40*, 1353-1362.

4 Krebs, F. C. *Sol. Energ. Mat. Sol. C.* **2009**, *93*, 394-412.

5 Brabec, C. J. *Sol. Energ. Mat. Sol. C.* **2004**, *83*, 273-292.

6 Saunders, B. R.; Turner, M. L. *Adv. Colloid Interfac.* **2008**, *138*, 1-23.

7 Spanggaard, H.; Krebs, F. C. *Sol. Energ. Mat. Sol. C.* **2004**, *83*, 125-146.

8 McNeill, C. R.; Watts, B.; Thomsen, L.; Belcher, W. J.; Kilcoyne, A. L. D.; Greenham, N. C.; Dastoor, P. C. *Small* **2006**, *2*, 1432-1435.

9 Pingree, L. S. C.; Reid, O. G.; Ginger, D. S.; *Adv. Mater.* **2009**, *21*, 19-28.

10 Kamat, P. V. *J. Phys. Chem. C* **2008**, *112*, 18737-18753.

11 Olson, D. C.; Shaheen, S. E.; Collins, R. T.; Ginley, D. S. *J. Phys. Chem. C* **2007**, *111*, 16670-16678.

12 Cadby, A.; Khalil, G.; Fox, A. M.; Lidzey, D. G. *J. Appl. Phys.* **2008**, *103*, 093715.

13 Rozanski, L. J.; Cone, C. W.; Ostrowski, D. P.; Vanden Bout, D. A. *Macromolecules* **2007**, *40*, 4524-4529.

14 Kwak, E. S.; Kang, T. J.; Vanden Bout, D. A. *Anal. Chem.* **2001**, *73*, 3257-3262.

15 Teetsov, J.; Vanden Bout, D. A. *Langmuir* **2002**, *18*, 897-903.

16 Gao, Y. Q.; Grey, J. K. *J. Am. Chem. Soc.* **2009**, *131*, 9654-9662.

17 Coffey,D. C.; Ginger, D. S. *Nat. Mater.* **2006**, *5*, 735-740.

18 Coffey, D. C.; Reid, O. G.; Rodovsky, D. B.; Bartholomew, G. P.; Ginger, D. S. *Nano Lett.* **2007**, *7*, 738-744.

19 Palermo, V. et al., *J. Am. Chem. Soc.* **2008**, *130*, 14605-14614.

20 Hoppe, H.; Glatzel, T.; Niggemann, M.; Hinsch, A.; Lux-Steiner, M. C.; Sariciftci, N. S. *Nano Lett.* **2005**, *5*, 269-274.

21 Douhéret, O.; Swinnen, A.; Bertho, S.; Haeldermans, I.; D'Haen, J.; D'Olieslaeger, M.; Vanderzande, D.; Manca, J. V;. *Prog. Photovoltaics* **2007**, *15*, 713-726.

22 Palermo, V.; Palma, M.; Samori, P. *Adv. Mater.* **2006**, *18*, 145-164.

23 Pingree, L. S. C.; Reid, O. G.; Ginger, D. S. *Nano Lett.* **2009**, *9*, 2946-2952.

24 Bull T. A.; Pingree,, L. S. C.; Jenekhe, S. A.; Ginger, D. S.; Luscombe, C. K. *ACS Nano* **2009**, *3*, 627-636.

25 Romero, M. J.; Morfa, A. J.; Reilly, T. H.; van de Lagemaat, J.; Al-Jassim, M. *Nano Lett.* **2009**, *9*, 3904-3908.

26 Durose, K., et al. *Prog. Photovoltaics* **2004**, *12*, 177-217.

27 Acciarri, M.; Binetti, S.; Racz, A.; Pizzini, S.; Agostinelli, G. *Sol. Energ. Mat. Sol. C.* **2002**, *72*, 417-424.

28 McNeill, C. R.; Frohne, H.; Holdsworth, J. L.; Dastoor, P. C. *Synthetic Met.* **2004**, *147*, 101-104.

29 McNeill, C. R.; Frohne, H.; Holdsworth, J. L.; Dastoor, P. C. *Nano Lett.* **2004**, *4*, 2503-2507.

30 McNeill, C. R.; Frohne, H.; Holdsworth, J. L.; Furst, J. E.; King, B. V.; Dastoor, P. C. *Nano Lett.* **2004**, *4*, 219-223.

31 Gao, Y. Q.; Martin, T. P.; Thomas, A. K.; Grey, J. K. *J. Phys. Chem. Lett.* **2010**, *1*, 178-182.

32 Thantsha, N. M.; Macabebe, E. Q. B.; Vorster, F. J;. van Dyk, E. E. *Physica B-Condensed Matter* **2009**, *404*, 4445-4448.

33 Riehn, R.; Stevenson, R.; Richards, D.; Kang, D.-J.; Blamire M.; Downes,, A.; Cacialli, F. *Adv. Funct. Mater.* **2006**, *16*, 469-476.

34 Panthani, M. G.; Akhavan, V.; Goodfellow, B.; Schmidtke, J. P.; Dunn, L.; Dodabalapur, A.; Barbara, P. F.; Korgel, B. A. *J. Am. Chem. Soc.* **2008**, *130*, 16770-16777.

35 Repins, I.; Contreras, M. A.; Egaas, B.; DeHart, C.; Scharf, J.; Perkins, C. L.; To, B.; Noufi, R. *Prog. Photovoltaics* **2008**, *16*, 235-239.

36 Derkaoui, Z.; Kebbab, Z.; Miloua, R.; Benramdane, N. *Solid State Commun.* **2009**, *149*, 1231-1235.

37 McCandless, B. E.; Shafarman, W. N. U.S. Patent 6,537,845, March 25, 2003.

Chapter 8: Conclusions and Future Research Directions

8.1 Conclusions

This dissertation has focused on the self-assembly of colloidal ligand-stabilized nanocrystals, the behavior of nanocrystal assemblies with exposure to mild heating and the use of colloidal nanocrystals in printable light-absorber layers for low-cost solar cells. The work presented in this dissertation provides an important step to 1) understanding the behavior of colloidal nanocrystal assembly and the rational design of nanocrystal-based materials with spatial complexity and unique properties and 2) realizing the ability to use nanocrystal-based inks to make printable low-cost inorganic solar cells.

8.1.1 Binary Nanocrystal Superlattices

Binary superlattices (BSLs) of sterically-stabilized, hydrophobic, large (A; 11.5 nm diameter) iron oxide and small (B; 6.1 nm diameter) Au nanocrystals were assembled by slow evaporation of colloidal dispersions on tilted substrates. A detailed analysis of the BSL structure was carried out using transmission and scanning electron microscopy (TEM and SEM) and grazing incidence small angle X-ray scattering (GISAXS). The BSLs were simple hexagonal (sh) AB_2 superlattices (isostructural with the compound AlB_2; space group 191, *P 6/mmm*) of large nanocrystals occupying a simple hexagonal lattice with small nanocrystals in the interstitial spaces. SEM and GISAXS confirmed long range order of the BSLs and GISAXS revealed that the superlattice is slightly contracted (8~12%) perpendicular to the substrate as a result of solvent drying in the deposition process. When the sh-AB_2 superlattice deposits on a (100) plane, this shrinkage occurs in the [210] direction and changes the lattice symmetry to centered orthorhombic. Additionally, nearly periodic superlattice dislocations consisting of inserted half-planes of gold nanocrystals were observed by SEM in some BSLs.

8.1.2 Non-Close-Packed Nanocrystal Superlattices

Dense collections of hard sphere particles order into close-packed face-centered cubic (fcc) lattices to maximize free volume entropy. Sterically-stabilized nanocrystals have relatively short-range repulsive interaction potentials and also tend to order into fcc superlattices. However, here we have shown that superlattices with non-close-packed body-centered cubic (bcc) structure are also relatively common, and presented grazing incidence small angle X-ray scattering (GISAXS) and transmission electron microscopy (TEM) data for bcc superlattices of 1.8 nm dodecanethiol-capped Au nanocrystals, 3.7 nm oleic acid-capped PbS nanocrystals, and 7.9 nm oleic acid-capped PbSe nanocrystals. We argued that bcc superlattices can be favored over fcc when entropic ligand packing frustration overcomes the packing entropy of the spheres. By considering the Wigner-Seitz cells for fcc and bcc and the distribution of ligand lengths needed to fill the cells, it was shown that the bcc arrangement of nanocrystals allows for a more uniform thickness of the ligand shell. By considering the change in conformational entropy as a collection of isolated nanocrystals assembles into a bcc or fcc superlattice, it was shown that the bcc arrangement of nanocrystals can be strongly favored over fcc when the ligands are allowed to interpenetrate with the ligands of a neighboring nanocrystal. This role of ligand packing frustration is consistent with our observation of a superlattice thickness-dependent change in structure from hexagonally close-packed monolayers to bcc superlattices in nanocrystal films. We also find that {112} twin planes are common to bcc superlattices.

8.1.3 Structural Transformations of Heated Nanocrystal Superlattices

The structural evolution of a body-centered cubic (bcc) superlattice of 6.6 nm diameter organic ligand-coated PbSe nanocrystals was studied in situ by small angle X-ray scattering (SAXS) as it was heated in air from room temperature to 350°C. As it was

heated above room temperature, the superlattice contracted slightly, but maintained bcc structure up to 110°C. Once the temperature rose above 110°C, the superlattice began to disorder, by first losing long-range translational order and then local positional order. At temperatures exceeding 168°C, the nanocrystals sintered and oxidized, transforming into $PbSeO_3$ nanorods.

Small angle X-ray scattering (SAXS) data reveal that superlattices of organic ligand-stabilized gold (Au) nanocrystals undergo a series of structural phase transitions at elevated temperature. A body-centered cubic (bcc) superlattice evolves into a hexagonal close-packed (hcp) structure, followed by the formation of simple cubic (sc) AB_{13} and hexagonal (hex) AB_5 binary superlattices before ultimately decomposing at high temperature to bicontinuous domains of Au and hydrocarbon. Transmission electron microscopy (TEM) revealed that these transformations result from Au nanocrystal growth during heating, which combined with partial desorption of the ligand shell, forces the observed changes in superlattice symmetry. These observations suggest a similarity between organic ligand-coated nanocrystals and microphase-segregating diblock copolymers: in this case, the thermally-induced nanophase-segregation of Au and organic determines the ordered arrangements in the superlattice.

8.1.4 Nanocrystal Inks for Photovoltaics

All-inorganic solar cells consisting of CdTe/CdSe,[1] PbSe/PbTe/PbS,[2-5] CIGS,[6,7] Cu_2S,[8] and Cu_2ZnSnS_4[9,10] absorber layers have been fabricated by printing nanocrystal inks. Efficiencies as high as 10% have been achieved, however, only when relatively high temperature annealing has been utilized.[11] CIGS nanocrystal film devices fabricated by spray-coating the absorber layer, without high temperature annealing, have achieved just over 3% efficiency. The mild processing conditions also enabled fabrication of

alternative device structures that are not compatible with conventional high temperature PV processing, including substrate and superstrate designs, and devices with transparent back contacts of conducting indium tin oxide (ITO) and plastic substrates. Device performance is observed to be limited by poor charge extraction from the nanocrystal films, with the highest efficiencies being obtained from PVs with relatively thin absorber layers. To improve light absorption without sacrificing internal quantum efficiency, stacked PVs were fabricated, which exhibited improved short-circuit current and power conversion efficiency compared to stand-alone single junction devices. At this point it is clear that nanocrystal inks can be formulated and used to construct PV devices with reasonable efficiency. The challenge is now to determine if low temperature printing of the nanocrystal inks can yield device layers that can meet the required 10% efficiency for commercialization. At the moment, it is not clear if this will be possible, as the large number of grain boundaries in the film serve as carrier traps that can significantly limit the device efficiency. Materials like CIGS, in which electrical conduction is relatively immune to the presence of grain boundaries, are going to be needed for the approach to work. There are ways to chemically passivate electrical traps at grain boundaries, and an understanding of how to do this and of what is possible in nanocrystal films is needed. If such an approach can be developed, the manufacturing of solar cells using nanocrystal inks will have tremendous commercial potential.

8.2 FUTURE RESEARCH DIRECTIONS

8.2.1 Predicting Self-Assembled Nanocrystal Superlattice Structures

One challenge of using complex ordered assemblies in useful applications is the lack of ability to accurately predict and control the self-assembled structure of

nanocrystal superlattices. While the discovery of many complex structures in recent years has garnered considerable attention, a detailed understanding of the important forces leading to such complex phase behavior has lagged significantly behind. In Chapters 3 and 5 of this dissertation, the contribution of the organic ligand shell of the nanocrystals was shown to be very important in determining the arrangement of the nanocrystals. In particular, it appears that the nanocrystals are behaving like a microphase-separated system where one phase is the inorganic cores and the other is the organic ligand. The self-assembly of other microphase-separated materials, like amphiphilic block copolymers, is well understood based on self-consistent field theory. Perhaps the established theory for microphase-separated organic materials could be applied to colloidal nanocrystals in order to understand and predict their complex phase behavior. This would be an important step to advancing the field of nanocrystal assembly from empirical to predictive.

8.2.2 Amorphous-Crystalline Transitions in Au NCSLs

As shown in Chapter 5, an initially bcc superlattice of sub-2nm Au nanocrystals undergoes order-order structural transformations when mildly heated. In some cases, the initial superlattice is amorphous. Upon mild heating or solvent vapor exposure, the amorphous nanocrystal assembly will crystalize into a crystalline bcc superlattice. Furthermore, when the amorphous-crystalline transition is induced by heating, the nanocrystal assembly does not revert back to amorphous. In other words, the transition is non-reversible. On the other hand, when the amorphous-to-crystalline transition is induced by exposure to solvent vapor, the assembly reverts back to amorphous when the solvent vapor is removed. In other words, the transition is completely reversible. GISAXS patterns of an assembly of sub-2nm dodecanethiol-capped Au nanocrystals

undergoing an amorphous-to-crystalline structural transition with exposure to heat and solvent vapor are shown in Figures 8.1 and 8.2, respectively.

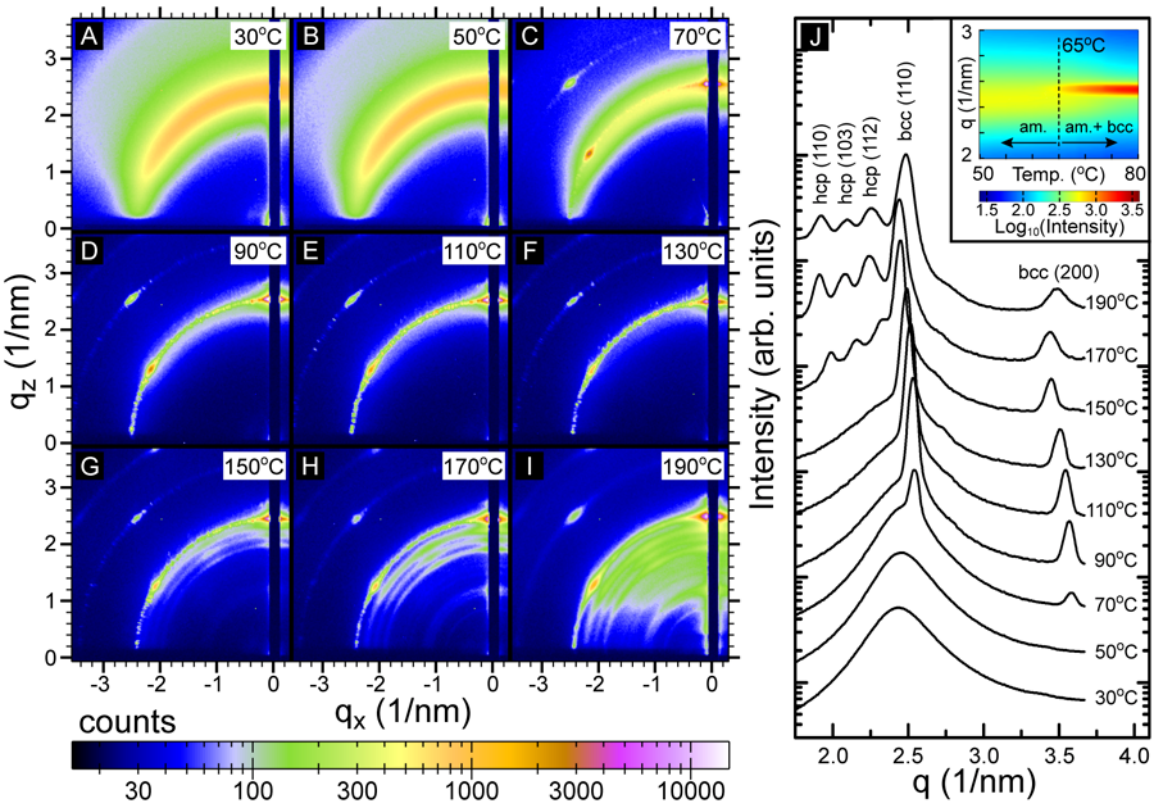

Figure 8.1: (A-I) GISAXS patterns from a heated Au nanocrystal superlattice and (J) radial integrations and indexing of the Bragg peaks in the GISAXS patterns. At approximately 65 °C, the nanocrystal assembly undergoes an amorphous-to-crystalline transition as shown by the emergence of the (110) and (200) Bragg spots of the bcc superlattice.

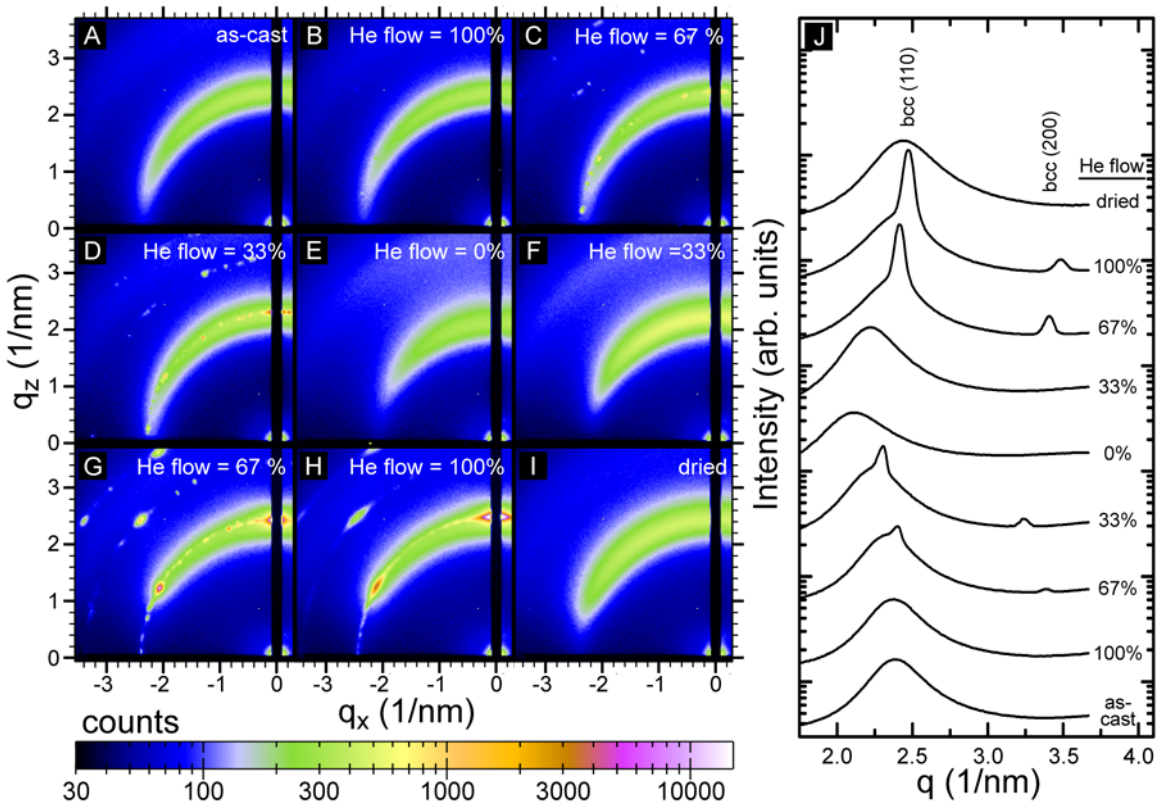

Figure 8.2: (A-I) GISAXS patterns from an Au nanocrystal superlattice as it is exposed to toluene vapor and (J) radial integrations and indexing of the Bragg peaks in the GISAXS patterns. As the nanocrystals are exposed to the solvent vapor, they crystalline into a bcc superlattice. Removal of the toluene vapor causes the nanocrystal assembly to revert back to the original amorphous structure.

It is interesting that the amorphous-to-crystalline transitions shown here are either non-reversible or reversible depending on the method in which they are induced. Further study of these transitions might lead to a better understanding of the role that the ligand plays in the assembly of the nanocrystals.

8.2.3 Selenization of CIGS Nanocrystal Layers and Composition Control

One potential method for increasing the efficiency of CIGS nanocrystal-based solar cells it to grow very large grains using a high temperature anneal under a selenium

rich atmosphere, or "selenization". Figure 8.3 shows TEM images of a nanocrystal film before and after selenization. While the nanocrystals are initially only 15-20 nm in diameter, the grains after selenization are on the order of 1 μm in size. Furthermore, XRD of a bilayer of $CuInSe_2$ and $CuGaSe_2$ showed that the composition of the CIGS film after selenization was uniform and intermediate between $CuInSe_2$ and $CuGaSe_2$. Since the band gap of $Cu(In_{1-x}Ga_x)Se_2$ can be tuned from about 1.0 eV to 1.7 eV by varying the composition (in particular the value of x), selenization of a mixture of nanocrystal inks to might be an attractive avenue for composition control and bandgap engineering in CIGS photovoltaic. Of course, selenization is a high temperature process which can limit the types of materials used in the solar cell (e.g. the substrate and back contact material).

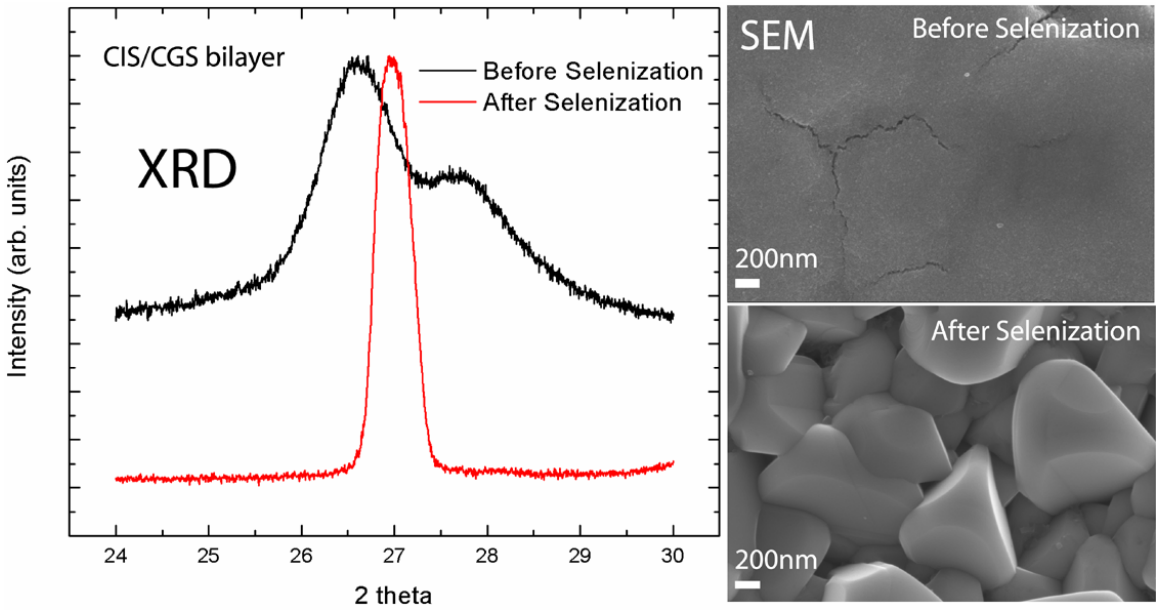

Figure 8.3: (left) XRD profiles of a bilayer of $CuInSe_2$ and $CuGaSe_2$ nanocrystals before and after selenization. (right) TEM images of a CIGS nanocrystal film before (top) and after (bottom) selenization.

8.3 REFERENCES AND NOTES

1. Gur I, Fromer NA, Geier ML, Alivisatos AP, *Science*, **2005**; 310:462-465.
2. Luther J.M, Law M, Beard MC, Song Q, Reese MO, Ellingson RJ, Nozik AJ, *Nano Lett*, **2008**; 8:3488–3492.
3. Ma W, Luther JM, Zheng H, Wu Y, Alivisatos AP,.*Nano Lett*, **2009**; 9:1699–1703.
4. Koleilat GI, Levina L, Shukla H, Myrskog SH, Hinds S, Pattantyus-Abraham AG, Sargent EH, *ACS Nano*, **2008**; 2:833-840.
5. Choi ,JJ Lim YF, Santiago-Berrios MB, Oh M, Hyun BR, Sun L, Bartnik AC, Goedhart A, Malliaras GG, Abruna HD, Wise FW, Hanrath T, *Nano Lett*, **2009**; 9:3749-3755.
6. Panthani MG, Akhavan V, Goodfellow B, Schmidtke JP, Dunn L, Dodabalapur A, Barbara PF, Korgel BA, *J Am Chem Soc*, **2008**; 130:16770-16777.
7. Guo Q, Kim SJ, Kar M, Shafarman WN, Birkmire RW, Stach EA, Agrawal R, Hillhouse HW, *Nano Lett*, **2008**; 8:2982-2987.
8. Wu Y, Wadia C, Ma W, Sadtler B, Alivisatos AP, *Nano Lett*, 2008 ; 8 :2551-2555.
9. Steinhagen C, Panthani MG, Akhavan V, Goodfellow B, Koo B, Korgel BA, *J Am Chem Soc*, **2009**; 131:12554-12555.
10. Guo Q, Hillhouse HW, Agrawal R, *J Am Chem Soc*, **2009**; 131:11672-11673.
11. Guo Q, Hillhouse HW, Agrawal R., *2009 AIChE Annual Meeting.* **2009**; 447C.

Bibliography

Acciarri, M.; Binetti, S.; Racz, A.; Pizzini, S.; Agostinelli, G. *Sol. Energ. Mat. Sol. C.* **2002**, *72*, 417-424.

Ackerson, B. J.; Clark, N. A., *Physical Review A* **1984,** 30, (2), 906-906.

Akhavan, V. A.; Goodfellow, B. W.; Panthani M. G. and Korgel, B. A. *Modern Energy Review* **2010**, 2, (2), 25-27.

Akhavan, V. A.; Goodfellow, B. W.; Panthani, M. G.; Reid, D. K.; Hellebusch, D. J.; Adachi, T.; Korgel, B. A. *Energy Environ. Sci.* **2010**, 3, 1600-1606.

Alder, B. J.; Wainwright, T. E., *The Journal of Chemical Physics* **1957,** 27, (5), 1208-1208.

Alivisatos, A. P. *J. Phys. Chem*. **1996**, 100, 13226-13239.

Alivisatos, A. P. *Nat. Biotechnol.* **2004,** *22*, 47-52.

Alivisatos, A. P., *The Journal of Physical Chemistry* **1996,** 100, (31), 13226-13239.

Arici, E.; Meissner, N. S. S., D. *Advanced Functional Materials* **2003**, *13*, 165-171.

Asakura, S.; Oosawa, F., *J. Chem. Phys.* **1954**, *22*, 1255-1256.

Baik, S. J.; Kim, K.; Lim, K. S.; Jung, S.; Park, Y.-C.; Han, D. G.; Lim, S.; Yoo, S.; Jeong, S. *J. Phys. Chem. C* **2011**, 115, 607-612.

Banger, K. K.; Jin, M. H.-C.; Harris, J. D.; Fanwick, P. E.; Hepp, A. F. *Inorg. Chem.* **2003**, *42*, 7713-7715.

Barkhouse, D. A. R.; Pattantyus-Abraham, A. G.; Levina, L.; Sargent, E. H. *ACS Nano* **2008**, 2, 2356-2362.

Bartlett, P.; Ottewill, R. H.; Pusey, P. N. *Phys. Rev. Lett.* **1992,** *68*, 3801-3804.

Berger, L. I. In *CRC Handbook of Chemistry and Physics*; 79 ed., 1999, pp 12-84.

Bian, K.; Choi, J. J.; Kaushik, A.; Clancy, P.; Smilgies, D.-M.; Hanrath, T., *ACS Nano* **2011,** 5, (4), 2815-2823.

Bigioni, T. P.; Lin, X. M.; Nguyen, T. T.; Corwin, E. I.; Witten, T. A.; Jaeger, H. M. *Nat. Mater.* **2006,** *5*, 265-270.

Bosworth, J. K.; M. Y. Paik; Ruiz, R.; Schwartz, E. L.; Huang, J. Q.; Ko, A. W.; Smilgies, D. M.; Black, C. T.; Ober, C. K. *ACS Nano* **2008**, *2*, 1396-1402.

Brabec, C. J. *Sol. Energ. Mat. Sol. C.* **2004**, *83*, 273-292.

Bredas, J.-L.; Durrant, J. R. *Acc. Chem. Res.* **2009**, *42*, 1689-1690.

Brus, L. *Appl. Phys. A: Mater. Sci. Process.* **1991**, 53, 465-474.

Brust, M.; Walker, M.; Bethell, D.; Schiffrin, D. J.; Whyman, R. *Chem. Commun.* **1994**, 801-802.

Bull T. A.; Pingree,, L. S. C.; Jenekhe, S. A.; Ginger, D. S.; Luscombe, C. K. *ACS Nano* **2009**, *3*, 627-636.

Buonsanti, R.; Grillo, V.; Carlino, E.; Giannini, C.; Curri, M. L.; Innocenti, C.; Sangregorio, C.; Achterhold, K.; Parak, F. G.; Agostiano, A.; Cozzoli, P. D. *J. Am. Chem. Soc.* **2006,** *128*, 16953-16970.

Burda, C.; Chen, X.; Narayanan, R.; El-Sayed, M. A., Chemistry and Properties of Nanocrystals of Different Shapes. *Chemical Reviews* **2005,** 105, (4), 1025-1102.

Burgelman, M.; Engelhardt, F.; Guillemoles, J. F.; Herberholz, R.; Igalson, M.; Klenk, R.; Lampert, M.; Meyer, T.; Nadenau, V.; Niemegeers, A.; Parisi, J.; Rau, U.; Schock, H–W.; Schmitt, M.; Seifert, O.; Walter T. and Zott, S., *Progress in Photovoltaics: Res. And Appl.* **1997**, 5, 121–130.

Cadby, A.; Khalil, G.; Fox, A. M.; Lidzey, D. G. *J. Appl. Phys.* **2008**, *103*, 093715.

Carbone, L.; Kudera, S.; Giannini, C.; Ciccarella, G.; Cingolani, R.; Cozzoli, P. D.; Manna, L. *J. Mater. Chem.* **2006,** *16*, 3952-3956.

Castro, S. L.; Bailey, S. G.; Raffaelle, R. P.; Banger, K. K.; Hepp, A. F. *J. Phys. Chem. B* **2004**, *108*, 12429-12435.

Castro, S. L.; Bailey, S. G.; Raffaelle, R. P.; Banger, K. K.; Hepp, A. F. *Chem. Mater.* **2003**, *15*, 3142-3147.

Chen, C.-C.; Herhold, A. B.; Johnson, C. S.; Alivisatos, A. P., *Science* **1997,** 276, (5311), 398-401.

Chen, Z. Y.; Moore, J.; Radtke, G.; Sirringhaus, H.; O'Brien, S. *J. Am. Chem. Soc.* **2007,** *129*, 15702-15709.

Chen, Z.; O'Brien, S. *ACS Nano* **2008**, *2*, 1219-1229.

Cheon, J.; Park, J. I.; Choi, J. S.; Jun, Y. W.; Kim, S.; Kim, M. G.; Kim, Y. M.; Kim, Y. J. *Proc. Natl. Acad. Sci.* **2006,** *103*, 3023-3027.

Cho, K.-S.; Lee, E. K.; Joo, W.-J.; Jang, E.; Kim, T.-H.; Lee, S. J.; Kwon, S.-J.; Han, J. Y.; Kim, B.-K.; Choi, B. L.; Kim, J. M. *Nature Photon*. **2009**, 3, 341-345.

Cho, K.-S.; Talapin, D. V.; Gaschler, W.; Murray, C. B. *J. Am. Chem. Soc.* **2005**, 127, 7140-7147.

Choi, J. J.; Bealing, C. R.; Bian, K.; Hughes, K. J.; Zhang, W.; Smilgies, D.-M.; Hennig, R. G.; Engstrom, J. R.; Hanrath, T., *Journal of the American Chemical Society* **2011,** 133, (9), 3131-3138.

Choi, J. J.; Lim, Y. F.; Santiago-Berrios, M. B.; Oh, M.; Hyun, B. R.; Sun, L.; Bartnik, A. C.; Goedhart, A.; Malliaras, G. G.; Abruna, H. D.; Wise F. W. and Hanrath, T. *Nano Lett.* **2009**, 9, 3749–3755.

Choi, J. J.; Luria, J.; Hyun, B.-R.; Bartnik, A. C.; Sun, L.; Lim, Y.-F.; Marohn, J. A.; Wise, F. W.; Hanrath, T. *Nano Lett.* **2010**, 10, 1805-1811.

Choi, J. S.; Jun, Y. W.; Yeon, S. I.; Kim, H. C.; Shin, J. S.; Cheon, J. *J. Am. Chem. Soc.* **2006,** *128*, 15982-15983.

Choi, S.-H.; Kim, E.-G.; Hyeon, T. *J. Am. Chem. Soc.* **2006**, *128*, 2520-2521.

Coe, S.; Woo, W.-K.; Bawendi, M.; Bulovic, V. *Nature* **2002**, 420, 800-803.

Coffey, D. C.; Reid, O. G.; Rodovsky, D. B.; Bartholomew, G. P.; Ginger, D. S. *Nano Lett.* **2007**, *7*, 738-744.

Coffey,D. C.; Ginger, D. S. *Nat. Mater.* **2006**, *5*, 735-740.

Collier, C. P.; Vossmeyer, T.; Heath, J. R. *Annu. Rev. Phys. Chem.* **1998,** *49*, 371-404.

Constantinides, M. G.; Jaeger, H. M.; Li, X.; Wang, J.; Lin, X.-M. *Z. Kristallogr.* **2007**, 222, 595-600.

Contreras, M. A.; Egaas, B.; Ramanathan, K.; Hiltner, J.; Swartzlander, A.; Hasoon, F.; Noufi, R. *Prog. Photovoltaics Res. Appl.* **1999**, *7*, 311-316.

Contreras, Miguel A.; AbuShama, K. R., J.; Hasoon, F.; Young, D. L.; Egaas, B.; Noufi, R. *Prog. Photovoltaics Res. Appl.* **2005**, *13*, 209-216.

Cottin, X.; Monson, P. A. *J. Chem. Phys.* **1995,** *102*, 3354-3360.

Cozzoli, P. D.; Pellegrino, T.; Manna, L. *Chem. Soc. Rev.* **2006,** *35*, 1195-1208.

Czekelius, C.; Hilgendorff, M.; Spanhel, L.; Bedja, I.; Lerch, M.; Müller, G.; Bloeck, U.; Su, D.-S.; Giersig, M. *Advanced Materials* **1999**, *11*, 643-646.

Derkaoui, Z.; Kebbab, Z.; Miloua, R.; Benramdane, N. *Solid State Commun.* **2009**, *149*, 1231-1235.

Devaney, W. E.; Chen, W. S.; Stewart, J. M.; Mickelsen, R. A. A.-M., R.A. *IEEE Trans. Electron Devices* **1990**, *37*, 428-433.

Douhéret, O.; Swinnen, A.; Bertho, S.; Haeldermans, I.; D'Haen, J.; D'Olieslaeger, M.; Vanderzande, D.; Manca, J. V;. *Prog. Photovoltaics* **2007**, *15*, 713-726.

Du, H.; Chen, C.; Krishnan, R.; Krauss, T. D.; Harbold, J. M.; Wise, F. W.; Thomas, M. G.; Silcox, J. *Nano Lett.* **2002**, 2, 1321-1324.

Dunphy, D.; Fan, H.; Li, X.; Wang, J.; Brinker, C. J. *Langmuir* **2008**; *24*, 10575-10578.

Durose, K., et al. *Prog. Photovoltaics* **2004**, *12*, 177-217.

Durr, N. J.; Larson, T.; Smith, D. K.; Korgel, B. A.; Sokolov, K.; Ben-Yakar, A. *Nano Lett.* **2007,** *7*, 941-945.

Eberspacher, C.; Fthenakis, V. M.; Moskowitz, P. D. *25th IEEE Photovoltaic Specialist Conference, Washington, D.C., 1996*; pp 1417-1420.

Eberspacher, C.; Pauls, K. L.; Serra, J. P. *Mat. Res. Soc. Symp. Proc.* **2003**, *763*, B8.27.21-26.

Eberspacher, C.; Pauls, K.; Serra, J. *28th IEEE Photovoltaic Specialist Conference, Anchorage, Alaska,* **2000**; pp 517-520.

Elim, H. I.; Ji, W.; Ng, M.-T.; Vittal, J. J. *Appl. Phys. Lett.* **2007**, *90*, 033106.

Finnefrock, A. C.; Ulrich, R.; Toombes, G. E. S.; Gruner, S. M.; Wiesner, U., *Journal of the American Chemical Society* **2003**, 125, (43), 13084-13093.

Fischbein, M. D.; Puster, M.; Drndic, M. *Nano Lett.* **2010**, 10, 2155-2161.

Gao, Y. Q.; Grey, J. K. *J. Am. Chem. Soc.* **2009**, *131*, 9654-9662.

Gao, Y. Q.; Martin, T. P.; Thomas, A. K.; Grey, J. K. *J. Phys. Chem. Lett.* **2010**, *1*, 178-182.

Gelbart, W. M.; Ben-Shaul, A. *J. Phys. Chem.* **1996**, *100*, 13169-13189.

Ghezelbash, A.; Korgel, B. A. *Langmuir* **2005**, *21*, 9451-9456.

Giersig, M.; Mulvaney, P., *Langmuir* **1993,** 9, (12), 3408-3413.

Glatter, O.; Kratky, O. Small-Angle X-Ray Scattering. Academic Press Inc.: New York, **1982**.

Goetzberger, A.; Hebling, C.; Schock, H. W. *Mat. Sci. Eng. R* **2003**, *40*, 1-46.

Goldstein, A. N.; Echer, C. M.; Alivisatos, A. P. *Science* **1992**, 256, 1425-1427.

Goodfellow, B. W.; Korgel, B. A., *ACS Nano* **2011,** 5, (4), 2419-2424.

Goodfellow, B. W.; Patel, R. N.; Panthani, M. G.; Smilgies, D.-M.; Korgel, B. A., *The Journal of Physical Chemistry C* **2011,** 115, (14), 6397-6404.

Green MA, Third Generation Photovoltaics: Advanced Solar energy Conversion. Springer, New York, 2003.

Green, M.A.; Emery, K.; King, D.L.; Hishikawa, Y.; Warta, W. *Prog. Photovoltaics Res. Appl.* **2007**, *15*, 35-40.

Gruner, S. M.; Tate, M. W.; Eikenberry, E. F. *Rev. Sci. Instrum.* **2002,** *73*, 2815-2842.

Guillemoles, J.-F.; Kronik, L.; Cahen, D.; Rau, U.; Jasenek, A.; Schock, H.-W. *J. Phys. Chem. B* **2000**, *104*, 4849-4862.

Guinier, A.; Fournet, G. Small-Angle Scattering of X-Rays. Wiley: New York, **1955**.

Guo Q, Kim SJ, Kar M, Shafarman WN, Birkmire RW, Stach EA, Agrawal R, Hillhouse HW, *Nano Lett*, **2008**; 8:2982-2987.

Guo, Q.; Ford, G. M.; Hillhouse H. W. and Agrawal, R. *Nano Lett.* **2009**, 9, 3060–3065.

Guo, Q.; Hillhouse H. W. and Agrawal, R. *J. Am. Chem. Soc.,* **2009**, 131, 11672–11673.

Guo, Q.; Hillhouse H.W. and Agrawal, R. *2009 AIChE Annual Meeting*, Nashville, **2009**, 447C.

Gur, I.; Fromer, N. A.; Geier, M. L.; Alivisatos, A. P. *Science* **2005**, *310*, 462-465.

Hamley, I. W., The Physics of Block Copolymers. Oxford University Press: Oxford, 1998.

Hammersley, A. P. ESRF Internal Report; ESRF97HA02T; **1997**.

Harfenist, S. A.; Wang, Z. L.; Whetten, R. L.; Vezmar, I.; Alvarez, M. M., *Adv. Mater.* **1997**, *9*, 817-822.

Harman, T. C.; Taylor, P. J.; Walsh, M. P.; LaForge, B. E. *Science* **2002**, 297, 2229-2232.

Heath, J. R.; Shiang, J. J.; Alivisatos, A. P. *J. Chem. Phys.* **1994**, *101*, 1607-1615.

Heiney, P. Datasqueeze Software. http://www.datasqueezesoftware.com/

Henry, A. I.; Courty, A.; Pileni, M. P.; Albouy, P. A.; Israelachvili, J., *Nano Letters* **2008,** 8, (7), 2000-2005.

Hines, M. A.; Scholes, G. D. *Adv. Mater.* **2003**, 15, 1844-1849.

Holmes, J. D.; Ziegler, K. J.; Doty, R. C.; Pell, L. E.; Johnston, K. P.; Korgel, B. A. *J. Am. Chem. Soc.* **2001**, *123*, 3743-3748.

Hoppe, H.; Glatzel, T.; Niggemann, M.; Hinsch, A.; Lux-Steiner, M. C.; Sariciftci, N. S. *Nano Lett.* **2005**, *5*, 269-274.

Houtepen, A. J.; Koole, R.; Vanmaekelbergh, D.; Meeldijk, J.; Hickey, S. G. *J. Am. Chem. Soc.* **2006**, 128, 6792-6793.

Huynh, W. U.; Dittmer, J. J.; Alivisatos, A. P. *Science* **2002**, *295*, 2425-2427.

Hyeon, T.; Lee, S. S.; Park, J.; Chung, Y.; Bin Na, H. *J. Am. Chem. Soc.* **2001,** *123*, 12798-12801.

Israelachvili, J. *Intermolecular & Surface Forces* (2nd ed., Academic Press, San Diego, CA, 1992).

Jiang CS, Noufi R, AbuShama JA, Rmanathan K, Moutinho HR, Pankow J, Al-Jassim MM, *Appl Phys Lett*, **2004**; 84:18.

Johnston, K. W.; Pattantyus-Abraham, A. G.; Clifford, J. P.; Myrskog, S. H.; MacNeil, D. D.; Levina, L.; Sargent, E. H. *Appl. Phys. Lett.* **2008**, 92, 151115.

Jun, Y. W.; Choi, J. S.; Cheon, J. *Angew. Chem., Int. Ed.* **2006,** *45*, 3414-3439.

Kamat, P. V. *J. Phys. Chem. C* **2008**, *112*, 18737-18753.

Kang, I.; Wise, F. W. J. Opt. Soc. Am. B **1997**, 14, 1632-1646.

Katagiri, H.; Jimbo, K.; Maw, W. S. ; Oishi, K. ; Yamazaki, M. ; Araki, H.; Takeuchi, A. *Thin Solid Films* **2009**, *517*, 2455-2460.

Kazmerski LL, *J Electron Spectroscopy*, **2006**; 150:103–135.

Kiely, C. J.; Fink, J.; Brust, M.; Bethell, D.; Schiffrin, D. J. *Nature* **1998,** *396*, 444-446.

Kigel, A.; Brumer, M.; Maikov, G.; Sashchiuk, A.; Lifshitz, E. *Superlattices Microstruct.* **2009**, 46, 272-276.

Klem, E. J. D.; Shukla, H.; Hinds, S.; MacNeil, D. D.; Levina, L.; Sargent, E. H. *Appl. Phys. Lett.* **2008**, 92, 212105.

Koleilat, G. I.; Levina, L.; Shukla, H.; Myrskog, S. H.; Hinds, S.; Pattantyus-Abraham A. G. and Sargent, E. H. *ACS Nano* **2008**, 2,833–840.

Konstantatos, G.; Levina, L.; Fischer, A.; Sargent, E. H., *Nano Letters* **2008**, 8 (5), 1446-1450.

Koo, B.; Patel, R. N.; Korgel, B. A. *J. Am. Chem. Soc.* **2009**, *131*, 3134-3135.

Korgel, B. A., *Physical Review Letters* **2001**, 86, (1), 127-127.

Korgel, B. A.; Fitzmaurice, D. *Phys. Rev. B* **1999**, *59*, 14191-14201.

Korgel, B. A.; Fitzmaurice, D., Small-angle X-ray Scattering Study of Silver-Nanocrystal Disorder-Order Phase Transitions. *Phys. Rev. B* **1999**, *59*, 14191-14201.

Korgel, B. A.; Fullam, S.; Connolly, S.; Fitzmaurice, D. *J. Phys. Chem. B* **1998,** *102*, 8379-8388.

Korgel, B. A.; Zaccheroni, N.; Fitzmaurice, D. *J. Am. Chem. Soc.* **1999**, 121, 3533-3534.

Krebs FC, *Solar Energy Materials & Solar Cells***, 2009**; 93:394–412.

Krebs, F. C. *Sol. Energ. Mat. Sol. C.* **2009**, *93*, 394-412.

Kremer, K.; Robbins, M. O.; Grest, G. S., *Physical Review Letters* **1986,** 57, (21), 2694-2694.

Kudera, S.; Carbone, L.; Casula, M. F.; Cingolani, R.; Falqui, A.; Snoeck, E.; Parak, W. J.; Manna, L. *Nano Lett.* **2005,** *5*, 445-449.

Kumar, A. P.; Reddy, K. V. *Thin Solid Films* **1997**, *304*, 365-370.

Kwak, E. S.; Kang, T. J.; Vanden Bout, D. A. *Anal. Chem.* **2001**, *73*, 3257-3262.

Kwon, K. W.; Lee, B. H.; Shim, M. *Chem. Mater.* **2006,** *18*, 6357-6363.

Landman, U.; Luedtke, W. D., *Faraday Discussions* **2004,** 125, 1-1.

Larsen, T. H.; Sigman, M.; Ghezelbash, A.; Doty, R. C.; Korgel, B. A. *J. Am. Chem. Soc.* **2003**, *125*, 5638-5639.

Law, M.; Luther, J. M.; Song, Q.; Hughes, B. K.; Perkins, C. L.; Nozik, A. J. *J. Am. Chem. Soc.* **2008**, 130, 5974-5985.

Lee, B.; Podsiadlo, P.; Rupich, S.; Talapin, D. V.; Rajh, T.; Shevchenko, E. V. *J. Am. Chem. Soc.* **2009**, 131, 16386-16388.

Lee, D. C.; Smith, D. K.; Heitsch, A. T.; Korgel, B. A. *Annu. Rep. Prog. Chem., Sect. C, Phys. Chem.* **2007,** *103*, 351-402.

Lee, J. H.; Huh, Y. M.; Jun, Y.; Seo, J.; Jang, J.; Song, H. T.; Kim, S.; Cho, E. J.; Yoon, H. G.; Suh, J. S.; Cheon, J. *Nat. Med.* **2007,** *13*, 95-99.

Lee, S.; Bluemle, M. J.; Bates, F. S., *Science* **2010**, 330, (6002), 349-353.

Lee, S.-M.; Jun, Y.-w.; Cho, S.-N.; Cheon, J. *J. Am. Chem. Soc.* **2002**, 124, 11244-11245.

Leschkies, K. S.; Beatty, T. J.; Kang, M. S.; Norris, D. J.; Aydil, E. S. *ACS Nano* **2009**, 3, 3638-3648.

Leslie-Pelecky, D. L.; Rieke, R. D., Magnetic Properties of Nanostructured Materials. *Chemistry of Materials* **1996,** 8, (8), 1770-1783.

Liang Y, Xu Z, Xia J, Tsai ST, Wu Y, Li G, Ray C, Yu L, *Adv. Mater.* **2010**; in press.

Lifshitz, E.; Bashouti, M.; Kloper, V.; Kigel, A.; Eisen, M. S.; Berger, S. *Nano Lett.* **2003**, 3, 857-862.

Liljeroth, P.; Overgaag, K.; Urbieta, A.; Grandidier, B.; Hickey, S. G.; Vanmaekelbergh, D. *Phys. Rev. Lett.* **2006**, 97, 096803.

Lin, Y.-M.; Dresselhaus, M. S. *Phys. Rev. B* **2003**, 68, 075304.

Liu, Y.; Gibbs, M.; Puthussery, J.; Gaik, S.; Ihly, R.; Hillhouse, H. W.; Law, M. *Nano Lett.* **2010**, 10, 1960-1969.

Liz-Marzan, L. M. *Mat. Today* **2004,** *7*, 26-31.

Lu, C.; Chen, Z.; O'Brien, S. *Chem. Mater.* **2008,** *20*, 3594-3600.

Lu, W.; Fang, J.; Ding, Y.; Wang, Z. L. *J. Phys. Chem. B* **2005**, 109, 19219-19222.

Lu, X.; Korgel, B. A.; Johnston, K. P. *Chem. Mater.* **2005**, *17*, 6479-6485.

Luedtke, W. D.; Landman, U. *J. Phys. Chem.* **1996**, *100*, 13323-13329.

Luther, J. M.; Law, M.; Beard, M. C.; Song, Q.; Reese, M. O.; Ellingson R. J. and Nozik, A. J. *Nano Lett.* **2008**, 8, 3488–3492.

Ma, W.; Luther, J. M.; Zheng, H.; Wu Y. and Alivisatos, A. P. *Nano Lett.* **2009**, 9, 1699–1703.

Matsen, M. W.; Bates, F. S., *Macromolecules* **1996**, 29, (4), 1091-1098.

McCandless, B. E. and Shafarman, W. N., U.S. Patent 6,537,845, 2003.

McConnell, G. A.; Lin, M. Y.; Gast, A. P., *Macromolecules* **1995,** 28, (20), 6754-6764.

McDonald, S. A.; Konstantatos, G.; Zhang, S.; Cyr, P. W.; Klem, E. J. D.; Levina, L.; Sargent, E. H. *Nature Mater.* **2005**, 4, 138-142.

McNeill, C. R.; Frohne, H.; Holdsworth, J. L.; Dastoor, P. C. *Nano Lett.* **2004**, *4*, 2503-2507.

McNeill, C. R.; Frohne, H.; Holdsworth, J. L.; Dastoor, P. C. *Synthetic Met.* **2004**, *147*, 101-104.

McNeill, C. R.; Frohne, H.; Holdsworth, J. L.; Furst, J. E.; King, B. V.; Dastoor, P. C. *Nano Lett.* **2004**, *4*, 219-223.

McNeill, C. R.; Watts, B.; Thomsen, L.; Belcher, W. J.; Kilcoyne, A. L. D.; Greenham, N. C.; Dastoor, P. C. *Small* **2006**, *2*, 1432-1435.

Mentzel, T. S.; Porter, V. J.; Geyer, S.; MacLean, K.; Bawendi, M. G.; Kastner, M. A. *Phys. Rev. B* **2008**, 77, 075316.

Michalet, X.; Pinaud, F. F.; Bentolila, L. A.; Tsay, J. M.; Doose, S.; Li, J. J.; Sundaresan, G.; Wu, A. M.; Gambhir, S. S.; Weiss, S. *Science* **2005,** *307*, 538-544.

Micic, O. I.; Curtis, C. J.; Jones, K. M.; Sprague, J. R.; Nozik, A. J. *J. Phys. Chem.* **1994**, *98*, 4966-4969.

Miller, A.; Mackinnon, A.; Weaire, D. *Solid State Physics* **1981**, *36*, 119-175.

Motte, L.; Billoudet, F.; Pileni, M. P. *J. Phys. Chem.* **1995**, *99*, 16425-16429.

Mueller, A. H.; Petruska, M. A.; Achermann, M.; Werder, D. J.; Akhadov, E. A.; Koleske, D. D.; Hoffbauer, M. A.; Klimov, V. I. *Nano Lett.* **2005**, 5, 1039-1044.

Murray, C. B.; Kagan, C. R.; Bawendi, M. G. *Science* **1995**, 270, 1335-1338.

Murray, C. B.; Norris, D. J.; Bawendi, M. G. *J. Am. Chem. Soc.* **1993**, *115*, 8706-8715.

Murray, C. B.; Sun, S.; Gaschler, W.; Doyle, H.; Betley, T. A.; Kagan, C. R. *IBM J. Res. Dev.* **2001**, *45*, 47.

Murray, M. J.; Sanders, J. V. *Philos. Mag. A* **1980,** *42*, 721-740.

Niemegeers, A.; Burgelman M. and De Vos, A., *Appl. Phys. Lett.* **1995**, 67 (6), 843–845.

Noufi R, Axton R, Herrington C, Deb SK, *Appl Phys Lett*, **1984**; 45:668–670.

Olson, D. C.; Shaheen, S. E.; Collins, R. T.; Ginley, D. S. *J. Phys. Chem. C* **2007**, *111*, 16670-16678.

Overgaag, K.; Evers, W.; de Nijs, B.; Koole, R.; Meeldijk, J.; Vanmaekelbergh, D. *J. Am. Chem. Soc.* **2008,** *130*, 7833-7835.

Paier, J.; Asahi, R.; Nagoya, A.; Kresse, G. *Phys. Rev. B* **2009**, *79*, 115126.

Palermo, V. et al., *J. Am. Chem. Soc.* **2008**, *130*, 14605-14614.

Palermo, V.; Palma, M.; Samori, P. *Adv. Mater.* **2006**, *18*, 145-164.

Panthani, M. G.; Akhavan, V.; Goodfellow, B.; Schmidtke, J. P.; Dunn, L.; Dodabalapur, A.; Barbara, P. F.; Korgel, B. A. *J. Am. Chem. Soc.* **2008**, *130*, 16770-16777.

Pellegrino, T.; Fiore, A.; Carlino, E.; Giannini, C.; Cozzoli, P. D.; Ciccarella, G.; Respaud, M.; Palmirotta, L.; Cingolani, R.; Manna, L. *J. Am. Chem. Soc.* **2006,** *128*, 6690-6698.

Pérez-Dieste, V.; Castellini, O. M.; Crain, J. N.; Eriksson, M. A.; Kirakosian, A.; Lin, J. L.; McChesney, J. L.; Himpsel, F. J.; Black, C. T.; Murray, C. B. *Appl. Phys. Lett.* **2003**, 83, 5053-5053.

Persson C, Zunger A, *Phys Rev Lett*, **2003**; 91:26.

Pingree, L. S. C.; Reid, O. G.; Ginger, D. S. *Nano Lett.* **2009**, *9*, 2946-2952.

Pingree, L. S. C.; Reid, O. G.; Ginger, D. S.; *Adv. Mater.* **2009**, *21*, 19-28.

Podsiadlo, P.; Krylova, G. V.; Demortière, A.; Shevchenko, E. V., *Journal of Nanoparticle Research* **2011,** 13, (1), 15-32.

Powalla, M.; Dimmler, B. *Thin Solid Films* **2000**, *361-362*, 540-546.

Pudov,A. O.; Sites, J. R.; Contreras, M. A.; Nakada T. and Schock, H.–W. *Thin Solid Films* **2005**,480–481, 273–278.

Pusey, P. N.; van Megen, W.; Bartlett, P.; Ackerson, B. J.; Rarity, J. G.; Underwood, S. M., *Physical Review Letters* **1989,** 63, (25), 2753-2753.

Rabideau, B. D.; Bonnecaze, R. T. *Langmuir* **2004,** *20*, 9408-9414.

Rasch, M. R.; Rossinyon, E.; Hueso, J. L.; Goodfellow, B. W.; Arbiol, J.; Korgel, B. A., *Nano Letters* **2010**, 10, (9), 3733-3739.

Rau, U. and Schock, H. W., *Appl. Phys. A,* **1999**, 69, 131–147.

Redl, F. X.; Cho, K. S.; Murray, C. B.; O'Brien, S. *Nature* **2003,** *423*, 968-971.

Repins, I.; Contreras, M. A.; Egaas, B.; DeHart, C.; Scharf, J.; Perkins, C. L.; To, B.; Noufi, R. *Prog. Photovoltaics* **2008**, *16*, 235-239.

Ridley, B. A.; Nivi, B.; Jacobson, J. M. *Science* **1999**, 286, 746-749.

Riehn, R.; Stevenson, R.; Richards, D.; Kang, D.-J.; Blamire M.; Downes,, A.; Cacialli, F. *Adv. Funct. Mater.* **2006**, *16*, 469-476.

Robel, I.; Lin, X.-M.; Sprung, M.; Wang, J. *J. Phys.: Condens. Matter* **2009**, 21, 264011-264011.

Rockett, A.; Birkmire, R. W. *J. App. Phys.* **1991**, *70*, R81-R97.

Rogach, A. L. *Angew. Chem., Int. Ed.* **2004,** *43*, 148-149.

Romero, M. J.; Morfa, A. J.; Reilly, T. H.; van de Lagemaat, J.; Al-Jassim, M. *Nano Lett.* **2009**, *9*, 3904-3908.

Rozanski, L. J.; Cone, C. W.; Ostrowski, D. P.; Vanden Bout, D. A. *Macromolecules* **2007**, *40*, 4524-4529.

Ruland, W.; Smarsly, B. M.; *J. Appl. Crystallogr.* **2007**, *40*, 409-417.

Rupich, S. M.; Shevchenko, E. V.; Bodnarchuk, M. I.; Lee, B.; Talapin, D. V., *Journal of the American Chemical Society* **2010,** 132, (1), 289-296.

Sandhyarani, N.; Antony, M. P.; Selvam, G. P.; Pradeep, T. *J. Chem. Phys.* **2000**, 113, 9794-9794.

Sarasqueta, G.; Choudhury, K. R.; So, F. *Chem. Mat.* **2010**, 22, 3496-3501.

Saunders, A. E.; Korgel, B. A. *ChemPhysChem* **2005,** *6*, 61-65.

Saunders, B. R.; Turner, M. L. *Adv. Colloid Interfac.* **2008**, *138*, 1-23.

Scheer, R.; Walter, T.; Schock, H. W.; Fearheiley, M. L.; Lewerenz, H. J. *Appl. Phys. Lett.* **1993**, *63*, 3294-3296.

Schock, H.-W.; Noufi, R. *Prog. Photovoltaics Res. Appl.* **2000**, *8*, 151-160.

Schofield, A. B.; Pusey, P. N.; Radcliffe, P. *Phys. Rev. E* **2005,** *72*, 031407.

Scofield, J. H.; Duda, A.; Albin, D.; Ballard, B. L.; Predecki, P. K. *Thin Solid Films* **1995**, *260*, 26-31.

Seddon, J. M.; Templer, R. H., Polymorphism of lipid-water systems. In Handbook of Biological Physics, Lipowsky, R.; Sackmann, E., Eds. 1995; Vol. 1A, pp 97-160.

Shevchenko, E. V.; Kortright, J. B.; Talapin, D. V.; Aloni, S.; Alivisatos, A. P. *Adv. Mater.* **2007,** *19*, 4183-4188.

Shevchenko, E. V.; Ringler, M.; Schwemer, A.; Talapin, D. V.; Klar, T. A.; Rogach, A. L.; Feldmann, J.; Alivisatos, A. P. *J. Am. Chem. Soc.* **2008,** *130*, 3274-3275.

Shevchenko, E. V.; Talapin, D. V.; Kotov, N. A.; O'Brien, S.; Murray, C. B. *Nature* **2006,** *439*, 55-59.

Shevchenko, E. V.; Talapin, D. V.; Murray, C. B.; O'Brien, S. *J. Am. Chem. Soc.* **2006,** *128*, 3620-3637.

Shevchenko, E. V.; Talapin, D. V.; O'Brien, S.; Murray, C. B. *J. Am. Chem. Soc.* **2005,** *127*, 8741-8747.

Shi, W. L.; Zeng, H.; Sahoo, Y.; Ohulchanskyy, T. Y.; Ding, Y.; Wang, Z. L.; Swihart, M.; Prasad, P. N. *Nano Lett.* **2006,** *6*, 875-881.

Shipway, A. N.; Katz, E.; Willner, I. ChemPhysChem **2000**, 1, 18-52.

Sigman, M. B.; Saunders, A. E.; Korgel, B. A. *Langmuir* **2004,** *20*, 978-983.

Singh PP, Singh S, *Renewable Energy*, **2010**; 35:563–569.

Smilgies, D.-M.; Blasini, D. R. *J. Appl. Crystallogr*. **2007**, 40, 716–718.

Smith, D. K.; Goodfellow, B.; Smilgies, D.-M.; Korgel, B. A., *J. Am. Chem. Soc.* **2009**, *131*, 3281-3290.

Smith, D. K.; Luther, J. M.; Semonin, O. E.; Nozik, A. J.; Beard, M. C. *ACS Nano* **2011**, 5, 183-190.

Spanggaard, H.; Krebs, F. C. *Sol. Energ. Mat. Sol. C.* **2004**, *83*, 125-146.

Steckel, J. S.; Coe-Sullivan, S.; Bulovic, V.; Bawendi, M. G. *Adv. Mater.* **2003**, 15, 1862-1866.

Steinhagen, C.; Panthani, M. G.; Akhavan, V.; Goodfellow, B.; Koo B. and Korgel, B. A. *J. Am. Chem. Soc.*,**2009**, 131, 12554–12555.

Sun, B.; Sirringhaus, H. Nano Lett. **2005**, 5, 2408-2413.

Sutter, E.; Sutter, P.; Zhu, Y. Nano Lett. **2005**, 5, 2092-2096.

Swanson RM, *Proceedings of the 31st IEEE Conference*. IEEE, New York, 2005. 889–894

Sykora, M.; Koposov, A. Y.; McGuire, J. A.; Schulze, R. K.; Tretiak, O.; Pietryga, J. M.; Klimov, V. I. *ACS Nano* **2010**, 4, 2021-2034.

Takagi, M. *J. Phys. Soc. Jpn.* **1954**, 9, 359-363.

Talapin, D. V.; Murray, C. B. *Science* **2005**, 310, 86-89.

Talapin, D. V.; Shevchenko, E. V.; Bodnarchuk, M. I.; Ye, X.; Chen, J.; Murray, C. B., *Nature* 2009, 461, (7266), 964-967.

Talapin, D. V.; Shevchenko, E. V.; Murray, C. B.; Titov, A. V.; Král, P., *Nano Lett.* **2007**, *7*, 1213-1219.

Talapin, D. V.; Yu, H.; Shevchenko, E. V.; Lobo, A.; Murray, C. B. *J. Phys. Chem. C* **2007**, 111, 14049-14054.

Tam, E.; Podsiadlo, P.; Shevchenko, E.; Ogletree, D. F.; Delplancke-Ogletree, M.-P.; Ashby, P. D., *Nano Letters* **2010,** 10, (7), 2363-2367.

Tao M, *Electrochemical Society Interface*. **2008**; 17:30-35.

Tate, M. P.; Urade, V. N.; Kowalski, J. D.; Wei, T. C.; Hamilton, B. D.; Eggiman, B. W.; Hillhouse, H. W. *J. Phys. Chem. B* **2006,** *110*, 9882-9892.

Teetsov, J.; Vanden Bout, D. A. *Langmuir* **2002**, *18*, 897-903.

Thantsha, N. M.; Macabebe, E. Q. B.; Vorster, F. J;. van Dyk, E. E. *Physica B-Condensed Matter* **2009**, *404*, 4445-4448.

Thomas, E. L.; Kinning, D. J.; Alward, D. B.; Henkee, C. S., *Macromolecules* **1987,** 20, (11), 2934-2939.

Tomaev, V. V.; Makarov, L. L.; Tikhonov, P. A.; Solomennikov, A. A. *Glass Phys. Chem.* **2004**, 30, 349-355.

Urban, J. J.; Talapin, D. V.; Shevchenko, E. V.; Kagan, C. R.; Murray, C. B. *Nat. Mater.* **2007,** *6*, 115-121.

van Dyk, E.E.; Meyer, E.L. *Renew. Energ.* **2004**, *29*, 333-344.

van Huis, M. A.; Kunneman, L. T.; Overgaag, K.; Xu, Q.; Pandraud, G.; Zandbergen, H. W.; Vanmaekelbergh, D. *Nano Lett.* **2008**, 8, 3959-3963.

Wadia, C.; Alivisatos, A. P.; Kammen, D. M. *Environmental Science & Technology* **2009**, *43*, 2072-2077.

Wang, N.; Cao, X.; Guo, L.; Yang, S.; Wu, Z. *ACS Nano* **2008**, 2, 184-190.

Wang, R. Y.; Feser, J. P.; Lee, J.-S.; Talapin, D. V.; Segalman, R.; Majumdar, A. *Nano Lett.* **2008**, 8, 2283-2288.

Wehrenberg, B. L.; Wang, C.; Guyot-Sionnest, P. *J. Phys. Chem. B* **2002**, 106, 10634-10640.

Wei, S.-H.; Zhang, S. B.; Zunger, A. *Appl. Phys. Lett.* **1998**, *72*, 3199-3201.

Whetten, R. L.; Khoury, J. T.; Alvarez, M. M.; Murthy, S.; Vezmar, I.; Wang, Z. L.; Stephens, P. W.; Cleveland, C. L.; Luedtke, W. D.; Landman, U., *Adv. Mater.* **1996**, *8*, 428-433.

Whetten, R. L.; Shafigullin, M. N.; Khoury, J. T.; Schaaff, T. G.; Vezmar, I.; Alvarez, M. M.; Wilkinson, A. *Acct. Chem. Res.* **1999**, *32*, 397-406.

Winey, K. I.; Thomas, E. L.; Fetters, L. J., *Journal of Chemical Physics* **1991**, 95, (12), 9367-9367.

Wu, Y.; Wadia, C.; Ma, W.; Sadtler, B.; Alivisatos, A. P. *Nano Lett*. **2008**, *8*, 2551-2555.

Xu, B. S.; Tanaka, S. I. *Acta Mater.* **1998**, 46, 5249-5257.

Yang, X.; Loos, J. *Macromolecules* **2007**, *40*, 1353-1362.

Ye, X.; Chen, J.; Murray, C. B., *Journal of the American Chemical Society* **2011,** 133, (8), 2613-2620.

Yu, H.; Chen, M.; Rice, P. M.; Wang, S. X.; White, R. L.; Sun, S. H. *Nano Lett.* **2005,** *5*, 379-382.

Zeng, H.; Li, J.; Liu, J. P.; Wang, Z. L.; Sun, S. *Nature* **2002,** *420*, 395-398.

Zhao, N.; Osedach, T. P.; Chang, L.-Y.; Geyer, S. M.; Wanger, D.; Binda, M. T.; Arango, A. C.; Bawendi, M. G.; Bulovic, V. *ACS Nano* **2010**, 4, 3743-3752.

Zhao, Z.; Zhang, K.; Zhang, J.; Yang, K.; He, C.; Dong, F.; Yang, B. *Colloids Surf., A* **2010**, 355, 114-120.

Vita

Brian William Goodfellow graduated from Dutch Fork High School in Irmo South Carolina in 2002 and went on to attend Cornell University in the fall of that year. In May of 2006, he graduated with a Bachelor of Science degree in Materials Science and Engineering. After graduation, he moved to Austin, Texas to pursue a Doctorate of Philosophy in Chemical Engineering at the University of Texas at Austin where he studied under the supervision of Dr. Brian A. Korgel in nanomaterials science and engineering. In April of 2012, he will join the Dow Chemical Company as a Senior Research Engineer in the Core Research and Development organization in Midland, Michigan.

Email address: bgoodfellow@utexas.edu

This dissertation was typed by the author.